

UNIVERSIDAD DE GRANADA



Tesis Doctoral

A Discontinuous Galerkin Finite Element Method for the Time-Domain Solution of Maxwell Equations

Memoria presentada por

Jesús Álvarez González

para optar al grado de Doctor por la Universidad de Granada

realizada en la

Facultad de Ciencias

Departamento de Electromagnetismo y Física de la Materia

Grupo de Electromagnetismo de Granada

en el programa de doctorado

Física y Ciencias del Espacio

Bajo la dirección de los Doctores

Amelia Rubio Bretones y Salvador González García

Editor: Editorial de la Universidad de Granada
Autor: Jesús Álvarez González
D.L.: GR 617-2014
ISBN: 978-84-9028-843-6

El doctorando **Jesús Álvarez González** y los directores de la tesis **D^a. Amelia Rubio Bretones** y **D. Salvador González García**, garantizamos, al firmar esta tesis doctoral, que el trabajo ha sido realizado por el doctorando bajo la dirección de los directores de la tesis y hasta donde nuestro conocimiento alcanza, en la realización del trabajo, se han respetado los derechos de otros autores a ser citados, cuando se han utilizado sus resultados o publicaciones.

Granada, dieciocho de Julio de dos mil trece

Director/es de la Tesis

Doctorando

Fdo. Amelia Rubio Bretones

Fdo. Jesús Álvarez González

Fdo. Salvador González García

Declaración de Autoría

D^a. Amelia Rubio Bretones, Doctora en Ciencias Físicas, Catedrática de Electromagnetismo del Departamento de Electromagnetismo y Física de la Materia de la Facultad de Ciencias de la Universidad de Granada,

y

D. Salvador González García, Doctor en Ciencias Físicas, Profesor Titular de Electromagnetismo del Departamento de Electromagnetismo y Física de la Materia de la Facultad de Ciencias de la Universidad de Granada,

CERTIFICAN

Que el trabajo de investigación que se presenta en esta Memoria, titulado A DISCONTINUOUS GALERKIN FINITE ELEMENT METHOD FOR THE TIME-DOMAIN SOLUTION OF MAXWELL EQUATIONS, ha sido realizado en este Departamento por el Ingeniero de Telecomunicación D. Jesús Álvarez González bajo nuestra dirección, y constituye su Tesis Doctoral.

Con esta fecha autorizamos su presentación ante la Comisión de Doctorado de la Universidad de Granada.

Granada, dieciocho de Julio de dos mil trece

Fdo. Amelia Rubio Bretones

Fdo. Salvador González García

“The computer offers another kind of creativity. You cannot ignore the creativity that computer technology can bring. But you need to be able to move between those two different worlds.”

“La computadora ofrece otro tipo de creatividad. No se puede ignorar la creatividad que puede aportar la tecnología de los ordenadores. Pero hay que tener la capacidad para moverse entre esos dos mundos diferentes.”

Tadao Ando

Agradecimientos

En esta página me gustaría agradecer a aquellos que han contribuido, ya sea con su apoyo, cariño y comprensión, o con su esfuerzo personal en transmitirme el conocimiento y la capacidad para llevar a cabo este trabajo.

Empezando por el final, debo en primer lugar agradecer a Salvador González por haber creído que esto era posible y haber trabajado tanto para conseguirlo, y a Amelia Rubio por su ayuda y generosidad.

A todo el Grupo de Electromagnetismo de Granada, en especial a Luis Díaz Angulo, mi compañero de estudios con el que he discutido y compartido dudas.

Sin duda, a José Manuel Alonso que generosamente me ha dado las herramientas y enseñado los métodos necesarios para poder estar por encima del sobresaliente.

A Antonio Martínez por enseñarme la profesión de ingeniero.

Debo agradecer la enorme paciencia de mis compañeros durante estos cinco años, Gema Soria, David Aparicio, David Manceras y Raúl Molero. En especial a Helena Carbajosa, por ayudarme a hacer las cosas más complicadas, y por su alegría.

Quiero también agradecer a mis amigos de siempre y para siempre, en especial a Sergio, por su enorme apoyo y comprensión, además de sus consejos.

Finalmente, a mis padres, Pedro y Pauli, papá y mamá, por su amor, infinito sacrificio y constante apoyo, y por los mismos motivos a mi hermana Ana, además de por su comprensión.

A todos sinceramente,

Gracias.

THE WORK DESCRIBED IN THIS DISSERTATION HAS BEEN PARTIALLY FUNDED THROUGH THE EUROPEAN COMMUNITY'S SEVENTH FRAMEWORK PROGRAMME FP7/2007-2013, UNDER GRANT AGREEMENT NO 205294 (HIRF SE PROJECT), AND THROUGH THE SPANISH NATIONAL PROJECTS TEC2010-20841-C04-04, CSD2008-00068, AND THE JUNTA DE ANDALUCIA PROJECT P09-TIC-5327.

Abstract

This dissertation deals with the development of efficient numerical techniques for the analysis of realistic problems of electromagnetic propagation, radiation, scattering, and coupling. For this purpose, the Discontinuous Galerkin (DG) methodology and its application to solve Maxwell equations in time domain is investigated. The main contributions are based on the combination of the efficient Leap-Frog (LF) time-integration scheme, together with a Local Time-Stepping (LTS) algorithm, with the DG spatial discretization method. The final approach is referred to as Leap-Frog Discontinuous Galerkin (LFDG) algorithm.

The DG formulation, in its semi-discrete form, is developed in a general framework which unifies different flux-evaluation schemes successfully applied to this method. A wide range of functionalities are developed in the DG context, such as typical boundary conditions (perfect electric/magnetic conductors, first-order Silver-Müller boundary condition, material interface), anisotropic materials modelization, electromagnetic sources (plane-waves, coaxial or waveguide ports, and delta-gap), and conformal uniaxial perfectly matched layer truncation condition. The LF scheme is applied to the semi-discrete DG formulation, rendering the LFDG algorithm, and a fully explicit LTS strategy is proposed in combination with the LFDG algorithm.

The DG semi-discrete scheme and the LFDG algorithm have been analyzed, and the accuracy limits and the computational cost of the LFDG method have been assessed. Firstly, the topic of spurious modes is revisited in the DG context, and the numerical spectrums of both schemes are studied. Then, the numerical dispersion and dissipation relationships, and the convergence and anisotropy of the errors of the DG and LFDG methods are compared and analyzed. Finally, a computational cost vs. accuracy analysis of the LFDG method is performed, including a comparison with the finite-difference time-domain method.

The LFDG algorithm has been implemented in a scalable parallel manner, making use of a hybrid OMP-MPI programming technique. The inherent DG parallelism is exploited, showing the capability of the method to deal with electrically large problems, keeping accuracy under control, and considering geometrical small details thanks to the use of the LTS strategy. The LFDG method is applied to different kinds of electromagnetic problems. Some of the results have been compared with measurements and others with results found with other computational methods. The algorithm, finally, is validated and the attractive properties of the LFDG method, which combines all the advantages of time-domain and finite-element methods, are demonstrated.

Contents

Declaración de Autoría	v
Agradecimientos	ix
Abstract	xiii
List of Figures	xix
List of Tables	xxiii
Abbreviations	xxv
Symbols	xxix
1 Introduction and Previous Work	1
1.1 Overview of Computational Electromagnetics	1
1.2 Discontinuous Galerkin Time Domain Survey	4
1.2.1 Background	4
1.2.2 Analysis, Improvements and Alternatives of the Discontinuous Galerkin Methods	6
1.2.3 Capabilities and Applications of Discontinuous Galerkin Time Do- main Methods	9
1.3 Motivation behind this work	11
1.4 Organization of the manuscript	13
2 Finite-Element Time-Domain Methods: Fundamentals	15
2.1 Space Discretization	16
2.2 Vector-Fields Discretization	19
2.2.1 Mapping Vector-Basis Functions to Curvilinear Elements	20
2.3 Finite-Element Time-Domain Methods	22
2.3.1 Single-Field Schemes	23
2.3.2 Dual-Field Schemes	24
2.3.2.1 E-B Finite-Element Time-Domain Method	25
2.3.2.2 E-H Finite-Element Time-Domain Method	27

3	Discontinuous Galerkin Time-Domain Methods: The Leap-Frog Discontinuous Galerkin Algorithm	31
3.1	Discontinuous Galerkin Formulation	31
3.1.1	Semi-Discrete Scheme Formulation	32
3.1.2	Boundary Conditions	38
3.2	Numerical-Flux Evaluation	39
3.2.1	Centered-Flux Evaluation	41
3.2.2	Upwind-Flux Evaluation	42
3.2.3	Partially Penalized Flux Evaluation	47
3.3	Discontinuous Galerkin for Anisotropic Materials	47
3.3.1	Flux Evaluation	48
3.3.2	Semi-Discrete Scheme Formulation	52
3.4	Absorbing Boundary Conditions	53
3.4.1	Conformal Uniaxial Perfectly Matched Layer Formulation	54
3.4.2	Discontinuous Galerkin Semi-Discrete Scheme Formulation	60
3.5	Temporal Integration	61
3.5.1	Runge-Kutta Scheme	62
3.5.2	Leap-Frog Scheme	63
3.5.2.1	Leap-Frog Discontinuous Galerkin Algorithm	64
3.5.2.2	The LFDG algorithm in PML regions	65
3.5.2.3	Local Time-Stepping Algorithm	66
3.6	Summary	70
4	Numerical Analysis: Accuracy, Stability, Dispersion and Dissipation	73
4.1	General Analysis of the Discontinuous Galerkin Semi-Discrete Scheme	74
4.1.1	Numerical Dispersion and Dissipation of the DG Semi-Discrete Scheme	75
4.1.2	Extension to Three Dimensions	80
4.2	Analysis of the Leap-Frog DG Algorithm	84
4.2.1	Eigenvalue Problem Setup of the LFDG Algorithm	84
4.2.2	Stability Analysis of the LFDG Algorithm	85
4.2.3	Numerical Results of the LFDG Eigen-Problem	87
4.3	Convergence of the Numerical Errors	89
4.3.1	Numerical Experiment	95
4.4	Anisotropy of the Numerical Errors	95
4.5	Computational Cost vs. Accuracy Analysis	101
4.6	Summary	104
5	Application and Validation	105
5.1	Microwave Filters	106
5.1.1	PEC Microwave Filter	106
5.1.2	Microwave Filter with Dielectric Material	108
5.2	Wideband Antennas	112
5.2.1	Antenna Feeding Models in DG	113
5.2.2	Wideband Bicone Antenna	115
5.2.3	Onboard Antenna Modeling	119
5.3	Estimation of the RCS of LO Targets	120

5.4	High Intensity Radiated Fields	128
5.4.1	Medium size 3D Object	128
5.4.2	Aircraft Simulation Case	130
5.5	Anisotropic Materials	137
5.6	Summary	138
6	Conclusion and Further Work	139
6.1	Contributions	139
6.2	Further Work	140
A	SEMBA: A parallel LFDG Computer Code for EM Analysis and Design	143
A.1	Description of SEMBA	143
A.2	Geometrical Discretization	144
A.3	Mesh Preprocessing	144
A.3.1	Mesh Distribution	145
A.3.2	Selection of the Basis Function	146
A.3.3	LTS Level Classification	146
A.4	Capabilities	148
A.4.1	Materials and Boundary Conditions	148
A.4.2	Electromagnetic Sources	149
A.4.3	General Time-Marching Algorithm	150
A.5	Postprocessing	151
A.6	Performance	152
B	Resumen de la Memoria	155
B.1	Contribuciones Científicas y Futuras Líneas de Trabajo	156
B.1.1	Contribuciones Científicas	156
B.1.2	Futuras Líneas de Trabajo	157
	Bibliography	161
	List of Publications	177
	Curriculum Vitae	181

List of Figures

1.1	Classification of purely numerical 3D computational electromagnetic methods.	2
2.1	Mapping from the reference tetrahedra to real cells.	17
3.1	Flux evaluation setup, without sources.	41
3.2	Riemann problem solution for homogeneous materials.	45
3.3	Riemann problem solution for anisotropic materials.	51
3.4	Conformal UPML setup.	55
3.5	Definition of a conformal UPML making use of canonical geometries.	60
3.6	2D classification example of two LTS levels and the interface.	67
3.7	Initial state of the LTS algorithm.	67
3.8	Sequence of the LTS algorithm (L=2).	69
4.1	Numerical dispersion and dissipation for scalar 1D-DGTD, centered flux.	78
4.2	Numerical dispersion and dissipation for scalar 1D-DGTD, upwind flux.	79
4.3	Geometry under analysis for the eigenvalue problem.	80
4.4	Periodic boundary condition.	81
4.5	Spectrum of the DG operator.	82
4.6	Cubic PEC cavity.	83
4.7	Power spectrum PEC cavity.	83
4.8	Stability analysis of the LFDG algorithm. Dependence with τ parameter.	86
4.9	Spectrum of the LFDG operator.	88
4.10	Spectrum of the LFDG operator for Δt close to Δt_{max}	89
4.11	Convergence of the dispersion, dissipation and global errors of the DG operator.	91
4.12	Convergence and influence of the τ parameter in the error of the DG operator.	92
4.13	Convergence of the dispersion, dissipation and global errors of the LFDG algorithm.	93
4.14	Influence of Δt in the error of the LFDG algorithm.	94
4.15	Convergence of the dispersion (left) and dissipation (right) errors of the LFDG algorithm computed with the numerical test (NT) and with the eigenvalue analysis (E). We have used in both cases $\tau = 0.1$, and $p = 2$. Analogous curves for the DG operator have been included for comparison.	96
4.16	Anisotropy of the error for $\tau = 0.1$, $p = 1$ and $h = 0.025$	97
4.17	Anisotropy of the error for $\tau = 0.1$, $p = 2$ and $h = 0.2$	98
4.18	Anisotropy of the error for $\tau = 0.1$, $p = 3$ and $h = 0.25$	99
4.19	Cuts of the dispersion error.	100

4.20	Computational cost of the LFDG algorithm.	103
5.1	Problem setup for the filter 1.	107
5.2	Filter 1 near fields.	109
5.3	Filter 1 response.	110
5.4	Filter 1 energy.	110
5.5	Problem setup for the filter 2.	111
5.6	Filter 2 energy.	111
5.7	Filter 2 response.	112
5.8	Delta-gap source model.	115
5.9	Conical antenna simulation-case.	116
5.10	Wideband biconical antenna.	117
5.11	Simulation setup of the wideband bicone antenna.	118
5.12	Distribution of the Δt_{MAX} with the elements.	118
5.13	Screenshots of the simulation of the wideband biconical antenna.	120
5.14	S11 and input impedance of the wideband bicone antenna.	121
5.15	Radiation patterns of the wideband bicone antenna.	121
5.16	V/UHF antenna installed on a infinite ground plane.	122
5.17	Theta vs. phi radiation patterns with the V/UHF antenna installed on an infinite ground plane.	122
5.18	V/UHF antenna integration concept.	123
5.19	Installed V/UHF antenna simulation setup.	123
5.20	Input impedance with the V/UHF antenna installed on the leading edge of the fin.	124
5.21	Radiation patterns for the V/UHF antenna installed in the leading edge of the fin at 132 MHz.	124
5.22	Radiation patterns for the V/UHF antenna installed in the leading edge of the fin at 312 MHz.	125
5.23	Geometry of the NASA almond.	126
5.24	Simulation setup for the NASA Almond.	127
5.25	Bistatic Radar Cross Sections of the NASA almond at 1 GHz.	129
5.26	Monostatic radar cross sections of the NASA almond.	130
5.27	Setup of the medium size 3D object.	131
5.28	Reception aperture results of the medium size 3D object.	132
5.29	Screenshots of the meshes of the medium size 3D object	132
5.30	External and internal geometry of the aircraft simulation case.	133
5.31	Simulation setup for the aircraft-simulation case.	134
5.32	Screenshots of the aircraft-simulation case.	135
5.33	Computed transfer functions for the aircraft-simulation case.	135
5.34	Bistatic RCS of an isotropic/anisotropic sphere.	138
A.1	Geometrical discretization.	144
A.2	Distribution of the mesh among the different MPI processes.	145
A.3	Selection of the expansion function.	147
A.4	Example of a distribution of maximum time step in a real problem.	147
A.5	Example of a LTS level classification.	148
A.6	Total field/scattered field decomposition.	150
A.7	MPI communication and updating schemes.	151

A.8 SEMBA scalability 153

List of Tables

3.1	Parameters to yield centered, upwind, and partially penalized numerical fluxes.	34
3.2	Coefficients for optimal 5-stage, 4 th order, 2N-Storage RK scheme.	64
4.1	Results of the numerical stability analysis of the LFDG algorithm.	87
4.2	Results of the computational cost analysis.	102
5.1	Number of elements for each set of basis functions for the DMCWF.	106
5.2	Local time-stepping level distribution for the DMCWF.	106
5.3	Computational requirements for the DMCWF.	108
5.4	Single resonator simulation description.	112
5.5	Number of elements in each local time-stepping level and interface for the biconical simulation case.	117
5.6	Number of elements for each set of basis functions for the biconical simulation case.	119
5.7	Number of elements for each set of basis functions for the aircraft simulation case.	136
5.8	Local time-stepping level distribution for the aircraft simulation case.	136
5.9	FDTD vs LFDG comparison for the aircraft simulation case.	136

Abbreviations

ABC	Absorbing B oundary C ondition
ADE	Auxiliary D ifferential E quation
ADER	Arbitrary DER ivatives in space and time
BEM	Boundary E lement M ethod
BI	Boundary I ntegral
C	Conformal
CAD	Computer- A ided D esign
CASA	Construcciones A eronauticas S ociedad A nónima
CCCIE	Combined C urrent and C harge I ntegral E quations
CEM	C omputational E lectro M agnetics
CFD	Computation F luid- D ynamics
CG	Continuous G alerkin
CPU	Central P rocessing U nit
dB	deci B el
DG	Discontinuous G alerkin
DGTD	Discontinuous G alerkin in T ime D omain
DMCWF	Dual-Mode C ircular W aveguide F ilter
dof	degrees of freedom
EADS	E uropean A eronautic D efence and S pace company
EM	E lectro M agnetism
EMC	E lectro M agnetic C ompatibility
EMI	E lectro M agnetic I nterference
FD	F requency D omain
FDFD	F inite D ifference in F requency D omain
FDTD	F inite D ifference in T ime D omain

FEM	F inite E lement M ethod
FEMTD	F inite E lement M ethod in T ime D omain
FIT	F inite I ntegral T echnique
FVTD	F inite V olume in T ime D omain
GHz	G iga H ertz
GO	G eometrical O ptics
GPR	G round P enetrating R adar
GPU	G raphics P rocessing U nit
GTD	G eometrical T heory of D iffraction
HIRF	H igh I ntensity R adiated F ields
IBC	I mpedance B oundary C ondition
LDG	L ocal D iscontinuous G alerkin
LF	L eap- F rog
LFDG	L eap- F rog D iscontinuous G alerkin
LLSF	L ow L evel S wept F ield
LO	L ow O bservability
LSRK	L ow- S torage R unge- K utta
LTS	L ocal T ime S tepping
Mcells	M illions of C ells
MHz	M ega H ertz
MLFMM	M ultilevel F ast M ultipole M ethod
MLFMA	M ultilevel F ast M ultipole A lgorithm
MoM	M ethod of M oments
MPI	M essage P assing I nterface
ODE	O rdinary D ifferential E quation
OMP	O pen M ulti- P rocessing
O2	O rders 2
PBC	P eriodic B oundary C ondition
PDE	P artial D ifferential E quation
PEC	P erfect E lectric C onductor
PMC	P erfect M agnetic C onductor
PML	P erfectly M atched L ayer
PO	P hysical O ptics

PTD	Physical Theory of Diffraction
RMA	Radar Absorber Material
RCS	Radar Cross-Section
RK	Runge-Kutta
RK4	4th-order Runge-Kutta
RKDG	Runge-Kutta Discontinuous Galerkin
SFZ	Scattered-Field Zone
SM	Silver-Müller
SMA	SubMiniature version A
SSP	Strong Stability Preserving
TD	Time Domain
TEM	Transverse ElectroMagnetic
TFZ	Total-Field Zone
TLM	Transmission Line Matrix
TWTD	Thin Wire Time Domain
UHF	Ultra High Frequency
UPML	Uniaxial Perfectly Matched Layer
UTD	Uniform Geometrical Theory of Diffraction
VHF	Very High Frequency
VSWR	Voltage Standing-Wave Ratio
1D	One Dimension
2D	Two Dimensions
3D	Three Dimensions

Symbols

x, X	Scalar
\mathbf{x}, \mathbf{X}	Vector
$A_x, \mathbf{A} _x$	Component x of the vector A
$\hat{\mathbf{x}}$	Unit vector
$\hat{\mathbf{n}}$	Outward-pointing normal vector of a referred surface or face of a tetrahedron
\mathbb{M}	Matrix
$\bar{\bar{R}}$	Tensor
\tilde{X}	Numerical approximation of X
\mathcal{T}_m	Volume of the m^{th} element
$\partial\mathcal{T}_m$	Boundaries of the m^{th} element
\mathbb{R}^3	Three space dimension
J	Jacobian matrix
ϕ_i^m	Vector-basis function of index i , defined in the element m
$\frac{d}{dx}, d_x$	Differential operator with respect to variable x
$\frac{\partial}{\partial x}, \partial_x$	Partial differential operator with respect to variable x
$\nabla \times \mathbf{X}$	Curl operation on a vector \mathbf{X}
∇X	Gradient operation on a variable X
$\langle \mathbf{u}, \mathbf{v} \rangle_{\mathcal{T}_m}$	Inner product in the volume \mathcal{T}_m
$\ \mathbf{u}\ _{\mathcal{T}_m}^2$	Norm in the volume \mathcal{T}_m
$\langle \mathbf{u}, \mathbf{v} \rangle_{\partial\mathcal{T}_m}$	Inner product in the surface $\partial\mathcal{T}_m$
B	Magnetic flux density (Wb m ⁻¹)
D	Electric flux density (C m ⁻²)
E	Electric field intensity (V m ⁻¹)

\mathbf{H}	Magnetic field intensity (A m^{-1})
\mathbf{J}	Polarization current (A m^{-2})
\mathbf{M}	magnetization current (V m^{-2})
\mathbf{J}_{imp}	Impressed electric current density (A m^{-2})
\mathbf{J}_s	Surface electric current density (A m^{-1})
\mathbf{M}_s	Surface magnetic current density (V m^{-1})
μ	Magnetic permeability (H m^{-1})
μ_0	Magnetic permeability of vacuum ($4\pi \cdot 10^{-7} \text{ H m}^{-1}$)
μ_r	Relative magnetic permeability
ε	Electric permittivity (F m^{-1})
ε_0	Electric permittivity of vacuum ($8.854187805806633 \cdot 10^{-12} \text{ F m}^{-1}$)
ε_r	Relative electric permittivity
c	Speed of a electromagnetic wave (m s^{-1})
c_0	Speed of a electromagnetic in vacuum ($299792458.2 \text{ m s}^{-1}$)
σ_e	Electric conductivity (S m^{-1})
σ_m	Magnetic conductivity ($\text{H s}^{-1} \text{ m}^{-1}$)

A mis padres

A Jimena y Carlota

Chapter 1

Introduction and Previous Work

This dissertation is the product of the research conducted in the Department of Electromagnetism and Matter Physics at the University of Granada, and EMI/EMC Department at Cassidian, EADS-CASA, both in Spain. The focus is on developing efficient and accurate the discontinuous Galerkin time-domain method and its application to real and practical engineering problems. A brief overview of the most relevant methods in computational electromagnetics, from this standpoint, is provided in this introductory chapter. In addition, the reasons, alternatives, and capabilities of the specific technique chosen for the current research are discussed, together with the current state of the art.

1.1 Overview of Computational Electromagnetics

Prior to the 1960s, the computation of electromagnetic (EM) fields was almost confined to analytical methods involving closed-form expressions or the solving-by-series approach. However, with the advent of powerful computers and the development of sophisticated algorithms, the art of computational electromagnetics (CEM), as in many other scientific disciplines, has undergone exponential growth during the last five decades. Nevertheless, the EM community has lacked a unique and suitable method capable of solving all real-world EM problems, such as radiation, scattering, coupling, or waveguiding. Furthermore, there is a wide spectrum of engineering applications of CEM: design and modeling of antenna and microwave devices, radar and communication systems, electromagnetic compatibility (EMC) (High-Intensity Radiating Fields (HIRF), cross-talk, lightning strikes on large structures), nanophotonic devices, medical imaging, etc.. As a consequence, the expertise of the user becomes crucial in choosing the most appropriate method for a given problem.

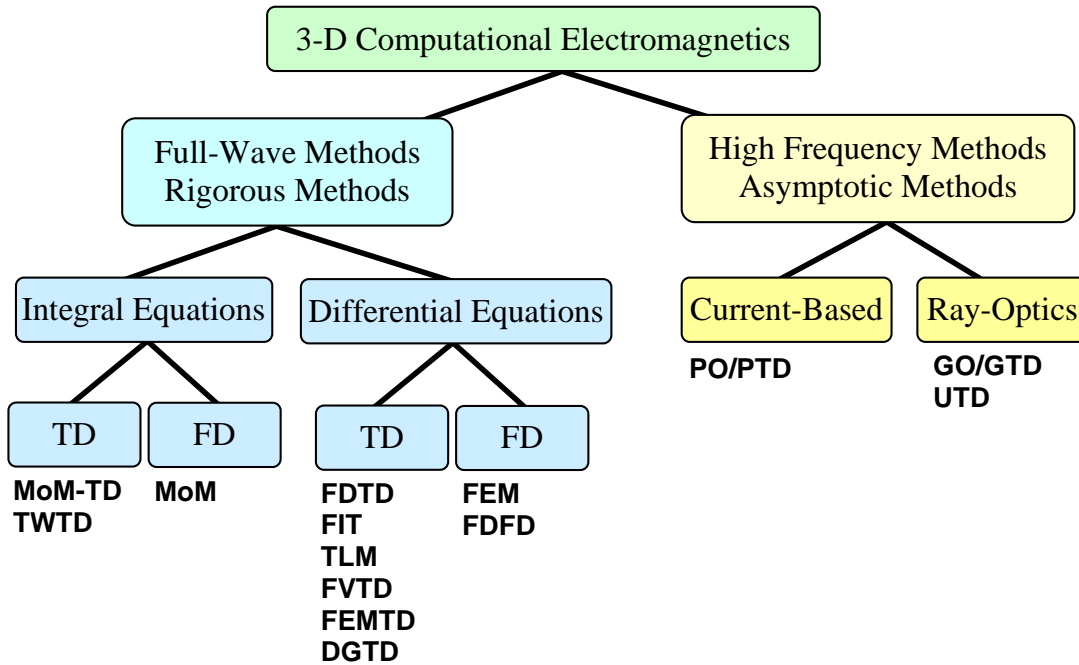


FIGURE 1.1: Classification of purely numerical 3D computational electromagnetic methods.

Many different numerical CEM techniques have been proposed. A conceptual classification of the most relevant ones appears in Figure 1.1. These can be classified into three different levels. At the highest level, we can distinguish between asymptotic and full-wave methods. Asymptotic methods are based on simplified versions of Maxwell equations or EM scattering models, typically formulated in frequency domain. They require low computational costs and their solutions converge to the analytical ones as frequency increases, thus making them useful for high frequency problems¹. Some of them are: Physical Optics (PO) methods, which locally applies the equivalent principle and computes an approximated solution of the EM currents, neglecting other effects. Physical Theory of Diffraction (PTD), which is an asymptotic correction to PO applicable to edged bodies. Geometrical Optics (GO) ray field, which consists of direct, reflected and refracted rays, obeying the Fermat principle, not considering the diffraction of waves around edges or smooth objects. Geometric Theory of Diffraction (GTD) methods was systematically formulated by generalizing Fermat principle to include a new class of diffracted rays, arising at geometrical and/or electrical discontinuities on the obstacle, and added to the GO rays. Uniform Theory of Diffraction (UTD), which overcomes some GTD singularities arising at GO ray shadow boundaries and ray caustics, in its original form.

¹In electromagnetics the term high or low frequency is always relative to the electrical size of the structures under study.

Full-wave methods, however, rigorously solve Maxwell equations, and the sources of error come from their discretization, reaching convergence when the space and time are infinitely refined. Full-wave methods can be classified in turn, according to the form, into integral and differential, depending on which Maxwell equations are solved. And according to the treatment of the time variable, into frequency- and time-domain methods.

Integral methods start from Maxwell equations in integral form. A main advantage of them is that only the surfaces and/or lines, where boundary conditions are enforced, need to be discretized, thus reducing the number of unknowns compared to volumetric methods, where also the space in-between is discretized. These methods make use of the Green-function concept, to find the solution after solving an algebraic system of equations found by applying the Method of Moments (MoM). The accuracy of integral methods, is well-known to be very high. Their main drawbacks appear when dealing with complex materials (composites, anisotropic, etc.) where the applicability of the method becomes difficult. Also for solving electrically large problems, since the condition number of the resulting linear system grows with the number of unknowns.

Methods based on differential equations are volumetric methods, and include those based on fully structured meshes, such as Finite Difference in Time or Frequency Domain (FDTD, FDFD), Finite Integral Technique (FIT) or Transmission-Line-Matrix (TLM); or those based on unstructured meshes, such as Finite Volume (FV), Finite Element (FE) or Discontinuous Galerkin (DG) methods. Among them, FE and DG methods are especially attractive for their ability to combine different orders of the basis-functions, to achieve fast convergence rates.

Both integral and differential methods, are found in Frequency Domain (FD) and in Time-Domain (TD). FD methods are often computationally inefficient in the computation of wideband frequency responses, since one frequency needs one complete simulation. This becomes especially critical for MoM or FEM methods, well-known for their accuracy when dealing with large structures with electrically small details, since they require the solution of a linear system of equations frequency-by-frequency. TD methods are an attractive alternative in these cases. Though integral equations can be formulated in TD, the matrix inversion or the solution of a linear system at each time step remains computationally unaffordable for most practical cases (except for thin-wire structures). The same consideration applies to differential methods based on FEM in TD methods (FEMTD).

For this reason, TD formulations are typically combined with differential-based methods on structured meshes (like FDTD, FIT, TLM) to yield explicit marching-on-in-time methods. They exhibit a high versatility to deal with arbitrary EM ultrawideband

(UWB) problems, limited only by the computational resources. However, their structured nature impose significant constraints on the geometrical discretization of complex objects, and on the accuracy and convergence of the methods. As mentioned above, FEMTD methods constitute an attractive alternative though computationally unaffordable. In this dissertation, alternatives to FEMTD based on Discontinuous Galerkin Time-Domain (DGTD) methods, are analyzed in detail. DGTD has most of the advantages of FDTD, FIT and TLM: explicit advancing algorithm, simplicity, easy parallelization, and memory and computational cost growing only linearly with the number of elements. At the same time, DGTD schemes retain most of the benefits of FEM: adaptability of the unstructured meshes and spatial high-order convergence.

1.2 Discontinuous Galerkin Time Domain Survey

In this section, we give a brief overview of the most relevant FEMTD literature, and a state-of-the-art of the DGTD method, object of this dissertation.

1.2.1 Background

During the 1980s, advances in meshing technology together with the FEM made it possible to solve Maxwell equations in complex geometries by using an unstructured mesh based on a tetrahedral tessellation. In this kind of mesh, complex objects, having arbitrary curvatures and intricate details, are accurately discretized. This is a major change from cube-based space partitioning of the previous FDTD method, which appeared in 1966 [1], TLM method in 1971 [2] and FIT proposed in 1977 [3]. This novel approach was initially applied in two-dimensions (2D) or axis-symmetric problems [4, 5, 6, 7], and later in three-dimensions (3D) [8, 9, 10], but always to solve Maxwell equations in FD. Typical applications of FEM in FD are S-parameter calculations, radiation pattern, RCS, etc.. They have shown to be ideal for low-frequency problems, highly resonant structures, and eigenmode computations. However, time-domain methods, as FDTD, FIT and TLM, are advantageous to deal with transient fields effects and arbitrary time-signal excitation (lightning strikes, EMC coupling, UWB antennas), and non-linear behavior of materials or components, where TD offer a direct and efficient approach.

During the 1990s, a variety of time-domain FEM schemes were proposed [11], these methods being based on both, Maxwell curl-curl equation, and the hyperbolic system of curl equations (Ampere and Faraday laws).

The second-order vector-wave curl-curl equation, typically solved by FEM in FD, can also be solved by FEM in TD. For this, a single field, electric or magnetic, has to be

computed. The major drawback is that a linear system of equations needs to be solved at each time step. To reduce the number of time steps, unconditionally an implicit time-integration schemes, like Newmark-beta, can be used, at the expense of yielding quite ill-conditioned matrices. This family of methods has been widely studied by Lynch, Mur, Lee, Gedney, Carpes, Jin et al., [12, 13, 14, 15, 16, 17, 18, 19, 20, 21, 22].

Alternatives to the single-field scheme are found by employing the two first-order coupled Maxwell curl equations, either formulated by considering the electric field intensity \mathbf{E} and the magnetic flux density \mathbf{B} (E-B), or the electric field intensity \mathbf{E} and magnetic field intensity \mathbf{H} (E-H). These formulations offer certain advantages with respect to the single-field formulation, such as the possibility of using different expansion functions, avoiding spurious solutions, or the fact that the first-order time derivatives allow the use of a conventional leap-frog time-integration method, which do not need to save in memory previous states. However, they still require to solve a sparse linear system at each time step, resulting in a computational cost comparable to that of the single-field scheme.

Current developments of the E-B methods can be found in [23, 24, 25, 26, 27, 28]. For the E-H formulation, two different families can be identified depending on how the continuity of the tangential components of \mathbf{E} and \mathbf{H} fields is treated at the interface between adjacent elements. If the continuity of the tangential components is enforced in a strong way, we get the classical Continuous Galerkin (CG) methods (which present the aforementioned limitation arising from the need to solve a linear system per time step). A second family is found by relaxing the tangential-continuity condition, yielding the so-called discontinuous Galerkin methods. For them, instead of continuity on the tangential components, continuous numerical fluxes are defined at the interface, in order to connect the solution between adjacent elements, in the manner used in FVTD, not requiring the resolution of a complete linear system at each time step.

The main advantage of DGTD over FVTD is its higher-order approximation in space. Over other FEM methods in TD the fact that the linear system to be solved becomes block-diagonal, only requires a single inversion of M square matrices of $Q \times Q$ elements (with M the number of elements and Q the number of basis functions per element) which can be done frontally at the preprocessing stage, while the larger matrices ($\simeq MQ \times MQ$) of FEM in TD require the solution of the system at each time step.

DGTD can be seen as a generalization of FVTD (which is a null-order DGTD method) and also FDTD methods, [29]. Thus, many of the ideas already developed in FVTD and FDTD can be adapted to DGTD.

Since the beginning of this century, the number of scientific publications on DGTD methods applied to CEM have been growing linearly, becoming a very active area of research. The efforts on the application of DGTD methods to solve Maxwell equations have followed two main different directions:

- Analysis of the different alternatives or improvements offered by the DGTD technique, and analysis of the method itself.
- Development of the capabilities and applications of the method, either adapting those of FDTD or FVTD, or developing new ones to prove the applicability of the method to real applications.

1.2.2 Analysis, Improvements and Alternatives of the Discontinuous Galerkin Methods

Discontinuous Galerkin techniques have been broadly used in other disciplines. The analysis, improvements, and alternatives of DG methods can be found mainly in the mathematics community. Most authors referred to in this subsection belong to this community.

The first DG method was introduced in 1973 by Reed and Hill [30] in the framework of neutron transport. Lesaint and Raviart [31] were the first to place this method on a firm mathematical basis. Since then, there has been an active development of DG methods for hyperbolic and nearly hyperbolic problems. In the case of linear equations, the nature of the method has been rigorously analyzed by Johnson and Pitkäranta [32], Richter [33], Peterson [34], and Bey and Oden [35]. For nonlinear equations, a major development was made by Cockburn, Shu and collaborators, in a series of papers [36, 37, 38, 39, 40], in which they established a framework for easily solving nonlinear time-dependent hyperbolic conservation laws using explicit, nonlinearly stable high-order Runge-Kutta time discretizations (RKDG). In 1997, Bassi and Rebay [41] introduced a DG method for the Navier-Stokes equations, in Computational Fluid-Dynamics (CFD), and in 1998, Cockburn and Shu [42] introduced the so-called Local Discontinuous Galerkin (LDG) methods, extending their approach to deal with time-dependent scalar advection-diffusion equation, and suggested how the approach could be applied to the Navier-Stokes equations, which generalize the original DG method of Bassi and Rebay. Around the same time, Oden and Bauman [43] introduced another DG method for diffusion problems and many other authors, since then, started to apply DG in CFD.

Lowrie et al. [44, 45] considered the space-time discontinuous Galerkin, which involves discontinuous elements in both time and space. In [45] a Fourier analysis of the scheme

was performed which shows a "super-convergence" property; i.e., the evolution error is $O(h^{2p+1})$ if the order of the polynomial space used is p while h is a measure for the size of elements. This property prompted Hu et al. to apply DG methods to advection and linearized Euler equations, in computational acoustics, in [46] and continue the analysis of DG applied to wave-propagation problems in [47, 48]. These researchers studied the dissipation, dispersion, and anisotropy of the errors introduced by the space discretization in the wave-propagation problem. The results of these analyses can be easily extended to the electromagnetic case.

Since 2002, DG methods have begun to find their way into CEM. Kopriva et al. [49], Perugia and Schötzau [50], and also Houston [51], or even Cockburn, Li and Shu [52] proposed and tested methods in 2D, applied to simple numerical cases, where high-order convergence of the semi-discrete spatial schemes were proved. However, it was Hesthaven and Warburton in [53] who established the basis for lengthy analyses that were performed before. For this, they employed nodal basis functions, upwind fluxes, and Runge-Kutta time-integration schemes. These authors analyzed the eigenvalue problem [54], finding results similar to those of Hu for the advection equation. The important point was that non-physical solutions (spurious modes) appear with a centered flux-evaluation scheme. These spurious modes are dissipative in case upwind flux or penalty terms were considered, which are typical in DG methods for other applications. Warburton and Embree give more details on this topic in [55], and Ainsworth et al. in [56, 57] and Grote et al. in [58] investigated the properties of interior penalty discontinuous Galerkin method considering the second-order wave equation.

Some convergence analyses were performed, also including the effect of the time-integration scheme, by Chen, Cockburn, and Reitich in [59] and Sármany et al. in [60]. Chen proposed the so-called m^{th} -order, m -stage Strong Stability Preserving Runge-Kutta (SSP-RK) scheme for the time marching. The idea is relating the time-integration order to the spatial order, so that high-order convergence is assured. Sármany made an in-depth study of the dispersion and dissipation errors of this scheme in [60].

A 3D scheme based on vector-basis functions in tetrahedral elements, non-dissipative centered-flux evaluation, and second-order leap-frog scheme for advancing in time, was introduced and analyzed by Fezoui et al. in [61]. Cohen et al. in [62] used a similar scheme but with non-structured hexahedral meshes in order to save memory and also introduced a local time-stepping scheme for leap-frog time integration. Cohen and Durflé in [63], and later Montseny et al. in [64] followed the same approach, but they introduced dissipative terms in order to improve accuracy, reducing the spurious modes present in centered flux schemes. Non-conforming locally refined grids were introduced

in this scheme by Canouet et al. in [65]. Fahs et al. thoroughly analyzed this technique in 2D and 3D in [66, 67, 68], and the use of curvilinear elements in 2D in [69].

Concerning the time integration, Runge-Kutta (RK) (traditionally used in CFD) and Leap-Frog (LF) are the most commonly used schemes, although other ones have been proposed and analyzed. Two main issues should be borne in mind when choosing a time scheme: (i) once arbitrary high-order accuracy in space is provided by DG, arbitrary high-order accuracy in time should be desirable; and (ii), local refinement of unstructured meshes can lead to very restrictive and diverse time steps, in order to preserve the stability of explicit time-integration schemes.

In relation to (i), Hesthaven and Warburton have made a detailed analysis of DGTD with RK schemes in their book [70]. Diehl et al. in [71] compared different multi-step Low-Storage Runge-Kutta (LSRK) methods of different orders. Chen, as mentioned above, introduced the SSP-RK scheme with the idea of attaining high-order accuracy in time, as well as in space. Dumbser et al. [72] introduced an arbitrary high-order scheme in the spatial part (ADER-DG), that can be implemented together with RK methods [70]. The ADER scheme can also be used for the time integration, as an alternative to RK, as proposed by Taube et al. in [73]. This method provides high-order accuracy in time, using a single-step advancing algorithm, which does not require an intermediate-stage calculation, as RK schemes do. In the case of LF methods, high-order in time, referred to as LF_N , was developed by Fahs in [74]. The implicit Crank-Nicolson time-integration scheme was applied to DGTD by Catella et al. in [75]. Afterwards, Dolean et al. in [76, 77] applied the same approach but locally, proposing a hybrid explicit-implicit time-integration scheme. Another possibility, quite similar to LF, known as symplectic time schemes originally developed for the numerical time integration of dynamical Hamiltonian systems [78] (molecular dynamics, astronomy, etc.), were introduced to CEM and applied to the DGTD method by Piperno, [79, 80]. Piperno developed both solutions, a locally implicit symplectic scheme and a multi-scale fully-explicit symplectic scheme.

Concerning the latter (ii) issue, there are basically two directions to cure this efficiency problem. The first one consists of using a Local Time-Stepping (LTS) algorithm combined with an explicit time-integration scheme, while the second approach relies on the use of an implicit or a hybrid explicit-implicit time-integration scheme. LTS strategies were introduced firstly by Flaherty et al. [81]. They have been also been tested by Canouet et al. in [65] and Montseny et al. in [64].

Finally, structured and unstructured mesh-domain decomposition has been explored by Davies et al. in [82] using triangles and cartesian elements in 2D. This idea has also been tested in 3D, in the Finite Volume Time-Domain (FVTD) context, hybridized

with FDTD in [83] by Edelvik and Ledfelt, splitting the geometry into regions of hexahedral and tetrahedral elements, geometrically coupling all these regions with pyramidal elements. A hybrid approach DGTD/FDTD was also discussed by Garcia et al. in [29].

1.2.3 Capabilities and Applications of Discontinuous Galerkin Time Domain Methods

The extension of ideas already developed for FVTD, which can be seen as an 0^{th} order DGTD, and FDTD, has allowed the vigorous development of DGTD during the last decade, and its application to the analysis of numerous electromagnetic problems. Some of them are summarized below.

Absorbing boundary conditions

The truncation of the space to deal with open/radiation problems or port terminations is a key point of all TD methods. Many techniques have been studied in depth in the FDTD context, applied to FVTD, and can be straightforwardly extended to DGTD. Firstly, Mohammadian, Shankar and Hall in [84, 85] proposed the simplest Absorbing Boundary Condition (ABC) in the FVTD context, which simply sets the incoming flux to zero, also known as first-order Silver-Müller ABC (SM-ABC). Kabakian in 2004, with Shankar and Hall, [86], extended this idea to DGTD and applied the method to antenna and scattering problems. The very well-known truncation technique, Perfectly Matched Layer (PML), widely used in FDTD, was introduced to DGTD by Xiao in 2005, [87], formulated on the cartesian coordinates. The Uniaxial PML (UPML) family has been widely studied in the FDTD, [88, 89, 90, 91] and they are very appropriate for FVTD and DGTD. The objective is to have a conformal PML layer in order to reduce the computational domain. They have been successfully tested in FVTD by Sankaran et al. in [92, 93, 94], and also used together by the same authors with SM-ABC with non-additional computational cost. Dosopoulos et al. in [95] formulated UPML in DGTD context for any conformal PML layer. Other implementations of UPML, based on the cartesian coordinates, are, Lu et al. in [96] and Niegemann et al. in [97], in 2D, and Gedney et al. in [98] in 3D using the so-called complex-frequency shifted PML in [99]. A noteworthy analysis performed by Niegemann et al. of their 2D version appears in [71]. The typical implementation, in all cases, is based on the Auxiliary Differential Equation (ADE) method.

Materials and sub-cell models

In 2004, Lu et al. [96], used also the ADE method to handle material-dispersion properties in 2D. Same authors in [100] applied the method to the Ground-Penetrating Radar (GPR) in dispersive media, and the same approach is used in [97, 101] by Stannigel and

Niegemann et al., to study nano-phonic systems and metallic nanostructures, also in 2D. König in [102] developed the formulation for the 2D case for the anisotropic material case. Thin-layer sub-cell models can be naturally modelled in FVTD and, therefore, in DGTD. Mohammadian et al. in [85] introduced resistive sheets and impedance surface models in FVTD. Following the same idea, Pebernet et al. in [103] proposed a low-frequency resistive model for thin composite materials in DGTD. Recently, Chun et al. in [104, 105] developed high-order accurate thin-layer approximations for DGTD for general metal-backed coatings and thin transmission layers. Concerning the thin-wire sub-cell models, Pebernet et al. in [103], and very recently Gödel in [106], introduced the traditional approximation, widely used in FDTD, to DGTD methods. Dosopoulos et al. developed models for lumped elements in [107].

High performance computing

DGTD method employs locally implicit, globally explicit space operator that provides an efficient high-order accurate time-dependent solution. This fact makes algorithms based on DGTD methods ideal for their implementation in highly parallel environments. Bernacki et al. in [108, 109] showed a parallel implementation based on mesh partitioning and message passing, demonstrating a good parallel speedup. Klöckner et al. in [110] implemented a DG method to run on off-the-shelf massively parallel Graphics Processing Units (GPU). Dosopoulos et al. in [95] showed the efficiency of the method, solving electrically large electromagnetic problems as a complete aircraft.

Real applications

With all the above features, many EM problems have been addressed by DGTD methods. In 2004, Kabakian et al. [86] used DGTD to deal with antenna and Radar Cross-Section (RCS) EM problems. In 2005, Ji et al. studied 2D waveguide-coupled microring resonators in [111], and Lu et al. in [100] applied the method to GPR. In both cases, high-order accuracy is desirable so DGTD proved superior to the traditional FDTD. Chauvière et al. in 2006 [112], discussed computationally efficient ways of accounting for the impact of uncertainty, e.g., lack of detailed knowledge about sources, materials, shapes, etc., in computational time-domain electromagnetics, using DGTD in his analysis. Shi et al. in [113] simulated left-handed media in DGTD. Again, Ji et al. in 2007 [114], studied the cross-sections of coupled nanowires. In 2008, Pebernet et al. [103] applied the DGTD method to EMC problems. In 2009, Niegemann, König, Stannigel and Busch [97, 101] used DGTD method to study nano-phonic systems, and metallic nanostructures. In 2010, Songoro et al. reviewed the main ideas of the DGTD method in [115]. Finally, at the beginning of 2011, ANSYS released the first commercial software based fully on the DGTD method.

1.3 Motivation behind this work

This work was developed within the framework of several research projects in which the Applied Electromagnetics Group of the University of Granada (UGR) participated with Cassidian and Airbus Military (EADS), between 2008 and 2013. The project HIRF-SE deserves special mention [116] supported by the 7th Framework Programme of the European Union, led by Alenia Aeronautica with a total cost of over 23 MEuros, and with the participation of 44 partners, including all major aeronautics companies and academic institutions across Europe. This project has been focused on the development of a synthetic framework for the integration and validation of mature numerical solvers in CEM, to deal with the EMC assessment of air vehicles under HIRF conditions. The author of this PhD dissertation, in conjunction with the dissertation advisors from the UGR team, has been responsible for developing a high-performance parallel computer-simulation tool based on the FDTD method, including all major state-of-the-art enhancements (subcell extensions, cable-bundle treatments, surface-impedance treatment of composite materials, etc.), and its validation with measurements and other methods provided by other partners. The tool built so far (UGRFDTD [117]) has passed all the validation steps, and is being proposed as a simulation tool suitable to replace certain tests in the HIRF certification of an air vehicle.

Since the FDTD method was firstly proposed by Yee in 1966 [1] for solving Maxwell equations, it has become undoubtedly the most widespread method among physicists and engineers, due to its simplicity and flexibility to deal with real problems. However, its inability to effectively handle complex geometries, due to stair-casing error, and the limitations in the accuracy (second order in space and time), prompted some scientists to search for alternatives long ago, the FE being the obvious alternative. Among all the schemes based on FE in the literature, DGTD approaches offer most of the advantages of FDTD: spatial explicit algorithm, simplicity, easy parallelization, and memory and computational cost growing linearly with the number of elements. In addition, DGTD schemes retain most of the advantages of FE: adaptability of the unstructured meshes, and spatial high-order convergence, enabling problems to be dealt with where the required precision varies over the entire domain, or when the solution lacks smoothness.

For these reasons, this dissertation has been focused solely on the DGTD method, without including the developments made in FDTD, given that the latter is a rather mature technique thoroughly described in the literature, while DGTD is still in its consolidation phase, relatively novel in CEM, and still undergoing fundamental developments to reach the maturity level of methods like FDTD.

In any case, some of the FDTD developments made in parallel during this PhD, have led to pioneer publications², in collaboration with several international groups. In particular, those related to the development of new numerical models, such as a novel surface-impedance boundary condition in [P4], modeling of graphene devices in [P9], and the excitation of waveguides in Crank-Nicolson FDTD in [P15]. Other publications have sought to show the applicability and validation of the FDTD method in real engineering problems, such as [P8] in which some guidelines are reported for the generation of finite-difference meshes, guidelines for the application of FDTD in the aerospace industry in [P27], some validations comparing simulation and measurements in [P2,P12,P18,P22], and a wide cross-comparison between different CEM methods and tools applied to a complex geometry (a full aircraft), presented in [P21, P23]. Special mention deserves some previous work of the author in the CEM field, specifically in Boundary Element Methods (BEM). In particular, the participation in the development of a state-of-the-art electromagnetic code (HPTESP-MAT), which is a fully industrialized Cassidian and Airbus Military MoM tool, with Multilevel Fast Multipole Algorithm (MLFMA), and the contribution to a hybrid method in FD, combining FEM, MoM and PO, published in [P16, P31, P32]. Finally, it should be stressed that many ideas presented in this dissertation have benefited from the challenges faced during the development of UGRFDTD, and comparisons with results found with this code, as well as frequent references to this method, are included throughout this manuscript.

In this dissertation, a detailed description is given for the development, analysis, implementation, and application of a discontinuous Galerkin formulation, employing a leap-frog time-integration scheme, and arbitrary order vector-basis functions in unstructured meshes based on curvilinear tetrahedra. The simplicity of the time-integration method has enabled the application of an efficient local time-stepping strategy. The generality and flexibility of the resulting method permits its application in a wide variety of electromagnetic problems such as microwave devices, antenna modeling, radar cross-section estimation, electromagnetic coupling, etc.. This technique has been implemented to be executed in modern and powerful parallel computers, providing good scalability performances. The capability of dealing efficiently with large differences in the element size, thanks to the LTS, and maintaining the accuracy level throughout the computational domain (by selecting different orders of the basis functions at each element), makes the Leap-Frog Discontinuous Galerkin (LFDG) a promising method, which combines the advantages of time-domain and finite-element methods. Moreover, the limitations of the LFDG method have also been assessed, opening new paths and broadening current knowledge in computational electromagnetics.

²In what follows, the publications derived from this dissertation will be numbered by prepending the character P to the reference number [Pxx].

The method developed during this work has been implemented in a Fortran code called SEMBA. This code is a fully parallelized (OMP-MPI) computational tool that has been successfully applied to the above-mentioned kinds of problems. The resulting tool fills a technological gap in computational electromagnetics, overcoming certain limitations of the traditional time-domain methods (FDTD, TLM or FIT). In particular, these include the stair-casing problem, which limits the geometrical discretization and the anisotropy of the errors, and the poor convergence rate of the spatial discretization of the electromagnetic fields.

Several publications have resulted from this work (others are still under submission or in preparation). Some of these papers have been aimed at analyzing the DGTD method and establishing the basis of the LFDG algorithm. In [P11] the topic of spurious modes in the DG context is revisited, this analysis being extended to the analysis of convergence, anisotropy of the errors, and computational cost of the LFDG in [P5]. The LTS strategy for the LFDG method is described in [P6], and a novel casual LTS algorithm for RK and LF is presented in [P3]. The formulation of the Conformal Uniaxial Perfectly Matched Layer (C-UPML) is stated in [P7], the source and boundary implementation in centered/upwind nodal/vector basis formulations of DGTD is described in [P14,P28], and a hybrid approach FEMTD and DGTD was presented in [P29]. Concerning the application of DGTD methods to real engineering problems, the LFDG algorithm is applied in [P6] to antennas, in [P11] to waveguide filters, in [P7,P17] to the estimation of HIRF transfer functions compared to FDTD, in [P13] to GPR, and in [P1,P19] to RCS computation. Finally, the applicability of the LFDG compared to FDTD in the aeronautic industry is presented in [P20,P24,P25,P26].

1.4 Organization of the manuscript

The rest of this manuscript is organized as follows. Chapter 2 briefly reviews the fundamentals of the finite-element methods for their application to time-domain schemes. The bases for the implementation of a FEMTD method are drawn, considering the use of vector-basis functions in tetrahedral elements. The most relevant FEMTD methods are also reviewed.

Chapter 3 firstly presents the proposed spatial discretization scheme, which is based on the DG method. The semi-discrete form is formulated in a general framework, which unifies different flux-evaluation schemes successfully applied to DG methods. The main electromagnetic capabilities, which have been developed for this method in 3D, are described, such as boundary-conditions treatment, anisotropic materials, and absorbing boundary conditions; the first-order Silver-Müller ABC, and the conformal uniaxial

perfectly matched layer. Then, temporal integration schemes are applied to the semi-discrete DG formulation (RK and LF). The leap-frog discontinuous Galerkin algorithm and the proposed local time-stepping strategy are described in detail.

In Chapter 4, the spatial semi-discrete scheme and the LFDG algorithm are studied, analyzing numerical dispersion and dissipation, spuriousness, stability, and the anisotropy and convergence of the errors. The high-order convergence property of the DG semi-discrete scheme is proven, finding the limits of the LFDG algorithm. A final assessment of the computational cost vs. accuracy is performed, and compared to the FDTD method.

Chapter 5 validates the LFDG method with microwave filters, antennas, scattering, and electromagnetic compatibility problems, comparing the results with measurements and other numerical techniques. Some important properties of the method are shown, such as robustness, stability, versatility, efficiency, scalability, and accuracy.

Chapters 6 and B summarize the main conclusions of this dissertation and the future lines of research and development.

Appendix A offers a description of the SEMBA simulation tool, which has been implemented during this work considering High Performance Computing (HPC) concepts, and validated in Chapter 5 with large and complex electromagnetic problems. Finally, some information is included on the author of this dissertation, a list of his publications, and his curriculum vitae.

Chapter 2

Finite-Element Time-Domain Methods: Fundamentals

Finite-element methods, to solve general EM problems, have been traditionally used in the FD. Today, modern computation and memory resources enable FEM to be applied to real problems in the TD. Finite-element time-domain methods offer some major advantages over the classical approaches to TD computation in CEM; FDTD, FIT and TLM. Firstly, the use of unstructured grids offers superior versatility in geometry discrimination, and permits the application of mesh refinement (h-refinement) to increase and control accuracy. Secondly, the Faedo-Galerkin procedure, used to develop the weak statement [11], provides a natural way to deal with continuity conditions at material interfaces, material properties such as anisotropy, different sources, etc.. Finally, the use of Galerkin formulation provides an immense variety of different choices, related to basis functions (p-refinement), including the use of different finite elements in the same mesh (e.g. tetrahedra, pyramids, and hexahedra) or non-conforming meshes.

The disadvantages compared to FDTD (or FIT and TLM) are mainly operative features. The increment in complexity of the algorithms makes it more difficult to apply some computational acceleration techniques, such as vectorization, cache management, or parallelization, which are very effective in FDTD. Moreover, in the case of analyzing large and complex geometries, such as an aircraft, the generation of meshes requires more simplified geometry for finite elements than for finite differences. Thus, the defeaturing or geometrical cleaning process, prior to the mesh generation, is much more difficult for FE, making the simulation setup more time consuming. Once the cell size, related to the accuracy and the minimum wavelength analyzed in the problem, is chosen, a finite difference mesher parses out what is electrically irrelevant, compared to the cell size, and

naturally simplifies the geometry. However, a FE mesher meticulously tries to resolve every detail, even irrelevant ones, from an electrical standpoint.

This chapter lays the basis for dealing with 3D Maxwell equations in the TD making use of FE methods. Then, the most relevant FEMTD approaches for electromagnetic modeling are reviewed.

2.1 Space Discretization

The numerical representation of a domain Ω under analysis by idealized cells determines how well that volume can be approximated (curvature, location, interfaces, etc.) with the materials and different objects inside. Any numerical analysis is limited by the geometrical discretization.

Scalar mappings to define curved shapes are widely used in connection with the finite-element solution of differential equations [118, 119, 120, 121, 122]. In this study, unstructured conforming meshes based on tetrahedral cells are used for the spatial discretization of the geometries. For these, each of the four faces of a tetrahedron coincides exactly with the face of some other tetrahedron. Non-conforming meshes relax this condition, and have also been used in DG methods to add flexibility in the discretization of complex domains or heterogeneous media. A detailed description of these approaches appears in [65, 66, 67, 68].

With the application of scalar mapping, the local coordinate system (L_1, L_2, L_3, L_4) , with $L_1 + L_2 + L_3 + L_4 = 1$ is mapped to the global coordinate system (x, y, z) , by making use of Lagrangian expansion functions. In tetrahedra the reference cell has the following vertices: $V_1 \equiv (0, 0, 0)$, $V_2 \equiv (1, 0, 0)$, $V_3 \equiv (0, 1, 0)$, $V_4 \equiv (0, 0, 1)$. For the straight tetrahedron, the geometric transformation needs four first-order Lagrange polynomials. If the tetrahedron is curved, the mapping from the reference one to real cells makes use of Lagrange polynomials of higher orders. Higher-order cells provide better accuracy, and permit larger mesh cells.

The mapping expressions are the following

$$x = \sum_{i=1}^{N_n} x_i B_i(L_1, L_2, L_3, L_4), \quad y = \sum_{i=1}^{N_n} y_i B_i(L_1, L_2, L_3, L_4), \quad z = \sum_{i=1}^{N_n} z_i B_i(L_1, L_2, L_3, L_4) \quad (2.1)$$

where (x_i, y_i, z_i) are the node cartesian coordinates of the real tetrahedron and N_n the number of Lagrange functions (4 for first order, 10 for second order, 20 for third order, ...) [118].

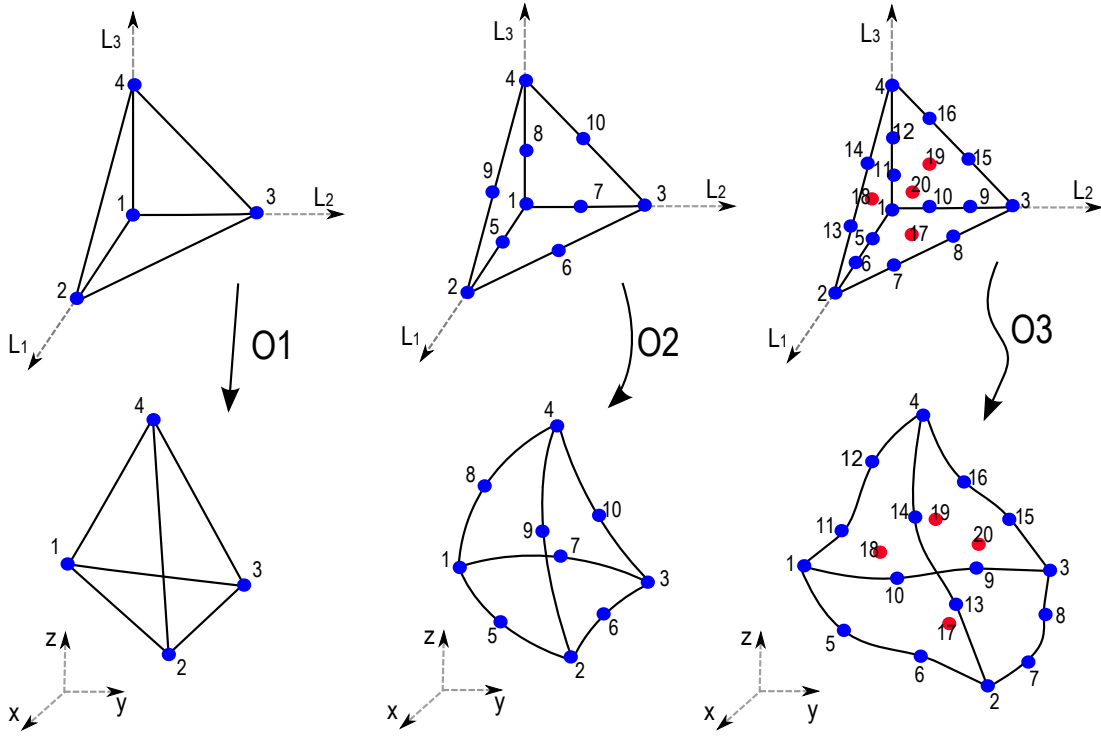


FIGURE 2.1: Mapping from the reference tetrahedra to the real cells for first (O1), second (O2) and third (O3) orders.

It is important to note that the same expressions can be used for mapping from the reference triangle to each curved face of the tetrahedron; just one of the four local tetrahedron coordinate will be zero, depending on the face.

The specific expressions for the tetrahedral cell in local coordinates for the biquadratic mapping are

$$\begin{aligned}
 B_1 &= (2L_1 - 1)L_1 & B_6 &= 4L_2L_3 \\
 B_2 &= (2L_2 - 1)L_2 & B_7 &= 4L_1L_3 \\
 B_3 &= (2L_3 - 1)L_3 & B_8 &= 4L_1L_4 \\
 B_4 &= (2L_4 - 1)L_4 & B_9 &= 4L_2L_4 \\
 B_5 &= 4L_1L_2 & B_{10} &= 4L_3L_4
 \end{aligned} \tag{2.2}$$

Let us recall some differential geometry basic concepts which will be needed for our purposes. The Jacobian matrix is defined as

$$J = \begin{bmatrix} \frac{\partial x}{\partial L_1} & \frac{\partial y}{\partial L_1} & \frac{\partial z}{\partial L_1} \\ \frac{\partial x}{\partial L_2} & \frac{\partial y}{\partial L_2} & \frac{\partial z}{\partial L_2} \\ \frac{\partial x}{\partial L_3} & \frac{\partial y}{\partial L_3} & \frac{\partial z}{\partial L_3} \end{bmatrix} \tag{2.3}$$

With it, the differential operator in the real coordinate system can be expressed as

$$\begin{bmatrix} \frac{\partial}{\partial x} \\ \frac{\partial}{\partial y} \\ \frac{\partial}{\partial z} \end{bmatrix} = [J]^{-1} \begin{bmatrix} \frac{\partial}{\partial L_1} \\ \frac{\partial}{\partial L_2} \\ \frac{\partial}{\partial L_3} \end{bmatrix} \quad (2.4)$$

The differential volume in the real coordinate system is evaluated by making use of the determinant of the Jacobian matrix,

$$dV = dx dy dz = |J| dL_1 dL_2 dL_3 \quad (2.5)$$

The normal vector to one face of the tetrahedron can be expressed as the following example for the face 3 ($L_3 = 0$),

$$\hat{\mathbf{n}} = \frac{\nabla L_1 \times \nabla L_2}{|\nabla L_1 \times \nabla L_2|} = \frac{\left(\frac{\partial x}{\partial L_1} \hat{\mathbf{x}} + \frac{\partial y}{\partial L_1} \hat{\mathbf{y}} + \frac{\partial z}{\partial L_1} \hat{\mathbf{z}} \right) \times \left(\frac{\partial x}{\partial L_2} \hat{\mathbf{x}} + \frac{\partial y}{\partial L_2} \hat{\mathbf{y}} + \frac{\partial z}{\partial L_2} \hat{\mathbf{z}} \right)}{|\nabla L_1 \times \nabla L_2|} \quad (2.6)$$

and the differential surface area is

$$dS = |\nabla L_1 \times \nabla L_2| dL_1 dL_2 \quad (2.7)$$

The magnitude of the cross product (2.6) plays the same role as the determinant of the Jacobian matrix for the differential volume.

$$|\nabla L_1 \times \nabla L_2| = \sqrt{\left(\frac{\partial y}{\partial L_1} \frac{\partial z}{\partial L_2} - \frac{\partial z}{\partial L_1} \frac{\partial y}{\partial L_2} \right)^2 + \left(\frac{\partial z}{\partial L_1} \frac{\partial x}{\partial L_2} - \frac{\partial x}{\partial L_1} \frac{\partial z}{\partial L_2} \right)^2 + \left(\frac{\partial x}{\partial L_1} \frac{\partial y}{\partial L_2} - \frac{\partial y}{\partial L_1} \frac{\partial x}{\partial L_2} \right)^2} \quad (2.8)$$

In this work, second-order (O2) tetrahedral cells have been used for the space discretization. This kind of cells permits the discretization errors to be reduced in typical cases, such as coaxial cables or double curved surfaces, compared to the commonly used straight or first-order cells. In those kinds of problems, the space-discretization errors are critical for the accuracy of the electromagnetic solution. Commercial software able to generate good-quality second-order tetrahedral meshes is available [123].

2.2 Vector-Fields Discretization

Two main families of basis functions, scalar and vector, have been generally proposed to solve electromagnetic problems with finite-element methods. In both cases, different piecewise polynomials are used to form the 3D vector space of order p to approximate and test the space dependence. The typical choice, in the case of scalar basis, is the use of Lagrange polynomials, giving rise to nodal finite elements. It is well known that when a straightforward nodal continuous Galerkin finite-element scheme is used to approximate Maxwell curl-curl equation in the frequency domain, nonphysical or spurious solutions appear [124, 125]. The cause of these is the impossibility to guarantee zero divergence in the solution of the curl-curl equation, not approximating the complete set of Maxwell equations (electric and magnetic Gauss' laws) [126, 127, 128]. To overcome the problem of spurious modes, special vector-curl-conforming basis [129, 130] have been proposed [126].

Currently, the dominant approach for finite-element frequency-domain methods is based upon curl-conforming elements, also known as Nédélec or edge elements [20, 131]. This approach guarantees weakly zero-divergence solutions. The main advantages of curl-conforming basis in FEM, frequency domain, and continuous Galerkin are: (i) the schemes are free of spurious solutions, (ii) boundary conditions are easy to implement, (iii) normal discontinuity and tangential continuity between different media are automatically satisfied, and (iv) the behavior is better in non-convex domains than nodal scalar basis [132]. The main disadvantage is found in large problems with a high number of degrees of freedom, where more ill-conditioned matrices result with curl conforming. This drawback can be improved with the use of potentials or Lagrange multipliers, but the number of unknowns increases by the presence of these scalar functions [133]. Another approach has been recently proposed in [134] based on nodal elements and the regularized Maxwell equations. The advantages of this approach are that it provides spurious-free solutions with well-conditioned matrices and, moreover, only the three components of the electric (or magnetic) are the unknowns. A comparison of the latter with the traditional approach (curl-conforming elements and curl-curl equation) appears in [135].

In DG methods, there are two important differences to bear in mind, compared to CG methods:

- (a) The nature and solutions of the spurious modes in continuous and discontinuous Galerkin approaches is different, and the lessons learned with the continuous case are not straightforwardly extrapolated to the discontinuous case. Spurious modes or non-physical solutions topic were analyzed in [54], based on

nodal scalar functions. The conclusion was that spurious modes are not a problem if upwind-flux evaluation, penalty or stabilization with purely dispersive terms, are introduced into the formulation. In case that straightforward centered fluxes are used, spectral pollution due to the presence of non-physical spurious modes is found. Similar results have been reported in [64], also with nodal scalar functions, where penalization of the centered fluxes by dissipative terms have also been introduced to find more accurate results. In this dissertation, a similar analysis was made (see Section 4.1.1) with vector-basis functions, giving similar results.

- (b) The DG method needs only the inversion of M small matrices of $Q \times Q$ elements (with Q the number of basis functions per element), while larger matrices ($\simeq MQ \times MQ$) are involved in continuous Galerkin. Therefore, no difficulties related to ill-conditioned matrices are expected in discontinuous methods.

Due to these two facts, it is not clear which kind of basis functions presents more advantages or disadvantages, and both families have been successfully applied in DG context, scalar [108] and vector [136] basis. In both cases, spurious modes can be avoided, applying the same strategies. From an implementation standpoint, both kinds of basis functions have advantages. In terms of matrix sharing between elements to save memory, both sets of functions have matrices which are identical, regardless of the cell size and aspect ratio, and can be shared among elements during the updating algorithm. Some matrices, on the other hand, are different and need to be kept in memory for each element. Consequently, there is no clear advantage for nodal- or vector-basis functions, as there is for FEM in frequency domain.

In any case, in this work, the vector basis was used and, more specifically, hierarchical high-order vector-basis functions, [136, 137, 138], which present some implementation advantages in order to reduce computation and memory requirements.

2.2.1 Mapping Vector-Basis Functions to Curvilinear Elements

As noted above, vector-basis functions, hierarchical high-order ones in our case, are used to discretize the vector fields (\mathbf{E} and \mathbf{H}). As has been introduced in Section 2.1, second-order tetrahedra will be used for space discretization. Expressions (2.1) and (2.2) will be used to map the reference cell to the curvilinear and real one. In the same way, a local mapping has to be established for the basis functions [125].

Let the reference cell be defined by local coordinates, (L_1, L_2, L_3, L_4) with $L_1 + L_2 + L_3 + L_4 = 1$, and the specific mapping in (x, y, z) space as (2.1). To define and manipulate

vector quantities within a curvilinear cell, we introduce the base vectors

$$\mathbf{l}_i = \frac{\partial x}{\partial L_i} \hat{\mathbf{x}} + \frac{\partial y}{\partial L_i} \hat{\mathbf{y}} + \frac{\partial z}{\partial L_i} \hat{\mathbf{z}} \quad \text{with } i = \{1, 2, 3\} \quad (2.9)$$

and the reciprocal base vectors

$$\mathbf{l}'_i = \nabla L_i = \frac{\partial L_i}{\partial x} \hat{\mathbf{x}} + \frac{\partial L_i}{\partial y} \hat{\mathbf{y}} + \frac{\partial L_i}{\partial z} \hat{\mathbf{z}} \quad \text{with } i = \{1, 2, 3\} \quad (2.10)$$

Note that the reciprocal base corresponds to the gradient of the local coordinates, and both notations ($\mathbf{l}'_i, \nabla L_i$) are used indifferently.

In general, neither the base vector nor the reciprocal one are mutually orthogonal within an element. Even the three vectors of each base are not orthogonal. However, they always satisfy two important properties:

$$\mathbf{l}_i \cdot \mathbf{l}'_i = 1 \quad \text{with } i = \{1, 2, 3\} \quad (2.11)$$

$$\mathbf{l}_i \cdot \mathbf{l}'_j = 0 \quad \text{with } i = \{1, 2, 3\} \text{ and } j = \{1, 2, 3\} \text{ being } i \neq j \quad (2.12)$$

These properties enable us to express any vector \mathbf{B} as a linear combination of any of the two bases, just projecting that vector over the other base,

- covariant components of a vector

$$\mathbf{B} = \sum_{i=1}^3 (\mathbf{B} \cdot \mathbf{l}_i) \mathbf{l}'_i \quad (2.13)$$

- contravariant components of a vector

$$\mathbf{B} = \sum_{i=1}^3 (\mathbf{B} \cdot \mathbf{l}'_i) \mathbf{l}_i \quad (2.14)$$

There are two kinds of vector-basis functions, known as div-conforming and curl-conforming. Div-conforming basis functions keep a known value of the normal component at the boundaries of the elements, being unknown the tangential components and depending on the element aspect. In the case of curl-conforming, the tangential component at the faces of the elements are known, independently of the element shape. Curl-conforming basis functions are used when the curl operation of the discretized fields is necessary to be evaluated, and div-conforming in the case of divergence operation. In our case, $\nabla \times \mathbf{E}$ and $\nabla \times \mathbf{H}$ will be evaluated, so curl-conforming basis functions is the right choice.

When a curl-conforming basis function is being constructed on a element, the appropriate mapping is given by

$$\begin{pmatrix} B_x \\ B_y \\ B_z \end{pmatrix} = J^{-1} \begin{pmatrix} B_{\nabla L_1} \\ B_{\nabla L_2} \\ B_{\nabla L_3} \end{pmatrix} \quad (2.15)$$

J being the Jacobian matrix defined by (2.3).

Therefore, we need to define our basis functions expressed in covariant components. The curl operation can be expressed also considering the covariant components of the basis functions as

$$\nabla \times \mathbf{B} = \frac{1}{|J|} \left[\left(\frac{\partial B_{\nabla L_3}}{\partial L_2} - \frac{\partial B_{\nabla L_2}}{\partial L_3} \right) \mathbf{l}_1 + \left(\frac{\partial B_{\nabla L_1}}{\partial L_3} - \frac{\partial B_{\nabla L_3}}{\partial L_1} \right) \mathbf{l}_2 + \left(\frac{\partial B_{\nabla L_2}}{\partial L_1} - \frac{\partial B_{\nabla L_1}}{\partial L_2} \right) \mathbf{l}_3 \right] \quad (2.16)$$

this giving a vector expressed in contravariant components. Thus, the right mapping for curl operation is the following

$$\begin{pmatrix} \nabla \times \mathbf{B}|_x \\ \nabla \times \mathbf{B}|_y \\ \nabla \times \mathbf{B}|_z \end{pmatrix} = J^T \begin{pmatrix} \nabla \times \mathbf{B}|_{l_1} \\ \nabla \times \mathbf{B}|_{l_2} \\ \nabla \times \mathbf{B}|_{l_3} \end{pmatrix} \quad (2.17)$$

To summarize, defining vector-basis functions in covariant components, which is the usual approach [138], and making use of Equations (2.5), (2.7), (2.15), (2.16) and (2.17), we find that all the calculations to evaluate volumetric and superficial integrals, needed in any FEM implementation, can be performed in the local coordinate system (L_1, L_2, L_3, L_4) .

2.3 Finite-Element Time-Domain Methods

The general procedure to develop numerical schemes for FEMTD is based on Faedo-Galerkin weak solutions of the 3D Maxwell equations, supplemented with boundary conditions, assuming that space-time variables can be separated. It can be applied to both, the hyperbolic system of the two curl equations, and the vector-wave equation. From this perspective, different approaches have been proposed [11], and the most relevant for this dissertation are reviewed in this section.

2.3.1 Single-Field Schemes

These schemes solve the second-order vector-wave equation, also known as double-curl or curl-curl Maxwell equation [12, 13, 14, 15, 16, 17, 18, 19, 20, 21, 22]. Let us assume a material region Ω characterized by the electric permittivity tensor $\bar{\bar{\epsilon}}$ and the magnetic permeability tensor $\bar{\bar{\mu}}$ (taking it lossless, electric and magnetic conductivity equal to zero, for simplicity). The electric field \mathbf{E} (a dual formulation could be expressed for \mathbf{H}) within the domain obeys the vector-wave equation given by

$$\nabla \times (\bar{\bar{\mu}}^{-1} \nabla \times \mathbf{E}) + \bar{\bar{\epsilon}} \frac{\partial^2 \mathbf{E}}{\partial t^2} = -\frac{\partial \mathbf{J}_{imp}}{\partial t} \quad \text{in } \Omega \quad (2.18)$$

where \mathbf{J}_{imp} accounts for the impressed currents.

The most common boundary conditions, perfect electric conductor (PEC), perfect magnetic conductor (PMC), and ABC for unbounded media are

$$\hat{\mathbf{n}} \times \mathbf{E} = 0 \quad \text{on } \partial_{PEC} \Omega \quad (2.19a)$$

$$\hat{\mathbf{n}} \times \nabla \times \mathbf{E} = 0 \quad \text{on } \partial_{PMC} \Omega \quad (2.19b)$$

$$\hat{\mathbf{n}} \times (\hat{\mathbf{n}} \times \nabla \times \mathbf{E}) = \frac{1}{c} \hat{\mathbf{n}} \times \frac{\partial \mathbf{E}}{\partial t} \quad \text{on } \partial_{\infty} \Omega \quad (2.19c)$$

where (2.19c) is the well-known Silver-Müller truncation condition or first-order ABC in free space.

Equation (2.18), in its variational form, can be expressed as

$$\int_{\Omega} \mathbf{w} \cdot \left[\nabla \times \bar{\bar{\mu}}^{-1} \nabla \times \mathbf{E} + \bar{\bar{\epsilon}} \frac{\partial^2 \mathbf{E}}{\partial t^2} + \frac{\partial \mathbf{J}_{imp}}{\partial t} \right] d\Omega = 0 \quad (2.20)$$

$\forall \mathbf{w} \in \mathcal{W}$, being \mathcal{W} the test space, and with the usual dot product for $(\mathcal{L}^2(\Omega))^2$.

The Galerkin procedure is the most common approach to obtain the numerical scheme. It employs the same set of basis functions to expand the unknown vector field \mathbf{E} and to test the equation.

Assuming that Ω is divided into a set of non-overlapping elements, a continuity requirement is imposed between adjacent elements. This condition is applied in a strong way, such that the following relations need to be satisfied,

$$\hat{\mathbf{n}} \times \mathbf{E}^+ = \hat{\mathbf{n}} \times \mathbf{E}^- \quad (2.21a)$$

$$\hat{\mathbf{n}} \times (\bar{\bar{\mu}}^{-1} \nabla \times \mathbf{E})^+ = \hat{\mathbf{n}} \times (\bar{\bar{\mu}}^{-1} \nabla \times \mathbf{E})^- \quad (2.21b)$$

where the superscript $+$ and $-$ refer to adjacent elements.

This is normally fulfilled by choosing vector-curl-conforming basis functions, where the mapping is performed by using a covariant projection, and relating then unknowns between adjacent elements.

The solution of the problem is a linear combination of the unknowns, and the expansion functions,

$$\tilde{\mathbf{E}} = \sum_{m=1}^M e_m(t) \boldsymbol{\phi}_m(\mathbf{r}) = \mathbf{E}^T \boldsymbol{\Phi} \quad (2.22)$$

where e_m are the unknowns and $\boldsymbol{\phi}_m$ the vector-basis functions. \mathbf{E} and $\boldsymbol{\Phi}$ are column vectors containing the M unknowns and basis functions, respectively.

Inserting (2.22) into (2.20) and using $\boldsymbol{\Phi}$ as test functions, we find a semi-discrete system of ordinary differential equations (ODE) as

$$\mathbb{M} \frac{d^2}{dt^2} \mathbf{E} + \mathbb{S} \mathbf{E} + \mathbf{J} = 0 \quad (2.23)$$

where

$$\mathbb{M}_{ij} = \int_{\Omega} \boldsymbol{\phi}_i \cdot \bar{\bar{\boldsymbol{\epsilon}}} \boldsymbol{\phi}_j \, d\Omega \quad (2.24a)$$

$$\mathbb{S}_{ij} = \int_{\Omega} \nabla \times \boldsymbol{\phi}_i \cdot \bar{\bar{\boldsymbol{\mu}}}^{-1} \nabla \times \boldsymbol{\phi}_j \, d\Omega \quad (2.24b)$$

$$\mathbf{J}_i = \int_{\Omega} \boldsymbol{\phi}_i \cdot \frac{\partial}{\partial t} \mathbf{J}_{imp} \, d\Omega \quad (2.24c)$$

The main advantage of the scheme (2.23), compared to dual-field schemes later described, is that only one field has to be computed, which reduces the number of unknowns. This scheme has two major drawbacks; the time-discretization of the second-order time derivative requires storage of previous time-step values, and the spatial semi-discrete scheme is implicit in space. The basis functions force continuity between elements, because of (2.21), and thus a complete banded linear system of equations has to be solved at each time step. A solution to find a explicit scheme is to invert the mass matrix \mathbb{M} . However, this can be very costly and the inverse mass matrix is, in general, full. This makes the scheme non-applicable for electrically large problems.

2.3.2 Dual-Field Schemes

Two main different approaches can be found in the literature. Both solve the two first-order coupled Maxwell curl equations given by Ampere and Faraday laws. In one case, the electric-field intensity (\mathbf{E}) and the magnetic-flux density (\mathbf{B}) are computed

[23, 24, 25, 26, 27, 28] and, in the other case, are the electric-field intensity (\mathbf{E}) and the magnetic-field intensity (\mathbf{H}). In the latter case, both the CG approach [139], and the DG approach, proposed in this work, can be used.

2.3.2.1 E-B Finite-Element Time-Domain Method

Again, let us take a lossless material region Ω characterized by the electric permittivity tensor $\bar{\bar{\epsilon}}$, and the magnetic permeability tensor $\bar{\bar{\mu}}$. The electric field \mathbf{E} and the magnetic flux \mathbf{B} within the domain obey the first-order coupled Maxwell curl equations given by

$$\bar{\bar{\epsilon}} \frac{\partial \mathbf{E}}{\partial t} = \bar{\bar{\mu}}^{-1} \nabla \times \mathbf{B} - \mathbf{J}_{imp} \quad (2.25a)$$

$$\frac{\partial \mathbf{B}}{\partial t} = -\nabla \times \mathbf{E} \quad (2.25b)$$

with \mathbf{J}_{imp} being the impressed. The PEC, PMC, and Silver-Müller ABC now become

$$\hat{\mathbf{n}} \times \mathbf{E} = 0 \quad \text{on } \partial_{PEC}\Omega \quad (2.26a)$$

$$\hat{\mathbf{n}} \times \mathbf{B} = 0 \quad \text{on } \partial_{PMC}\Omega \quad (2.26b)$$

$$\hat{\mathbf{n}} \times (\hat{\mathbf{n}} \times \mathbf{E}) = c \hat{\mathbf{n}} \times \mathbf{B} \quad \text{on } \partial_{\infty}\Omega \quad (2.26c)$$

Following the procedure described in [23, 24], let us expand the electric field \mathbf{E} in terms of Whitney edge basis functions (Whitney 1-form) \mathbf{w}_i^1 , $i = 1, 2, \dots, N_e$, and the magnetic flux \mathbf{B} in terms of Whitney face basis functions (Whitney 2-form) \mathbf{w}_i^2 , $i = 1, 2, \dots, N_f$. The expression for the unknown fields become

$$\tilde{\mathbf{E}} = \sum_{m=1}^{N_e} e_m(t) \mathbf{w}_m^1(\mathbf{r}) = \mathbf{E}^T \mathbf{W}^1 \quad (2.27a)$$

$$\tilde{\mathbf{B}} = \sum_{m=1}^{N_f} b_m(t) \mathbf{w}_m^2(\mathbf{r}) = \mathbf{B}^T \mathbf{W}^2 \quad (2.27b)$$

where e_m and b_m are the unknowns, and N_e and N_f are the number of edges and faces, respectively.

We denote column vectors containing the unknowns as, $\mathbf{E} = [e_1, e_2, \dots, e_{N_e}]^T$ and $\mathbf{B} = [b_1, b_2, \dots, b_{N_f}]^T$, and the sets of basis functions as, $\mathbf{W}^1 = [w_1^1, w_2^1, \dots, w_{N_e}^1]^T$ and $\mathbf{W}^2 = [w_1^2, w_2^2, \dots, w_{N_f}^2]^T$.

By inserting (2.27) into (2.25), we realize that the second equation (2.25b) does not need to be tested (if done, it would become a trivial identity). After testing the first Equation (2.25a), according to the Galerkin procedure, the result is a semi-discrete system of two

ODE,

$$[\star_\varepsilon] \frac{d}{dt} E = [d_{\text{curl}}^*] [\star_{\mu^{-1}}] B - J \quad (2.28a)$$

$$\frac{d}{dt} B = -[d_{\text{curl}}] E \quad (2.28b)$$

where the $N_f \times N_e$ matrix $[d_{\text{curl}}]$ and the $N_e \times N_f$ $[d_{\text{curl}}^*]$ are (metric free) sparse curl incidence matrices on the primal and dual grids, respectively, the elements of which assume only $\{-1, 0, 1\}$ values. The identity $[d_{\text{curl}}]^T = [d_{\text{curl}}^*]$ holds, in general, up to boundary terms. The incidence matrices fulfill the following expression,

$$\nabla \times W^1 = [d_{\text{curl}}^*] W^2 \quad (2.29)$$

J column vector corresponds with the source term,

$$J_i = \int_{\Omega} \mathbf{w}_i^1 \cdot \mathbf{J}_{\text{imp}} d\Omega \quad (2.30)$$

The discrete Hodge matrices $[\star_\varepsilon]$ (size $N_e \times N_e$) and $[\star_{\mu^{-1}}]$ (size $N_f \times N_f$) in (2.28) are given by the following integrals,

$$[\star_\varepsilon]_{ij} = \int_{\Omega} \mathbf{w}_i^1 \cdot \bar{\bar{\varepsilon}} \mathbf{w}_j^1 d\Omega \quad (2.31a)$$

$$[\star_{\mu^{-1}}]_{ij} = \int_{\Omega} \mathbf{w}_i^2 \cdot \bar{\bar{\mu}}^{-1} \mathbf{w}_j^2 d\Omega \quad (2.31b)$$

It is important to notice that this strategy retains conformality to the discrete de Rham diagram [140], this being the reason to choose \mathbf{B} , instead of \mathbf{H} as other schemes. This fact avoids spurious solutions of the form $t\nabla\phi$, which are present in the single-field FEMTD [15, 141, 142], particularly restrictive for the use of PML.

The result is a scheme composed by two ODE with two fields as unknowns. Its computational cost is comparable to the single-field scheme. The Hodge (mass) matrices are sparse, but not diagonal, and the solution of the associated linear system is the most computationally intensive part of the scheme. The sparse linear-system solution is required only for the electric-field update in (2.28a), with (2.28b) being explicit. Therefore, the size of the linear system to be solved is as large as the single-field scheme.

It is important to note that this scheme involves only first-order time derivatives instead of the second-order ones of the single-field case. This allows the use of a conventional LF time discretization which avoids to keep in memory previous states.

The main drawback of this scheme, as for the single-field case, is that is very costly for electrically large problems and becomes non-applicable in real problems.

2.3.2.2 E-H Finite-Element Time-Domain Method

Finally, let us take again the same simple lossless material region Ω , with permittivity $\bar{\bar{\epsilon}}$ and the permeability $\bar{\bar{\mu}}$. The electric field \mathbf{E} and the magnetic field \mathbf{H} within the domain obey the first-order coupled Maxwell curl equations given by

$$\bar{\bar{\epsilon}} \frac{\partial \mathbf{E}}{\partial t} = \nabla \times \mathbf{H} - \mathbf{J}_{imp} \quad (2.32a)$$

$$\bar{\bar{\mu}} \frac{\partial \mathbf{H}}{\partial t} = -\nabla \times \mathbf{E} \quad (2.32b)$$

where \mathbf{J}_{imp} is the impressed current, source of our problem. Now the boundary conditions, PEC, PMC, and Silver-Müller ABC are

$$\hat{\mathbf{n}} \times \mathbf{E} = 0 \quad \text{on } \partial_{PEC}\Omega \quad (2.33a)$$

$$\hat{\mathbf{n}} \times \mathbf{H} = 0 \quad \text{on } \partial_{PMC}\Omega \quad (2.33b)$$

$$\hat{\mathbf{n}} \times (\hat{\mathbf{n}} \times \mathbf{E}) = \eta_0 \hat{\mathbf{n}} \times \mathbf{H} \quad \text{on } \partial_{\infty}\Omega \quad (2.33c)$$

In the same way as in the E-B scheme, the electric and magnetic fields are expanded, and Equations (2.32) are tested. In this case, the basis function sets for electric and magnetic fields are the same. Thus, the expressions for the unknown fields, considering vector-basis functions, take the following form,

$$\tilde{\mathbf{E}} = \sum_{m=1}^N e_m(t) \phi_m(\mathbf{r}) = \mathbf{E}^T \Phi \quad (2.34a)$$

$$\tilde{\mathbf{H}} = \sum_{m=1}^N h_m(t) \phi_m(\mathbf{r}) = \mathbf{H}^T \Phi \quad (2.34b)$$

where e_m and h_m are the unknowns, ϕ_m represents the vector-basis functions, and N is the number of degrees of freedom (dof) or expansion/testing functions. We denote column vectors containing the unknowns as, $\mathbf{E} = [e_1, e_2, \dots, e_N]^T$ and $\mathbf{H} = [h_1, h_2, \dots, h_N]^T$, and the basis functions set as, $\Phi = [\phi_1, \phi_2, \dots, \phi_N]^T$.

There are two different approaches depending on how the continuity between adjacent elements is considered. It can be applied in a strong way, as it is in the single-field scheme, or, otherwise, discontinuity can be allowed across the boundaries, forcing the flux to be continuous.

In the first case, where field continuity is forced, an equivalent requirement for the basis functions such as (2.21) has to be established.

$$\hat{\mathbf{n}} \times \mathbf{E}^+ = \hat{\mathbf{n}} \times \mathbf{E}^- \quad (2.35a)$$

$$\hat{\mathbf{n}} \times \mathbf{H}^+ = \hat{\mathbf{n}} \times \mathbf{H}^- \quad (2.35b)$$

Inserting (2.34) into (2.32), and testing these two equations according to the Galerkin procedure, we obtain the following semi-discrete system of ODE,

$$\mathbb{M}_{\bar{\epsilon}} \frac{d}{dt} E = \mathbb{S} H - J \quad (2.36a)$$

$$\mathbb{M}_{\bar{\mu}} \frac{d}{dt} H = -\mathbb{S} E \quad (2.36b)$$

where

$$\mathbb{M}_{\bar{\alpha}}_{ij} = \int_{\Omega} \phi_i \cdot \bar{\alpha} \phi_j d\Omega, \quad \text{with } \bar{\alpha} = \{\bar{\epsilon}, \bar{\mu}\} \quad (2.37a)$$

$$\mathbb{S}_{ij} = \int_{\Omega} \phi_i \cdot \nabla \times \phi_j d\Omega \quad (2.37b)$$

$$J_i = \int_{\Omega} \phi_i \cdot \frac{\partial}{\partial t} \mathbf{J}_{imp} d\Omega \quad (2.37c)$$

The mass matrices $\mathbb{M}_{\bar{\alpha}}$ are sparse and not diagonal, due to the (2.35) requirement, which makes it necessary to share the same unknown in adjacent elements. Thus, the scheme (2.36) is implicit in space and requires the resolution of two linear systems each time step, making this approach computationally prohibitive for electrically large problems.

In the case that field discontinuity between elements were allowed, basis functions do not have the (2.35) requirement. Electric and magnetic fields are expanded element by element, and the solution is not forced to be continuous at the boundaries between adjacent elements. Instead, continuous numerical fluxes are defined at the interface in order to connect the solution between them in the manner used in FVTD methods, which is the main idea of DGTD methods. As described in detail in the next chapter, two common flux conditions are found in the literature: the centered flux [53], and the upwind flux [85]. The latter is the one actually employed in FVTD, and in fact, FVTD can be regarded as a special case of DGTD with this flux, and 0th order (constant) scalar basis functions [75]. Apart from these two flux conditions, a generalized flux can be expressed [54, 64] with a parameter that penalizes the jump of the vector tangential components between the elements.

The main advantage of DGTD over FVTD is its higher order in space, while over continuous FEMTD, the advantage resides in the fact that the mass matrices ($\mathbb{M}_{\bar{\alpha}}$) become block-diagonal, and DGTD needs only the inversion of M square matrices of $Q \times Q$ elements (with M the number of elements, and Q the number of basis functions per element), while larger matrices ($\simeq MQ \times MQ$) are involved in continuous FEMTD.

Chapter 3

Discontinuous Galerkin Time-Domain Methods: The Leap-Frog Discontinuous Galerkin Algorithm

This chapter begins with a description of the discontinuous Galerkin formulation, in its semi-discrete form, in a general framework which unifies different flux-evaluation schemes successfully applied to this method. The problem of dealing with anisotropic materials in DGTD is also addressed, in a 3D general form, as well as the implementation of conformal uniaxial perfectly matched layer-truncation conditions. Finally, the fully discrete form is derived, and the most usual explicit temporal integration schemes are presented. Full details are provided for the leap-frog discontinuous Galerkin algorithm, and a specific local time-stepping strategy.

3.1 Discontinuous Galerkin Formulation

Maxwell curl equations in three-dimensions (\mathbb{R}^3) for heterogeneous isotropic linear media without sources are

$$\mu \frac{\partial \mathbf{H}}{\partial t} = -\nabla \times \mathbf{E} - \sigma_m \mathbf{H} \quad (3.1a)$$

$$\varepsilon \frac{\partial \mathbf{E}}{\partial t} = \nabla \times \mathbf{H} - \sigma_e \mathbf{E} \quad (3.1b)$$

with electric permittivity $\varepsilon(\mathbf{r})$, electric conductivity $\sigma_e(\mathbf{r})$, magnetic permeability $\mu(\mathbf{r})$ and magnetic conductivity $\sigma_m(\mathbf{r})$, all possibly varying in space.

Let Ω be a bounded finite region of \mathbb{R}^3 for which the boundary is $\partial\Omega$, where a numerical solution of Equations (3.1) is intended to be computed. The domain Ω is subdivided into M non-overlapping and conformal cells (tetrahedra, as described previously in Section 2.1) which make up the computational domain, Ω_M . The m^{th} cell is defined by the volume \mathcal{T}_m , the boundaries $\partial\mathcal{T}_m$, and the electric and magnetic parameters ($\varepsilon(\mathbf{r})$, $\sigma_e(\mathbf{r})$, $\mu(\mathbf{r})$ and $\sigma_m(\mathbf{r})$).

$$\Omega \simeq \Omega_M = \bigcup_M \mathcal{T}_m \quad (3.2)$$

Let us define, the local inner product, and norm at each finite element \mathcal{T}_m as

$$\langle \mathbf{u}, \mathbf{v} \rangle_{\mathcal{T}_m} = \int_{\mathcal{T}_m} \mathbf{u} \cdot \mathbf{v} \, dv, \quad \|\mathbf{u}\|_{\mathcal{T}_m}^2 = \langle \mathbf{u}, \mathbf{u} \rangle \quad (3.3)$$

and also the local inner product over its boundaries $\partial\mathcal{T}_m$

$$\langle \mathbf{u}, \mathbf{v} \rangle_{\partial\mathcal{T}_m} = \oint_{\partial\mathcal{T}_m} \mathbf{u} \cdot \mathbf{v} \, ds, \quad (3.4)$$

In this section, a semi-discrete scheme, based upon the DG technique and vector-basis functions, is developed. Firstly, the basic semi-discrete scheme is formulated. Then, the implementation of the most common boundary conditions is described, which makes use of the flux terms to apply them in a weak way.

3.1.1 Semi-Discrete Scheme Formulation

Let us define the set of Q local vector-basis functions, described previously in Section 2.2, which, in general, are different for each cell \mathcal{T}_m ($Q(m) \equiv Q_m$), as

$$\mathcal{B}^m = \{\phi_1^m, \phi_2^m, \dots, \phi_{Q_m}^m\}, \quad m = 1, \dots, M \quad (3.5)$$

These basis functions are used to expand the unknown vector-field quantities (\mathbf{E} and \mathbf{H}), and to test Equation (3.1), as is usual in the Galerkin method. The weak form of

Maxwell equations (3.1) is found after using the inner product,

$$\int_{\mathcal{T}_m} \left[\mu \frac{\partial \mathbf{H}}{\partial t} + \nabla \times \mathbf{E} + \sigma_m \mathbf{H} \right] \cdot \phi_{q'}^m dv = 0 \quad (3.6a)$$

$$\int_{\mathcal{T}_m} \left[\varepsilon \frac{\partial \mathbf{E}}{\partial t} - \nabla \times \mathbf{H} + \sigma_e \mathbf{E} \right] \cdot \phi_{q'}^m dv = 0 \quad (3.6b)$$

$$m = 1, \dots, M \quad \text{and} \quad q' = 1, \dots, Q_m$$

Applying some algebra to the curl terms, we obtain

$$\begin{aligned} \int_{\mathcal{T}_m} (\nabla \times \mathbf{U}) \cdot \phi_{q'}^m dv &= \int_{\mathcal{T}_m} \nabla \cdot (\mathbf{U} \times \phi_{q'}^m) dv + \int_{\mathcal{T}_m} (\nabla \times \phi_{q'}^m) \cdot \mathbf{U} dv = \\ &= \oint_{\partial \mathcal{T}_m} (\hat{\mathbf{n}}^m \times \mathbf{U}) \cdot \phi_{q'}^m ds + \int_{\mathcal{T}_m} (\nabla \times \phi_{q'}^m) \cdot \mathbf{U} dv \end{aligned} \quad (3.7)$$

with $\mathbf{U} = \{\mathbf{E}, \mathbf{H}\}$, and $\hat{\mathbf{n}}^m$ the outward unit vector normal to the element m .

Introducing (3.7) into (3.6), together with a tangential field continuity condition between adjacent elements, we find the continuous FEMTD method [11]. Namely, adding the superscript $+$ to the fields at $\partial \mathcal{T}_m$ calculated in the element adjacent to m , the continuity on the tangential field components on the common face $\partial \mathcal{T}_m$ of two adjacent elements requires for continuous FEMTD that

$$\hat{\mathbf{n}}^m \times \mathbf{E}^{m+} = \hat{\mathbf{n}}^m \times \mathbf{E}^m, \quad \hat{\mathbf{n}}^m \times \mathbf{H}^{m+} = \hat{\mathbf{n}}^m \times \mathbf{H}^m \quad (3.8)$$

The main drawback of the resulting algorithm resides in its implicit nature, which requires the solution of large systems of linear equations [121]. The core idea of DGTD is to relax the continuity conditions to yield a quasi-explicit algorithm. That is, instead of plugging (3.8) into (3.7) and (3.6), DGTD defines numerical values of the tangential fields on $\partial \mathcal{T}_m$, henceforth called numerical fluxes ($\hat{\mathbf{n}}^m \times \mathbf{H}^{m*}$ and $\hat{\mathbf{n}}^m \times \mathbf{E}^{m*}$), which do not coincide with any of the values of the tangential fields on any side of $\partial \mathcal{T}_m$ but depend linearly on them,

$$\hat{\mathbf{n}}^m \times \mathbf{E}^{m*} = \hat{\mathbf{n}}^m \times (\mathbf{f}_E^-(\mathbf{E}^m, \mathbf{H}^m) + \mathbf{f}_E^+(\mathbf{E}^{m+}, \mathbf{H}^{m+})) \quad (3.9a)$$

$$\hat{\mathbf{n}}^m \times \mathbf{H}^{m*} = \hat{\mathbf{n}}^m \times (\mathbf{f}_H^-(\mathbf{H}^m, \mathbf{E}^m) + \mathbf{f}_H^+(\mathbf{H}^{m+}, \mathbf{E}^{m+})) \quad (3.9b)$$

where \mathbf{f}_E^\pm and \mathbf{f}_H^\pm are functions of the respective arguments.

This numerical flux is the one actually employed by any pair of adjacent elements to calculate the surface (flux) integrals in (3.7), instead of $\hat{\mathbf{n}}^m \times \mathbf{E}^m$ and $\hat{\mathbf{n}}^m \times \mathbf{H}^m$.

TABLE 3.1: Parameters in Equation (3.10) to yield centered, upwind, and partially penalized numerical fluxes. $Z^m = \sqrt{\frac{\mu^m}{\epsilon^m}} = \frac{1}{Y^m}$ is the intrinsic impedance of the element m , and $Z^{m+} = \frac{1}{Y^{m+}}$ is that of the adjacent one.

	κ_e^m	κ_h^m	ν_h^m	ν_e^m
centered	$\frac{1}{2}$	$\frac{1}{2}$	0	0
upwind	$\frac{Y^{m+}}{Y^m + Y^{m+}}$	$\frac{Z^{m+}}{Z^m + Z^{m+}}$	$\frac{1}{Y^m + Y^{m+}}$	$\frac{1}{Z^m + Z^{m+}}$
partially penalized	$\frac{Y^{m+}}{Y^m + Y^{m+}}$	$\frac{Z^{m+}}{Z^m + Z^{m+}}$	$\frac{\tau}{Y^m + Y^{m+}}$	$\frac{\tau}{Z^m + Z^{m+}}$

Three common choices for the numerical flux are reported in the literature (described in Section 3.2). A general form for all of them is

$$\hat{\mathbf{n}}^m \times \mathbf{E}^{m*} = \hat{\mathbf{n}}^m \times \mathbf{E}^m + \kappa_e^m [\hat{\mathbf{n}}^m \times (\mathbf{E}^{m+} - \mathbf{E}^m) + \mathbf{M}_s] + \nu_h^m [\hat{\mathbf{n}}^m \times (\hat{\mathbf{n}}^m \times (\mathbf{H}^{m+} - \mathbf{H}^m) - \mathbf{J}_s)] \quad (3.10a)$$

$$\hat{\mathbf{n}}^m \times \mathbf{H}^{m*} = \hat{\mathbf{n}}^m \times \mathbf{H}^m + \kappa_h^m [\hat{\mathbf{n}}^m \times (\mathbf{H}^{m+} - \mathbf{H}^m) - \mathbf{J}_s] - \nu_e^m [\hat{\mathbf{n}}^m \times (\hat{\mathbf{n}}^m \times (\mathbf{E}^{m+} - \mathbf{E}^m) + \mathbf{M}_s)] \quad (3.10b)$$

where we have also included possible surface currents \mathbf{M}_s and \mathbf{J}_s , to be used, for instance, in the implementation of Huygens sources¹. Table 3.1 shows the expressions for the κ and ν factors for centered, upwind, and partially penalized numerical fluxes. The terms which are multiplied by ν factors are known as dissipative terms. These terms introduce some dissipation to the scheme [60], but are essential to avoid the propagation of non-physical or spurious modes in the computational domain. As will be shown in Section 4.1.1, where dissipation rates are numerically evaluated in the eigenvalue problem, the dissipation rates for the spurious modes are much higher than for the physical modes [54]. In case of $\nu = 0$ (centered flux), there is no dissipation for either physical or spurious modes, at the cost of introducing spectral pollution to the method. In between the upwind and centered fluxes, a family of partially penalized fluxes can be defined [64], through the addition to the centered flux of dissipation terms that can be tuned to attenuate the spurious modes, and improve the accuracy.

¹These terms are the ones used to implement sources; plane-waves, waveguide ports, or delta-gaps. Full details of sources implementation appear in Sections 5.2.1 and A.4.2.

Plugging (3.10) into (3.7), the curl terms can be written as

$$\begin{aligned} \int_{\mathcal{T}_m} (\nabla \times \mathbf{E}^{m*}) \cdot \phi_{q'}^m dv &= \int_{\mathcal{T}_m} (\nabla \times \mathbf{E}^m) \cdot \phi_{q'}^m dv - \\ &\oint_{\partial\mathcal{T}_m} \kappa_e^m [\hat{\mathbf{n}}^m \times (\mathbf{E}^m - \mathbf{E}^{m+}) - \mathbf{M}_s] \cdot \phi_{q'}^m ds - \\ &\oint_{\partial\mathcal{T}_m} \nu_h^m [\hat{\mathbf{n}}^m \times (\hat{\mathbf{n}}^m \times (\mathbf{H}^m - \mathbf{H}^{m+}) + \mathbf{J}_s)] \cdot \phi_{q'}^m ds \end{aligned} \quad (3.11a)$$

$$\begin{aligned} \int_{\mathcal{T}_m} (\nabla \times \mathbf{H}^{m*}) \cdot \phi_{q'}^m dv &= \int_{\mathcal{T}_m} (\nabla \times \mathbf{H}^m) \cdot \phi_{q'}^m dv - \\ &\oint_{\partial\mathcal{T}_m} \kappa_h^m [\hat{\mathbf{n}}^m \times (\mathbf{H}^m - \mathbf{H}^{m+}) + \mathbf{J}_s] \cdot \phi_{q'}^m ds + \\ &\oint_{\partial\mathcal{T}_m} \nu_e^m [\hat{\mathbf{n}}^m \times (\hat{\mathbf{n}}^m \times (\mathbf{E}^m - \mathbf{E}^{m+}) - \mathbf{M}_s)] \cdot \phi_{q'}^m ds \end{aligned} \quad (3.11b)$$

The semi-discrete DG algorithm is found by assuming that the space and time dependencies of the fields can be separated. Thus, the spatial part is expanded, as stated above, within each element in the sets of vector-basis functions equal to the sets of test functions,

$$\mathbf{H} \simeq \tilde{\mathbf{H}} = \sum_{q=1}^{Q_m} h_q^m(t) \phi_q^m(\mathbf{r}) \quad (3.12a)$$

$$\mathbf{E} \simeq \tilde{\mathbf{E}} = \sum_{q=1}^{Q_m} e_q^m(t) \phi_q^m(\mathbf{r}) \quad (3.12b)$$

Finally, after expanding the vector magnitudes \mathbf{H} and \mathbf{E} , according to (3.12), and introducing the curl terms (3.11) into (3.6), the final form of the semi-discrete algorithm at the element m is

$$\mu \mathbb{M} d_t H^m + (\sigma_m \mathbb{M} - \mathbb{F}_{\nu h}) H^m + \mathbb{F}_{\nu h}^+ H^{m+} = -(\mathbb{S} - \mathbb{F}_{\kappa e}) E^m - \mathbb{F}_{\kappa e}^+ E^{m+} - M_{s\kappa} + J_{s\nu} \quad (3.13a)$$

$$\varepsilon \mathbb{M} d_t E^m + (\sigma_e \mathbb{M} - \mathbb{F}_{\nu e}) E^m + \mathbb{F}_{\nu e}^+ E^{m+} = (\mathbb{S} - \mathbb{F}_{\kappa h}) H^m + \mathbb{F}_{\kappa h}^+ H^{m+} - J_{s\kappa} - M_{s\nu} \quad (3.13b)$$

where we have assumed that the material properties are constant within each element, and with:

- H^m and E^m are column vectors varying in time with the field coefficients (dof) in the element m , and H^{m+} and E^{m+} with the field coefficients (dof) of the adjacent

elements,

$$H^m = (h_1^m(t), \dots, h_{Q_m}^m(t))^T \quad (3.14a)$$

$$E^m = (e_1^m(t), \dots, e_{Q_m}^m(t))^T \quad (3.14b)$$

- $M_{s\kappa}$, $M_{s\nu}$, $J_{s\kappa}$ and $J_{s\nu}$ are column vectors varying in time with the weak form of the surface source terms in the element m ,

$$M_{s\kappa} = \left(\langle \phi_1^m, \kappa_e^m \mathbf{M}_s(\mathbf{r}, t) \rangle_{\partial\mathcal{T}_m}, \dots, \langle \phi_{Q_m}^m, \kappa_e^m \mathbf{M}_s(\mathbf{r}, t) \rangle_{\partial\mathcal{T}_m} \right)^T \quad (3.15a)$$

$$M_{s\nu} = \left(\langle \phi_1^m, \nu_e^m \hat{\mathbf{n}}^m \times \mathbf{M}_s(\mathbf{r}, t) \rangle_{\partial\mathcal{T}_m}, \dots, \langle \phi_{Q_m}^m, \nu_e^m \hat{\mathbf{n}}^m \times \mathbf{M}_s(\mathbf{r}, t) \rangle_{\partial\mathcal{T}_m} \right)^T \quad (3.15b)$$

$$J_{s\kappa} = \left(\langle \phi_1^m, \kappa_h^m \mathbf{J}_s(\mathbf{r}, t) \rangle_{\partial\mathcal{T}_m}, \dots, \langle \phi_{Q_m}^m, \kappa_h^m \mathbf{J}_s(\mathbf{r}, t) \rangle_{\partial\mathcal{T}_m} \right)^T \quad (3.15c)$$

$$J_{s\nu} = \left(\langle \phi_1^m, \nu_h^m \hat{\mathbf{n}}^m \times \mathbf{J}_s(\mathbf{r}, t) \rangle_{\partial\mathcal{T}_m}, \dots, \langle \phi_{Q_m}^m, \nu_h^m \hat{\mathbf{n}}^m \times \mathbf{J}_s(\mathbf{r}, t) \rangle_{\partial\mathcal{T}_m} \right)^T \quad (3.15d)$$

- \mathbb{M} is the mass matrix,

$$[\mathbb{M}]_{q'q} = \langle \phi_{q'}^m, \phi_q^m \rangle_{\mathcal{T}_m} \quad (3.16)$$

- \mathbb{S} is the stiffness matrix,

$$[\mathbb{S}]_{q'q} = \langle \phi_{q'}^m, \nabla \times \phi_q^m \rangle_{\mathcal{T}_m} \quad (3.17)$$

- \mathbb{F} are the flux matrices,

$$[\mathbb{F}_{\kappa h}]_{q'q} = \langle \phi_{q'}^m, \hat{\mathbf{n}}^m \times \kappa_h^m \phi_q^m \rangle_{\partial\mathcal{T}_m}, \quad [\mathbb{F}_{\kappa e}]_{q'q} = \langle \phi_{q'}^m, \hat{\mathbf{n}}^m \times \kappa_e^m \phi_q^m \rangle_{\partial\mathcal{T}_m} \quad (3.18a)$$

$$[\mathbb{F}_{\nu h}]_{q'q} = \langle \phi_{q'}^m, \hat{\mathbf{n}}^m \times \hat{\mathbf{n}}^m \times \nu_h^m \phi_q^m \rangle_{\partial\mathcal{T}_m}, \quad [\mathbb{F}_{\nu e}]_{q'q} = \langle \phi_{q'}^m, \hat{\mathbf{n}}^m \times \hat{\mathbf{n}}^m \times \nu_e^m \phi_q^m \rangle_{\partial\mathcal{T}_m} \quad (3.18b)$$

$$[\mathbb{F}_{\kappa h}^+]_{q'q} = \langle \phi_{q'}^m, \hat{\mathbf{n}}^m \times \kappa_h^m \phi_q^{m+} \rangle_{\partial\mathcal{T}_m}, \quad [\mathbb{F}_{\kappa e}^+]_{q'q} = \langle \phi_{q'}^m, \hat{\mathbf{n}}^m \times \kappa_e^m \phi_q^{m+} \rangle_{\partial\mathcal{T}_m} \quad (3.18c)$$

$$[\mathbb{F}_{\nu h}^+]_{q'q} = \langle \phi_{q'}^m, \hat{\mathbf{n}}^m \times \hat{\mathbf{n}}^m \times \nu_h^m \phi_q^{m+} \rangle_{\partial\mathcal{T}_m}, \quad [\mathbb{F}_{\nu e}^+]_{q'q} = \langle \phi_{q'}^m, \hat{\mathbf{n}}^m \times \hat{\mathbf{n}}^m \times \nu_e^m \phi_q^{m+} \rangle_{\partial\mathcal{T}_m} \quad (3.18d)$$

Notice that κ and ν factors, when the upwind flux is employed, are a function of the electric and magnetic parameters of the material on the element m and all adjacent elements $m+$, so that there is no a constant value for all $[\mathbb{F}]_{q'q}$ coefficients. In case of centered flux, κ factors are constant ($\frac{1}{2}$) and ν factors are equal to 0, so that $\mathbb{F}_{\kappa h} = \mathbb{F}_{\kappa e}$, $\mathbb{F}_{\kappa h}^+ = \mathbb{F}_{\kappa e}^+$ and $\mathbb{F}_{\nu h} = \mathbb{F}_{\nu e} = \mathbb{F}_{\nu h}^+ = \mathbb{F}_{\nu e}^+ = 0$.

If we now use in the semi-discrete system (3.13), the space discretization described in Section 2.1, together with the vector-basis functions of Section 2.2, we find that the matrices \mathbb{S} , $\mathbb{F}_{\kappa e}$, $\mathbb{F}_{\kappa h}$, $\mathbb{F}_{\kappa e}^+$ and $\mathbb{F}_{\kappa h}^+$ can be shared between the elements. That is, since they are independent of the geometrical data, a large saving of memory is attained in its computer implementation.

Let us prove this for the \mathbb{S} matrix. The expression of a basis-function ϕ in the 3D reference cell can be written as

$$\phi = f_1(L_1, L_2, L_3) \nabla L_1 + f_2(L_1, L_2, L_3) \nabla L_2 + f_3(L_1, L_2, L_3) \nabla L_3 \quad (3.19)$$

where L_1, L_2, L_3 are local coordinates. This can also be written with the following notation,

$$\phi = \phi_{\nabla L_1} \nabla L_1 + \phi_{\nabla L_2} \nabla L_2 + \phi_{\nabla L_3} \nabla L_3 = \phi_x \hat{\mathbf{x}} + \phi_y \hat{\mathbf{y}} + \phi_z \hat{\mathbf{z}} \quad (3.20)$$

where $\phi_{\nabla L_i} = f_i(L_1, L_2, L_3)$, $i = 1, 2, 3$ are only polynomial functions.

For curl-conforming basis functions on curvilinear cells, the appropriate mapping is given by the contravariant transformation (2.15),

$$\begin{bmatrix} \phi_x \\ \phi_y \\ \phi_z \end{bmatrix} = J^{-1} \begin{bmatrix} \phi_{\nabla L_1} \\ \phi_{\nabla L_2} \\ \phi_{\nabla L_3} \end{bmatrix} \quad (3.21)$$

where J refers to the Jacobian matrix. The curl operation can be evaluated by making use of the expressions (2.16) and (2.17), which can be written in a compact form as

$$\begin{bmatrix} (\nabla \times \phi)_x \\ (\nabla \times \phi)_y \\ (\nabla \times \phi)_z \end{bmatrix} = \frac{J^T}{|J|} \begin{bmatrix} \frac{\partial \phi_{\nabla L_3}}{\partial L_2} - \frac{\partial \phi_{\nabla L_2}}{\partial L_3} \\ \frac{\partial \phi_{\nabla L_1}}{\partial L_3} - \frac{\partial \phi_{\nabla L_3}}{\partial L_1} \\ \frac{\partial \phi_{\nabla L_2}}{\partial L_1} - \frac{\partial \phi_{\nabla L_1}}{\partial L_2} \end{bmatrix} \quad (3.22)$$

Therefore, the \mathbb{S} matrix does not depend on the geometrical information,

$$\begin{aligned} [\mathbb{S}]_{q'q} &= \int_{V^m} \phi_{q'} \cdot (\nabla \times \phi_q) dV = \\ &= \int_{L_1} \int_{L_2} \int_{L_3} \left(J^{-1} \begin{bmatrix} \phi_{\nabla L_1} \\ \phi_{\nabla L_2} \\ \phi_{\nabla L_3} \end{bmatrix}_{q'} \right)^T \frac{J^T}{|J|} \begin{bmatrix} \frac{\partial \phi_{\nabla L_3}}{\partial L_2} - \frac{\partial \phi_{\nabla L_2}}{\partial L_3} \\ \frac{\partial \phi_{\nabla L_1}}{\partial L_3} - \frac{\partial \phi_{\nabla L_3}}{\partial L_1} \\ \frac{\partial \phi_{\nabla L_2}}{\partial L_1} - \frac{\partial \phi_{\nabla L_1}}{\partial L_2} \end{bmatrix}_q |J| dL_1 dL_2 dL_3 = \\ &= \int_{L_1} \int_{L_2} \int_{L_3} \begin{bmatrix} \phi_{\nabla L_1} & \phi_{\nabla L_2} & \phi_{\nabla L_3} \end{bmatrix}_{q'} \begin{bmatrix} \frac{\partial \phi_{\nabla L_3}}{\partial L_2} - \frac{\partial \phi_{\nabla L_2}}{\partial L_3} \\ \frac{\partial \phi_{\nabla L_1}}{\partial L_3} - \frac{\partial \phi_{\nabla L_3}}{\partial L_1} \\ \frac{\partial \phi_{\nabla L_2}}{\partial L_1} - \frac{\partial \phi_{\nabla L_1}}{\partial L_2} \end{bmatrix}_q dL_1 dL_2 dL_3 \end{aligned} \quad (3.23)$$

since the kernels of these integrals are a combination of polynomial functions that depend only on local coordinates. For $\mathbb{F}_{\kappa e}$, $\mathbb{F}_{\kappa h}$, $\mathbb{F}_{\kappa e}^+$ and $\mathbb{F}_{\kappa h}^+$ matrices, a similar proof can be performed.

3.1.2 Boundary Conditions

The flux conditions which serve to connect adjacent fields, also serve to implement the most common boundary conditions:

1. The interface between two elements with different ε and μ is handled in an indirect manner in DG, thanks to taking the same tangential components of the fields $\hat{\mathbf{n}}^m \times \mathbf{E}^{m*}$ and $\hat{\mathbf{n}}^m \times \mathbf{H}^{m*}$ in the flux integrals for two adjacent elements.
2. The PEC condition on a face of an element m requires the tangential component of the electric field employed in the flux integrals to be null, and the tangential magnetic field to be continuous.

$$\hat{\mathbf{n}}^m \times \mathbf{E}^{m+} = -\hat{\mathbf{n}}^m \times \mathbf{E}^m \quad (3.24a)$$

$$\hat{\mathbf{n}}^m \times \mathbf{H}^{m+} = \hat{\mathbf{n}}^m \times \mathbf{H}^m \quad (3.24b)$$

This is easily fulfilled, in a weak form, by considering different κ and ν factors at the face of the m element for which the PEC boundary condition is intended to be applied.

$$\kappa_e^m \text{PEC} = 2 \kappa_e^m, \quad \nu_e^m \text{PEC} = 2 \nu_e^m \quad (3.25a)$$

$$\kappa_h^m \text{PEC} = 0, \quad \nu_h^m \text{PEC} = 0 \quad (3.25b)$$

3. The PMC condition is the reciprocal of the PEC one,

$$\hat{\mathbf{n}}^m \times \mathbf{H}^{m+} = -\hat{\mathbf{n}}^m \times \mathbf{H}^m \quad (3.26a)$$

$$\hat{\mathbf{n}}^m \times \mathbf{E}^{m+} = \hat{\mathbf{n}}^m \times \mathbf{E}^m \quad (3.26b)$$

and the expressions for the κ and ν factors are

$$\kappa_h^m \text{PMC} = 2 \kappa_h^m, \quad \nu_h^m \text{PMC} = 2 \nu_h^m \quad (3.27a)$$

$$\kappa_e^m \text{PMC} = 0, \quad \nu_e^m \text{PMC} = 0 \quad (3.27b)$$

Note that for the upwind flux, both for PEC and PMC, we must also assume $Y^{m+} = Y^m$ and $Z^{m+} = Z^m$.

4. Regarding the ABC, the first-order SM-ABC [143] is straightly based on considering that the fields outside the computational domain propagate as plane waves normal to the interface, $\hat{\mathbf{n}} \times \hat{\mathbf{n}} \times \mathbf{E} = Z (\hat{\mathbf{n}} \times \mathbf{H})$, $\hat{\mathbf{n}} \times \hat{\mathbf{n}} \times \mathbf{H} = -Y (\hat{\mathbf{n}} \times \mathbf{E})$. For the upwind flux, this is directly handled since it is equivalent to assuming that

there is no contribution to the flux from outside the region of solution, with only $\mathbf{f}_{E,H}^-$ remaining in (3.9).

$$Y^m (\hat{\mathbf{n}}^m \times \mathbf{E}^{m+}) = -\hat{\mathbf{n}}^m \times \hat{\mathbf{n}}^m \times \mathbf{H}^{m+} \Rightarrow \hat{\mathbf{n}}^m \times \mathbf{f}_E^+ = \hat{\mathbf{n}}^m \times \frac{Y^m \mathbf{E}^{m+} + \hat{\mathbf{n}}^m \times \mathbf{H}^{m+}}{Y^m + Y^{m+}} = 0 \quad (3.28a)$$

$$Z^m (\hat{\mathbf{n}}^m \times \mathbf{H}^{m+}) = \hat{\mathbf{n}}^m \times \hat{\mathbf{n}}^m \times \mathbf{E}^{m+} \Rightarrow \hat{\mathbf{n}}^m \times \mathbf{f}_H^+ = \hat{\mathbf{n}}^m \times \frac{Z^m \mathbf{H}^{m+} - \hat{\mathbf{n}}^m \times \mathbf{E}^{m+}}{Z^m + Z^{m+}} = 0 \quad (3.28b)$$

In case of the centered and partially penalized fluxes, the SM-ABC is applied with a slightly different expressions,

$$\hat{\mathbf{n}}^m \times \mathbf{E}^{m+} = -\frac{1}{Y^m} (\hat{\mathbf{n}}^m \times \hat{\mathbf{n}}^m \times \mathbf{H}^m) \quad (3.29a)$$

$$\hat{\mathbf{n}}^m \times \mathbf{H}^{m+} = \frac{1}{Z^m} (\hat{\mathbf{n}}^m \times \hat{\mathbf{n}}^m \times \mathbf{E}^m) \quad (3.29b)$$

In all cases the final formulation is the same. The SM-ABC, as the previous boundary conditions, can be expressed as a function of the κ and ν factors,

$$\kappa_e^m \text{SM-ABC} = \kappa_h^m \text{SM-ABC} = \frac{1}{2} \quad (3.30a)$$

$$\nu_h^m \text{SM-ABC} = \frac{1}{2 Y^m}, \quad \nu_e^m \text{SM-ABC} = \frac{1}{2 Z^m} \quad (3.30b)$$

SM-ABC provides an ideally null reflection coefficient for normal incidence. In practice, its performance is reduced by the accuracy of the method, and depends on the order of the expansion functions p , and on the size of the elements h . Furthermore, its absorption characteristics rapidly degrade when the angle of incidence changes from normal incidence [144]. In Section 3.4.1, C-UPML are provided to overcome that limitation of SM-ABC. It is important to note that both ABC (SM-ABC and C-UPML) can be combined [92, 93, 145, 146], improving the overall performance. This can be done with no cost in the DG framework, since the implementation of SM-ABC removes only outside flux terms.

3.2 Numerical-Flux Evaluation

The flux concept appears in CEM in FVTD methods, [84, 85]. In FVTD, upwind-flux evaluation is the usual way to exchange information between elements. Centered flux has also been considered in DGTD due to its simplicity, versatility and efficiency, but raises the issue of spurious solutions. In between these two flux conditions, a generalized

flux can be found [54, 64] as a function of a parameter that penalizes the jump of the vector tangential components between the elements (see Table 3.1).

Let us consider Figures 3.1(a), 3.1(b) with the general case of the interface of two elements containing different materials (with/without surface currents), and let us focus on the evaluation of $\hat{\mathbf{n}} \times \mathbf{E}^*$ and $\hat{\mathbf{n}} \times \mathbf{H}^*$ (so-called flux functions) for all points P located in $\partial\mathcal{T}_m$. These flux functions are needed to compute the flux coming from \mathcal{T}_m+ to \mathcal{T}_m element, across the face $\partial\mathcal{T}_m$ (and reciprocally, $\hat{\mathbf{n}} \times \mathbf{E}^{*+}$ and $\hat{\mathbf{n}} \times \mathbf{H}^{*+}$ flux functions referring to the flux coming from \mathcal{T}_m into \mathcal{T}_m+).

The flux functions are found by solving exactly, as upwind does, or approximately, as centered or partially penalized, a one-dimensional Riemann problem in the direction $\hat{\mathbf{n}}$ perpendicular to the face $\partial\mathcal{T}_m$, where $\hat{\mathbf{n}} \times \mathbf{E}^m$ and $\hat{\mathbf{n}} \times \mathbf{E}^{m+}$, and $\hat{\mathbf{n}} \times \mathbf{H}^m$ and $\hat{\mathbf{n}} \times \mathbf{H}^{m+}$, are allowed to be discontinuous.

In order to break down all expressions into normal ($\hat{\mathbf{n}}$) and tangential ($\hat{\mathbf{t}}_1, \hat{\mathbf{t}}_2$) components at the face $\partial\mathcal{T}_m$, we define a set of local coordinates, t_1, t_2 and n , and the associated orthonormal local vector basis ($\hat{\mathbf{t}}_1, \hat{\mathbf{t}}_2, \hat{\mathbf{n}}$) as

$$\hat{\mathbf{t}}_1 = \frac{\partial \mathbf{r}}{\partial t_1} \left| \frac{\partial \mathbf{r}}{\partial t_1} \right|^{-1} \quad (3.31a)$$

$$\hat{\mathbf{t}}_2 = \frac{\partial \mathbf{r}}{\partial t_2} \left| \frac{\partial \mathbf{r}}{\partial t_2} \right|^{-1} \quad (3.31b)$$

$$\hat{\mathbf{n}} = \hat{\mathbf{t}}_1 \times \hat{\mathbf{t}}_2 \quad (3.31c)$$

with transformation matrices, $\bar{\bar{R}}$ and $\bar{\bar{R}}^{-1}$, between the local vectorial base of (3.31) and the cartesian vectorial basis being

$$\begin{pmatrix} \hat{\mathbf{x}} \\ \hat{\mathbf{y}} \\ \hat{\mathbf{z}} \end{pmatrix} = \bar{\bar{R}} \begin{pmatrix} \hat{\mathbf{t}}_1 \\ \hat{\mathbf{t}}_2 \\ \hat{\mathbf{n}} \end{pmatrix}, \quad \begin{pmatrix} \hat{\mathbf{t}}_1 \\ \hat{\mathbf{t}}_2 \\ \hat{\mathbf{n}} \end{pmatrix} = \bar{\bar{R}}^{-1} \begin{pmatrix} \hat{\mathbf{x}} \\ \hat{\mathbf{y}} \\ \hat{\mathbf{z}} \end{pmatrix} \quad (3.32)$$

Impressed electric and magnetic surface-current densities (\mathbf{J}_s and \mathbf{M}_s) at the face $\partial\mathcal{T}_m$ (Figure 3.1(b)) can be accounted for through the discontinuity in the tangential field components,

$$\hat{\mathbf{n}} \times (\mathbf{E}_2 - \mathbf{E}_1) = -\mathbf{M}_s \quad (3.33a)$$

$$\hat{\mathbf{n}} \times (\mathbf{H}_2 - \mathbf{H}_1) = \mathbf{J}_s \quad (3.33b)$$

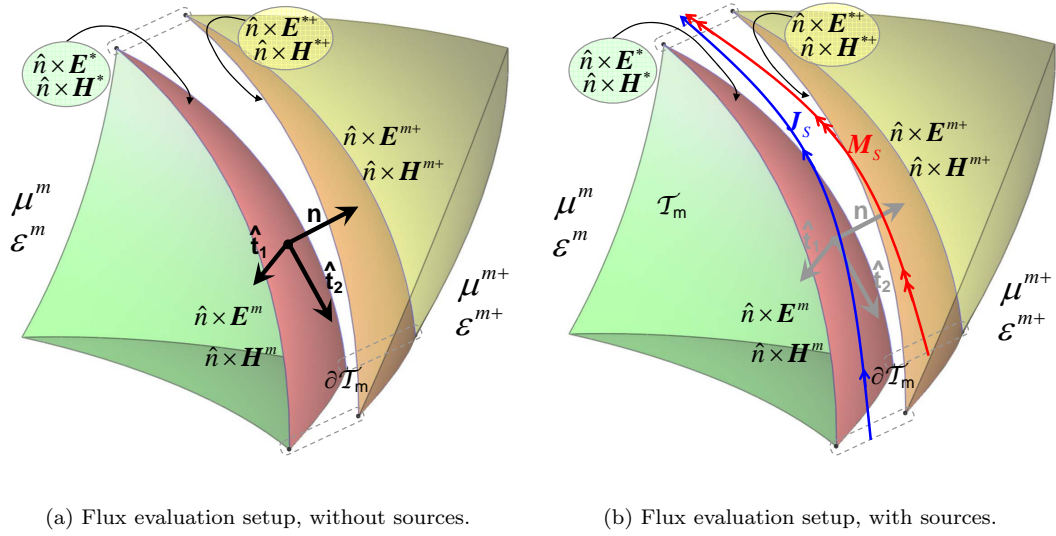


FIGURE 3.1: Flux evaluation setups

Both tetrahedra are physically in contact, and have been represented separately only for clarification.

The subscript m in the local vectors $\hat{\mathbf{t}}_1, \hat{\mathbf{t}}_2$ and $\hat{\mathbf{n}}$ has been removed for the same reason.

with subindexes 1 and 2 corresponding to the semi-spaces at either side of the surface where the currents are flowing: \mathbf{J}_s will produce a discontinuity in the vector $\hat{\mathbf{n}} \times \mathbf{H}$, and \mathbf{M}_s will produce a discontinuity in the vector $\hat{\mathbf{n}} \times \mathbf{E}$.

3.2.1 Centered-Flux Evaluation

The centered flux [108] can be evaluated simply by averaging the solutions of the fields at both sides of the interface. For instance, the expressions for the centered fluxes on the outer boundary-face of the problem of Figure 3.1(a) are the following,

$$\hat{\mathbf{n}} \times \mathbf{E}^* = \hat{\mathbf{n}} \times \mathbf{E}^{*+} = \hat{\mathbf{n}} \times \frac{\mathbf{E}^m + \mathbf{E}^{m+}}{2} \quad (3.34a)$$

$$\hat{\mathbf{n}} \times \mathbf{H}^* = \hat{\mathbf{n}} \times \mathbf{H}^{*+} = \hat{\mathbf{n}} \times \frac{\mathbf{H}^m + \mathbf{H}^{m+}}{2} \quad (3.34b)$$

For the problem including the surface currents (Figure 3.1(b)), the boundary conditions (3.33) further impose,

$$\hat{\mathbf{n}} \times (\mathbf{E}^* - \mathbf{E}^{*+}) = \mathbf{M}_s \quad (3.35a)$$

$$\hat{\mathbf{n}} \times (\mathbf{H}^* - \mathbf{H}^{*+}) = -\mathbf{J}_s \quad (3.35b)$$

Averaging the solutions at both sides of the interface we find

$$\hat{\mathbf{n}} \times \mathbf{E}^* = \frac{\hat{\mathbf{n}} \times \mathbf{E}^m}{2} + \frac{\hat{\mathbf{n}} \times \mathbf{E}^{m+} + \mathbf{M}_s}{2} = \frac{\hat{\mathbf{n}} \times (\mathbf{E}^m + \mathbf{E}^{m+}) + \mathbf{M}_s}{2} \quad (3.36a)$$

$$\hat{\mathbf{n}} \times \mathbf{H}^* = \frac{\hat{\mathbf{n}} \times \mathbf{H}^m}{2} + \frac{\hat{\mathbf{n}} \times \mathbf{H}^{m+} - \mathbf{J}_s}{2} = \frac{\hat{\mathbf{n}} \times (\mathbf{H}^m + \mathbf{H}^{m+}) - \mathbf{J}_s}{2} \quad (3.36b)$$

and for the reciprocal-flux,

$$\hat{\mathbf{n}} \times \mathbf{E}^{*+} = \frac{\hat{\mathbf{n}} \times (\mathbf{E}^m + \mathbf{E}^{m+}) - \mathbf{M}_s}{2} \quad (3.37a)$$

$$\hat{\mathbf{n}} \times \mathbf{H}^{*+} = \frac{\hat{\mathbf{n}} \times (\mathbf{H}^m + \mathbf{H}^{m+}) + \mathbf{J}_s}{2} \quad (3.37b)$$

It is important to note that all the centered-flux functions expressed above do not depend on the material parameters, so that these expressions are valid for any kind of material, whether dispersive, anisotropic, etc..

3.2.2 Upwind-Flux Evaluation

A standard approach for developing numerical schemes for multidimensional and/or hyperbolic problems with source terms² is to use a fractional-step or operator-splitting method [147]. In this approach, simpler problems are somehow solved, and the combination of them leads to a global scheme that approximates the solution of the overall problem.

Let us find the upwind-flux conditions for heterogeneous isotropic materials, only considering electric losses, by solving Maxwell time-domain curl equations as an initial-boundary value problem,

$$\mu \frac{\partial \mathbf{H}}{\partial t} + \nabla \times \mathbf{E} = 0 \quad (3.38a)$$

$$\varepsilon \frac{\partial \mathbf{E}}{\partial t} - \nabla \times \mathbf{H} + \sigma_e \mathbf{E} = 0 \quad (3.38b)$$

The electric and magnetic field vectors are expressed in the local basis of vectors of Figures 3.1 as: $\mathbf{E} = (E_{t_1}, E_{t_2}, E_n)$ and $\mathbf{H} = (H_{t_1}, H_{t_2}, H_n)$. The ∇ operator can be also broken down into two terms,

$$\nabla = \frac{\partial}{\partial n} \hat{\mathbf{n}} + \nabla_S \quad (3.39)$$

²In this context, source terms will not only refer to current sources. In an extended manner, they will include any term of the original formulation, except those strictly belonging to the hyperbolic conservative problem. For instance, dissipative terms due to electric or magnetic conductivity, or new terms included in the formulation for the treatment of special materials, like for dispersive or PML media.

where $\frac{\partial}{\partial n} = \nabla \cdot \hat{\mathbf{n}}$ and ∇_S denote the normal and surface derivatives with respect to the local coordinates, respectively. The breakdown of the term $\nabla \times \mathbf{E}$ (and similarly for $\nabla \times \mathbf{H}$) yields

$$\begin{aligned}\nabla \times \mathbf{E} &= \frac{\partial}{\partial n} \hat{\mathbf{n}} \times \mathbf{E} + \nabla_S \times \mathbf{E} \\ \frac{\partial}{\partial n} \hat{\mathbf{n}} \times \mathbf{E} &= -\partial_n E_{t_2} \hat{\mathbf{t}}_1 + \partial_n E_{t_1} \hat{\mathbf{t}}_2 \\ \nabla_S \times \mathbf{E} &= \partial_{t_2} E_n \hat{\mathbf{t}}_1 - \partial_{t_1} E_n \hat{\mathbf{t}}_2 + (\partial_{t_1} E_{t_2} - \partial_{t_2} E_{t_1}) \hat{\mathbf{n}}\end{aligned}\tag{3.40}$$

(3.38) can be rewritten as

$$\frac{\partial \mathbf{H}}{\partial t} + \frac{1}{\mu} \frac{\partial}{\partial n} \hat{\mathbf{n}} \times \mathbf{E} + \frac{1}{\mu} \nabla_S \times \mathbf{E} = 0\tag{3.41a}$$

$$\frac{\partial \mathbf{E}}{\partial t} - \frac{1}{\varepsilon} \frac{\partial}{\partial n} \hat{\mathbf{n}} \times \mathbf{H} - \frac{1}{\varepsilon} \nabla_S \times \mathbf{H} + \frac{\sigma_e}{\varepsilon} \mathbf{E} = 0\tag{3.41b}$$

The operator-splitting method for (3.41) can be applied by first splitting the system of equations into two subproblems:

$$\textit{Problem A:} \quad \frac{\partial \mathbf{H}}{\partial t} + \frac{1}{\mu} \frac{\partial}{\partial n} \hat{\mathbf{n}} \times \mathbf{E} = 0\tag{3.42a}$$

$$\frac{\partial \mathbf{E}}{\partial t} - \frac{1}{\varepsilon} \frac{\partial}{\partial n} \hat{\mathbf{n}} \times \mathbf{H} = 0\tag{3.42b}$$

$$\textit{Problem B:} \quad \frac{\partial \mathbf{H}}{\partial t} + \frac{1}{\mu} \nabla_S \times \mathbf{E} = 0\tag{3.43a}$$

$$\frac{\partial \mathbf{E}}{\partial t} - \frac{1}{\varepsilon} \nabla_S \times \mathbf{H} + \frac{\sigma_e}{\varepsilon} \mathbf{E} = 0\tag{3.43b}$$

Problem A is a homogeneous conservation law, requiring the solutions of a discontinuous Riemann problem at the interface between the elements, while Problem B is a fully continuous problem, whose solution will not be needed for our purposes. In summary, the spirit of this splitting is that different methods can be used to solve each subproblem, and eventually combined afterwards to establish a global solution scheme.

It is important to mention that this separation can always be made, although other source terms are considered in the formulation. The expressions derived below are therefore valid in a broad sense for any isotropic media (dissipative, dispersive, PML and so on), as soon as Problem A is identified. Other different subproblems could have been defined; for instance, the source terms could also be extracted in a new subproblem from Problem B. However, the proposed separation of the problems suffices for our purpose, since only Problem A is required to derive the upwind-flux-evaluation expressions.

Let us solve Problem A in the scenario shown in Figure 3.1, allowing discontinuities of the fields, and singularities in the normal derivative terms $\frac{\partial}{\partial n}$. Problem A can be rewritten as a first-order hyperbolic multidimensional system of four partial differential equations (PDE),

$$\partial_t H_{t_1} - \frac{1}{\mu} \partial_n E_{t_2} = 0 \quad (3.44a)$$

$$\partial_t H_{t_2} + \frac{1}{\mu} \partial_n E_{t_1} = 0 \quad (3.44b)$$

$$\partial_t E_{t_1} + \frac{1}{\varepsilon} \partial_n H_{t_2} = 0 \quad (3.44c)$$

$$\partial_t E_{t_2} - \frac{1}{\varepsilon} \partial_n H_{t_1} = 0 \quad (3.44d)$$

where the normal components have been removed, since they are not part of Problem A. These can be expressed in a compact manner as

$$\partial_t \bar{q} + \bar{\mathbb{A}}_n \partial_n \bar{q} = 0 \quad (3.45)$$

with $\bar{q} = (H_{t_1}, H_{t_2}, E_{t_1}, E_{t_2})^T$, and $\bar{\mathbb{A}}_n$ matrix

$$\bar{\mathbb{A}}_n = \begin{pmatrix} 0 & 0 & 0 & -\frac{1}{\mu} \\ 0 & 0 & \frac{1}{\mu} & 0 \\ 0 & \frac{1}{\varepsilon} & 0 & 0 \\ -\frac{1}{\varepsilon} & 0 & 0 & 0 \end{pmatrix} \quad (3.46)$$

The system (3.45) is hyperbolic because the matrix $\bar{\mathbb{A}}_n$ has 4 real eigenvalues (λ_p). We refer to the corresponding set of 4 linearly independent right eigenvectors as (r_p). Any vector \bar{q} or ($\hat{\mathbf{n}} \times \mathbf{H}$ and $\hat{\mathbf{n}} \times \mathbf{E}$) can be uniquely expressed as a linear combination of these eigenvectors (distinct waves). The corresponding eigenvalues of $\bar{\mathbb{A}}_n$ give the wave speeds at which each wave propagates in the medium. There are two negative eigenvalues $\frac{-1}{\sqrt{\mu\varepsilon}}$, and two positive ones $\frac{+1}{\sqrt{\mu\varepsilon}}$ (the minus sign accounts for waves coming into the element, and the plus sign for waves going out),

$$\begin{aligned} \lambda_1 = \lambda_2 &= \frac{-1}{\sqrt{\mu\varepsilon}}; & r_1 &= (0, -Y, 1, 0)^T; & r_2 &= (Y, 0, 0, 1)^T \\ \lambda_3 = \lambda_4 &= \frac{+1}{\sqrt{\mu\varepsilon}}; & r_3 &= (0, Y, 1, 0)^T; & r_4 &= (-Y, 0, 0, 1)^T \end{aligned} \quad (3.47)$$

where $Z = \sqrt{\frac{\mu}{\varepsilon}} = \frac{1}{Y}$.

It important to note that (3.45) corresponds to a piece-wise variable-coefficient linear system. We can identify a matrix $\bar{\mathbb{A}}_n^m$ in \mathcal{T}_m , and a possible different matrix $\bar{\mathbb{A}}_n^{m+}$ in \mathcal{T}_{m+} . Solving the Riemann problem consists on enforcing the Rankine-Hugoniot

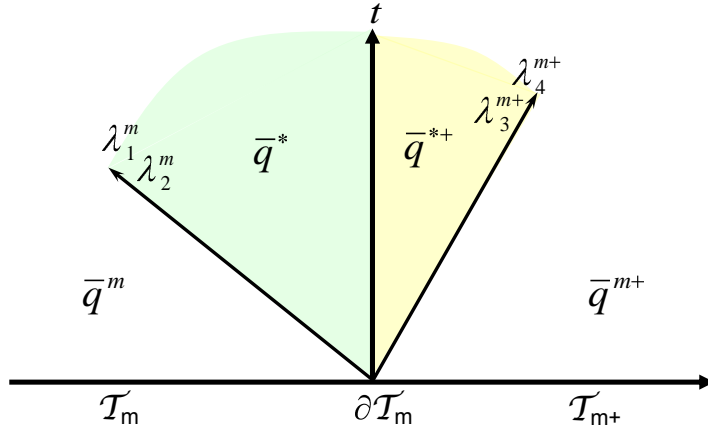


FIGURE 3.2: Structure of the solution to the Riemann problem for homogeneous materials (variable-coefficient), in the space-time plane (n - t plane). $\partial\mathcal{T}_m$ shows the interface between the two different elements. Each wave propagate at its speed in each material. Between these waves there are two states \bar{q}^* , \bar{q}^{*+} .

jump condition [147] at both sides of $\partial\mathcal{T}_m$. The Rankine-Hugoniot condition states that the jumps on the solution at each side of the interface is a linear combination of that side eigenvectors. This leads to two intermediate states (\bar{q}^* and \bar{q}^{*+}) which constitute the actual solution of the Riemann problem (Figure 3.2 shows the domains for these solutions).

The expression of these jumps, between the intermediate states and the values at both sides of $\partial\mathcal{T}_m$, in terms of the eigenvectors associated with the negative eigenvalues, for the element \mathcal{T}_m , and the eigenvectors associated with the positive eigenvalues, for the element \mathcal{T}_{m+} , is

$$\bar{q}^* - \bar{q}^m = \alpha_1^m r_1^m + \alpha_2^m r_2^m \quad (3.48a)$$

$$\bar{q}^{m+} - \bar{q}^{*+} = \alpha_3^{m+} r_3^{m+} + \alpha_4^{m+} r_4^{m+} \quad (3.48b)$$

for some scalar coefficients α_1^m , α_2^m , α_3^{m+} and α_4^{m+} . To solve the equation system (3.48), we need a relationship between \bar{q}^* and \bar{q}^{*+} . If no surface-current sources are present, as in Figure 3.1(a), then $\bar{q}^* = \bar{q}^{*+}$; otherwise, if there are surface-current sources, as in Figure 3.1(b), the jumps introduced by the boundary conditions of (3.35) must be considered.

The results for the scalar coefficients without surface-current sources are the following,

$$\begin{aligned}\alpha_1^m &= \frac{(H_{t_2}^m - H_{t_2}^{m+}) - Y^{m+}(E_{t_1}^m - E_{t_1}^{m+})}{Y^m + Y^{m+}} & \alpha_2^m &= -\frac{(H_{t_1}^m - H_{t_1}^{m+}) + Y^{m+}(E_{t_2}^m - E_{t_2}^{m+})}{Y^m + Y^{m+}} \\ \alpha_3^{m+} &= -\frac{(H_{t_2}^m - H_{t_2}^{m+}) + Y^m(E_{t_1}^m - E_{t_1}^{m+})}{Y^m + Y^{m+}} & \alpha_4^{m+} &= \frac{(H_{t_1}^m - H_{t_1}^{m+}) - Y^m(E_{t_2}^m - E_{t_2}^{m+})}{Y^m + Y^{m+}}\end{aligned}\quad (3.49)$$

Using Equations (3.48), we get the following solutions for each tangential field component,

$$H_{t_1}^* = H_{t_1}^{*+} = \frac{Z^m H_{t_1}^m + Z^{m+} H_{t_1}^{m+} - (E_{t_2}^m - E_{t_2}^{m+})}{Z^m + Z^{m+}} \quad (3.50a)$$

$$H_{t_2}^* = H_{t_2}^{*+} = \frac{Z^m H_{t_2}^m + Z^{m+} H_{t_2}^{m+} + (E_{t_1}^m - E_{t_1}^{m+})}{Z^m + Z^{m+}} \quad (3.50b)$$

$$E_{t_1}^* = E_{t_1}^{*+} = \frac{Y^m E_{t_1}^m + Y^{m+} E_{t_1}^{m+} + (H_{t_2}^m - H_{t_2}^{m+})}{Y^m + Y^{m+}} \quad (3.50c)$$

$$E_{t_2}^* = E_{t_2}^{*+} = \frac{Y^m E_{t_2}^m + Y^{m+} E_{t_2}^{m+} - (H_{t_1}^m - H_{t_1}^{m+})}{Y^m + Y^{m+}} \quad (3.50d)$$

which can also be expressed as

$$\hat{\mathbf{n}} \times \mathbf{E}^* = \hat{\mathbf{n}} \times \mathbf{E}^{*+} = \hat{\mathbf{n}} \times \frac{Y^m \mathbf{E}^m + Y^{m+} \mathbf{E}^{m+} + \hat{\mathbf{n}} \times (\mathbf{H}^{m+} - \mathbf{H}^m)}{Y^m + Y^{m+}} \quad (3.51a)$$

$$\hat{\mathbf{n}} \times \mathbf{H}^* = \hat{\mathbf{n}} \times \mathbf{H}^{*+} = \hat{\mathbf{n}} \times \frac{Z^m \mathbf{H}^m + Z^{m+} \mathbf{H}^{m+} - \hat{\mathbf{n}} \times (\mathbf{E}^{m+} - \mathbf{E}^m)}{Z^m + Z^{m+}} \quad (3.51b)$$

Finally, a general form of the solution of the Riemann problem, also including surface electric and magnetic current densities, is

$$\hat{\mathbf{n}} \times \mathbf{E}^* = \frac{\hat{\mathbf{n}} \times (Y^m \mathbf{E}^m + Y^{m+} \mathbf{E}^{m+}) + Y^{m+} \mathbf{M}_s + \hat{\mathbf{n}} \times [\hat{\mathbf{n}} \times (\mathbf{H}^{m+} - \mathbf{H}^m) - \mathbf{J}_s]}{Y^m + Y^{m+}} \quad (3.52a)$$

$$\hat{\mathbf{n}} \times \mathbf{H}^* = \frac{\hat{\mathbf{n}} \times (Z^m \mathbf{H}^m + Z^{m+} \mathbf{H}^{m+}) - Z^{m+} \mathbf{J}_s - \hat{\mathbf{n}} \times [\hat{\mathbf{n}} \times (\mathbf{E}^{m+} - \mathbf{E}^m) + \mathbf{M}_s]}{Z^m + Z^{m+}} \quad (3.52b)$$

$$\hat{\mathbf{n}} \times \mathbf{E}^{*+} = \frac{\hat{\mathbf{n}} \times (Y^m \mathbf{E}^m + Y^{m+} \mathbf{E}^{m+}) - Y^{m+} \mathbf{M}_s + \hat{\mathbf{n}} \times [\hat{\mathbf{n}} \times (\mathbf{H}^{m+} - \mathbf{H}^m) - \mathbf{J}_s]}{Y^m + Y^{m+}} \quad (3.52c)$$

$$\hat{\mathbf{n}} \times \mathbf{H}^{*+} = \frac{\hat{\mathbf{n}} \times (Z^m \mathbf{H}^m + Z^{m+} \mathbf{H}^{m+}) + Z^{m+} \mathbf{J}_s - \hat{\mathbf{n}} \times [\hat{\mathbf{n}} \times (\mathbf{E}^{m+} - \mathbf{E}^m) + \mathbf{M}_s]}{Z^m + Z^{m+}} \quad (3.52d)$$

3.2.3 Partially Penalized Flux Evaluation

The partially penalized flux [54, 64, 70, 71] generalizes both the upwind and centered-flux concept. Two different terms can be clearly identified in the upwind-flux expressions. Considering (3.52) (and similarly for (3.51)), and introducing the penalty parameter, τ , the general-flux-evaluation expressions is written as

$$\hat{\mathbf{n}} \times \mathbf{E}^* = \frac{\hat{\mathbf{n}} \times (Y^m \mathbf{E}^m + Y^{m+} \mathbf{E}^{m+}) + Y^{m+} \mathbf{M}_s}{Y^m + Y^{m+}} - \tau \frac{\hat{\mathbf{n}} \times [\hat{\mathbf{n}} \times (\mathbf{H}^m - \mathbf{H}^{m+}) + \mathbf{J}_s]}{Y^m + Y^{m+}} \quad (3.53a)$$

$$\hat{\mathbf{n}} \times \mathbf{H}^* = \frac{\hat{\mathbf{n}} \times (Z^m \mathbf{H}^m + Z^{m+} \mathbf{H}^{m+}) - Z^{m+} \mathbf{J}_s}{Z^m + Z^{m+}} + \tau \frac{\hat{\mathbf{n}} \times [\hat{\mathbf{n}} \times (\mathbf{E}^m - \mathbf{E}^{m+}) - \mathbf{M}_s]}{Z^m + Z^{m+}} \quad (3.53b)$$

$$\hat{\mathbf{n}} \times \mathbf{E}^{*+} = \frac{\hat{\mathbf{n}} \times (Y^m \mathbf{E}^m + Y^{m+} \mathbf{E}^{m+}) - Y^{m+} \mathbf{M}_s}{Y^m + Y^{m+}} - \tau \frac{\hat{\mathbf{n}} \times [\hat{\mathbf{n}} \times (\mathbf{H}^m - \mathbf{H}^{m+}) + \mathbf{J}_s]}{Y^m + Y^{m+}} \quad (3.53c)$$

$$\hat{\mathbf{n}} \times \mathbf{H}^{*+} = \frac{\hat{\mathbf{n}} \times (Z^m \mathbf{H}^m + Z^{m+} \mathbf{H}^{m+}) + Z^{m+} \mathbf{J}_s}{Y^m + Y^{m+}} + \tau \frac{\hat{\mathbf{n}} \times [\hat{\mathbf{n}} \times (\mathbf{E}^m - \mathbf{E}^{m+}) - \mathbf{M}_s]}{Z^m + Z^{m+}} \quad (3.53d)$$

where $\tau = 1$ is equivalent to the upwind flux, and $\tau = 0$ is the centered flux expression. Observe that (3.53) with $\tau = 0$ is not exactly (3.36) and (3.37), and some differences appear in the media interfaces, but in practice both expressions may be considered equivalent.

The penalty parameter plays the role of penalizing the jump terms ($\hat{\mathbf{n}} \times (\mathbf{E}^m - \mathbf{E}^{m+})$ and $\hat{\mathbf{n}} \times (\mathbf{H}^m - \mathbf{H}^{m+})$). These terms stabilize the solution, and eliminate spurious modes that appear with centered flux, introducing some dissipation much higher for the spurious modes than for the physical ones. A complete analysis of this topic is performed in Section 4.1.1.

3.3 Discontinuous Galerkin for Anisotropic Materials

The DGTD method can be straightforwardly extended to anisotropic materials, assuming that proper flux conditions are found. The first approach reported in the literature to deal with anisotropic materials in DGTD employed the centered flux [104], in spite of supporting spurious solutions. Recently, in [102], an upwind flux for 2D systems was derived. In this section, a generalized upwind-flux expression is found in 3D by using the general framework described in the previous section [P10]. The scheme reported in [102] could be seen as a special case of this.

Let us consider Maxwell time-domain curl equations (lossless for simplicity) for anisotropic media,

$$\bar{\mu} \frac{\partial \mathbf{H}}{\partial t} + \nabla \times \mathbf{E} = 0 \quad (3.54a)$$

$$\bar{\varepsilon} \frac{\partial \mathbf{E}}{\partial t} - \nabla \times \mathbf{H} = 0 \quad (3.54b)$$

with electric permittivity and magnetic permeability tensors symmetric positive $\bar{\varepsilon}$ and $\bar{\mu}$, respectively.

3.3.1 Flux Evaluation

We can express $\bar{\varepsilon}$ and $\bar{\mu}$, and their inverse, in the local base of vectors described in Figure 3.1 as

$$\bar{\varepsilon} = \begin{pmatrix} \epsilon_{11} & \epsilon_{12} & \epsilon_{1n} \\ \epsilon_{21} & \epsilon_{22} & \epsilon_{2n} \\ \epsilon_{n1} & \epsilon_{n2} & \epsilon_{nn} \end{pmatrix} \quad \bar{\varepsilon}^{-1} = \begin{pmatrix} \epsilon'_{11} & \epsilon'_{12} & \epsilon'_{1n} \\ \epsilon'_{21} & \epsilon'_{22} & \epsilon'_{2n} \\ \epsilon'_{n1} & \epsilon'_{n2} & \epsilon'_{nn} \end{pmatrix} \quad (3.55a)$$

$$\bar{\mu} = \begin{pmatrix} \mu_{11} & \mu_{12} & \mu_{1n} \\ \mu_{21} & \mu_{22} & \mu_{2n} \\ \mu_{n1} & \mu_{n2} & \mu_{nn} \end{pmatrix} \quad \bar{\mu}^{-1} = \begin{pmatrix} \mu'_{11} & \mu'_{12} & \mu'_{1n} \\ \mu'_{21} & \mu'_{22} & \mu'_{2n} \\ \mu'_{n1} & \mu'_{n2} & \mu'_{nn} \end{pmatrix} \quad (3.55b)$$

Following the same approach as in the case of isotropic materials, an operation-splitting method for (3.54) is applied by first splitting the equation system into two subproblems:

$$\text{Problem A:} \quad \frac{\partial \mathbf{H}}{\partial t} + \bar{\mu}^{-1} \frac{\partial}{\partial n} \hat{\mathbf{n}} \times \mathbf{E} = 0 \quad (3.56a)$$

$$\frac{\partial \mathbf{E}}{\partial t} - \bar{\varepsilon}^{-1} \frac{\partial}{\partial n} \hat{\mathbf{n}} \times \mathbf{H} = 0 \quad (3.56b)$$

$$\text{Problem B:} \quad \frac{\partial \mathbf{H}}{\partial t} + \bar{\mu}^{-1} \nabla_S \times \mathbf{E} = 0 \quad (3.57a)$$

$$\frac{\partial \mathbf{E}}{\partial t} - \bar{\varepsilon}^{-1} \nabla_S \times \mathbf{H} = 0 \quad (3.57b)$$

Again, with the same approach used in the isotropic case, we can derive the one-dimensional Riemann problem of (3.45), where in this case the $\bar{\mathbb{A}}_n$ matrix takes the following form,

$$\bar{\mathbb{A}}_n = \begin{pmatrix} 0 & 0 & \mu'_{12} & -\mu'_{11} \\ 0 & 0 & \mu'_{22} & -\mu'_{21} \\ -\epsilon'_{12} & \epsilon'_{11} & 0 & 0 \\ -\epsilon'_{22} & \epsilon'_{21} & 0 & 0 \end{pmatrix} \quad (3.58)$$

and the expression for the four PDE are

$$\partial_t H_{t_1} + \mu'_{12} \partial_n E_{t_1} - \mu'_{11} \partial_n E_{t_2} = 0 \quad (3.59a)$$

$$\partial_t H_{t_2} + \mu'_{22} \partial_n E_{t_1} - \mu'_{21} \partial_n E_{t_2} = 0 \quad (3.59b)$$

$$\partial_t E_{t_1} - \epsilon'_{12} \partial_n H_{t_1} + \epsilon'_{11} \partial_n H_{t_2} = 0 \quad (3.59c)$$

$$\partial_t E_{t_2} - \epsilon'_{22} \partial_n H_{t_1} + \epsilon'_{21} \partial_n H_{t_2} = 0 \quad (3.59d)$$

Let us define some 2×2 matrices to clarify the expressions:

$$\bar{\bar{\epsilon}}_2^{-1} = \begin{pmatrix} \epsilon'_{11} & \epsilon'_{12} \\ \epsilon'_{21} & \epsilon'_{22} \end{pmatrix}, \quad \bar{\bar{\mu}}_2^{-1} = \begin{pmatrix} \mu'_{11} & \mu'_{12} \\ \mu'_{21} & \mu'_{22} \end{pmatrix} \quad (3.60a)$$

$$\mathbb{D}_2 = \begin{pmatrix} 0 & -1 \\ 1 & 0 \end{pmatrix}, \quad \mathbb{D}_2^{-1} = \mathbb{D}_2^T = -\mathbb{D}_2 = \begin{pmatrix} 0 & 1 \\ -1 & 0 \end{pmatrix} \quad (3.60b)$$

$\bar{\bar{\mathbb{A}}}_n$ can be cast in a compact manner as

$$\bar{\bar{\mathbb{A}}}_n = \begin{pmatrix} \mathbb{O}_2 & \bar{\bar{\mu}}_2^{-1} \mathbb{D}_2 \\ \bar{\bar{\epsilon}}_2^{-1} \mathbb{D}_2^{-1} & \mathbb{O}_2 \end{pmatrix} \quad (3.61)$$

where \mathbb{O}_2 is a 2×2 matrix with all elements zero.

To solve the Riemann problem, we first diagonalize $\bar{\bar{\mathbb{A}}}_n$, and find the 4 real eigenvalues (λ_p) and the corresponding set of 4 linearly independent right eigenvectors (r_p),

$$\bar{\bar{\mathbb{A}}}_n = \mathbb{R}_{\bar{\bar{\mathbb{A}}}_n} \Lambda_{\bar{\bar{\mathbb{A}}}_n} \mathbb{R}_{\bar{\bar{\mathbb{A}}}_n}^{-1} \quad (3.62)$$

where each column of $\mathbb{R}_{\bar{\bar{\mathbb{A}}}_n}$ corresponds to one right eigenvector, and each element of the diagonal of the matrix $\Lambda_{\bar{\bar{\mathbb{A}}}_n}$ is the associated eigenvalue.

The eigenvalues of $\bar{\bar{\mathbb{A}}}_n$ are the solutions λ of

$$\det(\bar{\bar{\mathbb{A}}}_n - \lambda \mathbb{I}_4) = 0 \quad (3.63)$$

with \det being the determinant, and \mathbb{I}_n representing $n \times n$ identity matrices.

Operating with the block matrices defined above we find

$$\det(\bar{\bar{\mathbb{A}}}_n - \lambda \mathbb{I}_4) = -\det(\bar{\bar{\epsilon}}_2^{-1} \mathbb{D}_2^{-1} \bar{\bar{\mu}}_2^{-1} \mathbb{D}_2 - \lambda^2 \mathbb{I}_2) = -\det(\mathbb{M}_2 - \lambda^2 \mathbb{I}_2) = 0 \quad (3.64)$$

where we have defined a new matrix \mathbb{M}_2 , for which the eigenvalues (c_1^2 and c_2^2) are the square of the eigenvalues of $\bar{\mathbb{A}}_n$ matrix ($-c_1, -c_2, c_1$ and c_2). If we define

$$\mathbb{C}_2 = \begin{pmatrix} c_1 & 0 \\ 0 & c_2 \end{pmatrix}, \quad \mathbb{M}_2 = \bar{\varepsilon}_2^{-1} \mathbb{D}_2^{-1} \bar{\mu}_2^{-1} \mathbb{D}_2 \quad (3.65)$$

\mathbb{M}_2 can be expressed as

$$\mathbb{M}_2 = \mathbb{R}_{\mathbb{M}_2} \mathbb{C}_2 \mathbb{C}_2 \mathbb{R}_{\mathbb{M}_2}^{-1} \quad (3.66)$$

Now, we are ready to diagonalize $\bar{\mathbb{A}}_n$, as stated in (3.62), and to identify the 4 eigenvectors in the diagonalizing matrix from the expression,

$$\bar{\mathbb{A}}_n = \begin{pmatrix} \mathbb{O}_2 & \bar{\mu}_2^{-1} \mathbb{D}_2 \\ \bar{\varepsilon}_2^{-1} \mathbb{D}_2^{-1} & \mathbb{O}_2 \end{pmatrix} = \begin{pmatrix} -\mathbb{Y}_2 \mathbb{D}_2 \mathbb{R}_{\mathbb{M}_2} & \mathbb{Y}_2 \mathbb{D}_2 \mathbb{R}_{\mathbb{M}_2} \\ \mathbb{R}_{\mathbb{M}_2} & \mathbb{R}_{\mathbb{M}_2} \end{pmatrix} \begin{pmatrix} -\mathbb{C}_2 & \mathbb{O}_2 \\ \mathbb{O}_2 & \mathbb{C}_2 \end{pmatrix} \frac{1}{2} \begin{pmatrix} -\mathbb{R}_{\mathbb{M}_2}^{-1} \mathbb{Z}_2 \mathbb{D}_2^{-1} & \mathbb{R}_{\mathbb{M}_2}^{-1} \\ \mathbb{R}_{\mathbb{M}_2}^{-1} \mathbb{Z}_2 \mathbb{D}_2^{-1} & \mathbb{R}_{\mathbb{M}_2}^{-1} \end{pmatrix} \quad (3.67)$$

Operating with expression (3.67), we can easily find the expressions for two matrices, referred to here as "impedance" (\mathbb{Z}_2) and "admittance" (\mathbb{Y}_2), which play a role equivalent to the scalar impedance (Z) and admittance (Y) magnitudes defined for the isotropic case.

$$\mathbb{Y}_2 = \bar{\mu}_2^{-1} \mathbb{D}_2 \mathbb{R}_{\mathbb{M}_2} \mathbb{C}_2^{-1} \mathbb{R}_{\mathbb{M}_2}^{-1} \mathbb{D}_2^{-1} \quad (3.68a)$$

$$\mathbb{Z}_2 = \mathbb{R}_{\mathbb{M}_2} \mathbb{C}_2^{-1} \mathbb{R}_{\mathbb{M}_2}^{-1} \bar{\varepsilon}_2^{-1} \quad (3.68b)$$

Note that the condition of (3.67) is fulfilled, and also the following, $\mathbb{Z}_2 \mathbb{D}_2^{-1} \mathbb{Y}_2 \mathbb{D}_2 = \mathbb{I}_2$.

We can identify a matrix $\bar{\mathbb{A}}_n^m$ in \mathcal{T}_m and, in general, a different matrix $\bar{\mathbb{A}}_n^{m+}$ in \mathcal{T}_{m+} . The solution of the Riemann problem, after requiring the fulfillment of the Rankine-Hugoniot jump condition on both sides of $\partial \mathcal{T}_m$, yields the intermediate states (\bar{q}^* and \bar{q}^{*+}), whose domain is shown in Figure 3.3.

Expressing the jumps between the intermediate states and the values at both sides of $\partial \mathcal{T}_m$ as, a linear combination of the eigenvectors associated with the negative eigenvalues for the element \mathcal{T}_m and the eigenvectors associated to the positive eigenvalues for the element \mathcal{T}_{m+} , we find

$$\bar{q}^{m+} - \bar{q}^m = \begin{pmatrix} -\mathbb{Y}_2^m \mathbb{D}_2 \mathbb{R}_{\mathbb{M}_2^m} & \mathbb{Y}_2^{m+} \mathbb{D}_2 \mathbb{R}_{\mathbb{M}_2^{m+}} \\ \mathbb{R}_{\mathbb{M}_2^m} & \mathbb{R}_{\mathbb{M}_2^{m+}} \end{pmatrix} \begin{pmatrix} \alpha_1^m \\ \alpha_2^m \\ \alpha_3^{m+} \\ \alpha_4^{m+} \end{pmatrix} \quad (3.69)$$

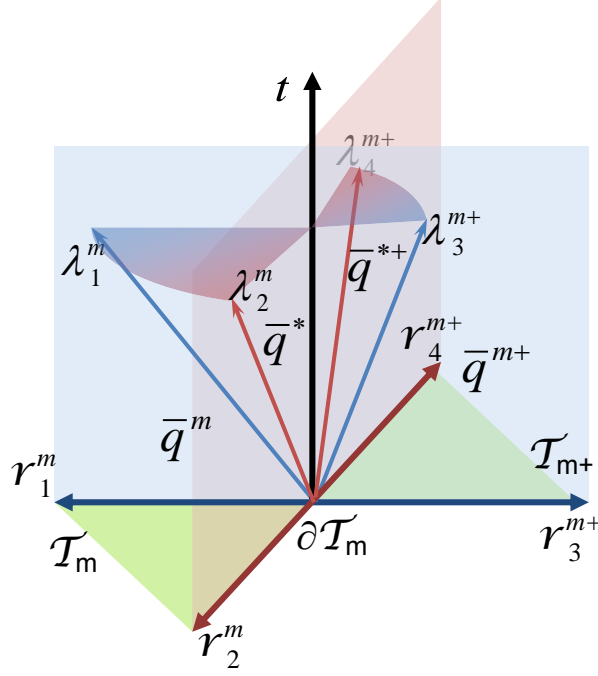


FIGURE 3.3: The structure of the solution to the Riemann problem for anisotropic materials (variable-coefficient), in a 3D representation of the space(2D)-time(1D) independent variables. $\partial\mathcal{T}_m$ shows the interface between the two different elements. The waves propagate at its speed in each material. Between these waves, there are two states $(\bar{q}^*, \bar{q}^{*+})$, which are linear combinations of the right eigenvectors, r_p and r_p^+ respectively.

which can be solved for the scalar coefficients, considering there are no surface currents, finding

$$\begin{pmatrix} \alpha_1^m \\ \alpha_2^m \\ \alpha_3^{m+} \\ \alpha_4^{m+} \end{pmatrix} = \begin{pmatrix} -\mathbb{R}_{M_2^m}^{-1} \mathbb{D}_2^{-1} (\mathbb{Y}_2^m + \mathbb{Y}_2^{m+})^{-1} & \mathbb{R}_{M_2^m}^{-1} \mathbb{D}_2^{-1} (\mathbb{Y}_2^m + \mathbb{Y}_2^{m+})^{-1} \mathbb{Y}_2^{m+} \mathbb{D}_2 \\ \mathbb{R}_{M_2^{m+}}^{-1} \mathbb{D}_2^{-1} (\mathbb{Y}_2^m + \mathbb{Y}_2^{m+})^{-1} & \mathbb{R}_{M_2^{m+}}^{-1} \mathbb{D}_2^{-1} (\mathbb{Y}_2^m + \mathbb{Y}_2^{m+})^{-1} \mathbb{Y}_2^m \mathbb{D}_2 \end{pmatrix} \begin{pmatrix} H_{t_1}^{m+} - H_{t_1}^m \\ H_{t_2}^{m+} - H_{t_2}^m \\ E_{t_1}^{m+} - E_{t_1}^m \\ E_{t_2}^{m+} - E_{t_2}^m \end{pmatrix} \quad (3.70)$$

Finally, substituting the scalar coefficients α into Equations (3.48), the solutions for the tangential components of the electric and magnetic fields are

$$\begin{pmatrix} H_{t_1}^* \\ H_{t_2}^* \end{pmatrix} = \mathbb{D}_2 (\mathbb{Z}_2^m + \mathbb{Z}_2^{m+})^{-1} \left[\mathbb{Z}_2^m \mathbb{D}_2^{-1} \begin{pmatrix} H_{t_1}^m \\ H_{t_2}^m \end{pmatrix} + \mathbb{Z}_2^{m+} \mathbb{D}_2^{-1} \begin{pmatrix} H_{t_1}^{m+} \\ H_{t_2}^{m+} \end{pmatrix} - \begin{pmatrix} E_{t_1}^{m+} - E_{t_1}^m \\ E_{t_2}^{m+} - E_{t_2}^m \end{pmatrix} \right] \quad (3.71a)$$

$$\begin{pmatrix} E_{t_1}^* \\ E_{t_2}^* \end{pmatrix} = \mathbb{D}_2^{-1} (\mathbb{Y}_2^m + \mathbb{Y}_2^{m+})^{-1} \left[\mathbb{Y}_2^m \mathbb{D}_2 \begin{pmatrix} E_{t_1}^m \\ E_{t_2}^m \end{pmatrix} + \mathbb{Y}_2^{m+} \mathbb{D}_2 \begin{pmatrix} E_{t_1}^{m+} \\ E_{t_2}^{m+} \end{pmatrix} - \begin{pmatrix} H_{t_1}^{m+} - H_{t_1}^m \\ H_{t_2}^{m+} - H_{t_2}^m \end{pmatrix} \right] \quad (3.71b)$$

or in electric and magnetic field format,

$$\hat{\mathbf{n}} \times \mathbf{E}^* = \left(\bar{\bar{Y}}^m + \bar{\bar{Y}}^{m+} \right)^{-1} \left[\bar{\bar{Y}}^m \hat{\mathbf{n}} \times \mathbf{E}^m + \bar{\bar{Y}}^{m+} \hat{\mathbf{n}} \times \mathbf{E}^{m+} + \hat{\mathbf{n}} \times \hat{\mathbf{n}} \times (\mathbf{H}^{m+} - \mathbf{H}^m) \right] \quad (3.72a)$$

$$\hat{\mathbf{n}} \times \mathbf{H}^* = \left(\bar{\bar{Z}}^m + \bar{\bar{Z}}^{m+} \right)^{-1} \left[\bar{\bar{Z}}^m \hat{\mathbf{n}} \times \mathbf{H}^m + \bar{\bar{Z}}^{m+} \hat{\mathbf{n}} \times \mathbf{H}^{m+} - \hat{\mathbf{n}} \times \hat{\mathbf{n}} \times (\mathbf{E}^{m+} - \mathbf{E}^m) \right] \quad (3.72b)$$

The new tensors are built from matrices defined by subindex 2 but completed to dimension 3 as follows,

$$\bar{\bar{A}} = \begin{pmatrix} & & 0 \\ \mathbb{A}_2 & & 0 \\ 0 & 0 & 1 \end{pmatrix}, \quad \text{with } \bar{\bar{A}} = \{ \bar{\bar{Z}}, \bar{\bar{Y}} \} \quad (3.73)$$

3.3.2 Semi-Discrete Scheme Formulation

Following the DG procedure, described in Section 3.1.1, with (3.54), we can find the general semi-discrete algorithm at element m for anisotropic materials. Sources and medium losses, which could be also anisotropic, have been omitted for simplicity,

$$\mathbb{M}_{\bar{\bar{\mu}}} d_t H^m - \mathbb{F}_{\nu h} H^m + \mathbb{F}_{\nu h}^+ H^{m+} = -(\mathbb{S} - \mathbb{F}_{\kappa e}) E^m - \mathbb{F}_{\kappa e}^+ E^{m+} \quad (3.74a)$$

$$\mathbb{M}_{\bar{\bar{\varepsilon}}} d_t E^m - \mathbb{F}_{\nu e} E^m + \mathbb{F}_{\nu e}^+ E^{m+} = (\mathbb{S} - \mathbb{F}_{\kappa h}) H^m + \mathbb{F}_{\kappa h}^+ H^{m+} \quad (3.74b)$$

where:

- H^m, H^{m+}, E^m and E^{m+} are column vectors with the dof varying in time defined in (3.14).
- $\mathbb{M}_{\bar{\bar{\mu}}}$ and $\mathbb{M}_{\bar{\bar{\varepsilon}}}$ are the mass matrices,

$$\left[\mathbb{M}_{\bar{\bar{\mu}}} \right]_{q'q} = \langle \phi_{q'}^m, \bar{\bar{\mu}} \phi_q^m \rangle_{\mathcal{T}_m} \quad (3.75a)$$

$$\left[\mathbb{M}_{\bar{\bar{\varepsilon}}} \right]_{q'q} = \langle \phi_{q'}^m, \bar{\bar{\varepsilon}} \phi_q^m \rangle_{\mathcal{T}_m} \quad (3.75b)$$

- \mathbb{S} is the stiffness matrix, which does not change from the homogeneous case (3.17).

- \mathbb{F} are the flux matrices,

$$[\mathbb{F}_{\kappa h}]_{q'q} = \left\langle \phi_{q'}^m, \bar{\bar{R}} \left(\bar{\bar{Z}}^m + \bar{\bar{Z}}^{m+} \right)^{-1} \bar{\bar{Z}}^{m+} \bar{\bar{R}}^{-1} \left(\hat{\mathbf{n}}^m \times \phi_q^m \right) \right\rangle_{\partial\mathcal{T}_m} \quad (3.76a)$$

$$[\mathbb{F}_{\kappa e}]_{q'q} = \left\langle \phi_{q'}^m, \bar{\bar{R}} \left(\bar{\bar{Y}}^m + \bar{\bar{Y}}^{m+} \right)^{-1} \bar{\bar{Y}}^{m+} \bar{\bar{R}}^{-1} \left(\hat{\mathbf{n}}^m \times \phi_q^m \right) \right\rangle_{\partial\mathcal{T}_m} \quad (3.76b)$$

$$[\mathbb{F}_{\nu h}]_{q'q} = \left\langle \phi_{q'}^m, \bar{\bar{R}} \left(\bar{\bar{Y}}^m + \bar{\bar{Y}}^{m+} \right)^{-1} \bar{\bar{R}}^{-1} \left(\hat{\mathbf{n}}^m \times \hat{\mathbf{n}}^m \times \phi_q^m \right) \right\rangle_{\partial\mathcal{T}_m} \quad (3.76c)$$

$$[\mathbb{F}_{\nu e}]_{q'q} = \left\langle \phi_{q'}^m, \bar{\bar{R}} \left(\bar{\bar{Z}}^m + \bar{\bar{Z}}^{m+} \right)^{-1} \bar{\bar{R}}^{-1} \left(\hat{\mathbf{n}}^m \times \hat{\mathbf{n}}^m \times \phi_q^m \right) \right\rangle_{\partial\mathcal{T}_m} \quad (3.76d)$$

$$[\mathbb{F}_{\kappa h}^+]_{q'q} = \left\langle \phi_{q'}^m, \bar{\bar{R}} \left(\bar{\bar{Z}}^m + \bar{\bar{Z}}^{m+} \right)^{-1} \bar{\bar{Z}}^{m+} \bar{\bar{R}}^{-1} \left(\hat{\mathbf{n}}^m \times \phi_q^{m+} \right) \right\rangle_{\partial\mathcal{T}_m} \quad (3.76e)$$

$$[\mathbb{F}_{\kappa e}^+]_{q'q} = \left\langle \phi_{q'}^m, \bar{\bar{R}} \left(\bar{\bar{Y}}^m + \bar{\bar{Y}}^{m+} \right)^{-1} \bar{\bar{Y}}^{m+} \bar{\bar{R}}^{-1} \left(\hat{\mathbf{n}}^m \times \phi_q^{m+} \right) \right\rangle_{\partial\mathcal{T}_m} \quad (3.76f)$$

$$[\mathbb{F}_{\nu h}^+]_{q'q} = \left\langle \phi_{q'}^m, \bar{\bar{R}} \left(\bar{\bar{Y}}^m + \bar{\bar{Y}}^{m+} \right)^{-1} \bar{\bar{R}}^{-1} \left(\hat{\mathbf{n}}^m \times \hat{\mathbf{n}}^m \times \phi_q^{m+} \right) \right\rangle_{\partial\mathcal{T}_m} \quad (3.76g)$$

$$[\mathbb{F}_{\nu e}^+]_{q'q} = \left\langle \phi_{q'}^m, \bar{\bar{R}} \left(\bar{\bar{Z}}^m + \bar{\bar{Z}}^{m+} \right)^{-1} \bar{\bar{R}}^{-1} \left(\hat{\mathbf{n}}^m \times \hat{\mathbf{n}}^m \times \phi_q^{m+} \right) \right\rangle_{\partial\mathcal{T}_m} \quad (3.76h)$$

$\bar{\bar{R}}$ and $\bar{\bar{R}}^{-1}$ are the transformation matrices from the local vectorial base to cartesian vectorial base defined in (3.32).

This semi-discrete scheme corresponds to the upwind-flux-evaluation case. In case of partially penalized flux, the factor τ should be included in the terms $\mathbb{F}_{\nu h}$, $\mathbb{F}_{\nu h}^+$, $\mathbb{F}_{\nu e}$ and $\mathbb{F}_{\nu e}^+$. For the centered-flux scheme, the simpler expression (3.18) for the flux matrices can be used, keeping (3.75) for the mass matrices.

3.4 Absorbing Boundary Conditions

Many problems appearing in CEM are posed in unbounded domains. To compute a numerical solution to such problems, it is necessary to truncate the space, by introducing artificial boundaries and/or regions that define a finite domain. These boundaries, known as absorbing boundary conditions, should simulate the extension of the domain to infinity. ABC should ideally be non-reflecting, and computationally efficient in terms of memory and computational time.

Many ABC types have been reported during the last three decades, most of them in the FDTD world. Formerly based on Taylor series approximation of some analytical conditions. Their computational cost increase with the order of the series and the desired accuracy [148, 149, 150, 151]. A major advance on this topic, employing a totally different approach, appeared in 1994 with the paper of J. P. Bérenger [152], describing

a new technique called perfectly matched layer conditions. The idea was to add a non-physical region to the computational domain, able to attenuate waves impinging upon it with no reflection.

In this dissertation, two ABC types are employed: the first-order Silver-Müller ABC, described in Section 3.1.2, and the conformal uniaxial perfectly matched layer, evolved from Bérenger seminal work, described in this section [P7]. It is important to note that both ABC (SM-ABC and C-UPML) can be used together [92, 93, 145, 146] to improve the overall performance in practical problems.

3.4.1 Conformal Uniaxial Perfectly Matched Layer Formulation

PML consists on an artificial absorbing region designed so that waves incident upon this region do not reflect back to the main domain, and are strongly absorbed inside it, along a predefined direction.

Since Bérenger work many different implementations and types of PML have been reported. Two of them are prevalent. The original one, known as non-Maxwellian PML or split-field PML, is derived by splitting the curl operator into the different cartesian components, and creating new nonphysical electric and magnetic pseudo-fields in the PML region. The right combination of these recovers the original Maxwell equations. Once these new components have been introduced, different electric and magnetic conductivities can be applied to attenuate the energy inside the PML while keeping impedance continuity with the Maxwellian medium. The second kind of formulation, also called Maxwellian PML or uniaxial PML, was proposed in [88], and it is described as an artificial anisotropic absorbing material, fulfilling Maxwell equations, also attenuating the energy inside the PML without reflection.

Both formulations, split-field and UPML, were derived independently in an attempt to avoid reflection of the incident field on the PML. However, both formulations were shown to be equivalent, using the general approach of stretched spatial coordinates [89, 90, 91], though the information inside the degrees of freedom differs in each case. In this section we review the formulation of the UPML, implemented in the DGTD context of this work.

Let us consider the setup of Figure 3.4 used for the conformal UPML problem. There, the interface of the PML region with the non-PML medium is the surface S , and S' is a surface conformal to S containing the PML internal point P' , where we intend to formulate the UPML. Considering the projected point P of P' on S , we can define local coordinates ξ_1, ξ_2 and ξ_3 , so that both surfaces S and S' can be expressed as functions

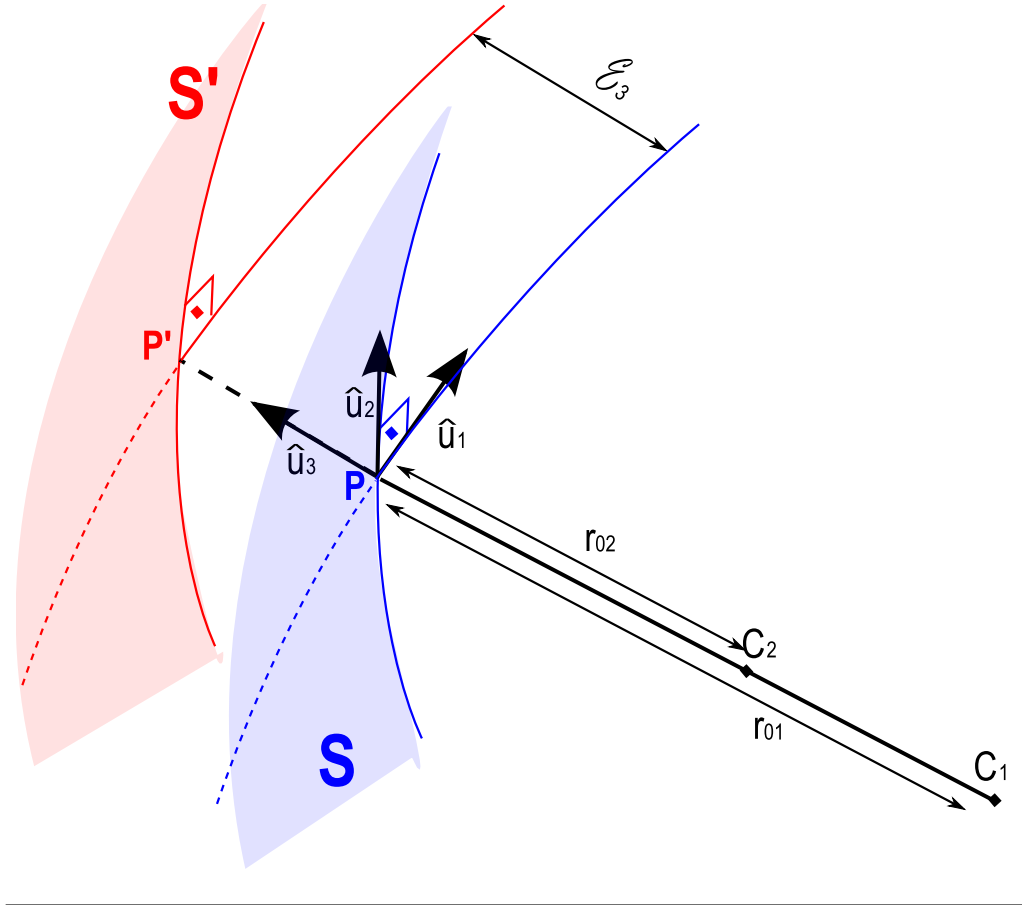


FIGURE 3.4: Conformal UPML setup.

of these local coordinates,

$$S \equiv f(\xi_1, \xi_2), \quad \xi_3 = 0 \quad (3.77a)$$

$$S' \equiv f(\xi_1, \xi_2) + \xi_3 \quad (3.77b)$$

The isoparametric locus of points of constant ξ_3 correspond to parallel surfaces at a distance of ξ_3 to S .

An orthonormal local vector-basis can be defined as

$$\hat{\mathbf{u}}_1 = u_1(\xi_1, \xi_2) = \frac{\partial \mathbf{r}}{\partial \xi_1} \left| \frac{\partial \mathbf{r}}{\partial \xi_1} \right|^{-1} \quad (3.78a)$$

$$\hat{\mathbf{u}}_2 = u_2(\xi_1, \xi_2) = \frac{\partial \mathbf{r}}{\partial \xi_2} \left| \frac{\partial \mathbf{r}}{\partial \xi_2} \right|^{-1} \quad (3.78b)$$

$$\hat{\mathbf{u}}_3 = \hat{\mathbf{u}}_1 \times \hat{\mathbf{u}}_2 \quad (3.78c)$$

related to the cartesian basis through the basis-change matrix $\bar{\bar{R}}$, and the principal radii of curvature of the doubly curved surface S and S' ,

$$r_{01} = r_{01}(\xi_1, \xi_2), \quad r_{02} = r_{02}(\xi_1, \xi_2) \quad (3.79a)$$

$$r_1 = r_{01} + \xi_3, \quad r_2 = r_{02} + \xi_3 \quad (3.79b)$$

which are functions of the local coordinates.

The UPML consists of a change on the metric of the space to the complex space in the vectorial base $(\hat{\mathbf{u}}_1, \hat{\mathbf{u}}_2, \hat{\mathbf{u}}_3)$ of the local coordinate ξ_3 ($\hat{\mathbf{u}}_3$ being the predefined direction in which the outgoing waves are attenuated). In the imaginary part of the new complex space, a conductivity (σ) is introduced to absorb outgoing waves in the $\hat{\mathbf{u}}_3$ direction but maintaining adaptation, that is, perfectly matched impedance compared to the non-PML medium. Hence, the spatial coordinates inside the PML are mapped to the complex variable domain through

$$\xi_3 \longrightarrow \tilde{\xi}_3 = \int_0^{\xi_3} s(\tau) d\tau \quad (3.80)$$

where $s(\tau)$ is the complex stretching variable. To reduce numerical reflection, we can use different profiles for σ inside the PML [93, 153]. In this work, we have used the following expression for $s(\tau)$,

$$s(\tau) = 1 + \frac{1}{j\omega} \sigma_{max} \left(\frac{\tau}{\Delta\xi_3} \right)^2 \quad (3.81)$$

where $\Delta\xi_3$ is the PML thickness, and σ_{max} is the maximum conductivity inside the PML. These two parameters characterize the PML layer and determine the rate of decay of the energy of the transmitter wave into the PML. Note that we have chosen a parabolic dependence of the stretching variable; this means that the conductivity (σ) inside the PML medium will grow with a second-order profile. This growing rate can be tuned to minimize the reflection of the PML [152], but the optimum value is usually problem dependent (the parabolic profile is a typical choice).

The analytical reflection coefficient depends on the incident angle (θ), and can be evaluated with the expression [88]

$$R_0(\theta) = e^{-\frac{2}{3} \frac{\sigma_{max} \Delta\xi_3}{c} \cos(\theta)} \quad (3.82)$$

where $c = \frac{1}{\sqrt{\mu\epsilon}}$ is the speed at which the wave travels along the direction of $\hat{\mathbf{u}}_3$.

The resulting expression of the spatial coordinate is given by

$$\tilde{\xi}_3 = \xi_3 + \frac{1}{j\omega} \sigma_{max} \frac{\xi_3}{3} \left(\frac{\xi_3}{\Delta\xi_3} \right)^2 \quad (3.83)$$

and the stretching curvature radii by

$$\tilde{r}_1 = r_{01} + \tilde{\xi}_3 = r_1 + \frac{1}{j\omega} \sigma_{max} \frac{\xi_3}{3} \left(\frac{\xi_3}{\Delta\xi_3} \right)^2 \quad (3.84a)$$

$$\tilde{r}_2 = r_{02} + \tilde{\xi}_3 = r_2 + \frac{1}{j\omega} \sigma_{max} \frac{\xi_3}{3} \left(\frac{\xi_3}{\Delta\xi_3} \right)^2 \quad (3.84b)$$

The following expressions define the metric coefficients,

$$\begin{aligned} h_1 &= \frac{r_1}{r_{01}}, & \tilde{h}_1 &= \frac{\tilde{r}_1}{r_{01}} \\ h_2 &= \frac{r_2}{r_{02}}, & \tilde{h}_2 &= \frac{\tilde{r}_2}{r_{02}} \\ h_3 &= 1, & \tilde{h}_3 &= s \end{aligned} \quad (3.85)$$

The change of the space metric of (3.80) and (3.81) can be easily implemented as an artificial anisotropic material [89, 90, 91], for which general metric tensor, in local coordinates, can be expressed in terms of the metric coefficients as

$$\bar{\bar{\Lambda}} = \hat{\mathbf{u}}_1 \hat{\mathbf{u}}_1 \left(s \frac{h_1 \tilde{h}_2}{\tilde{h}_1 h_2} \right) + \hat{\mathbf{u}}_2 \hat{\mathbf{u}}_2 \left(s \frac{h_2 \tilde{h}_1}{\tilde{h}_2 h_1} \right) + \hat{\mathbf{u}}_3 \hat{\mathbf{u}}_3 \left(\frac{1}{s} \frac{\tilde{h}_1 \tilde{h}_2}{h_1 h_2} \right) = \begin{pmatrix} s \frac{h_1 \tilde{h}_2}{\tilde{h}_1 h_2} & 0 & 0 \\ 0 & s \frac{h_2 \tilde{h}_1}{\tilde{h}_2 h_1} & 0 \\ 0 & 0 & \frac{1}{s} \frac{\tilde{h}_1 \tilde{h}_2}{h_1 h_2} \end{pmatrix} \quad (3.86)$$

Inserting (3.79), (3.84) and (3.85) in (3.86), we can define three different conductivities, corresponding to each space direction, depending on the curvature radius and the distance to the S surface,

$$\sigma_3(\xi_3) = \sigma_{max} \left(\frac{\xi_3}{\Delta\xi_3} \right)^2 \quad (3.87a)$$

$$\sigma_1(\xi_3) = \sigma_3 \frac{\xi_3}{3r_1} \quad (3.87b)$$

$$\sigma_2(\xi_3) = \sigma_3 \frac{\xi_3}{3r_2} \quad (3.87c)$$

Finally the expression of the metric tensor is

$$\bar{\bar{\Lambda}} = \begin{pmatrix} \frac{\left(1 + \frac{\sigma_3}{j\omega}\right)\left(1 + \frac{\sigma_2}{j\omega}\right)}{\left(1 + \frac{\sigma_1}{j\omega}\right)} & 0 & 0 \\ 0 & \frac{\left(1 + \frac{\sigma_3}{j\omega}\right)\left(1 + \frac{\sigma_1}{j\omega}\right)}{\left(1 + \frac{\sigma_2}{j\omega}\right)} & 0 \\ 0 & 0 & \frac{\left(1 + \frac{\sigma_1}{j\omega}\right)\left(1 + \frac{\sigma_2}{j\omega}\right)}{\left(1 + \frac{\sigma_3}{j\omega}\right)} \end{pmatrix} \quad (3.88)$$

The UPML can be expressed in the frequency domain in a Maxwellian form, and in the local basis as

$$\nabla \times \mathbf{E} = -j\omega\mu\bar{\bar{\Lambda}}\mathbf{H} \quad (3.89a)$$

$$\nabla \times \mathbf{H} = j\omega\varepsilon\bar{\bar{\Lambda}}\mathbf{E} \quad (3.89b)$$

Writing, for simplicity, only one component of (3.89a) (similar results can be found for the other components and (3.89b)) results

$$\begin{aligned} (\nabla \times \mathbf{E})|_{\hat{\mathbf{u}}_1} &= -j\omega\mu \frac{\left(1 + \frac{\sigma_3}{j\omega}\right)\left(1 + \frac{\sigma_2}{j\omega}\right)}{\left(1 + \frac{\sigma_1}{j\omega}\right)} \mathbf{H}|_{\hat{\mathbf{u}}_1} \\ &= -j\omega\mu \mathbf{H}|_{\hat{\mathbf{u}}_1} - \mu(\sigma_3 + \sigma_2 - \sigma_1) \mathbf{H}|_{\hat{\mathbf{u}}_1} - \mu \frac{(\sigma_3 - \sigma_1)(\sigma_2 - \sigma_1)}{j\omega + \sigma_1} \mathbf{H}|_{\hat{\mathbf{u}}_1} \end{aligned} \quad (3.90)$$

Equation (3.90) can be solved by introducing an auxiliary field \mathbf{M} for the last term, for which the first component is

$$\mathbf{M}|_{\hat{\mathbf{u}}_1} = \mu \frac{(\sigma_3 - \sigma_1)(\sigma_2 - \sigma_1)}{j\omega + \sigma_1} \mathbf{H}|_{\hat{\mathbf{u}}_1} \quad (3.91)$$

An auxiliary differential equation is used to express Equation (3.91) in the time domain,

$$\left. \frac{\partial \mathbf{M}}{\partial t} \right|_{\hat{\mathbf{u}}_1} = -\sigma_1 \mathbf{M}|_{\hat{\mathbf{u}}_1} + \mu(\sigma_3 - \sigma_1)(\sigma_2 - \sigma_1) \mathbf{H}|_{\hat{\mathbf{u}}_1} \quad (3.92a)$$

$$\mu \left. \frac{\partial \mathbf{H}}{\partial t} \right|_{\hat{\mathbf{u}}_1} = -(\nabla \times \mathbf{E})|_{\hat{\mathbf{u}}_1} - \mu(\sigma_3 + \sigma_2 - \sigma_1) \mathbf{H}|_{\hat{\mathbf{u}}_1} - \mathbf{M}|_{\hat{\mathbf{u}}_1} \quad (3.92b)$$

Finally, the set of equations for the PML layer for the fields magnitudes \mathbf{E} , \mathbf{H} and the auxiliary fields (polarization currents) \mathbf{M} and \mathbf{J} , can be written as

$$\frac{\partial \mathbf{M}}{\partial t} = -\bar{\bar{A}}_2 \mathbf{M} + \mu \bar{\bar{A}}_3 \mathbf{H} \quad (3.93a)$$

$$\mu \frac{\partial \mathbf{H}}{\partial t} = -\nabla \times \mathbf{E} - \mathbf{M} - \mu \bar{\bar{A}}_1 \mathbf{H} \quad (3.93b)$$

$$\frac{\partial \mathbf{J}}{\partial t} = -\bar{\bar{A}}_2 \mathbf{J} + \varepsilon \bar{\bar{A}}_3 \mathbf{E} \quad (3.93c)$$

$$\varepsilon \frac{\partial \mathbf{E}}{\partial t} = \nabla \times \mathbf{H} - \mathbf{J} - \varepsilon \bar{\bar{A}}_1 \mathbf{E} \quad (3.93d)$$

where all vector magnitudes are expressed in the cartesian basis $(\hat{\mathbf{x}}, \hat{\mathbf{y}}, \hat{\mathbf{z}})$. The tensors $\bar{\bar{A}}_1$, $\bar{\bar{A}}_2$ and $\bar{\bar{A}}_3$ take the form:

$$\bar{\bar{A}}_1 = \bar{\bar{R}} \begin{pmatrix} \sigma_3 + \sigma_2 - \sigma_1 & 0 & 0 \\ 0 & \sigma_1 + \sigma_3 - \sigma_2 & 0 \\ 0 & 0 & \sigma_2 + \sigma_1 - \sigma_3 \end{pmatrix} \bar{\bar{R}}^{-1} \quad (3.94a)$$

$$\bar{\bar{A}}_2 = \bar{\bar{R}} \begin{pmatrix} \sigma_1 & 0 & 0 \\ 0 & \sigma_2 & 0 \\ 0 & 0 & \sigma_3 \end{pmatrix} \bar{\bar{R}}^{-1} \quad (3.94b)$$

$$\bar{\bar{A}}_3 = \bar{\bar{R}} \begin{pmatrix} (\sigma_2 - \sigma_1)(\sigma_3 - \sigma_1) & 0 & 0 \\ 0 & (\sigma_3 - \sigma_2)(\sigma_1 - \sigma_2) & 0 \\ 0 & 0 & (\sigma_1 - \sigma_3)(\sigma_2 - \sigma_3) \end{pmatrix} \bar{\bar{R}}^{-1} \quad (3.94c)$$

where $\bar{\bar{R}}$ and $\bar{\bar{R}}^{-1}$ are the transformation matrices from the local vectorial base, defined in (3.78), and the cartesian basis.

$$\begin{pmatrix} \hat{\mathbf{x}} \\ \hat{\mathbf{y}} \\ \hat{\mathbf{z}} \end{pmatrix} = \bar{\bar{R}} \begin{pmatrix} \hat{\mathbf{u}}_1 \\ \hat{\mathbf{u}}_2 \\ \hat{\mathbf{u}}_3 \end{pmatrix}, \quad \begin{pmatrix} \hat{\mathbf{u}}_1 \\ \hat{\mathbf{u}}_2 \\ \hat{\mathbf{u}}_3 \end{pmatrix} = \bar{\bar{R}}^{-1} \begin{pmatrix} \hat{\mathbf{x}} \\ \hat{\mathbf{y}} \\ \hat{\mathbf{z}} \end{pmatrix} \quad (3.95)$$

To solve (3.93), we need to evaluate σ_1 , σ_2 and σ_3 at every point inside the PML region. According to (3.87), these conductivity values depend on the two principal curvature radii r_1 , r_2 of a general (doubly curved) surface and the distance to the PML border ξ_3 . Finding these variables in a general problem is not easy, and some solutions have been proposed in 2D [26, 89, 154]. In this work, solutions for canonical geometries have been implemented, so that, in a particular problem, one or a combination of different canonical geometries, can be applied to truncate the computational domain, as is depicted in Figure 3.5. In this case, the space, which encloses the structure under analysis (Figure 3.5(a)) is truncated by a closed surface (S) composed of pieces of toroids and plane

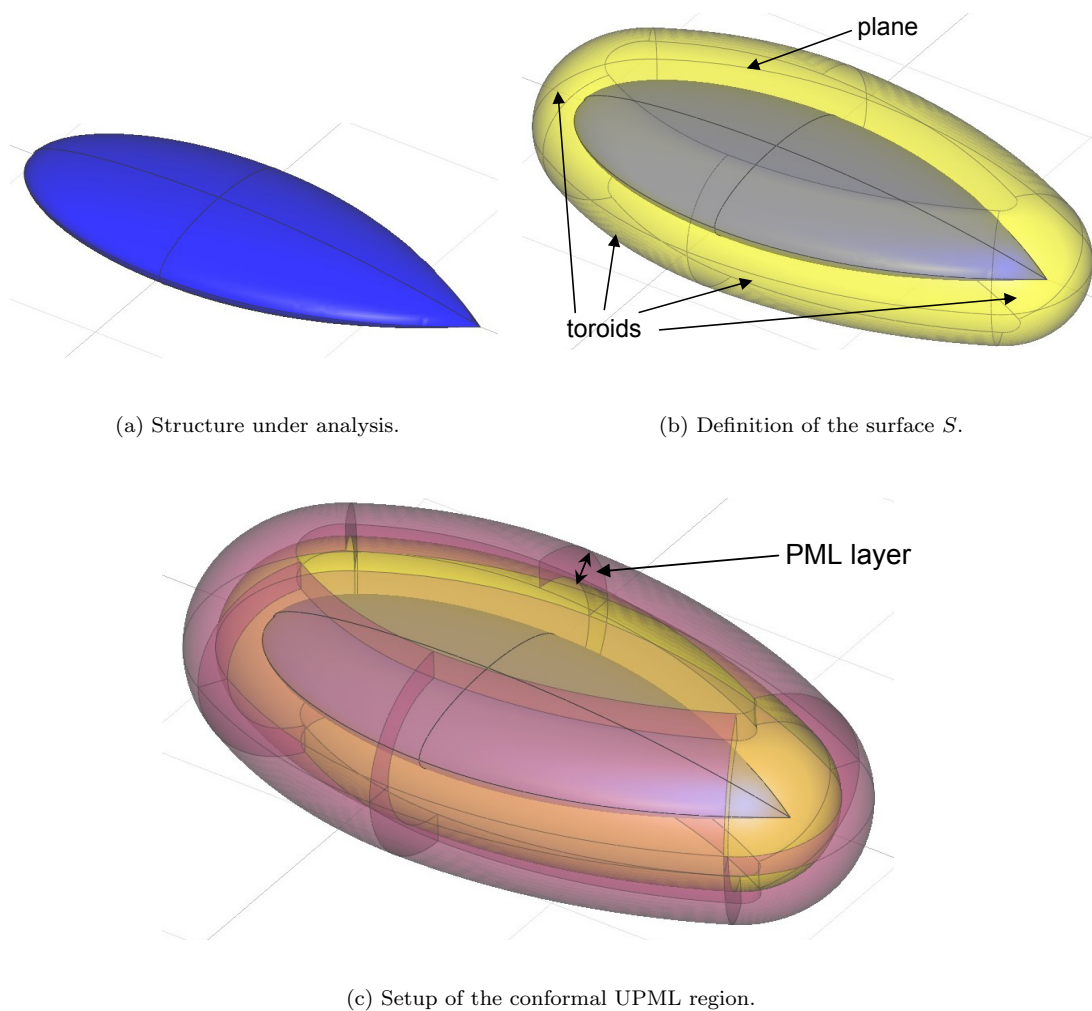


FIGURE 3.5: Definition of a conformal UPML making use of canonical geometries.

surfaces (Figure 3.5(b)). After this frontier is established, the PML region is created with the required thickness (Figure 3.5(c)).

3.4.2 Discontinuous Galerkin Semi-Discrete Scheme Formulation

The Galerkin procedure jointly with the DG spatial technique, of Section 3.1.1, can be straightforwardly applied to (3.93), since the curl terms in Equations (3.93a) and (3.93c) do not change from regular Maxwell equations. Hence, considering that the auxiliary fields are expanded with the same set of basis functions, and auxiliary differential equations are tested following the Galerkin procedure, we find the following spatial

semi-discrete scheme for the element m located in a PML region,

$$\mathbb{M}d_t M^m + \mathbb{M}_{A_2} M^m = \mu \mathbb{M}_{A_3} H^m \quad (3.96a)$$

$$\mu \mathbb{M}d_t H^m + (\mu \mathbb{M}_{A_1} - \mathbb{F}_{\nu h}) H^m + \mathbb{F}_{\nu h}^+ H^{m+} = -(\mathbb{S} - \mathbb{F}_{\kappa e}) E^m - \mathbb{F}_{\kappa e}^+ E^{m+} - \mathbb{M} M^m \quad (3.96b)$$

$$\mathbb{M}d_t J^m + \mathbb{M}_{A_2} J^m = \varepsilon \mathbb{M}_{A_3} E^m \quad (3.96c)$$

$$\varepsilon \mathbb{M}d_t E^m + (\varepsilon \mathbb{M}_{A_1} - \mathbb{F}_{\nu e}) E^m + \mathbb{F}_{\nu e}^+ E^{m+} = (\mathbb{S} - \mathbb{F}_{\kappa h}) H^m + \mathbb{F}_{\kappa h}^+ H^{m+} - \mathbb{M} J^m \quad (3.96d)$$

where:

- H^m , H^{m+} , E^m , E^{m+} , M^m and J^m are column vectors with the dof varying in time as (3.14).
- \mathbb{M} is the mass matrix defined in (3.16) and \mathbb{M}_{A_1} , \mathbb{M}_{A_2} and \mathbb{M}_{A_3} are mass matrices but affected by the tensors defined previously in (3.94),

$$[\mathbb{M}_{A_i}]_{q'q} = \left\langle \phi_{q'}^m, \bar{A}_i \phi_q^m \right\rangle_{\mathcal{T}_m} \quad \text{with } i = \{1, 2, 3\} \quad (3.97)$$

- \mathbb{S} is the stiffness matrix defined in (3.17).
- \mathbb{F} are the flux matrices defined in (3.18).

3.5 Temporal Integration

The choice of the time-integration scheme is a crucial step for the overall efficiency and viability of a numerical method. There are two major families: implicit and explicit methods. Implicit schemes, such as Crank-Nicolson [75], require a system of linear equations to be solved at each time step, which may become impractical in electrically large problems. Usually, implicit methods are unconditionally stable, and an arbitrarily large time step can be chosen, trying to properly resolve only the highest frequency under analysis, thus reducing to the minimum the number of required time steps in a complete simulation. On the other hand, explicit schemes usually are conditionally stable with a maximum time step depending on the spatial discretization, possibly resulting into a large number of time steps per simulation, with a low computational effort per time step.

It should be borne in mind here, that the main advantage of DGTD, compared to classical FEMTD, is the relaxation of the continuity conditions across elements, to yield a simpler quasi-explicit algorithm. For the sake of this simplicity, only explicit time-integration schemes will be considered in this dissertation. There are two main families of

these usually employed in DGTD: (i) the well-proven and versatile Runge-Kutta schemes [53], and (ii) the efficient leap-frog scheme, classically used in FDTD. Both are reviewed in this dissertation, but the main effort is placed on LF, and an algorithm, henceforth referred to as Leap-Frog Discontinuous Galerkin (LFDG), is described in detail in this section. Finally, a fully explicit local time-stepping strategy is presented in combination with the LFDG algorithm, designed to overcome unnecessary global constraints on the time step.

3.5.1 Runge-Kutta Scheme

Explicit RK methods are particularly popular due to their robustness, flexibility, and good performance [36, 37, 38, 39, 40]. The main advantage of RK schemes, compared to LF, is that these schemes easily allow to adjust the order of time integration m to the order p of the spatial discretization, in order to prevent the spoiling of the high-order convergence of the global scheme. These schemes typically require the calculation of the field at a number of auxiliary stages s (depending on the order), to calculate the time derivatives. Two drawbacks appear: first, the results of all stages must be kept in memory at each time step, leading to memory requirements proportional to sN (N being number of the dof), which may become prohibitive for electrically large problems. Second, the maximum allowed time step in each element becomes quite restrictive, specially for higher orders.

In order to overcome these problems, several authors [53, 59, 155] have explored the use of Low-Storage Runge-Kutta (LSRK) methods, reducing the memory required to $2N$, independently of the number of auxiliary stages. Additionally, the use of a larger number of stages $s > m$, is shown to permit a more relaxed stability condition. A disadvantage is that such methods are only known up to order $m = 4$, though for most real problems that is enough. The popular LSRK scheme derived by Carpenter and Kennedy [156], with $m = 4$ and $s = 5$, is described in some detail below (an interesting comparison of the different available RK methods applied to DGTD method in Maxwell equations can be found in [71]).

Let us consider the matrix form of the semi-discrete system within each element m without sources expressed as

$$d_t H^m = \frac{1}{\mu} \mathbb{M}^{-1} \left[-(\mathbb{S} - \mathbb{F}_{\kappa e}) E^m - \mathbb{F}_{\kappa e}^+ E^{m+} + \mathbb{F}_{\nu h} H^m - \mathbb{F}_{\nu h}^+ H^{m+} - \sigma_m \mathbb{M} H^m \right] \quad (3.98a)$$

$$d_t E^m = \frac{1}{\epsilon} \mathbb{M}^{-1} \left[(\mathbb{S} - \mathbb{F}_{\kappa h}) H^m + \mathbb{F}_{\kappa h}^+ H^{m+} + \mathbb{F}_{\nu e} E^m - \mathbb{F}_{\nu e}^+ E^{m+} - \sigma_e \mathbb{M} E^m \right] \quad (3.98b)$$

which can be written in a compact form as

$$d_t U = F[t, U(t)]. \quad (3.99)$$

with $U = [H, E]$ containing the N dof of the problem.

The classical 4th-order 5-stage explicit RK scheme permits to advance a time step Δt , from t_n to $t_n + \Delta t$, by

$$k_1 = F(t_n, U^n) \quad (3.100a)$$

$$k_i = F\left(t_n + c_i \Delta t, U^n + \Delta t \sum_{j=1}^{i-1} a_{i,j} k_j\right) \quad i = 2, 3, 4, 5 \quad (3.100b)$$

$$U_{n+1} = U^n + \Delta t \sum_{j=1}^5 b_j k_j \quad (3.100c)$$

where $U^n = U(t_n)$ and $U_{n+1} = U(t_n + \Delta t)$ and the fixed scalars $a_{i,j}$, b_j and c_i are the coefficients of the RK formula. Note that all intermediate stage quantities are used by the last advancing equation (3.100c), thus requiring the storage of $2Ns$ values.

The LSRK method is found by reworking (3.100), to express each stage as a function of the previous one as

$$dU_j^n = A_j dU_{j-1} + \Delta t F(t_n + c_j \Delta t, U_j^n) \quad (3.101a)$$

$$U_j^n = U_{j-1} + B_j dU_j^n \quad j = 1, 2, 3, 4, 5 \quad (3.101b)$$

The final algorithm is self-starting, ($A_1 = 0$), and only dU^n and U^n must be kept in memory, thus only requiring the storage of $2N$ values. Table 3.2 shows the values of A_j , B_j and c_j to get a 4th order scheme (see also [156] for other possible values).

3.5.2 Leap-Frog Scheme

The LFDG algorithm is based on the spatial DG operator described in Section 3.1.1, integrated in time by the explicit LF scheme, well-known in the FDTD world [1].

A typical limitation of the LF time-integration scheme is the conditional stability criterion, which imposes a maximum time step (Δt_{MAX}^m) element-by-element. The time step is found to be dependent on the element electrical size, and on the order of the basis functions employed in that particular element. The material of adjacent elements, boundary conditions on its faces, aspect-ratio, and curvature (in case of quadratic elements) also influence the stability condition [64]. This fact, when we are dealing with

TABLE 3.2: Coefficients for optimal 5-stage, 4th order, 2N-Storage RK scheme.

COEFFICIENT	VALUE
A_1	0.0
A_2	$-\frac{567301805773}{1357537059087}$
A_3	$-\frac{2404267990393}{2016746695238}$
A_4	$-\frac{3550918686646}{2091501179385}$
A_5	$-\frac{1275806237668}{842570457699}$
B_1	$\frac{1432997174477}{9575080441755}$
B_2	$\frac{5161836677717}{13612068292357}$
B_3	$\frac{1720146321549}{2090206949498}$
B_4	$\frac{3134564353537}{44814673103381}$
B_5	$\frac{2277821191437}{14882151754819}$
c_1	0.0
c_2	$\frac{1432997174477}{9575080441755}$
c_3	$\frac{2526269341429}{6820363962896}$
c_4	$\frac{2006345519317}{32243100637761}$
c_5	$\frac{2802321613138}{2924317926251}$

unstructured meshes, results in strong disparities in the required time steps among elements, leading to a global time step constrained by the smallest one, in order to ensure global stability. This leads to a major waste of computational time in updating elements at a rate much higher than its own maximum time step. To avoid this problem, a fully explicit LTS strategy has been developed for the LF scheme [P6]. Other alternatives are found in [64, 79, 80].

3.5.2.1 Leap-Frog Discontinuous Galerkin Algorithm

Let us consider the matrix form of the DG semi-discrete system of 3.13, within each element m without sources which can be expressed as

$$\mu \mathbb{M} d_t H^m + \sigma_m \mathbb{M} H^m - \mathbb{F}_{\nu h} H^m + \mathbb{F}_{\nu h}^+ H^{m+} = -(\mathbb{S} - \mathbb{F}_{\kappa e}) E^m - \mathbb{F}_{\kappa e}^+ E^{m+} \quad (3.102a)$$

$$\varepsilon \mathbb{M} d_t E^m + \sigma_e \mathbb{M} E^m - \mathbb{F}_{\nu e} E^m + \mathbb{F}_{\nu e}^+ E^{m+} = (\mathbb{S} - \mathbb{F}_{\kappa h}) H^m + \mathbb{F}_{\kappa h}^+ H^{m+} \quad (3.102b)$$

The idea of the LF scheme is to sample the unknown fields in a staggered way: the electric field is evaluated at $t_n = n\Delta t$, and the magnetic field at $t_{n+\frac{1}{2}} = (n + \frac{1}{2})\Delta t$. In the same way, Equation (3.102a) is evaluated (or tested in time, if we think in terms of a point matching testing procedure) at t_n , and Equation (3.102b) at $t_{n+\frac{1}{2}}$.

The first-order time derivatives are replaced by second-order centered differences,

$$(d_t H^m)_n = \frac{H_{n+\frac{1}{2}}^m - H_{n-\frac{1}{2}}^m}{\Delta t} + O(\Delta t^2); \quad (d_t E^m)_{n+\frac{1}{2}} = \frac{E_{n+1}^m - E_n^m}{\Delta t} + O(\Delta t^2) \quad (3.103)$$

For the terms with the electric and magnetic conductivity, which require the identity operation, an average approximation is used,

$$H_n^m = \frac{H_{n+\frac{1}{2}}^m + H_{n-\frac{1}{2}}^m}{2} + O(\Delta t^2); \quad E_{n+\frac{1}{2}}^m = \frac{E_{n+1}^m + E_n^m}{2} + O(\Delta t^2) \quad (3.104)$$

Notice that both approximations are of second order.

For the two extra dissipative terms arising from the upwind flux formulation, a backwards approximation ($H_n^m \simeq H_{n-\frac{1}{2}}^m$ and $E_{n+\frac{1}{2}}^m \simeq E_n^m$) must be used, since an average approximation, like (3.104), would yield a globally implicit scheme, due to the coupling terms from the adjacent elements [95]. This fact introduces a slight penalization in the stability condition.

For a purely upwind-flux evaluation, a quite smaller time step is required. The alternative is to use partially penalized fluxes [64]. When we choose an appropriate value of the τ parameter, the effect in the stability of the scheme is small (analyzed in detail in Section 4.2.2). If centered fluxes are used instead, the dissipative terms are null, and problems arise in relation to spurious modes (see Section 4.1.1).

When the temporal approximations for the dof are inserted in (3.102) the resulting fully explicit LFDG algorithm is

$$H_{n+\frac{1}{2}}^m = \alpha_m H_{n-\frac{1}{2}}^m + \beta_m \mathbb{M}^{-1} \left[-(\mathbb{S} - \mathbb{F}_{\kappa e}) E_n^m - \mathbb{F}_{\kappa e}^+ E_n^{m+} + \mathbb{F}_{\nu h} H_{n-\frac{1}{2}}^m - \mathbb{F}_{\nu h}^+ H_{n-\frac{1}{2}}^{m+} \right] \quad (3.105a)$$

$$E_{n+1}^m = \alpha_e E_n^m + \beta_e \mathbb{M}^{-1} \left[(\mathbb{S} - \mathbb{F}_{\kappa h}) H_{n+\frac{1}{2}}^m + \mathbb{F}_{\kappa h}^+ H_{n+\frac{1}{2}}^{m+} + \mathbb{F}_{\nu e} E_n^m - \mathbb{F}_{\nu e}^+ E_n^{m+} \right] \quad (3.105b)$$

with

$$\alpha_m = \frac{1 - \frac{\Delta t \sigma_m}{2\mu}}{1 + \frac{\Delta t \sigma_m}{2\mu}}, \quad \beta_m = \frac{\Delta t}{\mu \left(1 + \frac{\Delta t \sigma_m}{2\mu} \right)} \quad (3.106a)$$

$$\alpha_e = \frac{1 - \frac{\Delta t \sigma_e}{2\varepsilon}}{1 + \frac{\Delta t \sigma_e}{2\varepsilon}}, \quad \beta_e = \frac{\Delta t}{\varepsilon \left(1 + \frac{\Delta t \sigma_e}{2\varepsilon} \right)} \quad (3.106b)$$

3.5.2.2 The LFDG algorithm in PML regions

The extension of the LF temporal integration scheme to the semi-discrete system of (3.96) is straightforward. The auxiliary unknown field \mathbf{M} must be evaluated at $t_n = n\Delta t$, as the electric field, and the auxiliary unknown field \mathbf{J} , at $t_{n+\frac{1}{2}} = (n + \frac{1}{2}) \Delta t$, as the magnetic field. In the same way, Equation (3.96c) is sampled at t_n , as Equation (3.96b), and the Equation (3.96a) at $t_{n+\frac{1}{2}}$, as (3.96d).

Making the usual approximations (time derivatives replaced by central differences, identity operator by centered averages, and flux dissipative terms by backwards formula), we can formulate the following fully explicit algorithm for the PML medium,

$$M_n^m = \mathbb{A}_2 M_{n-1}^m + \mu \Delta t \mathbb{A}_3 H_{n-\frac{1}{2}}^m \quad (3.107a)$$

$$H_{n+\frac{1}{2}}^m = \mathbb{A}_{11} H_{n-\frac{1}{2}}^m + \beta_m \mathbb{A}_{12} \left[-(\mathbb{S} - \mathbb{F}_{\kappa e}) E_n^m - \mathbb{F}_{\kappa e}^+ E_n^{m+} + \mathbb{F}_{\nu h} H_{n-\frac{1}{2}}^m - \mathbb{F}_{\nu h}^+ H_{n-\frac{1}{2}}^{m+} - \mathbb{M} M_n^m \right] \quad (3.107b)$$

$$J_{n+\frac{1}{2}}^m = \mathbb{A}_2 J_{n-\frac{1}{2}}^m + \varepsilon \Delta t \mathbb{A}_3 E_n^m \quad (3.107c)$$

$$E_{n+1}^m = \mathbb{A}_{11} E_n^m + \beta_e \mathbb{A}_{12} \left[(\mathbb{S} - \mathbb{F}_{\kappa h}) H_{n+\frac{1}{2}}^m + \mathbb{F}_{\kappa h}^+ H_{n+\frac{1}{2}}^{m+} + \mathbb{F}_{\nu e} E_{n-1}^m - \mathbb{F}_{\nu e}^+ E_{n-1}^{m+} - \mathbb{M} J_{n+\frac{1}{2}}^m \right] \quad (3.107d)$$

where

$$\mathbb{A}_2 = \left(\mathbb{M} + \frac{\Delta t}{2} \mathbb{M}_{A_2} \right)^{-1} \left(\mathbb{M} - \frac{\Delta t}{2} \mathbb{M}_{A_2} \right) \quad (3.108a)$$

$$\mathbb{A}_3 = \left(\mathbb{M} + \frac{\Delta t}{2} \mathbb{M}_{A_2} \right)^{-1} \mathbb{M}_{A_3} \quad (3.108b)$$

$$\mathbb{A}_{11} = \left(\mathbb{M} + \frac{\Delta t}{2} \mathbb{M}_{A_1} \right)^{-1} \left(\mathbb{M} - \frac{\Delta t}{2} \mathbb{M}_{A_1} \right) \quad (3.108c)$$

$$\mathbb{A}_{12} = \left(\mathbb{M} + \frac{\Delta t}{2} \mathbb{M}_{A_1} \right)^{-1} \quad (3.108d)$$

3.5.2.3 Local Time-Stepping Algorithm

The fully explicit algorithm proposed in this section is directly inspired from the one introduced by Montseny et al. [64], called Recursive Leap-Frog (R-LF) method. All the mesh elements are arranged into L levels, and the different LTS levels communicate among themselves by making use of average approximations (or linear interpolations) when needed, instead of using magnitudes at unknown times by others evaluated at different time instants, as in [64]. The time step for the level l is $\Delta t_l = (2k + 1)^{l-1} \Delta t_1$, k being a positive real integer, and Δt_1 the effective time step for the first level ($l = 1$). All the elements of the l level must fulfill the condition $\Delta t_l < \Delta t_{MAX}^m$ (being Δt_{MAX}^m the maximum Δt for stability at the element m). For instance, $k = 1$ means that there is a factor 3 between the time steps of consecutive levels.

First of all, at the preprocess stage, we classify all the mesh elements into $(2L - 1)$ possible sets requiring different treatment: L different levels plus the $(L - 1)$ interfaces. Let us illustrate the procedure for simplicity for the 2D example shown in Figure 3.6, with two LTS levels ($L = 2$). The procedure can be easily generalized to any problem

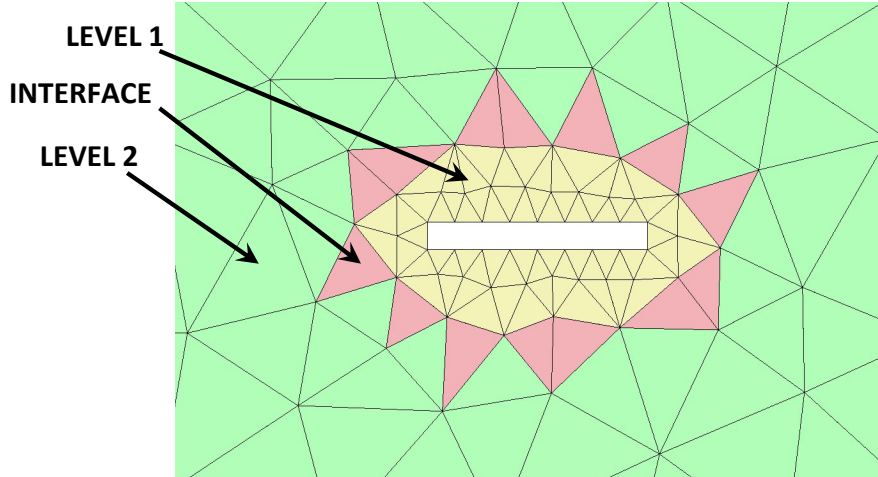


FIGURE 3.6: 2D classification example of two LTS levels and the interface.

with L levels. We first define two updating expressions, one for the electric field and the other for the magnetic field, from the LFDG algorithm of (3.105),

$$H_{n+\frac{p}{2}}^m = f_H \left(p\Delta t_1, H_{n-\frac{p}{2}}^m, H_{n-\frac{p}{2}}^{m+}, E_n^m, E_n^{m+} \right) \quad (3.109a)$$

$$E_{n+p}^m = f_E \left(p\Delta t_1, E_n^m, E_n^{m+}, H_{n+\frac{p}{2}}^m, H_{n+\frac{p}{2}}^{m+} \right) \quad (3.109b)$$

where p is an integer value, which allows us to use the updating functions to compute samples of the fields at any multiple of Δt_1 .

time	LEVEL 1	INTERFACE	LEVEL 2
$(n-3/2)\Delta t_1$	H		H
$(n-1)\Delta t_1$	E		
$(n-1/2)\Delta t_1$	H		H
$(n)\Delta t_1$	E	E	E
$(n+1/2)\Delta t_1$			
$(n+1)\Delta t_1$			
$(n+3/2)\Delta t_1$			
$(n+2)\Delta t_1$			
$(n+5/2)\Delta t_1$			
$(n+3)\Delta t_1$			

 FIGURE 3.7: Initial state of the electromagnetic fields for the three different sets of the scenario of figure 3.6, ($L=2$).

The starting state for the full sequence is shown in Figure 3.7. The sequence of the proposed LTS algorithm continues as follows (see also Figure 3.8):

- *Step 1. Update the magnetic field, f_H , for the level 1 ($H_{n+\frac{1}{2}}$), interface and level 2 ($H_{n+\frac{3}{2}}$).*
In case of level 1, $p = 1$ must be used, and for the level 2 and the interface, $p = 3$. All E_n needed are all available.
- *Step 2. Update electric field, f_E , for the level 1 and interface (E_{n+1}).*
In both cases $p = 1$ must be used. We need $H_{n+\frac{1}{2}}$; this information is available in level 1, but has to be evaluated in the interface, by averaging $H_{n+\frac{3}{2}}$ and $H_{n-\frac{1}{2}}$, and in level 2, by interpolating $H_{n+\frac{1}{2}} = \frac{2}{3}H_{n+\frac{3}{2}} + \frac{1}{3}H_{n-\frac{3}{2}}$.
- *Step 3. Update the magnetic field, f_H , for the level 1 ($H_{n+\frac{3}{2}}$).*
Clearly, $p = 1$ must be used. E_{n+1} is needed, in level 1 and in the interface, both available.
- *Step 4. Update the electric field, f_E , for the level 1 (E_{n+2}), interface and level 2 (E_{n+3}).*
In case of level 1, $p = 1$ must be used, and for the level 2 and the interface, $p = 3$. We need $H_{n+\frac{3}{2}}$, which are available.
- *Step 5. Update the magnetic field, f_H , for the level 1 and for the interface ($H_{n+\frac{5}{2}}$).*
In both cases, $p = 1$ must be used. We need E_{n+2} ; this information is available in level 1, but has to be evaluated in the interface, by averaging E_{n+1} and E_{n+3} , and in level 2, by interpolating $E_{n+2} = \frac{2}{3}E_{n+3} + \frac{1}{3}E_n$.
- *Step 6. Update electric field, f_E , for the level 1 (E_{n+3}).*
Obviously, $p = 1$ must be used. $H_{n+\frac{5}{2}}$ is needed, both in level 1 and in the interface, both available.

This algorithm retains most of the advantages of R-LF method (full explicitness and simplicity), but avoids the use of magnitudes at unknown times. Instead, they are calculated from previous dof, by means of averages and interpolations (also requiring the additional computation of certain states). Some specific differences appear in Steps 2 and 5, where we make the averaging operation at the interface, and we compute the fields there, thus requiring an interpolation on the upper level; also in Steps 3 and 6, where we use samples at known times, since they have been computed in the previous steps. Notice that the algorithm requires storing two states of the electric and magnetic fields in the interfaces, and in the highest level of that interface.

Concerning the stability of the scheme, as has been reported in [64, 95], the stability condition must be strengthened in general. From our experience, we need to apply a multiplicative factor 0.8 to the estimated Δt_{MAX}^m of the non-LTS case, but only at the interface and its neighboring elements. This means an extra stability condition

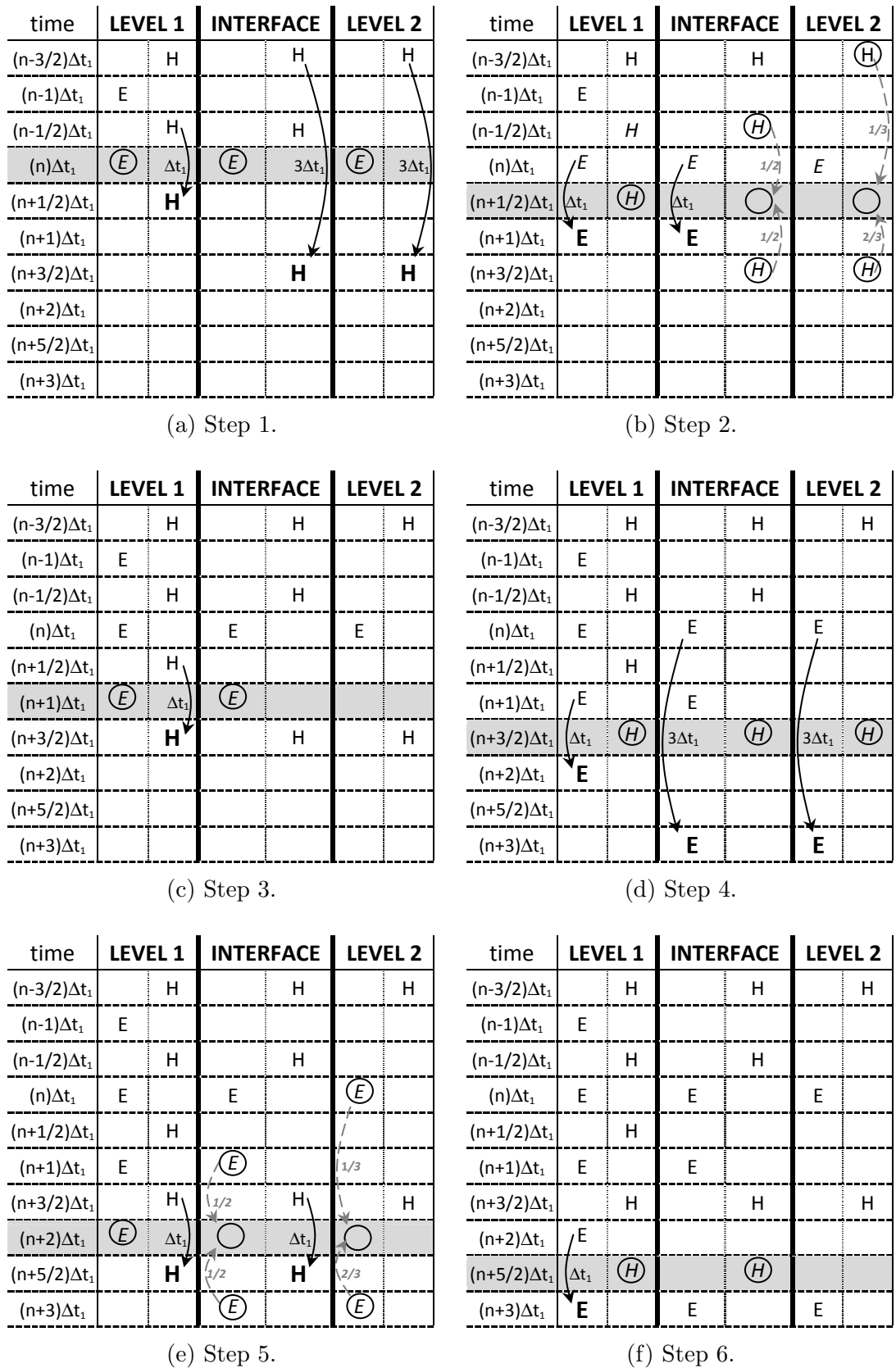


FIGURE 3.8: Sequence of the LTS algorithm for the scenario of Figure 3.6, ($L=2$). Leap-frog steps are drawn in solid lines, and interpolation in dashed format. The required samples for an updating step appear inside a circle, and the computed samples in bold.

is imposed in those elements. The algorithm has been tested in long and complex simulations in Section 5, exhibiting a robust late-time stability. No additional dissipation (or spurious solutions) is introduced by the LTS algorithm, apart from that described in Section 4.1.

The implementation of this scheme in a general multilevel ($L > 2$) case can be straightforwardly performed, just by assuring that the interface elements of different levels are not in contact. This is a minor requirement for practical meshes and avoids the use of a more restrictive multiplicative factor in the stability condition at the interfaces.

3.6 Summary

In this chapter, the semi-discrete DG method and the fully discrete LFDG algorithm were described in detail. The spatial-discretization scheme is based on the high-order discontinuous Galerkin methodology, employing curvilinear tetrahedra, and hierarchal vector-basis functions (detailed in Chapter 2). Expressions were developed for the flux evaluation, capable of easily dealing with the most common boundary conditions (dielectrics, PEC, PMC, and SM-ABC), as well as with propagation inside anisotropic materials. The formulation of the conformal UPML truncation condition was reviewed and integrated into the DG semi-discrete scheme. Finally, a specific LTS strategy was developed for the LFDG algorithm, to make the method efficient enough to deal with real problems.

Three different schemes were proposed for the evaluation of the flux between adjacent elements. These are listed next with a short rationale, which is further discussed and analyzed in Chapter 4:

- The centered flux: the simplest method, but exhibiting problems with non-physical solutions or spurious modes.
- The upwind flux: typically used in FVTD and including dissipative terms yields a spurious-free method in which the spurious solutions dissipate more than the physical ones. This flux is found by solving the Riemann problem at the discontinuity of the tangential field components, obtaining a quasi-explicit semi-discrete scheme in space (not fully explicit).
- The partially penalized flux: based on the upwind scheme by weighting the dissipative terms by a factor, and also yielding a spurious-free method. This reduction of the dissipative terms, responsible for the implicitness in space, permits a more efficient use of the LF scheme, at the cost of a lower dissipation of spurious modes

(compared to that of the upwind flux), but still much higher than for the physical solutions, if conveniently tuned.

Chapter 4

Numerical Analysis: Accuracy, Stability, Dispersion and Dissipation

In this chapter, the numerical dispersion, stability, and anisotropy of the errors of the DG and LFDG methods are analyzed. Unlike in FDTD, where closed analytical expressions can be easily derived, thanks to its structured meshing [157], in FEMTD methods, where unstructured meshes are used, these cannot in general be found. For these, the relationship between the order of the basis functions (p), element size (h), and time step (Δt) with stability, dispersion, dissipation, anisotropy, etc., is problem-dependent, and must be found in a semi-analytical manner, by numerically solving eigenvalue problems for simplified setups.

This process begins by the analysis of the DG semi-discrete scheme in 1D (with an extension to 3D), where the spurious numerical spectrum, and numerical dispersion and dissipation relations are found, and the nature of the errors are discussed. Then, the fully discrete LFDG algorithm is analyzed based on the resolution of the eigenvalue problem on a canonical geometry, which can be used to easily compare to the FDTD method, addressing stability, and numerical-spectrum topics. A convergence and anisotropy analysis of the errors is performed both for the DG semi-discrete operator, and for the LFDG algorithm, the conclusions of which can be considered general. Finally, a computational cost vs. accuracy analysis of the LFDG method is made, proving that LFDG outperforms FDTD in these terms.

4.1 General Analysis of the Discontinuous Galerkin Semi-Discrete Scheme

The traditional approach to analyze the space-time accuracy, and dispersion and dissipation errors, of DG methods is based upon the eigenvalue problem. Hu et al. in 2002 [48], presented a detailed study of the eigensolution of the DG method with uniform and nonuniform grids applied to a system of hyperbolic equations in one-dimension. In CEM, some studies appear in 2004 [54], describing the presence and behavior of spurious modes in the DG operator. Ainsworth in [56, 57] studied the dispersive and dissipative properties of the DG methods in the advection and second-order wave equation, respectively. In 2006, Warburton and Embree [55] described the role of the penalty in DG methods. Cohen and Duruflé, in 2007 [63] showed the need of dissipation terms to avoid spurious modes in the DG schemes. Sármány et al. [60], also studied the dispersion and dissipation errors, also considering the time-integration scheme.

Classical continuous FEM methods, both in curl-curl and in the mixed formulations, are well known for supporting spurious modes, which are non-physical solutions arising in the numerical approximation, and which are not present in the analytical problem. Especially harmful are non-divergent spurious modes (for divergence-free analytical problems) excited at non-null frequencies, since they severely corrupt near-field solutions. Many strategies to reduce them are found in the literature. For nodal (scalar basis) FEM, regularization techniques including conditions on the divergence of the solution, have been successfully employed [134]. For vector FEM, it is possible to use curl-conforming elements for which the basis vectors respect the natural (dis)continuity of the electromagnetic fields¹, only supporting spurious modes at null-frequency [27]. Higher-order hierarchal basis functions were introduced in [138] with this purpose.

DGTD also exhibits the appearance of spurious modes [48, 54, 55, 56, 57, 60, 63]. However, an added advantage of DGTD over FEMTD resides in its discontinuous nature that permits them to be removed by the use of upwind/penalized fluxes [55, 56, 57, 60, 63]. As stated in the previous chapter, these fluxes are characterized by the addition of dissipative terms to Maxwell equations, and are proven to attenuate spurious modes in space more strongly than physical modes. The suppression of spurious modes becomes a critical issue for DGTD formulations of the PML truncation condition, since instabilities appear otherwise [71]. Both DGTD approaches, for vector and scalar basis, are spurious-free for penalized fluxes, and have been successfully developed by several authors [29, 53, 59, 61, 70, 87, 96, 98, 103, 109], finding comparable levels of accuracy.

¹Continuity on the tangential components, and discontinuity in the normal ones.

In this section, we revisit the topic of spurious modes for simple 1D and 3D problems in DGTD, and the nature of the different errors (dispersion and dissipation) are identified. The analysis shown in this section appears also in [P11].

4.1.1 Numerical Dispersion and Dissipation of the DG Semi-Discrete Scheme

The dispersion and dissipation of the numerical method will be studied by searching for plane-wave solutions of frequency ω and wavevector \mathbf{k} , in general complex. These functions, replaced in the original equations, lead to an eigen-problem, with eigenvalues providing the numerical dispersion and dissipation relationships $\omega = f(k)$, and with eigenvectors providing the numerical-structure relationships between the dof or field components. For instance, the analytical Maxwell equations support plane-waves in free-space with the well-known dispersion relationship $\omega^2 = k^2/c^2$, and eigenvectors related by $\eta_0 \mathbf{H} = \hat{\mathbf{k}} \times \mathbf{E}$, with c and η_0 being the free-space speed of light and impedance, respectively.

A practical way to study the dispersion of a numerical scheme approaching Maxwell equations consists of restricting the space of solution to a bounded region with periodic boundary conditions (PBC), since they can be numerically enforced in an easy way. Let us assume for simplicity a 1D-domain $x \in [0, \Delta]$, and let us search for modes fulfilling PBC in space,

$$\Psi(x = \Delta, t) = e^{-j\alpha} \Psi(x = 0, t), \forall t, \quad \Psi = \{\mathbf{E}, \mathbf{H}\} \quad (4.1)$$

for arbitrary $\alpha \in [0, 2\pi)$. Plane-wave solutions of the form $e^{j(\omega t - kx)}$ (leftwards $k > 0$ and rightwards $k < 0$) comply with the PBC condition (4.1) for a infinite numerable spectrum of real wavenumbers k_n (each oscillating at a complex frequency ω_n),

$$k_n = \pm \left(\frac{\alpha}{\Delta} + \frac{\pi}{\Delta} 2n \right), \quad n = 0, -1, +1, -2, +2, \dots$$

$$\omega_n = f(k_n) \quad (4.2)$$

where we will refer to $k_0 = \frac{\alpha}{\Delta}$ as a fundamental mode, and to all other k_n as harmonic modes.

Let us apply this technique to the DG method in a semi-discrete form in space,

$$d_t H^m = \frac{1}{\mu} \mathbb{M}^{-1} \left[-(\mathbb{S} - \mathbb{F}_{\kappa e}) E^m - \mathbb{F}_{\kappa e}^+ E^{m+} + \mathbb{F}_{\nu h} H^m - \mathbb{F}_{\nu h}^+ H^{m+} \right] \quad (4.3a)$$

$$d_t E^m = \frac{1}{\varepsilon} \mathbb{M}^{-1} \left[(\mathbb{S} - \mathbb{F}_{\kappa h}) H^m + \mathbb{F}_{\kappa h}^+ H^{m+} + \mathbb{F}_{\nu e} E^m - \mathbb{F}_{\nu e}^+ E^{m+} \right] \quad (4.3b)$$

which is a simplified version of (3.13) for the m element, formulated in free-space without sources.

We define a column vector $\mathbf{U} = \left[\left(h_1^1, \dots, h_Q^1 \right), \dots, \left(h_1^M, \dots, h_Q^M \right), \left(e_1^1, \dots, e_Q^1 \right), \dots, \left(e_1^M, \dots, e_Q^M \right) \right]^T$ with all the dof of a given problem, and express the homogeneous semi-discrete DG Equations (4.3) as

$$j\omega\mathbf{U} = \mathcal{A}_{DG}\mathbf{U} \quad (4.4)$$

with \mathcal{A}_{DG} the semi-discrete DG operator. PBC are easily enforced in DG through the flux conditions by setting

$$\begin{aligned} \hat{\mathbf{n}}^m \times \Psi^{m+}|_{x=\Delta} &= e^{-j\alpha}(\hat{\mathbf{n}}^m \times \Psi^m|_{x=0}), \\ \hat{\mathbf{n}}^m \times \Psi^{m+}|_{x=0} &= e^{j\alpha}(\hat{\mathbf{n}}^m \times \Psi^m|_{x=\Delta}), \quad \Psi = \{\mathbf{E}, \mathbf{H}\} \end{aligned} \quad (4.5)$$

Plugging (4.5) into (4.4), we find a homogeneous algebraic system of equations, with a number of unknowns equal to the number of dof. Nontrivial solutions correspond to the eigenvectors of the semi-discrete space operator. Under the assumption that the space operator is diagonalizable, there will exist a basis of eigenvectors \mathbf{U}_m , $m = (0, 1, \dots, \text{dof} - 1)$, each propagating with a complex frequency $\omega = \tilde{k}_m$, with \tilde{k}_m its corresponding eigenvalue.

It should be noted that the Shannon sampling theorem [158] establishes an upper limit to the maximum wavenumber which can be sampled in a spatial domain discretized with dof samples. For instance, let us assume a one-element domain in 1D-DGTD, solved with p^{th} -order polynomials [($p+1$) electric dof plus ($p+1$) magnetic dof]. The analytical bandwidth (4.2) which can be represented numerically is restricted to

$$|k_n| = \left| k_0 + \frac{\pi}{\Delta} 2n \right| \leq \frac{\pi}{\Delta} (p+1), \quad n = (0, -1, +1, \dots) \quad (4.6)$$

That is, for each $k_0 \neq \pi/\Delta$ there² are $(p+1)$ leftward analytical modes $+|k_n|$ plus $(p+1)$ rightward ones $-|k_n|$, which can be numerically approximated. Of course, numerical eigenvalues \tilde{k} fulfilling the Shannon sampling theorem are not necessarily proper approximation of the analytical ones k . In a broad sense, we will refer to these numerical modes which do not *properly* approximate any analytical one, as *spurious* or *nonphysical* modes.

²See Figures 4.1 and 4.2 to see the case $k_0 = \pi/\Delta$.

Let us illustrate this for our simple 1D 1-element case solved by nodal-DGTD and Lagrange polynomial p^{th} -order basis. Figures 4.1 and 4.2 show the dispersion and dissipation relation for 1st- and 2nd-order basis (with centered and upwind fluxes). We note that, for $p = 1$, there appear one rightward and one leftward solution which approximate the fundamental mode for well-resolved problems ($L \equiv k_0\Delta/(p+1) \rightarrow 0$). Another two modes (one leftward plus rightward) solutions are found, which should correspond to the first harmonics ($|k_{-1}| = \frac{2\pi}{\Delta} - k_0$). Due to the coarse discretization of these modes, close to their own Shannon limit for $L \rightarrow 0$, the numerical phase speed is far from the analytical one. These poorly sampled modes (for a well-resolved fundamental one) with an undesired behavior are the spurious or nonphysical modes. It bears noting that, in case of ($L \rightarrow \pi$), when $|k_{-1}| \approx 0$ and $|k_0| \approx \frac{2\pi}{\Delta}$, the situation is the opposite: the fundamental modes numerically propagate in a wrong way, providing a good approximation of what has been defined as harmonics.

For $p = 2$, a similar analysis can be made. Apart from the two fundamental modes, another four modes (two leftward plus two rightward) appear. In case of $L \rightarrow 0$, the first harmonics ($\pm k_{-1}$) can be distinguished in the numerical dispersion functions, but the second harmonics $\pm k_{+1}$ present wrong behavior on the phase speed. For different intervals of L , the different solutions, fundamental or harmonic modes, ($\pm \tilde{k}_0, \pm \tilde{k}_{-1}, \pm \tilde{k}_{+1}$) offer a better or worse approximation to the analytical solutions ($\pm k_0, \pm k_{-1}, \pm k_{+1}$). In case of upwind flux, much better approximation over more bandwidth is achieved than for centered flux.

A noteworthy point here is to analyze the dissipation relationship of the upwind flux. All modes propagate with an attenuation that is larger for poorly resolved modes than for well-resolved ones. Clearly, for the fundamental mode, dissipation is minimum for $L \rightarrow 0$. In the case of the harmonics, this situation takes place for different intervals of L , where they are properly resolved. Furthermore, in all cases, good phase dispersion corresponds to low dissipation, and poor phase dispersion corresponds to a high dissipation relationship. However, for the centered flux, the numerical modes do not attenuate in any case, and poorly sampled analytical modes with wrong behavior (spurious) may appear together with the well-resolved ones in a simulation.

The definition we use here of spurious solutions is broad in the sense that it provides information for the whole spectrum of the semi-discrete space operator (which constitutes a basis for all possible solutions or diagonalizable operators): it provides criteria to distinguish physical from nonphysical behavior, just in terms of the correct approximation between the analytical and numerical solutions. However, the qualification of spurious mode actually depends on the analytical problem under study. For instance, if we excite the PBC-analytical problem with the fundamental mode as initial values, we might not

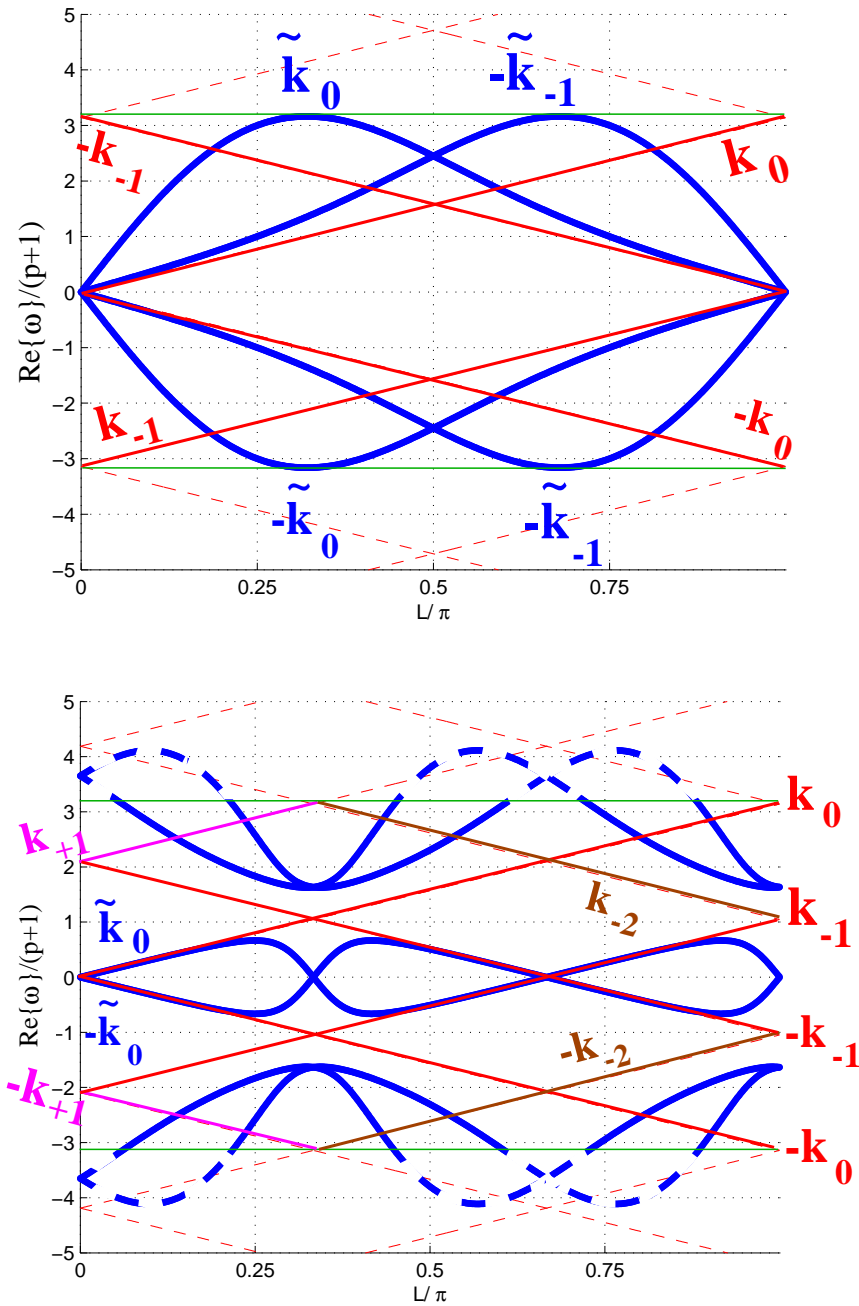


FIGURE 4.1: Numerical dispersion and dissipation $\omega = f(\tilde{k}_n)$ as a function of $L = k_0\Delta/(p+1)$, for scalar 1D-DGTD. Analytical dispersion in red $\omega = k_n = ((p+1)L + 2n\pi)/\Delta$. Sub-index in \tilde{k}_m has been added *a posteriori* according to the analytical mode matched for some L region (no identification for \tilde{k}_m has been guessed for $p=2$ in the centered case). Up: Centered $p=1$, Down: Centered $p=2$. The bandwidth allowed by Shannon theorem is delimited with green lines, while dashed lines indicate modes outside this band. Blue is used for numerical modes and red (magenta & brown) for the analytical ones. ($\Delta = 1, \mu_0 = 1, \varepsilon_0 = 1$)

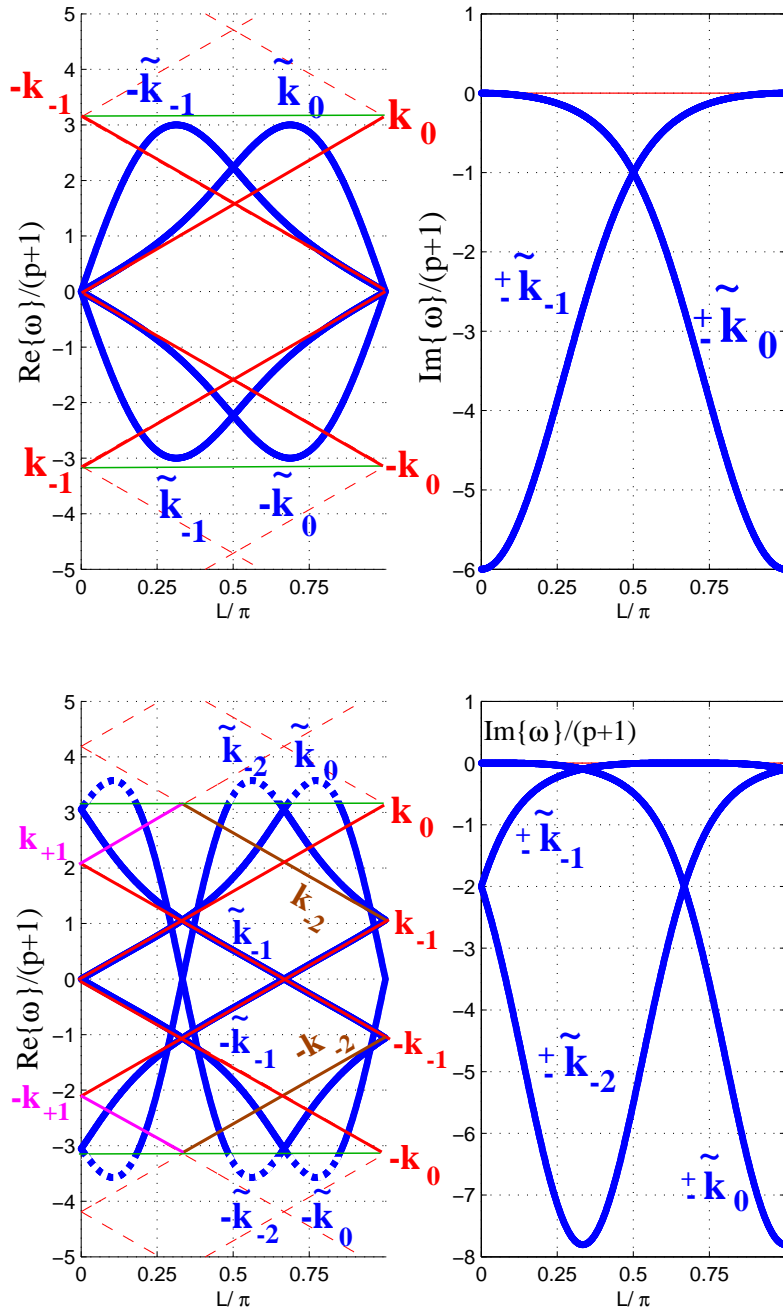


FIGURE 4.2: Numerical dispersion and dissipation $\omega = f(\tilde{k}_n)$ as a function of $L = k_0\Delta/(p+1)$, for scalar 1D-DGTD. Analytical dispersion in red $\omega = k_n = ((p+1)L + 2n\pi)/\Delta$. Sub-index in \tilde{k}_m has been added *a posteriori* according to the analytical mode matched for some L region (no identification for \tilde{k}_m has been guessed for $p = 2$ in the centered case). Up: Upwind $p=1$, Bottom: Upwind $p=2$. The bandwidth allowed by Shannon theorem is delimited with green lines, while dashed lines indicate modes outside this band. Blue is used for numerical modes and red (magenta & brown) for the analytical ones. ($\Delta = 1, \mu_0 = 1, \varepsilon_0 = 1$)

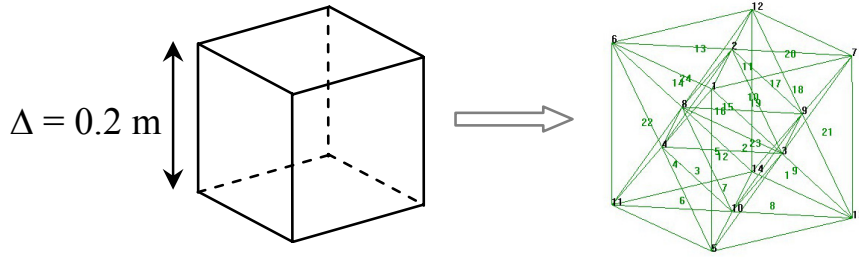


FIGURE 4.3: Geometry under analysis for the 3D eigenvalue problem.

expect the appearance of any of the higher harmonics in its numerical counterpart. In this narrow sense, any solution apart from that corresponding to the fundamental mode might also be considered spurious (see [54]), even if it is well resolved in space. To illustrate this, we have projected the fundamental (rightward) analytical mode k_0 , expanded in a $p = 10$ polynomial basis, into the basis of numerical eigenvectors. Since these are not orthogonal, we cannot assume a modal separation of the energy, but we still find that for a good resolution $L = 0.005$, the numerical mode propagates with $\tilde{k}_0 \approx k_0$ with an amplitude ~ 572 times higher than that of the next mode, whereas this ratio lowers to ~ 28 for a resolution of $L = 0.11$.

4.1.2 Extension to Three Dimensions

Let us move to a 3D case solved with hierarchical vector basis that is complete up to order $p = 2$, both for the gradient and the rotational spaces. We have meshed a cubic domain in a symmetrical way composed of 24 tetrahedra, as is depicted in Figure 4.3.

The 3D-PBC in space can be expressed as

$$\begin{aligned} \hat{\mathbf{n}} \times \mathbf{H}|_{i+\Delta i} &= \hat{\mathbf{n}} \times \mathbf{H}|_i e^{-j\alpha_i}, \\ \hat{\mathbf{n}} \times \mathbf{E}|_{i+\Delta i} &= \hat{\mathbf{n}} \times \mathbf{E}|_i e^{-j\alpha_i} \quad \text{with } i = \{x, y, z\} \end{aligned} \quad (4.7)$$

where α_i is the phase shift in each direction of the space. Considering that $\mathbf{k}_0 = k_{0x}\hat{\mathbf{x}} + k_{0y}\hat{\mathbf{y}} + k_{0z}\hat{\mathbf{z}}$ is the fundamental mode, the phase shift can be evaluated by $\alpha_i = k_{0i}\Delta_i$. In this case, we enforced PBC in the x-direction with $\alpha_x = 2\pi\Delta$, being $\Delta = 0.2$, and PBC conditions at the YZ and ZX -planes with $\alpha_y = \alpha_z = 0$ (no delay). An example of the application of the 3D-PBC is depicted in Figure 4.4.

The numerical eigenvalue \tilde{k} is plotted in Figure 4.5. There are $2MQ = 1440$ modes corresponding to the number of dof of the problem ($M = 24$ tetrahedra and $Q = 30$ dof per element). Again, we find that the spectrum of the DG operator depends heavily on the flux-evaluation scheme. It can be seen that, for the centered scheme, none of

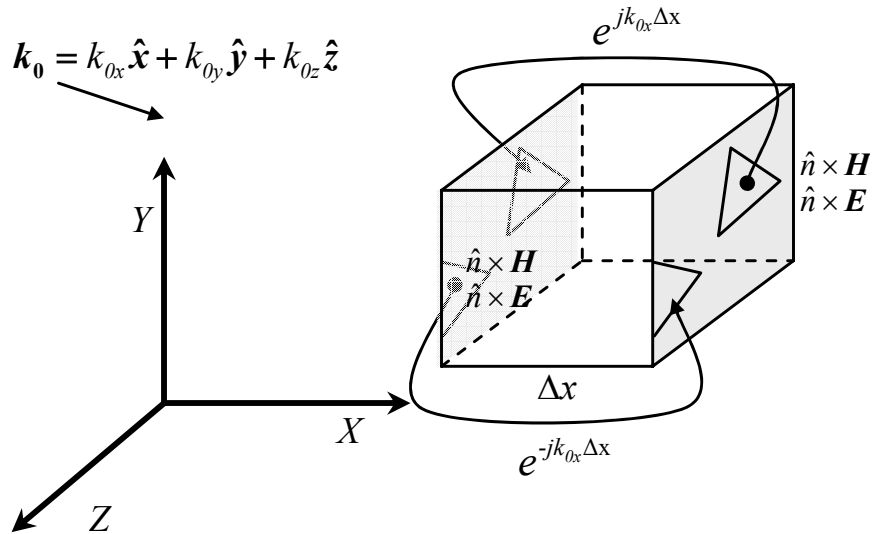


FIGURE 4.4: Examples of the application of the 3D-PBC between contour faces from elements located on opposite sides.

the modes supported by the numerical method has dissipation $\tilde{k}_{imag} = 0$. Therefore, all numerical modes, both well-resolved physical and poorly resolved spurious solutions, could be present in a numerical simulation and propagate on the computational domain. On the contrary, for the upwind case, we can clearly distinguish between well-resolved physical modes³ and poorly resolved spurious modes by looking at their attenuation $\tilde{k}_{imag} \approx 0$. Hence, poorly resolved spurious modes decrease exponentially with the spatial position and do not propagate along the computational domain. It is important to note that some undesirable dissipation also affects the well-resolved physical modes, depending on their spatial resolution.

For the penalized flux with $\tau = 0.1$, similar conclusions are drawn. The main difference is that the dissipation of the spurious modes decreases compared to the upwind case. However, the choice of the τ parameter also has an impact on the stability conditions of the final numerical scheme, as appears following (Section 4.2.2) for the LF scheme and in [71] for RK. In general, the upper limit of stability in Δt becomes more restrictive when τ increases. The use of partially penalized flux with small values of the τ parameter has negligible effects on the stability of the scheme while keeping sufficient practical attenuation in the poorly resolved spurious modes.

Finally, let us consider a more realistic case: a 1m-side cubic 3D PEC cavity meshed with 5025 tetrahedra (see Figure 4.6). The fields in the cavity are then excited via an electric-current source with a Gaussian pulse time signal, with 10dB bandwidth of

³Four fundamental rightward/leftward planewaves (two polarizations) and their corresponding harmonics.

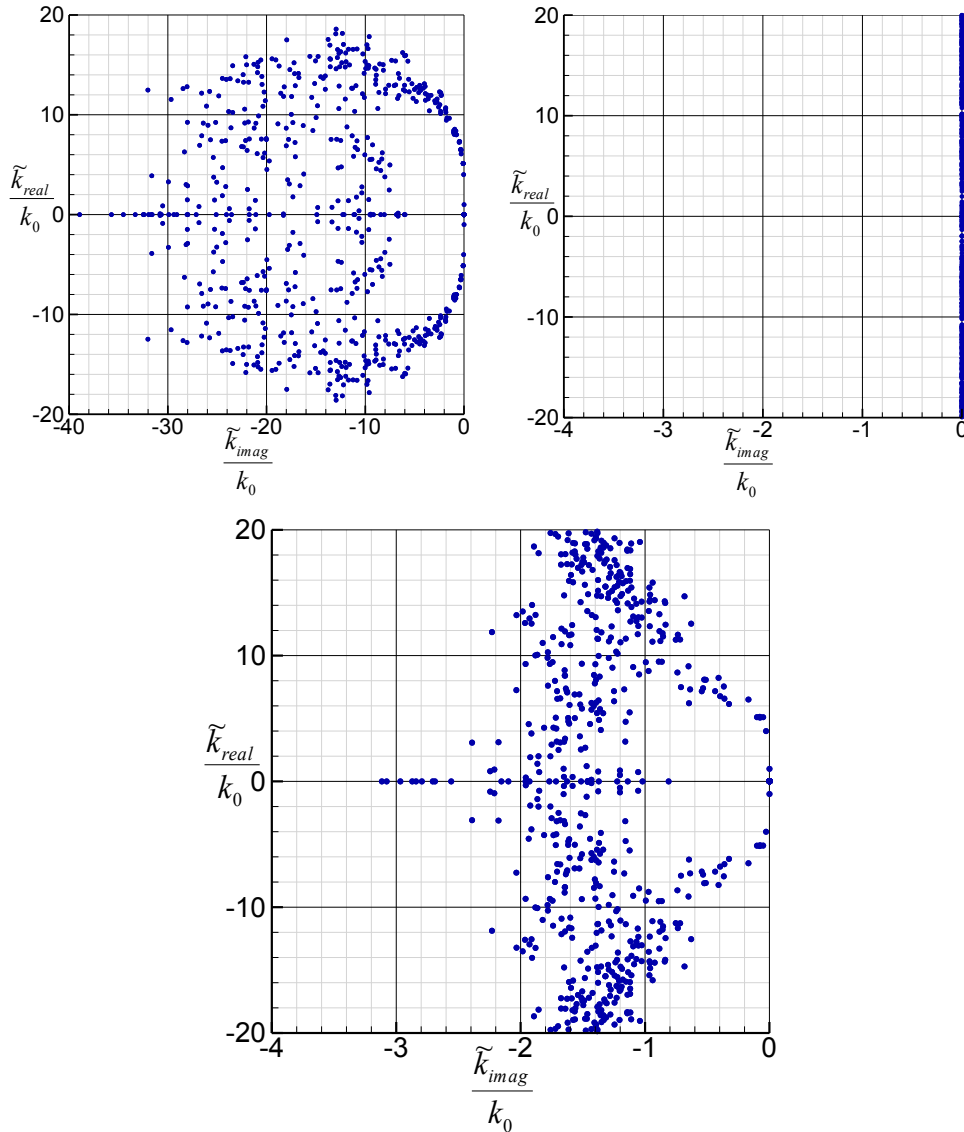


FIGURE 4.5: Spectrum of the DG operator for a cubic domain (meshed with 24 tetrahedra) with PBC ($\mathbf{k}_0 = 2\pi\hat{\mathbf{x}}$, $\Delta = 0.2$ and $p = 2$). Upwind flux (upper left), Centered flux (upper right), Partially penalized flux $\tau = 0.1$ (lower).

approximately 400 MHz. The problem has been simulated up to a physical time of $0.5 \mu\text{s}$ by means of a fourth-order Runge-Kutta (RK4) time-integration scheme. This problem was computed with centered, upwind, and partially penalized flux, with very low $\tau = 0.025$ with hierarchal vector-basis functions of complete order $p = 2$.

The electric field is sampled at one point and the Fourier transform performed for the vertical component (see Figure 4.7). The power spectrum computed with centered flux is noisy and shows spectral pollution due to the presence of nonphysical spurious modes. In case of upwind or partially penalized flux (even for such a low value of τ), we can clearly distinguish the different resonant frequencies.

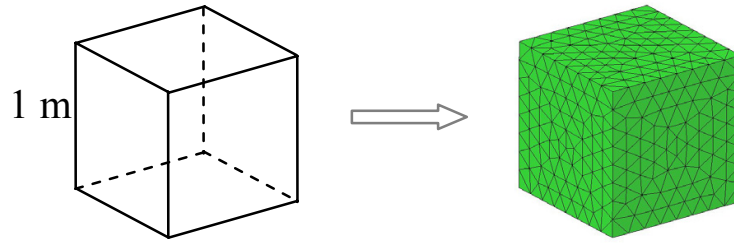
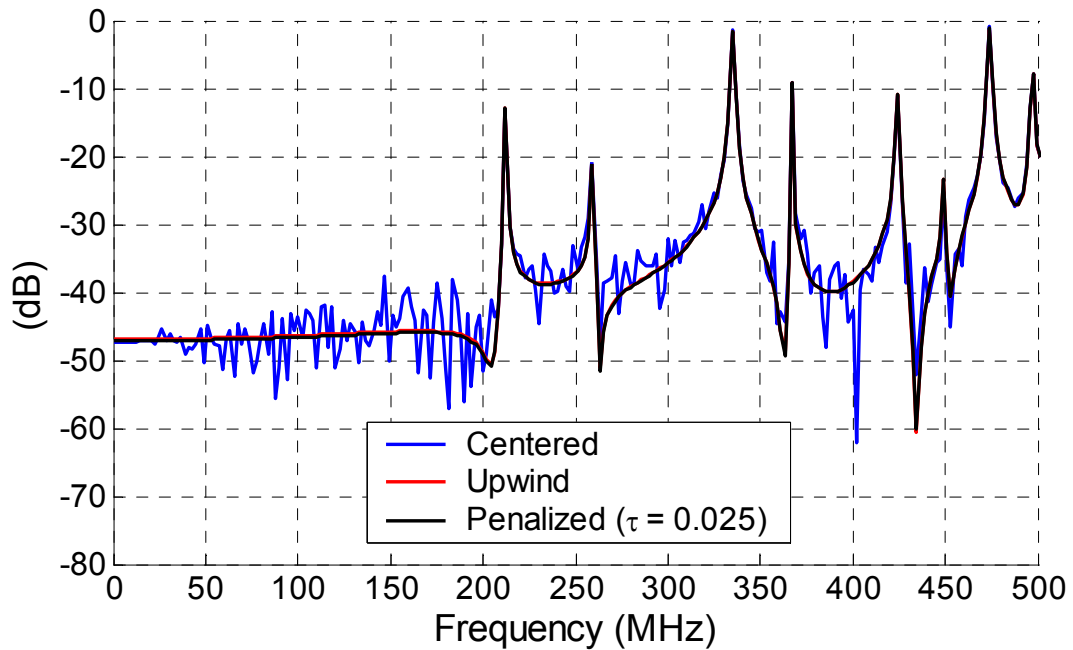


FIGURE 4.6: Cubic PEC cavity.

FIGURE 4.7: Power spectrum of the vertical component of electric field sampled at a point inside the cavity, computed using centered, upwind, and partially penalized ($\tau = 0.025$) fluxes, 4^{th} -order 2N-storage Runge-Kutta and $p = 2$.

A similar analysis appears in [54] with nodal functions, where the presence of spurious modes, in case of centered flux, were reported as well. In case of upwind or penalized schemes, the spurious modes are also present but have a significant dissipation associated only with them (very little dissipation for the physical models depending on the level of discretization), avoiding spectral pollution and the contamination of the solutions. This fact, as demonstrated above, does not depend on the kind of basis functions used by the scheme, as has been widely investigated in FEM in frequency domain, and it is a remarkable difference in DGTD methods, compared to the continuous formulation.

4.2 Analysis of the Leap-Frog DG Algorithm

In order to characterize a FEMTD method both, the spatial semi-discrete operator (element size (h) and order of the basis functions (p)) and the time-integration method (time step (Δt)), have to be considered. In this section, we establish the basis to analyse the LFDG algorithm. Firstly, the eigenvalue problem is formulated. Next, a simple stability analysis is performed to support the choice of the Δt . Finally, some results of the eigenvalue problem are shown to understand the influence of the time-integration method in the numerical spectrum, comparing to the ones shown in the previous section for the semi-discrete case.

4.2.1 Eigenvalue Problem Setup of the LFDG Algorithm

The LFDG algorithm (3.105) for a lossless medium without sources is

$$H_{n+\frac{1}{2}}^m = H_{n-\frac{1}{2}}^m + \frac{\Delta t}{\mu} \mathbb{M}^{-1} \left[-(\mathbb{S} - \mathbb{F}_{\kappa e}) E_n^m - \mathbb{F}_{\kappa e}^+ E_n^{m+} + \mathbb{F}_{\nu h} H_{n-\frac{1}{2}}^m - \mathbb{F}_{\nu h}^+ H_{n-\frac{1}{2}}^{m+} \right] \quad (4.8a)$$

$$E_{n+1}^m = E_n^m + \frac{\Delta t}{\varepsilon} \mathbb{M}^{-1} \left[(\mathbb{S} - \mathbb{F}_{\kappa h}) H_{n+\frac{1}{2}}^m + \mathbb{F}_{\kappa h}^+ H_{n+\frac{1}{2}}^{m+} + \mathbb{F}_{\nu e} E_n^m - \mathbb{F}_{\nu e}^+ E_n^{m+} \right] \quad (4.8b)$$

Let us define three column vectors with the magnetic and electric dof staggered in time,

$$\begin{aligned} \mathbf{H}_{n-\frac{1}{2}} &= \left[\left(H_{n-\frac{1}{2}}^1 \right)^T, \dots, \left(H_{n-\frac{1}{2}}^M \right)^T \right]^T \\ \mathbf{E}_n &= \left[\left(E_n^1 \right)^T, \dots, \left(E_n^M \right)^T \right]^T \\ \mathbf{U}_n &= \left[\left(\mathbf{H}_{n-\frac{1}{2}} \right)^T, \left(\mathbf{E}_n \right)^T \right]^T \end{aligned}$$

Equations (4.8) can be expressed in a compact manner, for the whole spatial domain as

$$\mathbf{H}_{n+\frac{1}{2}} = \left(\mathbb{I}_{MQ} + \frac{\Delta t}{\mu} \mathbb{M}_{\nu h} \right) \mathbf{H}_{n-\frac{1}{2}} + \frac{\Delta t}{\mu} \mathbb{M}_{S\kappa e} \mathbf{E}_n \quad (4.10a)$$

$$\mathbf{E}_{n+1} = \left(\mathbb{I}_{MQ} + \frac{\Delta t}{\varepsilon} \mathbb{M}_{\nu e} \right) \mathbf{E}_n + \frac{\Delta t}{\varepsilon} \mathbb{M}_{S\kappa h} \mathbf{H}_{n+\frac{1}{2}} \quad (4.10b)$$

where \mathbb{I}_{MQ} is the $MQ \times MQ$ identity matrix, and $\mathbb{M}_{\nu h}$, $\mathbb{M}_{S\kappa e}$, $\mathbb{M}_{\nu e}$ and $\mathbb{M}_{S\kappa h}$ are $MQ \times MQ$ matrices, which are the result of assembling the element-matrices of (4.8).

Inserting (4.10a) into (4.10b), the following fully explicit system is obtained,

$$\mathbf{H}_{n+\frac{1}{2}} = \left(\mathbb{I}_{MQ} + \frac{\Delta t}{\mu} \mathbb{M}_{\nu h} \right) \mathbf{H}_{n-\frac{1}{2}} + \frac{\Delta t}{\mu} \mathbb{M}_{S\kappa\epsilon} \mathbf{E}_n \quad (4.11a)$$

$$\mathbf{E}_{n+1} = \left(\mathbb{I}_{MQ} + \frac{\Delta t}{\epsilon} \mathbb{M}_{\nu\epsilon} + \frac{(\Delta t)^2}{\mu\epsilon} \mathbb{M}_{S\kappa h} \mathbb{M}_{S\kappa\epsilon} \right) \mathbf{E}_n + \frac{\Delta t}{\epsilon} \left(\mathbb{M}_{S\kappa h} + \frac{\Delta t}{\mu} \mathbb{M}_{S\kappa h} \mathbb{M}_{\nu h} \right) \mathbf{H}_{n-\frac{1}{2}} \quad (4.11b)$$

which can be written in a compact manner as

$$\mathbf{U}_{n+1} = \mathcal{A}_{LFDG} \mathbf{U}_n \quad (4.12)$$

where the matrix \mathcal{A}_{LFDG} is the DG operator with the LF algorithm. It is the result of assembling all the element-matrices of (4.11) into a $2MQ \times 2MQ$ matrix. The matrix \mathcal{A}_{LFDG} depends on the DG spatial discretization features, such as mesh size (h), penalization factor (τ), and order of the basis functions (p), and also on the LF time-integration scheme with a time step Δt .

Following a procedure similar to that of Section 4.1 for the analysis of the DG spatial semi-discrete scheme, let us consider a time-harmonic plane wave of the form $e^{j(\omega t - \mathbf{k}_0 \mathbf{r})}$, where ω is the angular frequency and \mathbf{k}_0 is the physical wavevector, and let us seek for plane-wave solutions. The relationship between \mathbf{U}_{n+1} and \mathbf{U}_n becomes

$$\mathbf{U}_{n+1} = e^{j\omega\Delta t} \mathbf{U}_n \quad (4.13)$$

with $e^{j\omega\Delta t}$ the so-called the amplification factor, which is found after solving the following eigen-problem,

$$e^{j\omega\Delta t} \mathbf{U}_n = \mathcal{A}_{LFDG} \mathbf{U}_n \quad (4.14)$$

Finding the $2MQ$ eigenvalues ($\lambda_{\mathcal{A}_{LFDG}}^m, m = 1, \dots, 2MQ$), we obtain the complex-valued numerical wave-vectors ($\tilde{k}^m = \tilde{k}_{real}^m + j\tilde{k}_{imag}^m, m = 1, \dots, 2MQ$), related to the eigenvalues by

$$\tilde{k}^m = j \frac{\ln \left(\lambda_{\mathcal{A}_{LFDG}}^m \right)}{c\Delta t}, \quad m = 1, \dots, 2MQ \quad (4.15)$$

4.2.2 Stability Analysis of the LFDG Algorithm

The LFDG algorithm is an explicit and conditionally stable scheme. Some stability analyses appear in [61, 63, 64, 136], where heuristic or analytical sufficient-stability closed conditions were derived. These analyses find a stability condition based on the maximum eigenvalue that can be supported by the scheme. To avoid solving complex

eigenvalue problems for each specific problem, a maximum limit for the highest eigenvalue can be estimated to ensure stability. Thus, a Δt_{max} can be chosen *a priori* based on geometrical properties of the elements. Following this procedure, larger Δt does not mean an unstable scheme, but shorter Δt guarantees the stability of the scheme. For the first-order $p = 1$, LFDG with $\tau = 0$ or centered flux, in an homogeneous medium, the following condition must be satisfied by all the m elements to achieve stability [64],

$$c\Delta t \frac{8 + \sqrt{40}}{3} < \frac{4V_m}{\partial V_m} \quad (4.16)$$

where V_m is the element volume, and ∂V_m the element perimeter or the sum of the surface of all faces of the element.

In the case of $\tau \neq 0$, this expression is not valid, and the stability condition becomes more restrictive and difficult for an *a priori* estimation, [64].

In this work, a simple numerical-stability analysis has been performed on the 3D geometry (Figure 4.3) described in Section 4.1.2: a cubic spatial domain meshed in a symmetrical way into 24 tetrahedra, with 3D-PBC conditions (4.7) at the box faces (Figure 4.4). The maximum Δt has been numerically found for different p orders, and τ values. The numerical strategy is to solve the eigenvalue problem of (4.14) for different Δt until we find the maximum value (Δt_{max}), which keeps all the complex-valued \tilde{k}^m with a negative imaginary part ($\tilde{k}_{imag}^m < 0, m = 1, \dots, 2MQ$).

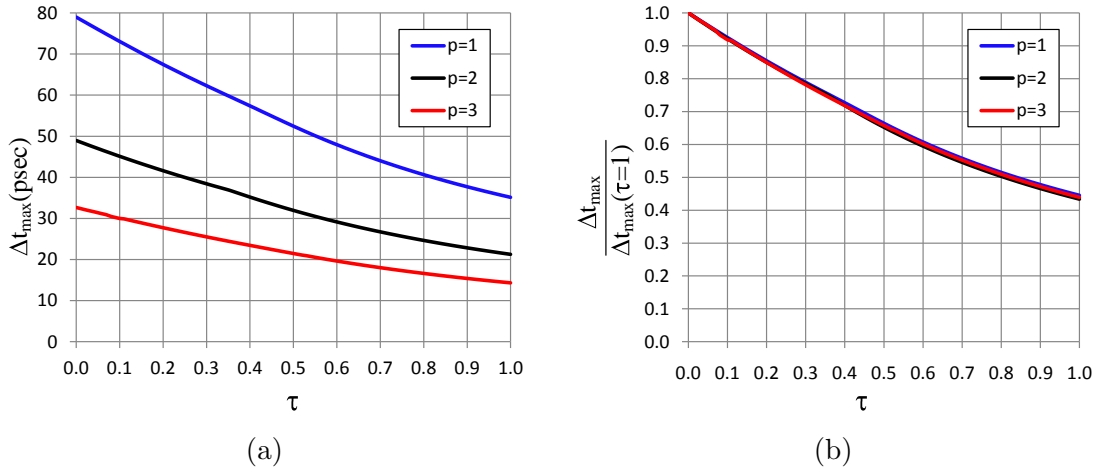


FIGURE 4.8: Numerical stability analysis of the LFDG algorithm for the geometry of figure 4.3 with $\mathbf{k}_0 = 2\pi\hat{\mathbf{x}}$ and $\Delta = 0.2$. (a) Dependence of Δt_{max} with τ parameter. (b) Relative penalization of Δt_{max} with τ parameter.

Figure 4.8 shows the results. A ($\propto \frac{1}{\tau}$) dependence of the Δt_{max} with the penalization parameter can be guessed, as derived in [64]. The relative penalization of Δt_{max} does

not depend on the order of the basis functions p . Higher values of the τ parameter require lower Δt values to maintain the stability. For this reason, it is desirable to keep the τ parameter as low as possible so as not to penalize the stability condition, but high enough to eliminate spurious modes: a tradeoff between stability and spurious-mode reduction is required.

Table 4.1 shows some notable values taken from the results. The penalization for using $\tau = 0.1$ is about 9% in the Δt . In case of $\tau = 1.0$, upwind flux, the computation cost would be increased by a factor of 2.25. The third column shows a estimation of the increment in the number of time steps due to the reduction of time step when order p is increased. This factor is about 1.6 from $p = 1$ to $p = 2$, and 2.5 from $p = 1$ to $p = 3$.

It is important to note that the computational cost for different orders does not depend only on Δt . If higher orders are used, the number of dof also increases and therefore the computational cost per time step. On the other hand, accuracy is better for higher-order p , so that the number of elements can be reduced by increasing h . For all these reasons, a tradeoff is needed between the size of the mesh, accuracy, and order p . This analysis, from the standpoint of computational cost, appears in Section 4.5.

TABLE 4.1: Results of the numerical stability analysis of the LFDG algorithm.

	$\frac{\Delta t_{max}(p, \tau=0)}{\Delta t_{max}(p, \tau=0.1)}$	$\frac{\Delta t_{max}(p, \tau=0)}{\Delta t_{max}(p, \tau=1)}$	$\frac{\Delta t_{max}(p=1, \tau=0.1)}{\Delta t_{max}(p, \tau=0.1)}$
$p = 1$	1.08	2.25	1.00
$p = 2$	1.09	2.30	1.62
$p = 3$	1.09	2.28	2.44

4.2.3 Numerical Results of the LFDG Eigen-Problem

The results of the previous section permit the choice of the Δt relative to Δt_{max} , since the eigen-problem depends on this value. Hereinafter, the following parameters have been fixed: $\mathbf{k}_0 = 2\pi\hat{\mathbf{x}}$, $p = 2$, and $\Delta = 0.2$.

Figures 4.9 and 4.10 show the spectrum of the LFDG algorithm for different flux-evaluation schemes and Δt , respectively. The analyzed cases that appear in Figure 4.9 are similar to those of Figure 4.5 solved with the DG spatial operator. It can be seen that the time-integration scheme has an impact on the eigenvalue problem, which is slightly distorted, but the nature of the spectrum remains. Hence, the same conclusions related to non-physical solutions or spurious modes made for the semi-discrete scheme in Section 4.1.2, can be extended for the LFDG algorithm.

Figure 4.10 shows the spectrum of the LFDG algorithm for Δt close to Δt_{max} . It can be seen that the spectrum of LFDG is not symmetrical respect to the real part. In the DG

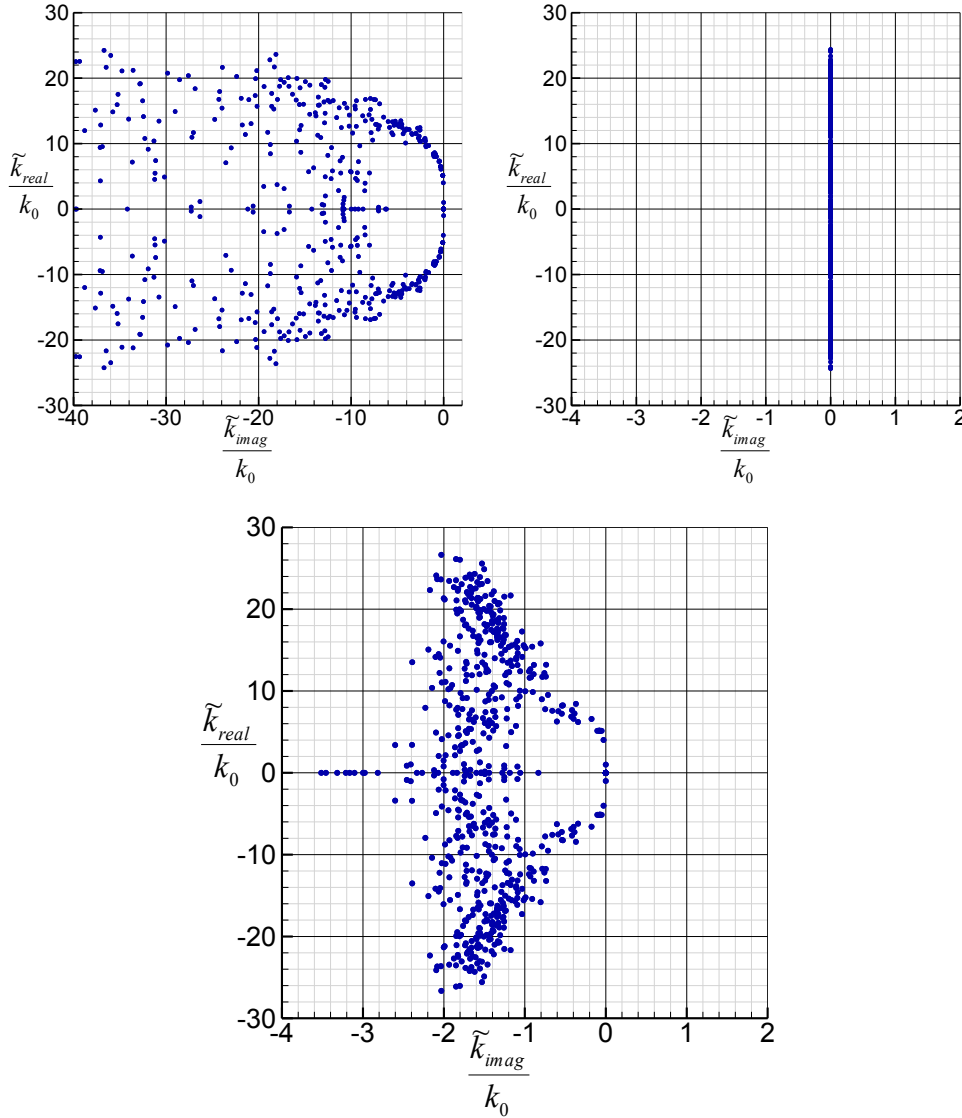


FIGURE 4.9: Spectrum of the LFDG operator for a cubic domain (meshed with 24 tetrahedra) with PBC ($\mathbf{k}_0 = 2\pi\hat{\mathbf{x}}$, $\Delta = 0.2$ and $p = 2$). Upwind flux (upper left), Centered flux (upper right), Partially penalized flux $\tau = 0.1$ (lower).

operator, for all the numerical wavenumbers i , defined as $\tilde{k}^i = \tilde{k}_{real}^i + j\tilde{k}_{imag}^i$, another j wavenumber can be found which fulfills the following condition, $\tilde{k}^j = -\tilde{k}_{real}^i + j\tilde{k}_{imag}^i$. In the LFDG case, this symmetry condition is not exactly fulfilled, and it is more clear in the case of Δt close to Δt_{max} , and in the wavenumbers close to the instability limits (large value of $|\tilde{k}_{real}^m|$ and \tilde{k}_{imag}^m close to zero, even positive in case of an unstable situation). The reason for this phenomenon is that a backward approximation of the penalization terms is being used, instead of central differences, this fact enables a fully explicit scheme to be found. Hence, delayed samples of the fields are used instead of updated samples, which drives to non-symmetrical eigenvalues. This fact makes the stability condition

slightly more restrictive.

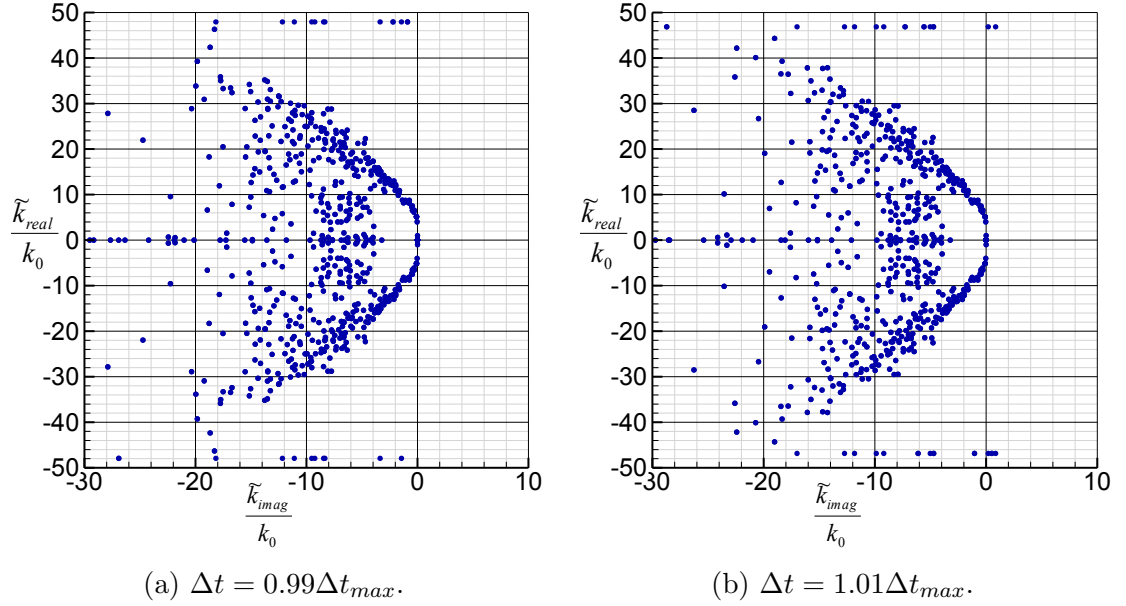


FIGURE 4.10: Results of the eigenvalue problem (spectrum of the LFDG operator) for Δt close to Δt_{max} , of the problem of Figure 4.3 with PBCs, with $\tau = 0.4$, $\mathbf{k}_0 = 2\pi\hat{\mathbf{x}}$, $p = 2$ and $\Delta = 0.2$.

4.3 Convergence of the Numerical Errors

In this section, an estimation is made of the convergence rates of the semi-discrete DG operator and the fully discrete LFDG algorithm. The influence of the τ penalization parameter, and Δt is also studied [P5]. The convergence of DG methods has been dealt with in a number of works [48, 56, 57]. In this case, the alternative strategy used previously for the study of the spurious modes and the numerical spectrum is followed. The convergence is analyzed by searching for numeric plane-wave solutions $e^{j(\omega t - \mathbf{k}\mathbf{r})}$ of real frequency ω and complex wave-vector \mathbf{k} , for the simple problem of Figure 4.3 with PBC. The numerical wavevector compared to the analytical one will provide a measure for the error of the numerical scheme.

For this analysis, we take $\alpha_x = 2\pi\Delta$, and no phase shift for the other directions $\alpha_y = \alpha_z = 0$ ($\mathbf{k}_0 = k_0\hat{\mathbf{z}}$), since the convergence rates do not depend on the illumination direction. The eigen-problem (4.4) is numerically solved for different h , to find the numerical eigenvalue \tilde{k}_m . We define h (a measure for the size of the elements) equal to the dimension of the cube $\Delta \equiv h$. For the error analysis, we retain only the \tilde{k}_m closest to the analytical one $\mathbf{k}_0 = \omega\sqrt{\mu_0\epsilon_0}$ (the rest can be considered spurious in the sense discussed previously), referred to here as $\tilde{k}_0 = \tilde{k}_{real} + j\tilde{k}_{imag}$.

Three different Root Mean Square (RMS) error functions per wavelength ($\lambda = 2\pi/k_0$) can be defined:

$$\text{RMS error per wavelength (dispersion): } \left| e^{-jk_0\lambda} - e^{-j\tilde{k}_{real}\lambda} \right| \quad (4.17a)$$

$$\text{RMS error per wavelength (dissipation): } \left| 1 - e^{\tilde{k}_{imag}\lambda} \right| \quad (4.17b)$$

$$\text{RMS error per wavelength (global): } \left| e^{-jk_0\lambda} - e^{-j\tilde{k}_0\lambda} \right| \quad (4.17c)$$

The first one measures the dispersion error (phase delay), depending on the real part of the numerical eigenvalue (\tilde{k}_{real}); the second one measures the dissipation error (decrease in amplitude), depending on its imaginary part (\tilde{k}_{imag}); and the third one measures the global combination of both errors.

For the DG semi-discrete scheme, the RMS, for basis orders $p = 1, 2, 3$ and upwind flux ($\tau = 1$), and for five values of τ penalization parameter (from $\tau = 1$, to $\tau = 0.025$), are shown in Figures 4.11 and 4.12 respectively, as a function of the spatial resolution ($h/\lambda = k_0h/(2\pi)$).

From Figures 4.11 and 4.12, we can derive the following conclusions:

- High-order convergence of the error is found in all cases. The phase error increases as $O(h^{2p+2})$ and the amplitude error follows $O(h^{2p+1})$, p being the order of the polynomial space for the vector-basis functions [48, 56, 57].
- In general, most of the practical and real applications need an error of about 10^{-2} . Note that in this zone the convergence rate becomes exponential.
- Since the convergence rate for the dissipation error is worse than for the dispersion error ($2p + 2 > 2p + 1$), dissipation places higher constraints on the scheme resolution (h/λ) than does the dispersion error. This fact should be considered when choosing the time-integration scheme, to avoid the introduction of more dissipation, keeping dispersion under control. For instance, Runge-Kutta schemes optimize the stability region, while holding dispersion and dissipation fixed. It is found [159] that maximizing dispersion minimizes dissipation, and *vice versa*. LF, as shown below, does not add dissipation error, but only dispersion.
- The parameter τ has little influence in the dispersion and dissipation error of the physical mode, considered here. However, it bears noting that the dissipation of the spurious modes is strongly affected by the τ parameter, as demonstrated in the previous sections, and also in the stability condition [64, 71], as analyzed in Section 4.2.2.

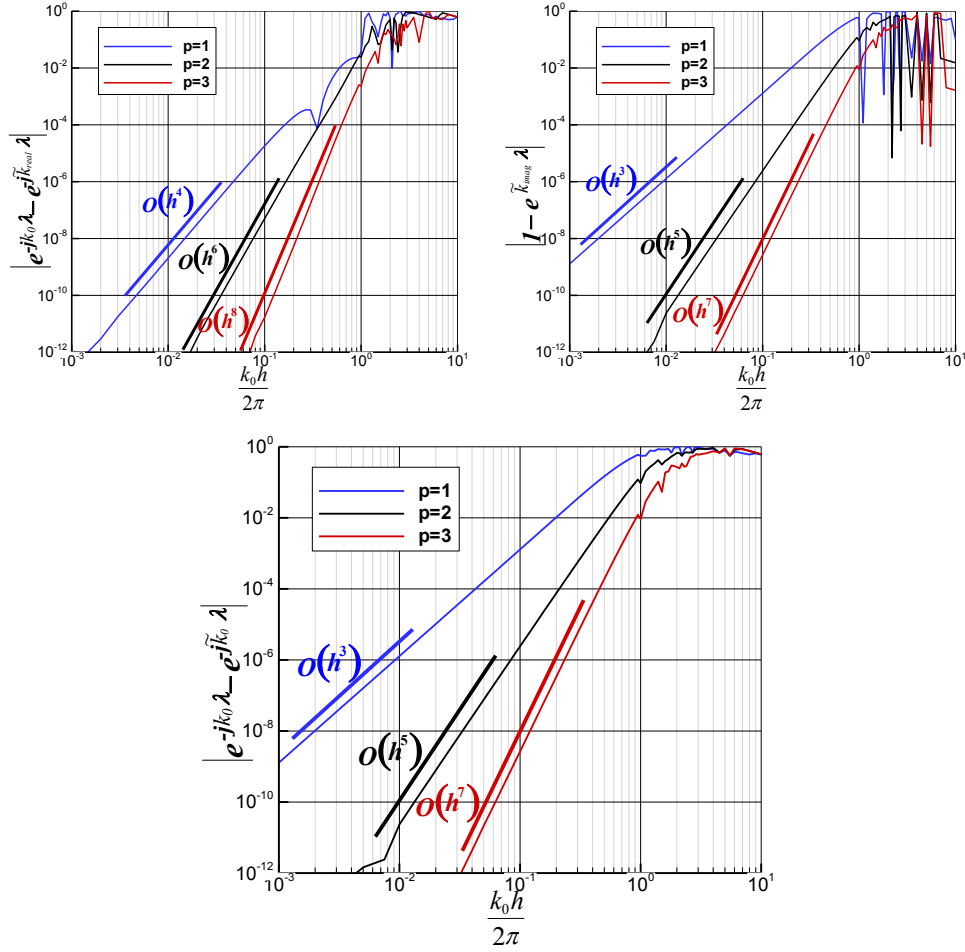


FIGURE 4.11: Convergence of the dispersion (upper left), dissipation (upper right) and global (lower) errors of the physical mode for the DG operator with upwind flux. The thicker line plots the function $O(h^n)$ corresponding to each case.

We now analyze the fully discrete LFDG scheme, and compare it with the previous results of the spatial DG operator alone, and with the well-known FDTD method. Since the influence of the τ parameter on the accuracy of the physical mode has been seen to be negligible for the semi-discrete case, we have fixed a value of $\tau = 0.1$. This value has been chosen as a trade-off between stability and spurious-mode reduction.

Results for RMS errors are shown in Figure 4.13 for different orders p , taking $\Delta t = 0.7\Delta t_{max}$. We have observed, from our experience that this choice avoids instabilities due to other numerical aspects. Figure 4.14 also shows results for different $\Delta t < \Delta t_{max}$ (for $p = 2$).

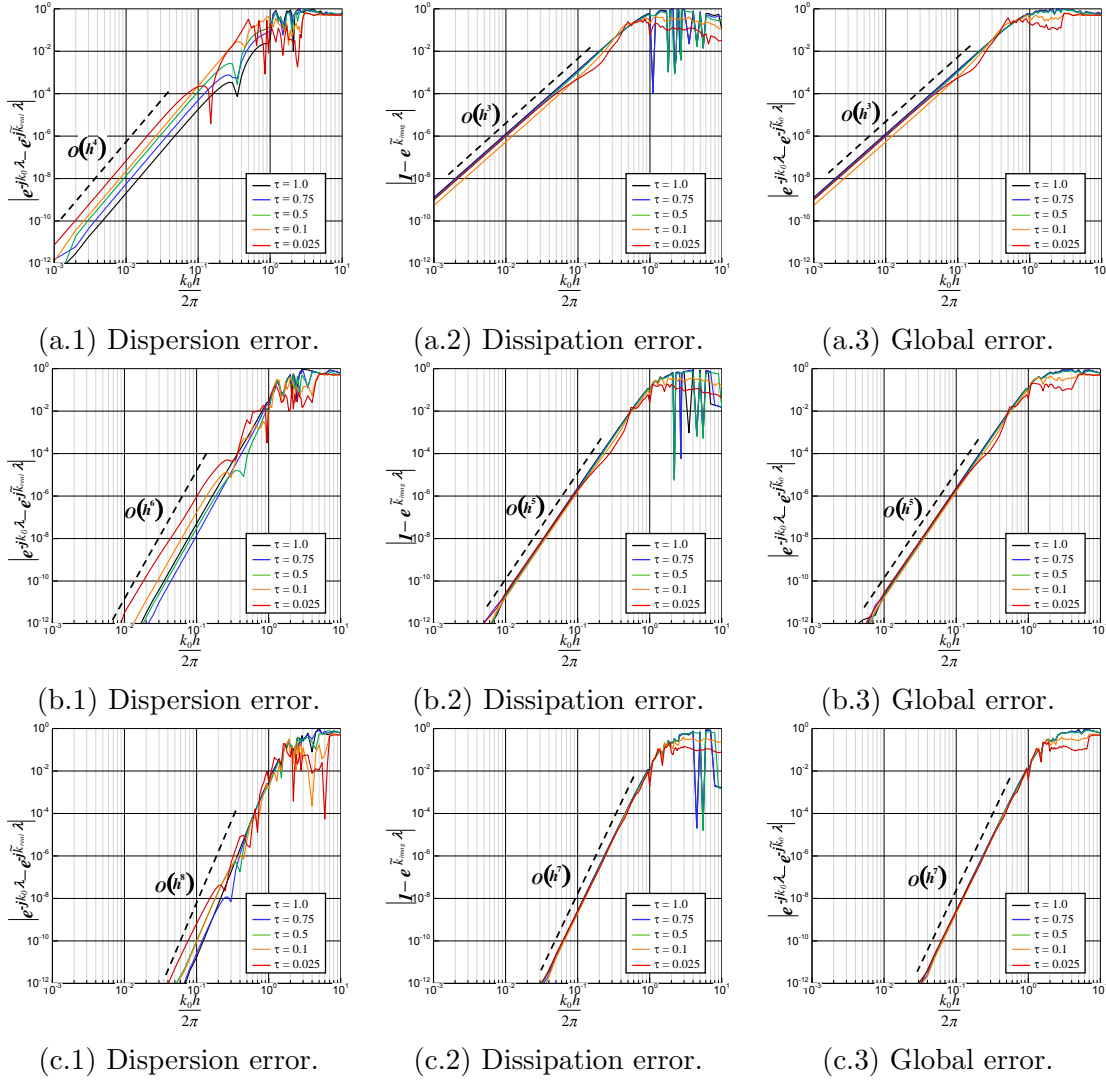


FIGURE 4.12: Convergence and influence of the τ parameter in the error of the DG operator for different p orders. (a) $p = 1$, (b) $p = 2$ and (c) $p = 3$. The black discontinuous line plots the function $O(h^n)$ corresponding to each case.

The expression to evaluate \tilde{k}_0 for the FDTD case is the very well-known numerical dispersion relation for this method, written below [157],

$$\tilde{k}_0 = \frac{2}{h} \arcsin \left(\frac{h}{c \Delta t} \sin \left(\frac{k_0 c \Delta t}{2} \right) \right) \quad (4.18)$$

and the stability condition

$$\Delta t_{max} = \frac{h}{c\sqrt{3}} \quad (4.19)$$

We can conclude from Figures 4.13 and 4.14:

- The high-order convergence property of the DG spatial operator is maintained up

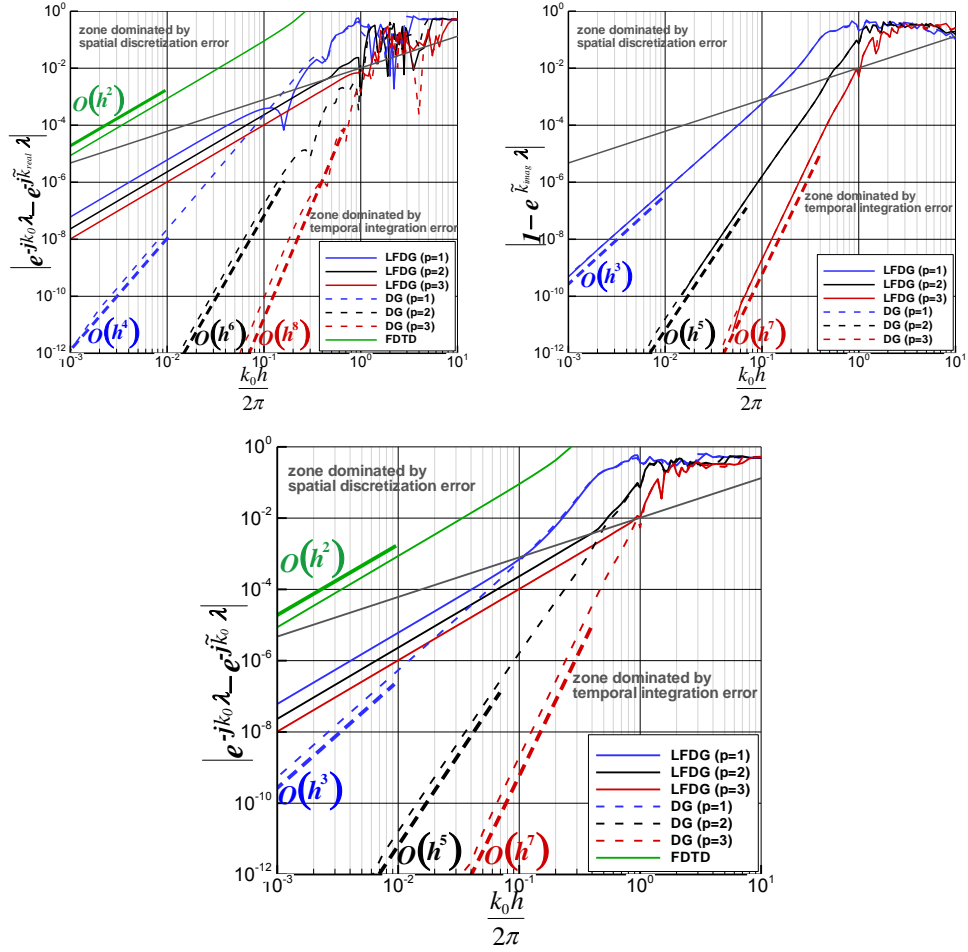


FIGURE 4.13: Convergence of the dispersion (upper left), dissipation (upper right) and global (lower) errors of the physical mode for the LFDG algorithm with $\tau = 0.1$ and $\Delta t = 0.7\Delta t_{max}$. Analogous curves for the DG operator and FDTD have been included for comparison. In the case of the dissipation error, FDTD curve has been omitted, since the error is zero, and notice that the LFDG and DG curves are superposed.

to an error limit where the convergence of the error becomes $O(h^2)$ dominated by the LF time-integration scheme (only 2^{nd} -order). This fact depends neither on the order of functions p , nor on Δt , and coincides with that found for the FDTD method. Higher-order Leap-Frog (LF_N) schemes have been proposed to improve this [68].

- Since LF is non-dissipative, only the dispersion error is affected. The dissipation error coincides with that of the semi-discrete case.
- The limit between the zones where the error is dominated by the spatial discretization and by the temporal integration methods, depends on Δt , as shown in Figure 4.14. This limit can be improved by reducing Δt , at the cost of increasing the computational cost.

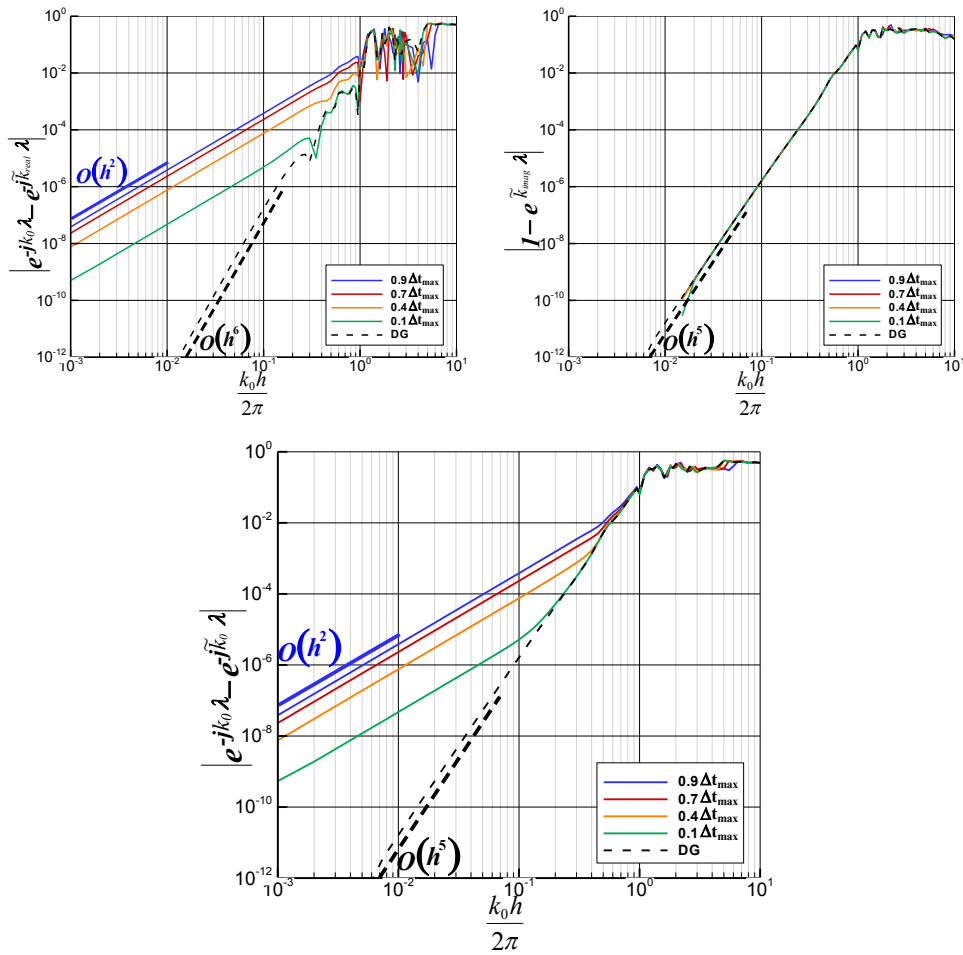


FIGURE 4.14: Influence of Δt in the dispersion (upper left), dissipation (upper right) and global (lower) errors of the LFDG algorithm with $\tau = 0.1$ and $p = 2$. Analogous curves for the DG operator have been included.

- The typical 10^{-2} accuracy value is in the zone dominated by the spatial discretization error for the LFDG method, for $p=1$, $p=2$ and $p=3$ and $\Delta t = 0.7\Delta t_{max}$ with resolutions ranging from $\sim \frac{\lambda}{4.5}$, $\sim \frac{\lambda}{1.9}$ and $\sim \frac{\lambda}{1.1}$, respectively. This characteristic is not expected to be fulfilled by higher orders that $p=3$. In FDTD a resolution of $\sim \frac{\lambda}{28.5}$ is required to reach a 10^{-2} accuracy⁴.

Notice that this analysis has been performed considering a plane wave traveling in a homogenous medium. The conclusions to any general problem should be extended with care. When we have geometrical singularities, as corners or vertices, the convergence rate considerably decreases. These regions shall be dealt with h-refinement techniques. It is important to note that, for these kinds of cases the temporal integration error

⁴Notice the resolution for FDTD is for the cubic spatial domain of Figure 4.3 meshed with one cell, and for LFDG the same domain is meshed into 24 tetrahedra. The influence of the resolution is taken into account in Section 4.5 to compare in terms of computational cost.

loses influence, and the spatial discretization of the fields determines the accuracy of the numerical method. The LFDG method becomes a very efficient method for these cases, if combined with a local time-stepping technique (see Section 3.5.2.3), to avoid the use of unnecessarily small time steps.

4.3.1 Numerical Experiment

A simple numerical experiment has been performed, in order to reproduce, with a real simulation, some results from the previous analysis. A region of $(0.6 \times 0.6 \times 12)$ m. has been meshed into $(3 \times 3 \times 60)$ cubes, each one equal to that used for the previous eigenvalue analysis (Fig. 4.3, with $\Delta = 0.2$ m.). A y-polarized plane wave, propagating along the z-axis, has been excited at the lower z-plane, by using perfect electric conductor at the y-boundaries, and perfect magnetic conductor at the x-boundaries (which support the plane wave propagation). Silver-Müller absorbing (impedance) boundary conditions have been taken at the z-boundaries.

Two probes separated by $L = 10$ m. along z, have been taken to estimate the error in the propagation of the y-component of the electric field ($e_0(t), e_L(t)$). The RMS dissipation error per wavelength has been computed in the frequency domain ($E_0(f), E_L(f)$) by

$$\left| 1 - \left[\frac{|E_L(f)|}{|E_0(f)|} \right]^{\frac{\lambda}{L}} \right| \quad (4.20)$$

where we have taken into account the multiplicative effect along the propagation path, in order to express it in terms of a per-wavelength error, and compare to Equation (4.17b). For the RMS dispersion error per wavelength, we have computed the numerical phase error, with respect to the analytical phase $(-\frac{2\pi L}{\lambda})$, and normalized by the wavelengths traveled by the wave $(\frac{L}{\lambda})$, to compare with Equation (4.17a). Figure 4.15 shows this comparison for two different Δt . A good agreement is found for errors above 10^{-7} . Errors below this level happen at very low frequency, and are due to truncation of the signals, and the presence of spurious modes (a further study of these has been performed in Sections 4.1 and 4.2.3).

4.4 Anisotropy of the Numerical Errors

In this section, we analyze the anisotropic behavior of the errors in both schemes, the semi-discrete DG operator and the fully discrete LFDG algorithm [P5]. A 2D analysis for the wave propagation problem appears in [47]. In this case, we follow the same strategy that used for the convergence analysis. Again, we have fixed a value of $\tau = 0.1$,

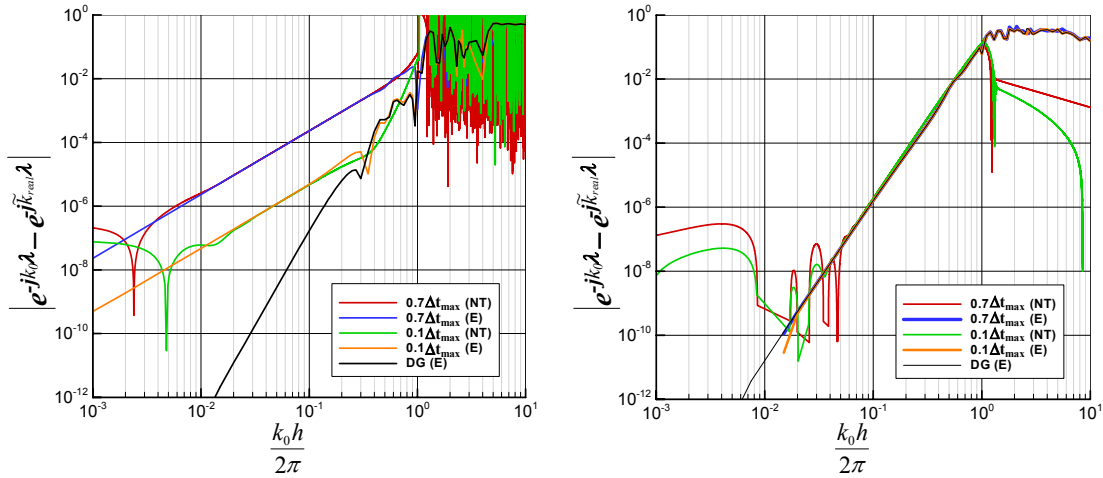


FIGURE 4.15: Convergence of the dispersion (left) and dissipation (right) errors of the LFDG algorithm computed with the numerical test (NT) and with the eigenvalue analysis (E). We have used in both cases $\tau = 0.1$, and $p = 2$. Analogous curves for the DG operator have been included for comparison.

and $\Delta t = 0.7\Delta t_{max}$ for LFDG. The anisotropic behavior of the error is analyzed by solving the eigenvalue problems for different \mathbf{k}_0 .

Figures 4.16, 4.17 and 4.18 show 2D plots of the anisotropic errors for different illumination angles (due to the symmetry of problems, $\theta = [0^\circ, 90^\circ]$ and $\phi = [0^\circ, 90^\circ]$ include all the possible illuminations) and basis orders $p = 1, 2, 3$, respectively. 3D representations of the normalized real part of the numerical eigenvalue, referred to as dispersion rate (notice that this magnitude is the inverse of the normalized numerical phase speed, which is an alternative magnitude represented in some works, [47, 157]) and dissipation rates have been included to show the shape of the anisotropy. In figure 4.19 has been plotted cuts in θ angle of the dispersion error for $\phi = 45^\circ$, comparing the DG operator and the LFDG algorithm for different orders p .

From the present analysis, we can derive the following conclusions:

- The anisotropy of the error, both dispersive and dissipative, is given by the spatial discretization. The LF temporal integration only introduces an offset in the dispersion error in all directions, and no dissipation error (as expected).
- For conciseness, plots for different values of h and p have been omitted, but we have observed, in general, that the shape of the anisotropy of the error (both dispersive and dissipative) only depends on the order of the basis functions (p), while the h -parameter mainly affects to the error amplitude.
- For the semi-discrete DG operator (as well as for LFDG algorithm if the error is dominated by the spatial discretization), the numerical phase speed is higher than

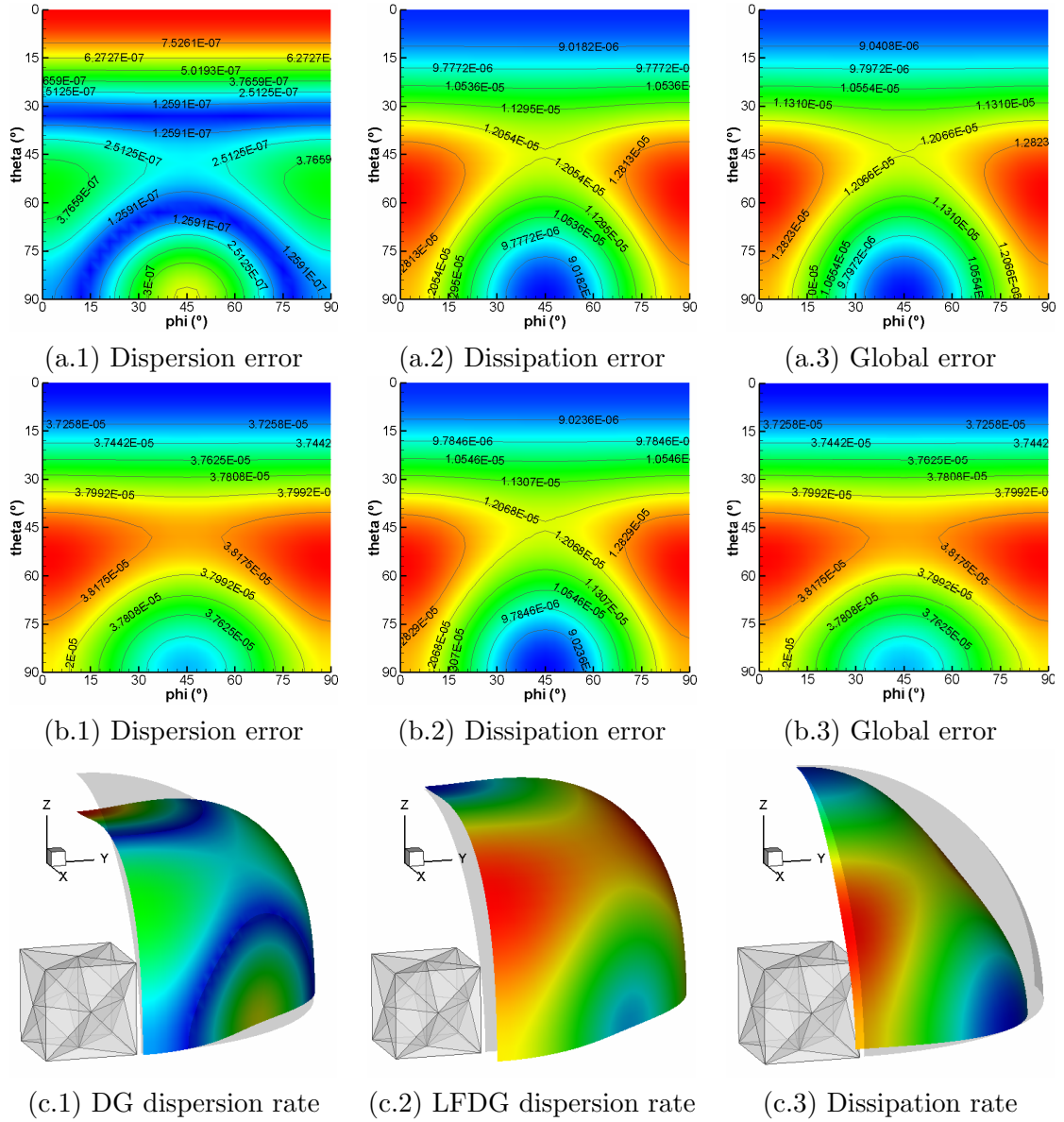


FIGURE 4.16: Anisotropy of the error for $\tau = 0.1$, $p = 1$ and $h = 0.025$. (a) DG semi-discrete scheme, (b) LFDG scheme with $\Delta t = 0.7\Delta t_{max}$ (c) 3D representation. The error has been amplified in order to represent the shape of the anisotropy. The analytical solution has been represented in grey (sphere of radius 1).

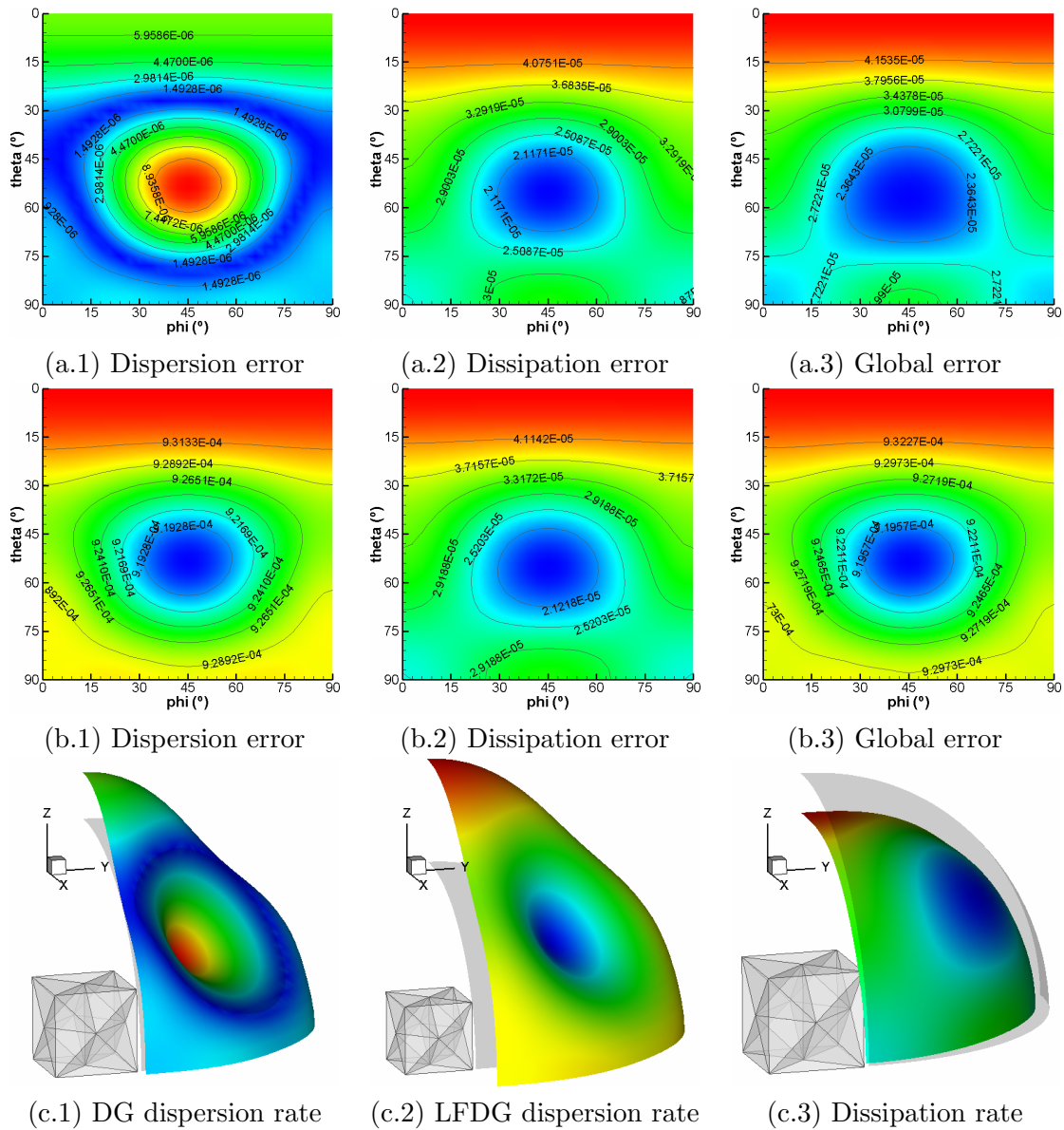


FIGURE 4.17: Anisotropy of the error for $\tau = 0.1$, $p = 2$ and $h = 0.2$. (a) DG semi-discrete scheme, (b) LFDG scheme with $\Delta t = 0.7\Delta t_{max}$ (c) 3D representation. The error has been amplified in order to represent the shape of the anisotropy. The analytical solution has been represented in grey (sphere of radius 1).

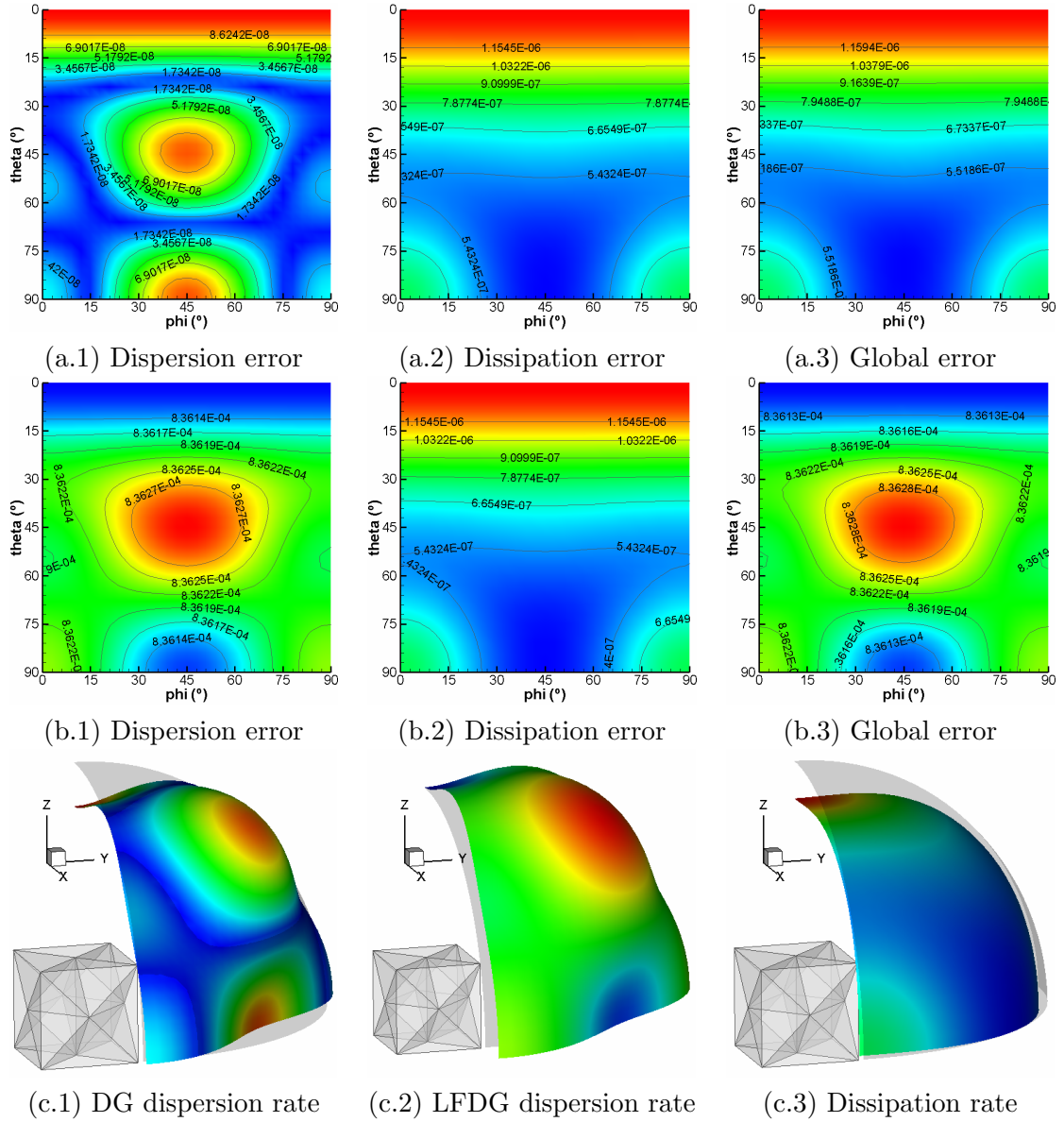
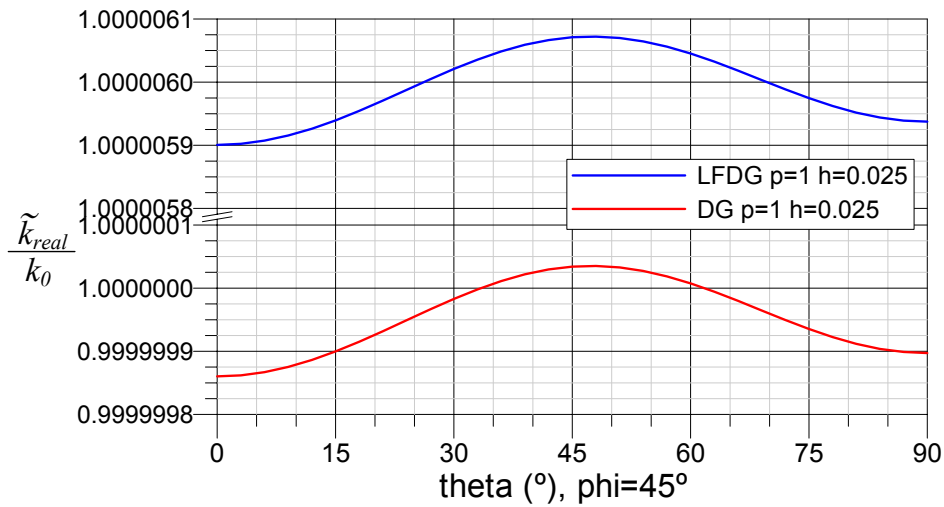
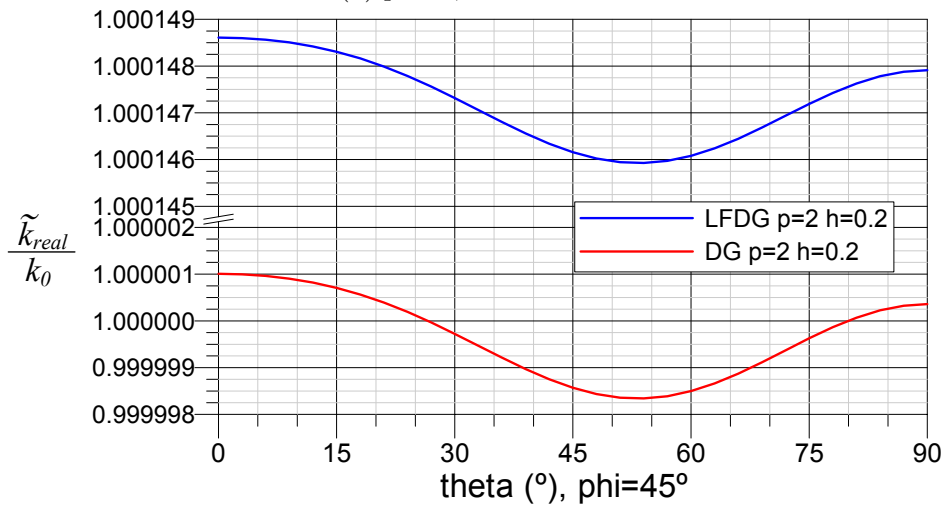


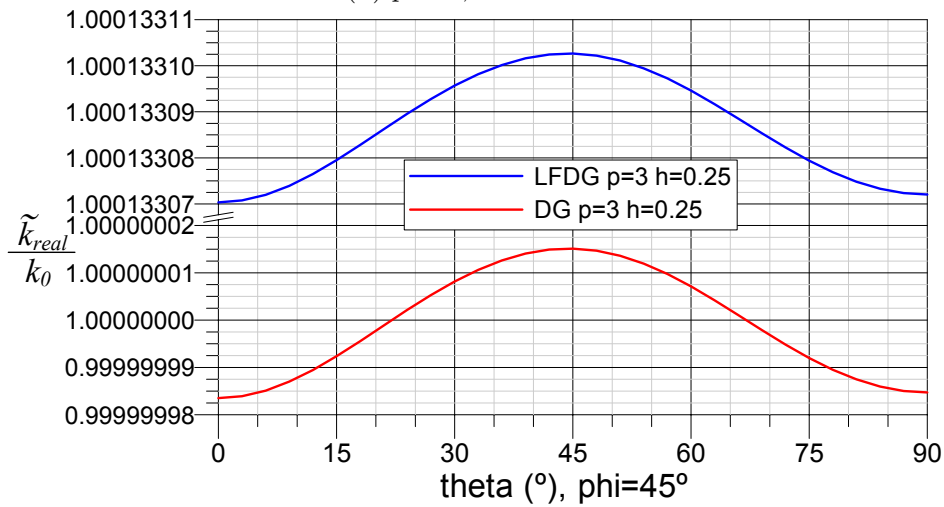
FIGURE 4.18: Anisotropy of the error for $\tau = 0.1$, $p = 3$ and $h = 0.25$. (a) DG semi-discrete scheme, (b) LFDG scheme with $\Delta t = 0.7\Delta t_{max}$ (c) 3D representation. The error has been amplified in order to represent the shape of the anisotropy. The analytical solution has been represented in grey (sphere of radius 1).



(a) $p = 1, h = 0.025$.



(b) $p = 2, h = 0.02$.



(c) $p = 3, h = 0.25$.

FIGURE 4.19: Cuts of the dispersion error comparing the DG operator and the LFDG algorithm for different orders p and h . The Y axes have been broken in all cases, maintaining the same spacing, in order to show the offset in the dispersion error.

1.0 for some directions, and lower for some others. That implies that there are dispersion-free propagation directions.

- For real cases, the natural inhomogeneity of the unstructured mesh will result in a general reduction of the error anisotropy. It bears noting, that this reduction does not occur for methods like classical FDTD, where the use of structured meshes makes systematic this anisotropy.

4.5 Computational Cost vs. Accuracy Analysis

The differences in accuracy between LFDG and FDTD (apparently high from Figure 4.13) should be analyzed with both methods under fair comparison conditions. In this section, we study the computational cost vs. accuracy, in order to draw an effective application of the proposed scheme in real problems, and explore the limitations and the efficiency of the method [P5]. The main trade-off involves the order of the basis functions p , the mesh resolution h , and accuracy, with the aim of minimizing the computational cost. We must take into account that:

- Increasing p improves accuracy, but requires shorter Δt for stability, and the computational cost per element is higher.
- Decreasing h improves accuracy, but requires shorter Δt for stability for smaller elements, and the number of elements increases.

To compare the different configurations of the method, a computational cost per λ^3 and picosecond (psec) has been defined. Firstly, we can establish that the computational cost for one element of a DG scheme is proportional to the square of the number of basis functions Q in that element,

$$C_{element} \propto Q^2 \quad (4.21)$$

Then, the cost for one time step per λ^3 , will be approximately the number of elements M per λ^3 multiplied by the cost per element,

$$\frac{C_{time\ step}}{\lambda^3} \approx \frac{M}{\lambda^3} C_{element} \quad (4.22)$$

Finally, we can define the following figure of merit (CC) to measure the global cost of the method, also including the effect of the Δt taken for stability,

$$CC = K \frac{M}{\lambda^3} Q^2 \frac{1}{\Delta t(\text{in psec.})} \quad (4.23)$$

TABLE 4.2: Results of the computational cost analysis for an accuracy of 10^{-2} per wavelength.

	Q	$\frac{\lambda}{h}$	$\frac{N_{element}}{\lambda^3}$	$\frac{N_{functions}}{\lambda^3}$	$c \Delta t 10^3$	$C_{element} \propto$	$\frac{C_{iter}}{\lambda^3} \propto$	CC	Gain $\left(\frac{CC(p-1)}{CC(p)}\right)$
FDTD	3	28.5	23149	69447	14.1	9	208341	4432	–
$p = 1$	12	4.5	2187	26244	17.6	144	314928	9660	–
$p = 2$	30	1.9	165	4950	85.3	900	148500	3270	2.95
$p = 3$	60	1.1	32	1920	97.1	3600	115200	2260	1.45

with K being a factor that has been considered equal to 1 for the FDTD case, and equal to 2 for the LFDG method (heuristically taken into account for the additional LFDG terms). This simple estimation is based on the fact that FDTD can be seen as a kind of FVTD method, which in turn is equivalent to a $p = 0$ LFDG, where the elements are cubes instead of tetrahedra [29] (we will not consider here specific architecture-based computer-optimized FDTD codes that might render $K < 1$).

The CC magnitude has been computed for the results of the convergence analysis of Figure 4.13, and shown in Figure 4.20, where CC is on the X-axis and, accuracy is on the Y-axis, on the upper side of the plot, and the resolution of the mesh, h , on the lower side.

The numerical values of CC , for the 10^{-2} accuracy case, appear in Table 4.2. As expected, for higher-orders p , the size of the elements to reach this accuracy ($\frac{\lambda}{h}$) can be increased, and larger Δt are allowable. Thus, the overall computational cost decreases with higher-order p . However, if we require higher accuracies ($< 10^{-3}$), this is no longer true, as seen in Figure 4.20, because the global error is dominated by the 2^{nd} -order temporal integration method, and the high-order convergence behavior is lost. The same reasoning explains that the gain for using $p = 3$ instead of $p = 2$ is not as high as the gain from $p = 1$ to $p = 2$. We conclude that orders $p > 3$ are not efficient in practical problems in the LFDG algorithm. This is a major limitation of the method, which prevents us from taking full advantage of p refinement techniques. On the other hand, the method has a comparable computational cost to FDTD for practical applications (from the plane-wave analysis standpoint), but preserving most of the advantages of finite-element methods (e.g. the conformal meshing or h-refinement in regions with strong spatial variations of the fields, where time-integration errors are negligible).

We can summarize the results given in Figure 4.20 and Table 4.2 as:

- The computational cost of the LFDG method is of the same order of magnitude as the traditional FDTD method. Therefore, it is expected that LFDG has all the advantages of finite-element methods as a similar computational cost of the FDTD method.

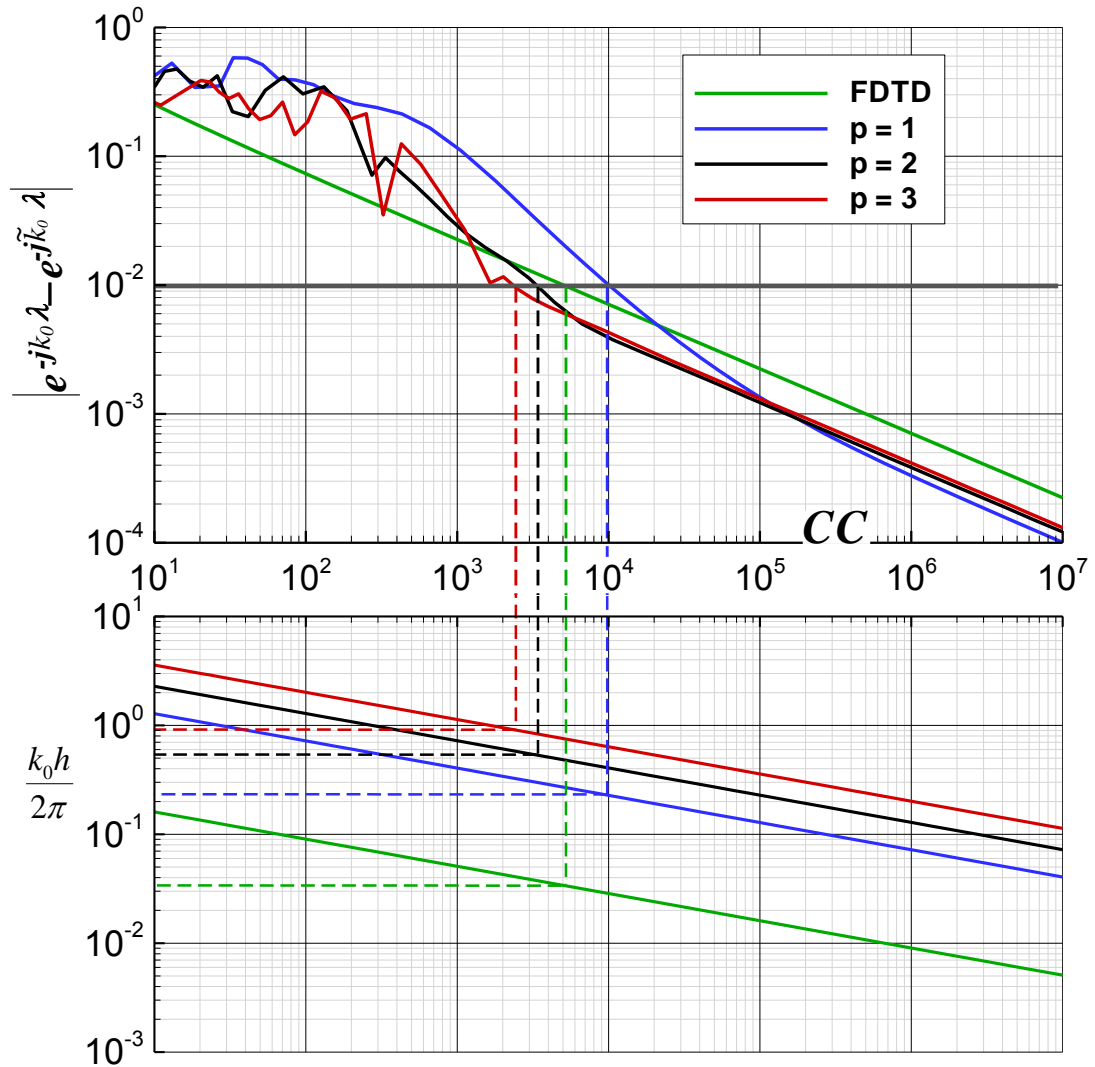


FIGURE 4.20: Computational cost of the LFDG algorithm for $\tau = 0.1$, $\Delta t = 0.7\Delta t_{max}$ and different order of the basis functions p . CC is on the X-axis and, accuracy is on the Y-axis, on the upper side of the plot, and the resolution of the mesh, h , on the lower side. A similar curve of the FDTD method has been included for comparison.

- Due to the limitations of using a 2^{nd} -order accurate time-integration scheme, it will not be worthwhile to use basis functions of order p higher than 3.
- For the typical accuracy required in practical and real electromagnetic problems, from 10^{-2} to 10^{-3} global error per wavelength, LFDG method is an efficient algorithm. For higher accuracies, higher-order time-integration methods are required to take greater advantage of the high-order convergence property of the DG operator.

The information shown in this section is valuable for the setup of real simulations, since it allows us to devise *a priori* a simple hp-refinement strategy. Figure 4.20 enables us to choose the most efficient element size h (in terms of computational cost), establishing a target accuracy. Once the mesh has been generated, Figure 4.20 again enables us to choose the appropriate p order in each element, depending on its size and required accuracy.

4.6 Summary

In this chapter, the topic of spurious mode reduction was revisited, and it was found that they can be minimized by means of penalized fluxes. The attenuation on the spurious modes appearing in DGTD is a remarkable difference with respect to the continuous formulation of FEMTD, and does not depend on the kind of basis-functions used by the scheme, making both the vector and scalar, spurious-free schemes for penalized fluxes.

Next, a semi-analytical eigenvalue analysis was used to study the convergence of the DG semi-discrete scheme, comparing it with the fully discrete LFDG method. The semi-discrete DG method with penalized flux was found to exhibit a high-order convergence behavior, with a dissipative error increasing with the basis order p , more rapidly than the dispersive one. When it is combined with the 2^{nd} order LF scheme, dispersion (not dissipation) is added, and corruption of the high-order convergence behavior occurs. The anisotropy of the semi-discrete DG and the LFDG scheme was also analyzed. A numerical plane-wave propagation experiment was employed to corroborate the results found with the eigenvalue approach, and illustrate the appearance of other numerical artifacts.

The accuracy limits and the computational cost of the LFDG method were explored, providing efficient criteria to tune the simulation parameters. It was shown that, for the typical accuracies required in practical problems, the LFDG method is efficient for orders $p \leq 3$. Higher accuracies could be achieved for $p > 3$ if combined with higher-order time-integration methods. It was also shown that, even for the simple plane-wave propagation, the computational costs of the LFDG method are in the same order of magnitude of the traditional FDTD method, with similar accuracy. This makes the LFDG method an especially attractive alternative to FDTD for realistic problems, thanks to its superior accuracy when dealing with curved objects, and to the adaptability of the unstructured meshes.

Chapter 5

Application and Validation

The LFDG method, presented in the previous chapters, has been implemented from scratch into a parallel computer code further described in Appendix A. The solver can handle different electromagnetic sources (waveguide ports, plane waves, etc.), isotropic and anisotropic materials, PEC, PMC, and PML boundary conditions, etc..

In this chapter, this LFDG solver is validated with several electromagnetic problems. Some of the results are compared with measurements, and some others with results found with other computational methods. The problems were chosen to test the capabilities of the method from different viewpoints:

- Microwave filters, which are ideal to show the robustness, accuracy, and stability of the method due to their strong resonant behavior.
- Antenna problems considering different excitations, to show the versatility and efficiency of the method.
- Radar cross-section of low-observable (LO) targets, to show the accuracy of the approach.
- Response of electrically medium and large-structures under high-intensity radiated field (HIRF) conditions, including a complete aircraft simulation, to prove the efficiency, scalability, and robustness of the method.
- Anisotropic materials.

TABLE 5.1: Number of elements (M) for each set of basis functions for the DMCWF. GxRy stand for x order for the gradient space, y order for the rotational space

	G1R1	G1R2	G2R2	G2R3	G3R3	Total
M	38988	2258	804	2734	15102	59886
dof	935712	90320	48240	246600	1927320	3248192

TABLE 5.2: Local time-stepping level distribution for the DMCWF.

	L1	L2	L3	L4
M	7	13101	22556	24222
Δt (psg)	$6.96 \cdot 10^{-3}$	$20.88 \cdot 10^{-3}$	$62.64 \cdot 10^{-3}$	$187.92 \cdot 10^{-3}$

5.1 Microwave Filters

Waveguide filters are especially challenging problems for TD techniques traditionally solved by methods in frequency domain, such as finite-element methods, integral-equation methods, or analytical methods (like mode matching). Due to the strong resonances that these structures present, two main features are required to deal with them in TD. One is the stability of the method, since very long simulations are necessary. The other is its accuracy, to maintain the coherence of the electromagnetic field throughout the structure. In this work, we use waveguide filters to provide a proof of the robustness and accuracy of the LFDG method.

5.1.1 PEC Microwave Filter

A dual-mode circular waveguide filter (DMCWF) is discussed in this section, which has been analyzed in detail in [160] and measurements are available. The filter is composed of a circular cavity resonator that includes the input and output slots of a DMCWF. Due to the symmetries of the structure, vertical perfect magnetic conductor-wall and horizontal perfect electric conductor-wall symmetry were considered in the numerical simulations, as is depicted in the simulation setup of the Figure 5.1.

It is important to note that a dense discretization of the slots is critical for accurate results. This forces to chose small time steps in these elements to satisfy stability condition. The use of curvilinear 2^{nd} -order tetrahedra permits to have high geometrical discretization accuracy in the cylindrical waveguide, without reducing element size. The basis functions used in each tetrahedron element have been selected depending on its size (see Section 4.5). Table 5.1 gives the number of elements for each set of basis functions, while Table 5.2 gives the number of elements and time step for each level of the LTS algorithm (see Section 3.5.2.3).

Three observables have been considered:

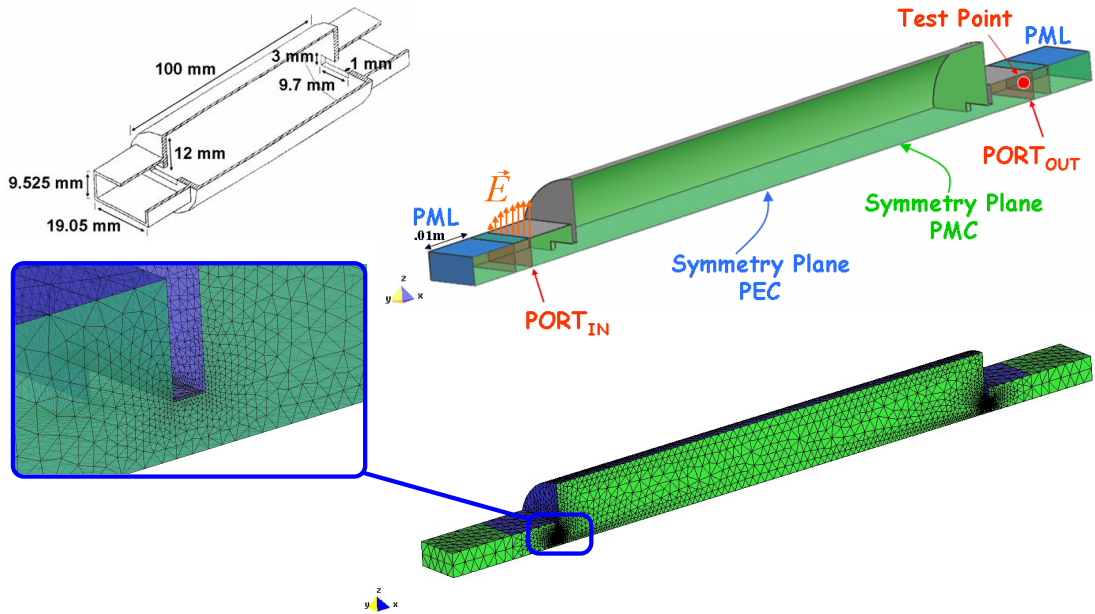


FIGURE 5.1: Dual-mode circular waveguide filter dimensions and problem setup (E_z results overimpose for both fluxes).

1. A field probe inside the rectangular waveguide to record the field evolution in time. Figure 5.2 shows different results for partially penalized ($\tau = 0.025$) and centered flux cases. In the case of centered flux, and due to the spurious modes, E_y and E_x are not null. No noticeable difference is appreciated between centered and penalized for E_z .
2. The filter response in terms of the S_{21} parameter. No remarkable differences were found between centered/upwind or LF/RK4 schemes. For instance, Figure 5.3 shows the comparison between measurement, centered, and partially penalized ($\tau = 0.025$) computed with LF and local time-stepping, with excellent agreement. No influence on the S_{21} parameter appears to exist due to spurious modes, reaching excellent agreement in all cases.
3. The evolution of the energy inside the structure. Figure 5.4 shows the curves for the two cases referred above. It can be seen that the energy needs considerable time to leave the filter, since the structure is very resonant. This leads to long physical simulation times to achieve accurate results, as listed in Table 5.3. For the centered flux, there is more energy inside the structure because of the spurious modes. However, they do not have influence to find good and accurate results for the S_{21} parameter, though some deviations are found in the computed near fields. This behavior, i. e. no effect of spurious modes in average magnitudes (far field, impedance, S parameters, etc.), has been systematically observed, not only in DG methods, but in general finite-element methods as well.

Table 5.3 summarizes the computational requirements of the different simulations performed. It should be noted that the 2nd-order LF scheme, combined with a 5-level LTS provide the algorithm about 8 times faster than do non-LTS schemes for this numerical case.

TABLE 5.3: Computational requirements of the different cases (for a 8 processors AMD OPTERON dual core 1.8GHz.). The computed physical time has been 35 nsec. Fluxes: C=centered, U=upwind, P=penalized with $\tau = 0.025$.

Flux	Scheme	Δt (³)	steps(¹)	memory	CPU(²)
C	RK4	24.5 - 24.5	1428572	2.0 GB	121.2 h
U	RK4	24.1 - 24.1	1452282	4.1 GB	213.3 h
C	LF	19.6 - 19.6	1785715	2.0 GB	63.5 h
P	LF	19.2 - 19.2	1822917	4.1 GB	118.5 h
C	LF,5L-LTS	6.96 - 187.9	186250	2.1 GB	8.9 h
P	LF,5L-LTS	6.81 - 183.9	190320	4.3 GB	15.5 h

(¹) Number of steps for the maximum Δt in the problem.

(³) Minimum-Maximum values in units of 10^{-15} sec.

5.1.2 Microwave Filter with Dielectric Material

Next, we have simulated a microwave filter with dielectric materials. The filter is composed of a single resonator based on a rectangular cavity loaded by a dielectric cylindrical puck. This structure has been reported in [161] and measurements are available. Again, the rectangular cavity is excited by two rectangular slots centered on opposite lateral faces. The resonator is chosen with a high permittivity ($\varepsilon_r = 29$) (see setup in Figure 5.5). The TE_{10} mode is excited in the input port, by impressing surface magnetic currents with its profile. The backwards propagated mode is absorbed by the PML, and the forward-propagated one is the incident wave used to excite the structure. The reflected wave required to evaluate the S_{21} parameter is computed by projecting the computed electric fields with the TE_{10} profile at the output port. The energy (Figure 5.6) takes a long time to leave the cavity due to the presence of the dielectric puck, which makes the structure very resonant. Excellent agreement in the S_{21} parameter between simulation and the measurements is found in Figure 5.7. Only the results for a partially penalized ($\tau = 0.025$) flux are shown (similar results can be found with the centered flux, since, as with the previous filter, spurious modes have no noticeable effect on the transmission coefficient).

The computed physical time, as appears in Table 5.4, was 180 nsec, which corresponds to 1980 cycles of the lowest frequency and 2880 of the highest frequency under analysis. 2nd-order LF with local time-stepping has been used with no instability problems. Due to the marked differences in the size of the elements, up to 6 levels in the LTS have been used, and the ratio between the shortest and largest time step was 729. Again,

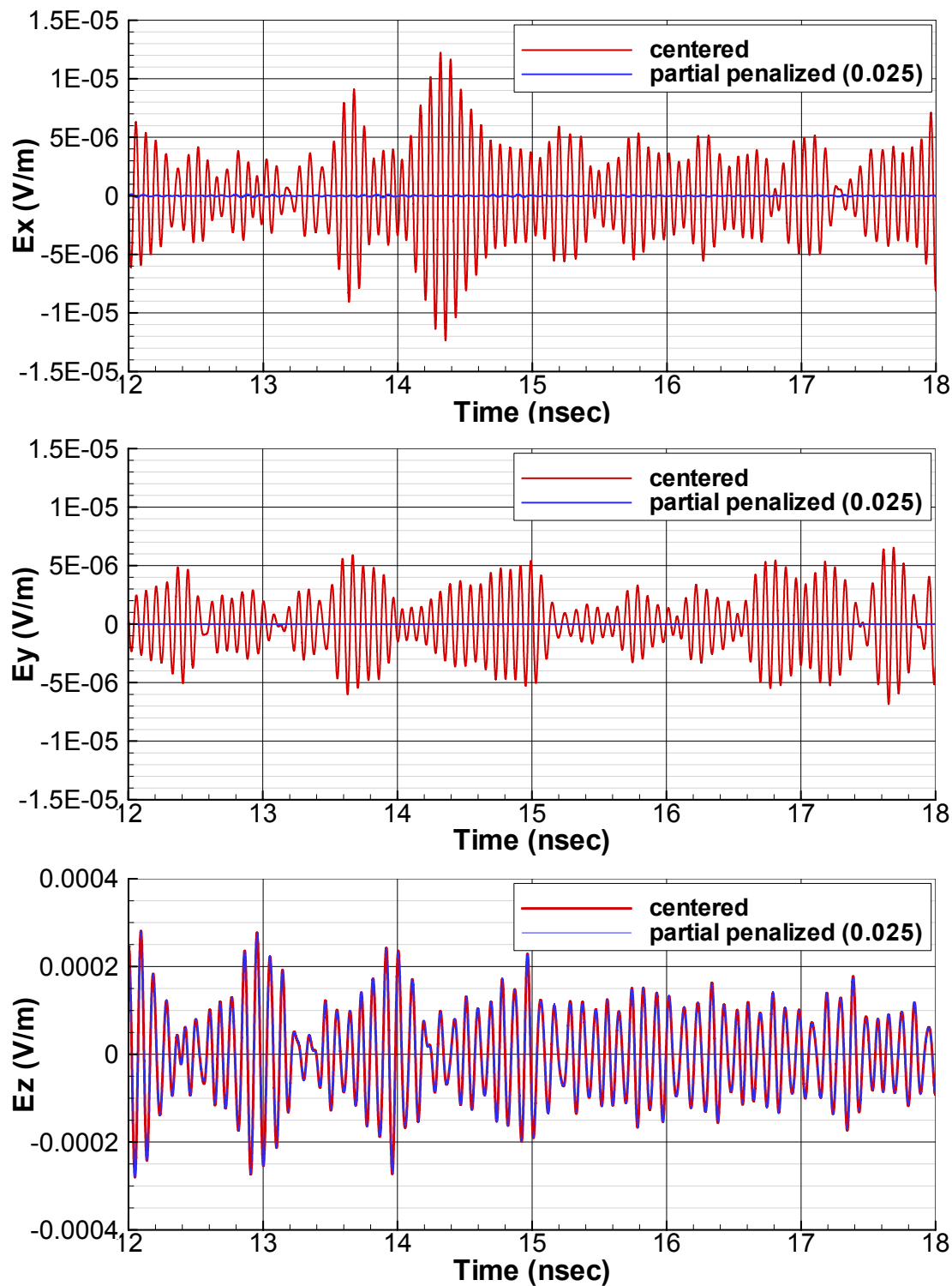


FIGURE 5.2: Dual-mode circular waveguide filter near fields computation.

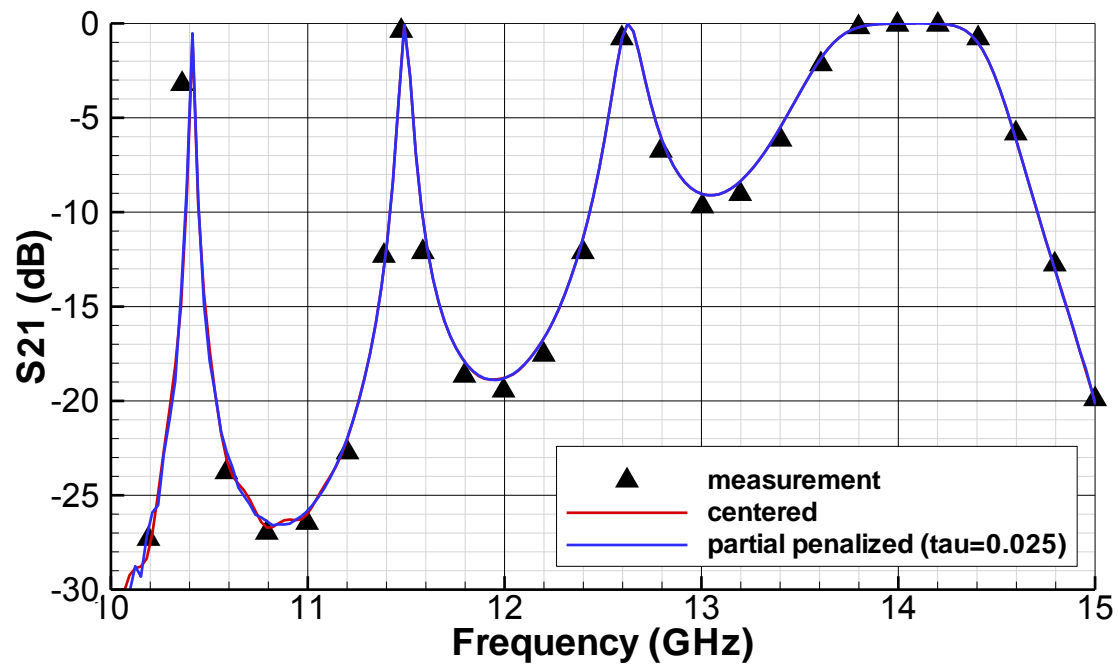


FIGURE 5.3: Dual-mode circular waveguide filter response. Measured and computed data comparison.

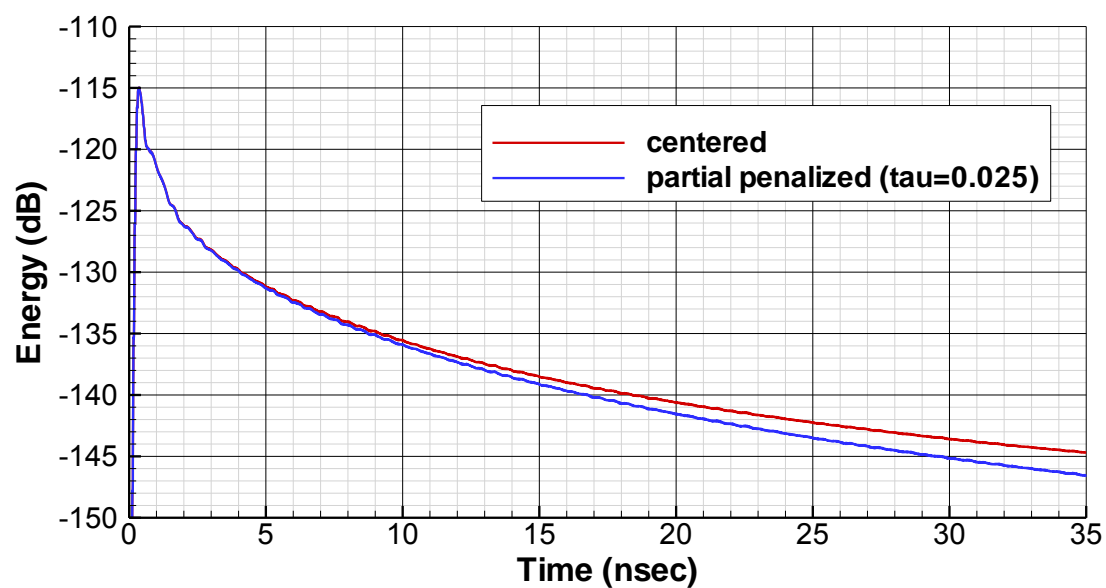


FIGURE 5.4: Evolution of the energy inside the dual-mode circular waveguide filter.

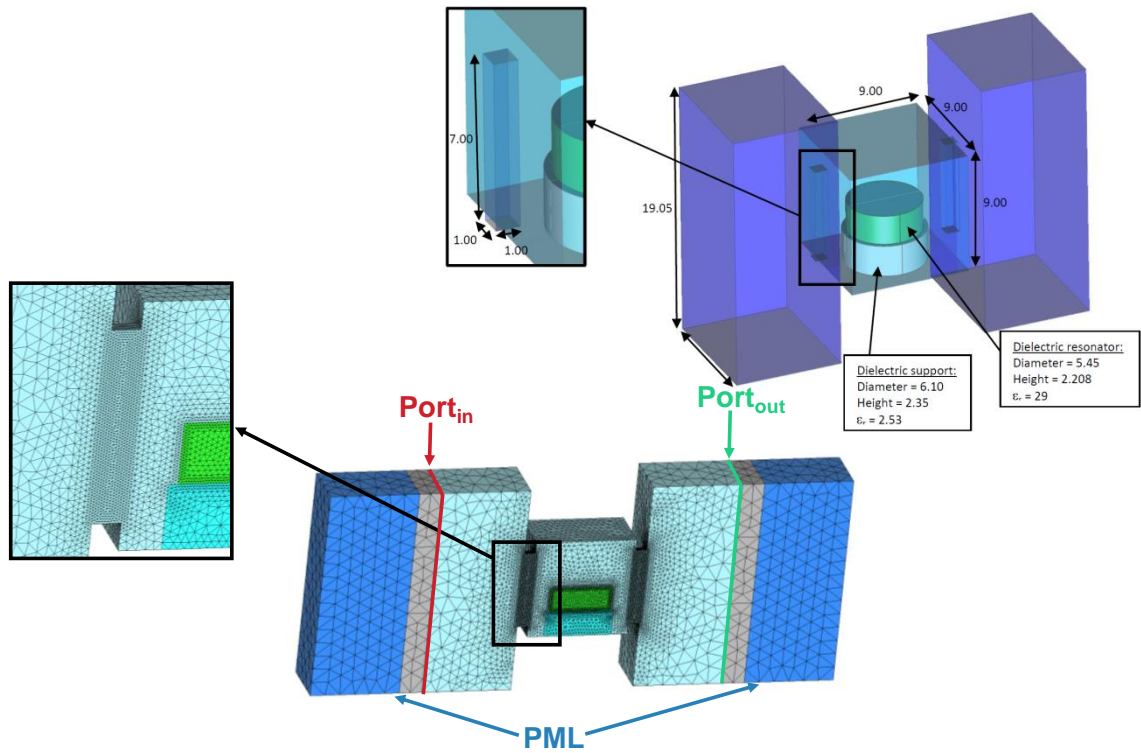


FIGURE 5.5: Single resonator composed of a rectangular cavity loaded by a dielectric cylindrical puck. Simulation setup.

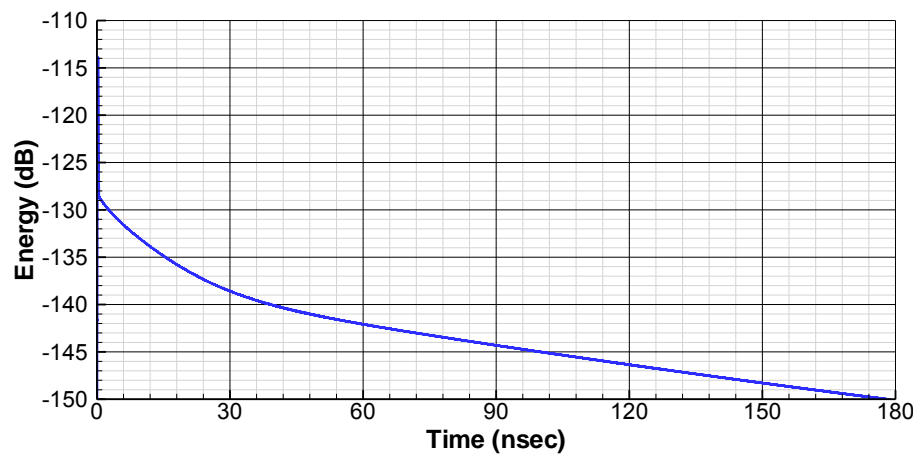


FIGURE 5.6: Evolution of the energy inside the single resonator filter.

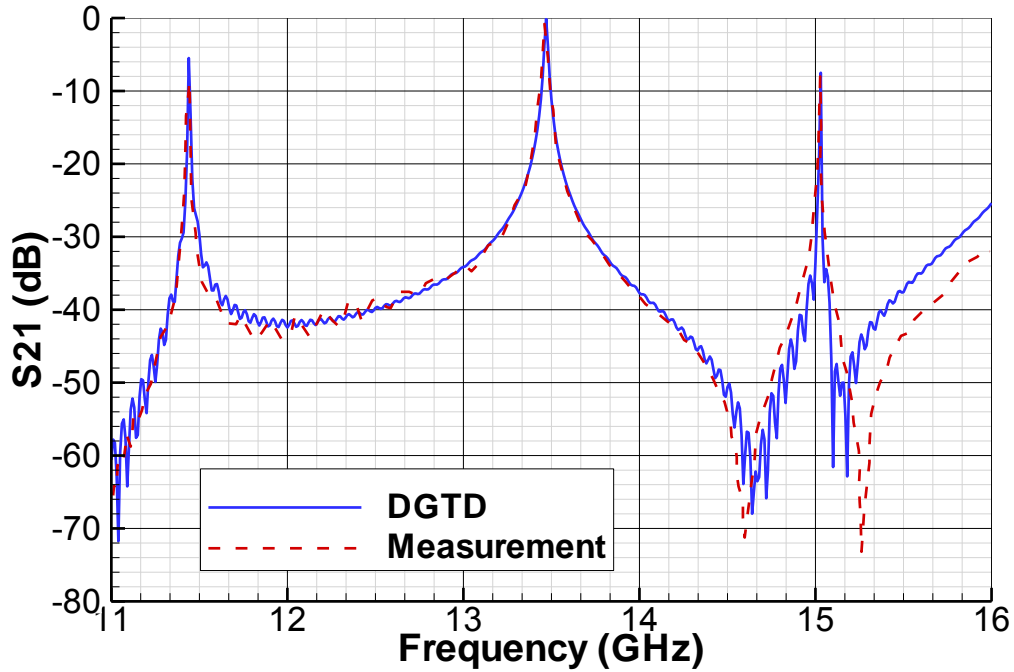


FIGURE 5.7: S_{21} response of the single resonator filter. Measured and computed data comparison.

depending on the size of the elements, a different order p of the basis functions has been chosen.

TABLE 5.4: Single resonator simulation description.

flux	partially penalized ($\tau = 0.025$)					
time scheme	2^{nd} -order LF (6-LTS)					
number of elements	362706					
number of d.o.f.	18505352					
computed physical time	180.0 nsec.					
LTS level	1	2	3	4	5	6
number of elements	2	26	390	177768	94036	90484
number of elements(%)	$5.5 \cdot 10^{-4}$	$7.2 \cdot 10^{-3}$	0.11	49.0	25.9	24.9
Δt (ps)	$6.0 \cdot 10^{-4}$	$1.8 \cdot 10^{-3}$	$5.4 \cdot 10^{-3}$	$1.6 \cdot 10^{-2}$	$4.8 \cdot 10^{-2}$	$1.5 \cdot 10^{-1}$
number of steps	297977292	99325764	33108588	11036196	3678732	1226244
order basis functions	$(\mathcal{G}_0, \mathcal{R}_1)$	$(\mathcal{G}_1, \mathcal{R}_1)$	$(\mathcal{G}_1, \mathcal{R}_2)$	$(\mathcal{G}_2, \mathcal{R}_2)$	$(\mathcal{G}_2, \mathcal{R}_3)$	$(\mathcal{G}_3, \mathcal{R}_3)$
number of elements	0	298113	9302	3535	27577	24177
number of elements(%)	0	82.2	2.6	1.0	7.6	6.7

5.2 Wideband Antennas

Wideband antennas are key components in many different applications such as short-range and indoor ultra-wideband communication systems, sensors for electronic countermeasure, or high-performance radar military systems. In these kinds of structures, an accurate modeling is critical in zones with small geometrical details, such as feeding

ports. Frequency-domain methods, such as MoM or FEM, are the usual choices for their capability of accurately modeling fine geometrical details. However, FD methods may become computationally inefficient for ultra-wideband analysis, since each frequency needs a complete simulation, typically involving a linear system resolution.

When DGTD is applied to antennas with small geometrical details, such as the feeding port, strong disparities among element size are found in the unstructured mesh, and, hence, in the local time steps required for stability. For this reason, the LFDG algorithm combined with the LTS strategy to deal with the high contrast in the element sizes becomes a competitive method, for the electromagnetic modeling of these kinds of structures.

Another essential aspect in the simulation of antennas by DGTD, is the numerical modeling of their feeding. In practice, most antennas are fed by coaxial, waveguide, or microstrip ports. The most simplified numerical model of the feeding port is known as delta-gap. This model usually permits the accurate estimation of the antenna radiation pattern, and in many cases also its input impedance, e.g. if the antenna is fed by a matching network [21]. However, it presents limitations [162, 163] for accurately predicting the S-parameters and the input impedance, when the actual geometry of the port has a strong influence on the antenna behavior.

The aim of this section is to discuss efficient strategies to apply LFDG algorithm for the accurate simulation of wideband antennas. We describe an alternative to the delta-gap feeding model, based on simple coaxial port, where both the excitation and the truncation of the port can be incorporated by making use of the flux terms at practically no cost. Several numerical examples serve to illustrate the accuracy of our approach. We demonstrate the affordability of DGTD methods for problems typically addressed by MoM, permitting us to simulate the complete antenna system including the structure where it is installed.

5.2.1 Antenna Feeding Models in DG

The implementation of transverse electric and magnetic (TEM) transmission lines in DG can be easily carried out by making use of the flux terms, both for excitation and for absorption. In case of a coaxial waveguide, the first TEM coaxial mode can be injected into the coaxial port in a weak manner through the flux terms by introducing surface electric and magnetic current-density sources of the form,

$$\mathbf{M}_s = \hat{\mathbf{n}}_p \times \mathbf{E}^{inc} \quad (5.1a)$$

$$\mathbf{J}_s = -\hat{\mathbf{n}}_p \times \mathbf{H}^{inc} \quad (5.1b)$$

where $\hat{\mathbf{n}}_p$ is the unit vector normal to the port along the direction of propagation of the injected TEM mode. This technique permits the total-field to be separated from the scattered-zone as in the usual plane-wave generation. The incident fields, expressed in cylindrical coordinates (ρ and ϕ), are

$$\mathbf{E}^{inc} = V^{inc}(t) \frac{1}{\ln(b/a)} \frac{1}{\rho} \hat{\boldsymbol{\rho}} \quad (5.2a)$$

$$\mathbf{H}^{inc} = V^{inc}(t) \frac{1}{\eta \ln(b/a)} \frac{1}{\rho} \hat{\boldsymbol{\phi}} \quad (5.2b)$$

being a and b the inner and outer radii of the concentric conductors, respectively, with the space between them filled with a dielectric of impedance $\eta = \sqrt{\frac{\mu}{\epsilon}}$. The time variation of the excitation signal is $V^{inc}(t)$.

The coaxial port, considered in single-mode, is accurately truncated with a Silver-Müller impedance boundary condition, making it unnecessary to use the PML. In addition, the SM-ABC can be located in the same surface as the port, avoiding the use of the scattered zone. The Silver-Müller condition, as shown in Section 3.1.2, is easily and costless applied by slightly modification of the flux terms at the port surface.

We can evaluate the antenna impedance and S_{11} parameter from the computation of total voltage V^{tot} from the fields at the port surface. Notice that the space and time dependencies are separated in Equations (5.2) and, once the TEM mode is projected on the test functions, all the source-terms remain unchanged over the simulation, except for a time-dependent common factor depending on the time instant.

A simple alternative to the coaxial port is the well-known delta-gap feed model, which is computationally less costly than the first one, and which can be accurate in some situations. Many implementations can be found in the literature [163]. In the present work, we choose to establish the given excitation voltage $V^{inc}(t)$ across the points of a surface gap (assumed to be PEC¹) through surface magnetic currents (coupled into the DG equations in the usual weak form). These are found from $\mathbf{E}^{inc} = V^{inc}(t) \frac{1}{\Delta} \hat{\mathbf{l}}_g$, where Δ is the gap width, and $\hat{\mathbf{l}}_g$ the unit vector following the gap orientation (see Figure 5.8), according to

$$\mathbf{M}_s = \hat{\mathbf{n}}_g \times \mathbf{E}^{inc} = V^{inc}(t) \frac{1}{\Delta} \left(\hat{\mathbf{n}}_g \times \hat{\mathbf{l}}_g \right) \quad (5.3)$$

where $\hat{\mathbf{n}}_g$ is the unit vector normal to the gap. Notice that the space and time dependencies are also separated in Equation (5.3). The PEC condition must be applied making used of the flux terms as described in Section 3.1.2.

To evaluate the antenna impedance, we need only to compute the current flowing through the delta-gap and divide it over the incident voltage.

¹Commonly referred as hard-source [162, 163], similar approach could be applied to the soft-source.

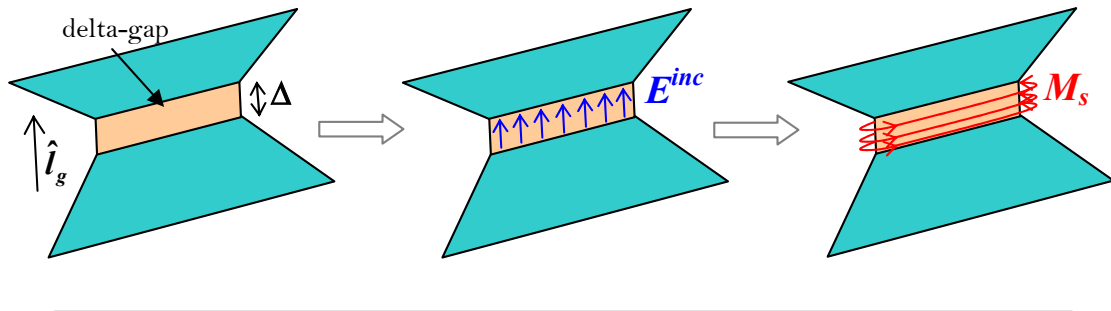


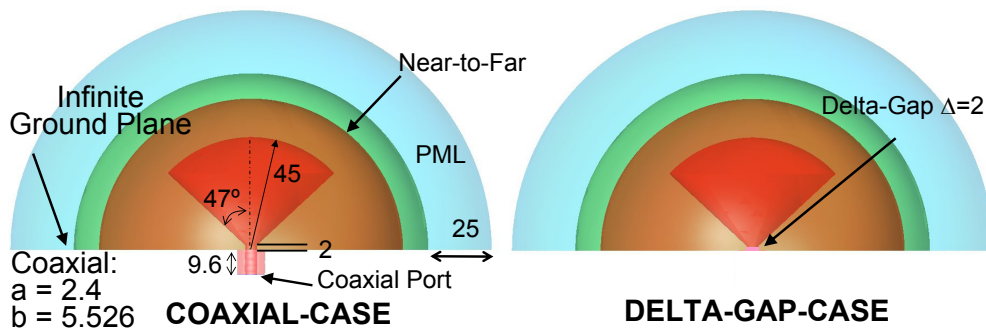
FIGURE 5.8: Delta-gap source model.

To illustrate this, we computed the input impedance and radiation patterns for some frequencies of a conical antenna over an infinite ground plane. Figure 5.9(a) shows the setup and dimensions of the two simulated cases, where the structure is excited by a coaxial port and delta-gap. Notice that the impedance is not calculated at the same physical point, since, between the radiating element and the coaxial port, there is a section of coaxial waveguide of 9.6 mm, not considered in the delta-gap case. Figure 5.9(b) compares the computed impedance, showing reasonable agreement at high frequency and differences at low frequency, as expected, since in the coaxial case the low-frequency impedance tends to open-circuit, while for the delta-gap it tends to short-circuit. Despite this, no significant differences are detectable in the radiation patterns of Figure 5.9(c), which demonstrates that the simplified delta-gap model can be used to predict the antenna radiation performance.

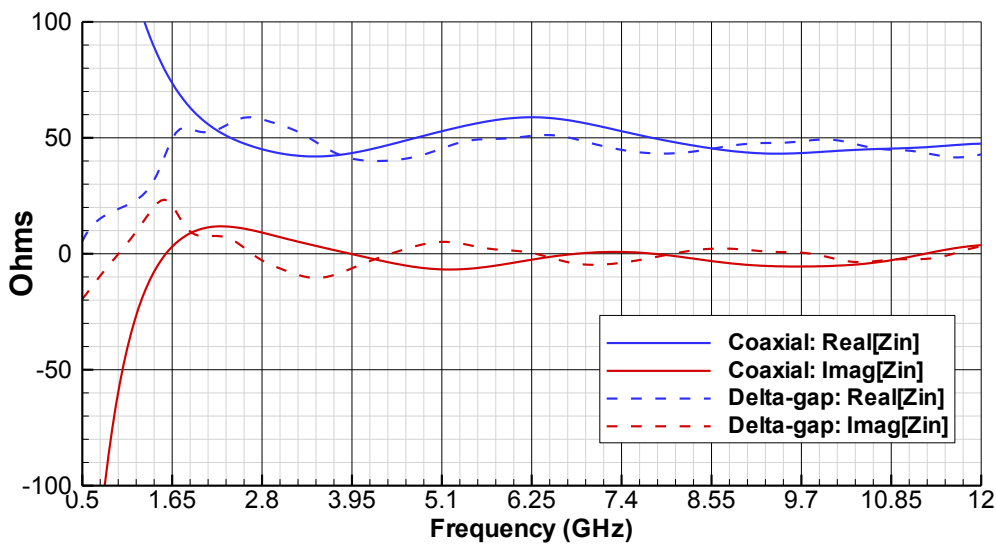
5.2.2 Wideband Bicone Antenna

A biconical antenna was manufactured and measured to be used as a field sensor for Low Level Swept Field (LLSF) measurements and it has also been simulated. The main objective of a LLSF test is to evaluate the transfer function between external and internal fields in a structure. This is a typical test in the aerospace EMC sector, to assess the shielding effectiveness inside the fuselage in the equipment bays. Key requirements for these antennas are: small size, since it must fit inside any kind of cavity, and wide frequency band. The biconical antenna shown in Figure 5.10 fulfills these requirements. It is formed by two cones, connected by two sections of coaxial waveguides. Figure 5.11 shows the geometry, and the simulation setup, where the high contrast of the elements sizes in the mesh is evidenced. Figure 5.12 and Table 5.5 display the distribution of Δt_{MAX} with the elements and the different LTS levels for this simulation case.

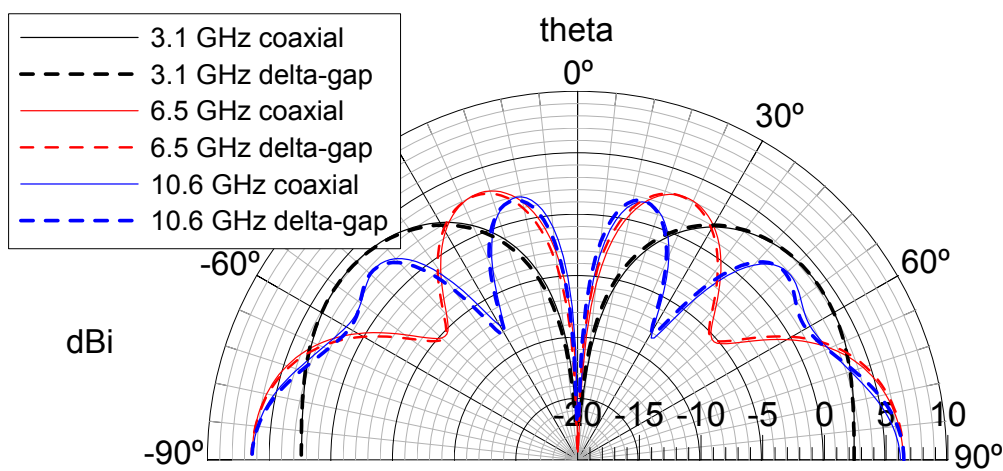
The following aspects have been considered in the antenna modeling:



(a) Simulation antenna setups. All dimensions are in millimeters.



(b) Input impedance results.



(c) Radiation patterns results.

FIGURE 5.9: Conical antenna simulation-case.



FIGURE 5.10: Wideband biconical antenna. Left: antenna assembly. Right: antenna with radome.

TABLE 5.5: Number of elements (M) in each local time-stepping level and interface for the biconical simulation case.

	L1	(L1/L2)	L2	(L2/L3)	L3	(L3/L4)	L4	(L4/L5)	L5
M	5	19	96	166	10338	5839	44728	35732	123093
M (%)	0.01	0.01	1.42	2.46	96.10	2.46	96.10	2.46	96.10
Δt (fs)	6.2	18.8	18.8	56.3	56.3	169.0	169.0	506.9	506.9

- The antenna is meshed with quadratic (2^{nd}) tetrahedra. This is a key point because the geometry has revolution symmetry, so that all the surfaces are curved (e.g. coaxial waveguide), and some of them doubly curved. Curvilinear cells significantly improve the spatial discretization, and consequently the accuracy of the simulation.
- The order p of basis functions to discretize the electric and magnetic fields has been chosen depending on the element size (see Section 4.5), in order to maintain uniform accuracy throughout the spatial domain with reasonable computational effort. We combined gradient spaces of reduced order $p - 1$, with rotational spaces of complete order p . The numbers of elements and dof per basis-function set are shown in Table 5.6.
- A conformal UPML technique (see Section 3.4 and 3.5.2.2) has been used to truncate the computation space. This technique is shown to be reflectionless for any angle of incidence, polarization, and frequency. The conformity is used to reduce the buffer space, and thus time and memory requirements of each simulation.

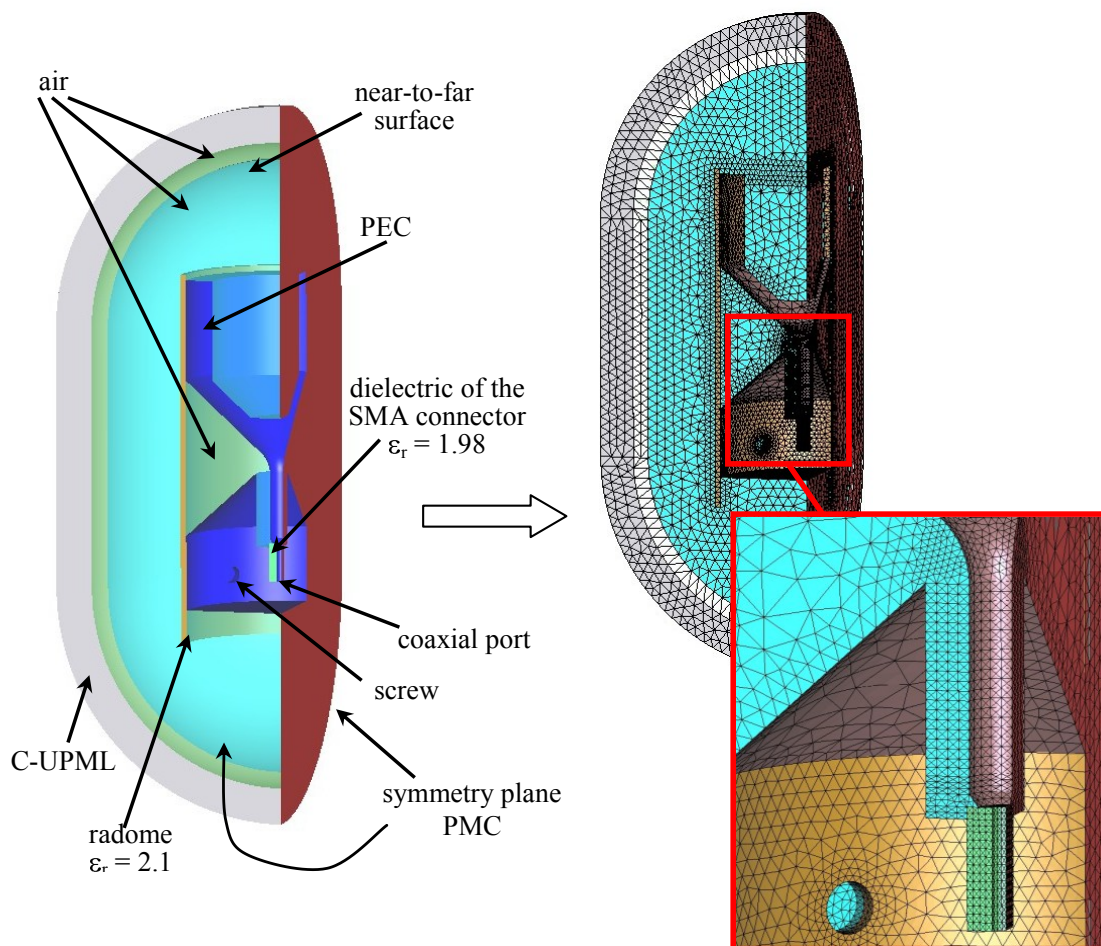


FIGURE 5.11: Simulation setup of the wideband bicone antenna.

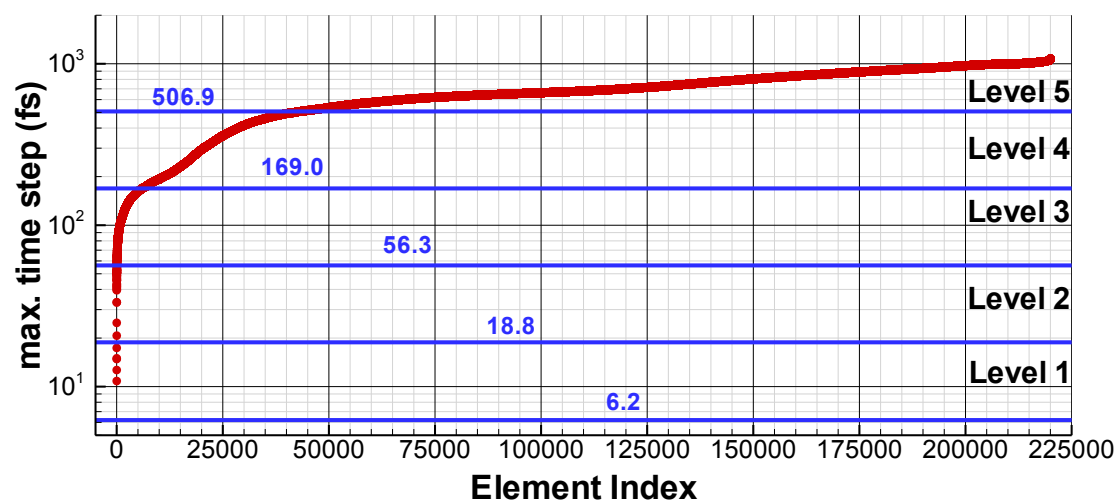


FIGURE 5.12: Distribution of the Δt_{MAX} with the elements.

- Due to the symmetry of the antenna, we have simulated one quarter of the antenna, considering perfect magnetic conductor boundary condition in the symmetry planes. This fact reduces by a factor of 4 the simulation times.

TABLE 5.6: Number of elements (M) for each set of basis functions for the biconical simulation case. GxRy stand for x order for the gradient space, y order for the curl

	space			Total
	G1R1	G1R2	G2R2	
M	177933	41906	177	220016
M (%)	80.87	19.05	0.08	100.00
dof	5260368	2392560	14220	7667148
dof (%)	68.61	31.21	0.18	100.00

The coaxial port is excited with a Gaussian pulse time signal, with 12 dB bandwidth at 20 GHz. The problem has been simulated until a physical time of 1.0 ns. Some screenshots of the simulation appear in Figure 5.13. The simulation time was 8.9 minutes for 20 processors AMD OPTERON dual core 1.8GHz. A reduction of 32 times in the CPU computational time is achieved by using the LTS algorithm, compared to the time required without employing LTS.

The computed and measured S_{11} and input impedances are shown in Figure 5.14, where excellent agreement between can be appreciated. The radiation patterns for different frequencies were evaluated and are shown in Figure 5.15.

5.2.3 Onboard Antenna Modeling

In this case, we will use the LFDG method to analyze the effect in the radiation performance of an antenna designed to work in the VHF and UHF bands, installed in the leading edge of an aircraft fin, in comparison to its behavior with the antenna installed on an infinite ground plane (Figure 5.16), assuming a delta-gap model for the feeding. In order to keep the antenna size small, these on-board aircraft antennas are typically fed by a matching network. Figure 5.17 shows the radiation pattern of the ground-plane configuration. As expected, the loading structure on the top of the radiating element causes some energy to be radiated in the cross-polar component, which slightly reduces the antenna gain in the co-polar component. This effect is more discernible in the UHF band.

The integration of this antenna in a leading edge of a generic aircraft fin is depicted in Figure 5.18. As a preliminary approach we only simulated a piece of metallic tail, as is depicted in the simulation setup of Figure 5.19. The antenna impedance, and radiation patterns for two frequencies (132 MHz (VHF) and 312 MHz (UHF)) are shown in Figures 5.20, 5.21, and 5.22. We find relatively low degradation of the adaptation parameter

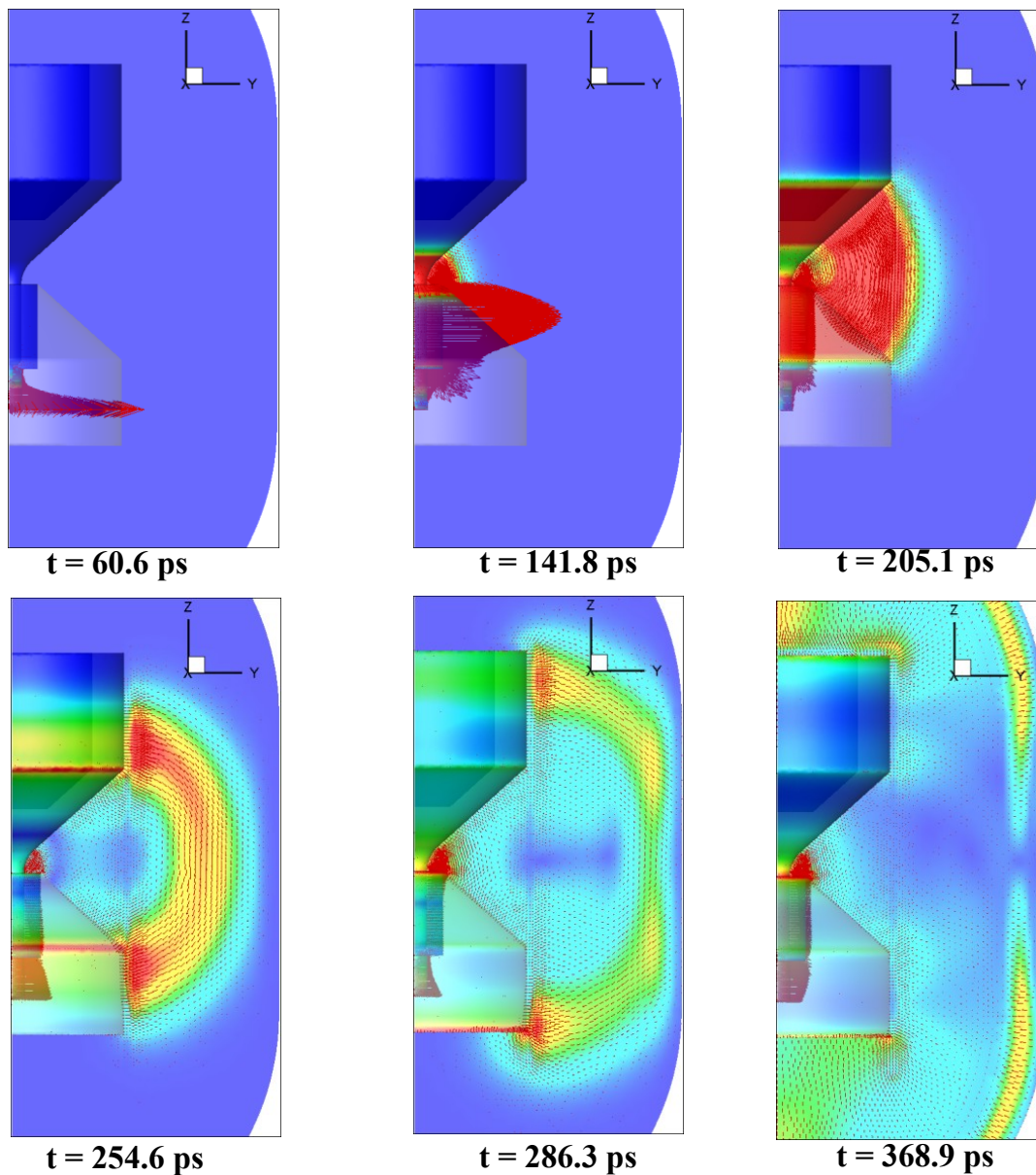


FIGURE 5.13: Screenshots of the simulation of the wideband biconical antenna.

compared to the infinite ground case. However, as expected, major differences, due to the masking effect of the fin, are found in the radiation patterns. For validation, we have included impedance results in Figures 5.20 computed with HFSS commercial software. A good agreement is found.

5.3 Estimation of the RCS of LO Targets

To validate and test the accuracy of the presented method, we find the radar cross-section of a typical LO target: the NASA almond. This geometry is a benchmark of the

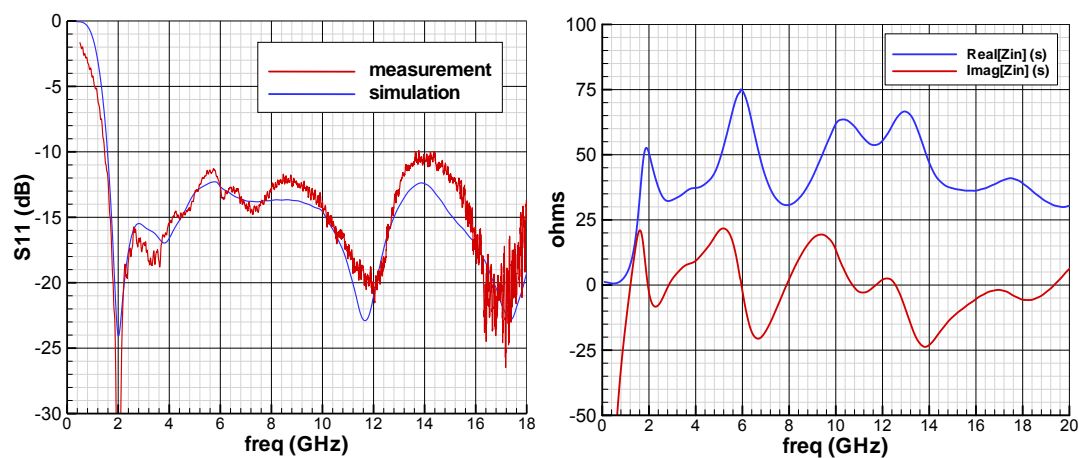


FIGURE 5.14: S_{11} and input impedance of the wideband bicone antenna. Measurement results of the S_{11} have been included for validation proposes.

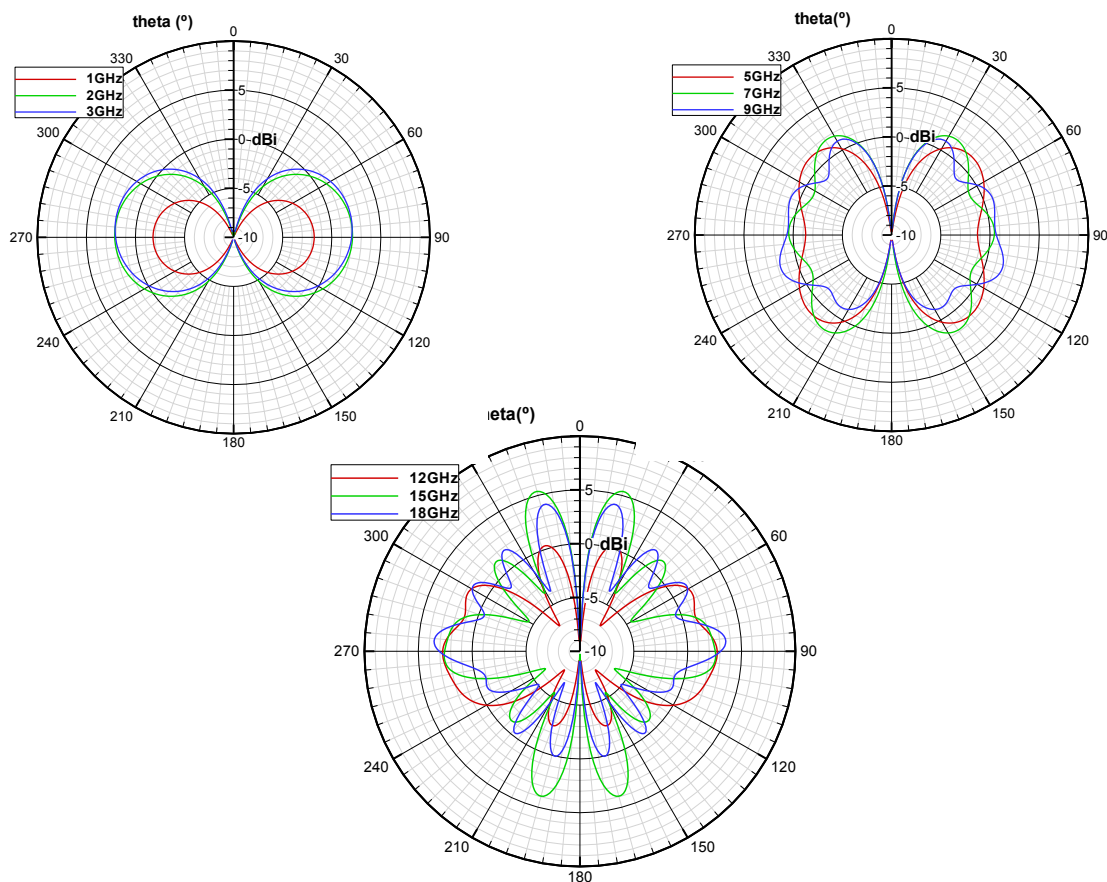


FIGURE 5.15: Radiation patterns of the wideband bicone antenna. The curves show antenna gain for different frequencies in dBi.

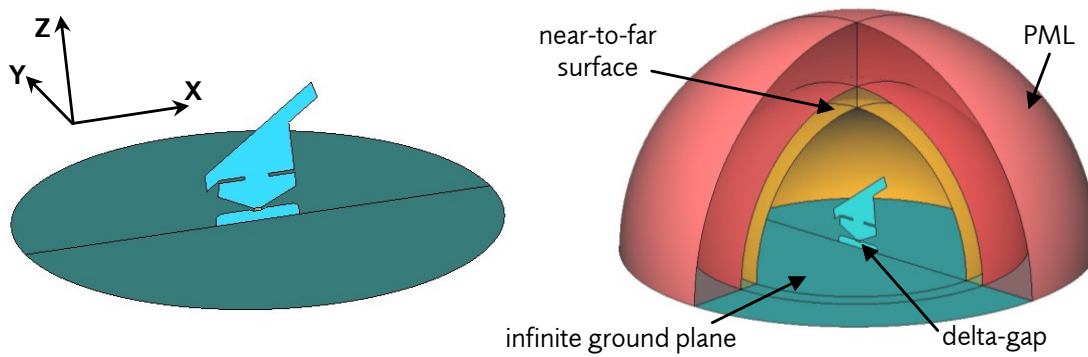


FIGURE 5.16: V/UHF antenna installed on an infinite ground plane.

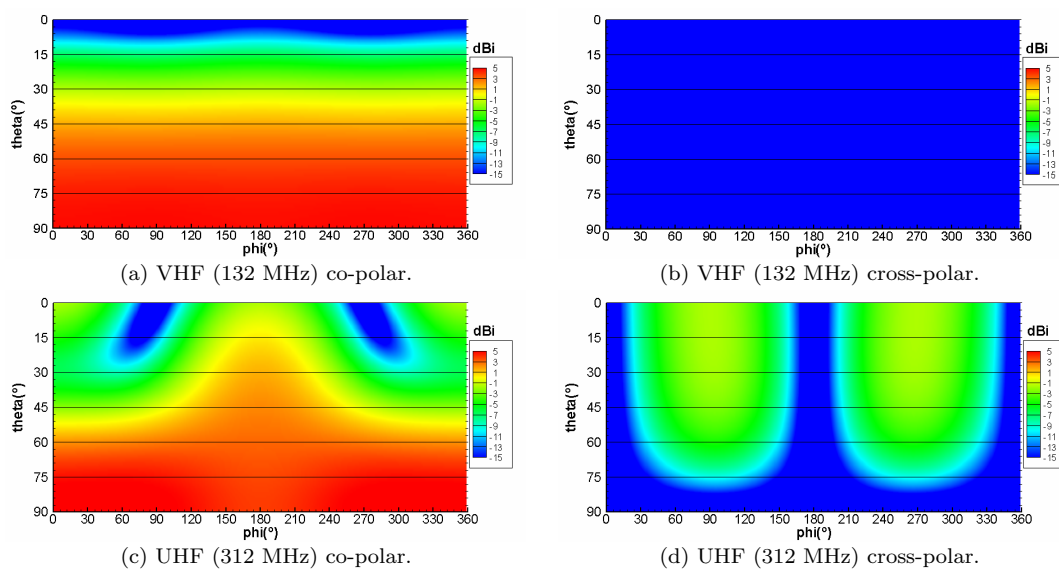


FIGURE 5.17: Theta vs. phi radiation patterns with the V/UHF antenna installed on an infinite ground plane.

Electromagnetic Code Consortium, for validation purposes. It is defined in [164] and some measurements for a perfect electric conductor case are reported. Due to the low RCS of this target, high accuracy is a must to deal with these kinds of EM problems, and are typically solved with MoM in FD. In this work, for comparison, we have taken a MoM Multilevel Fast Multipole Method (MoM-MLFMM) in-house Cassidian tool (HPTESP-MAT), based on the Combined Current and Charge Integral Equation (CCCIE) [165, 166], which is able to deal with composed metallic and homogeneous dielectric structures.

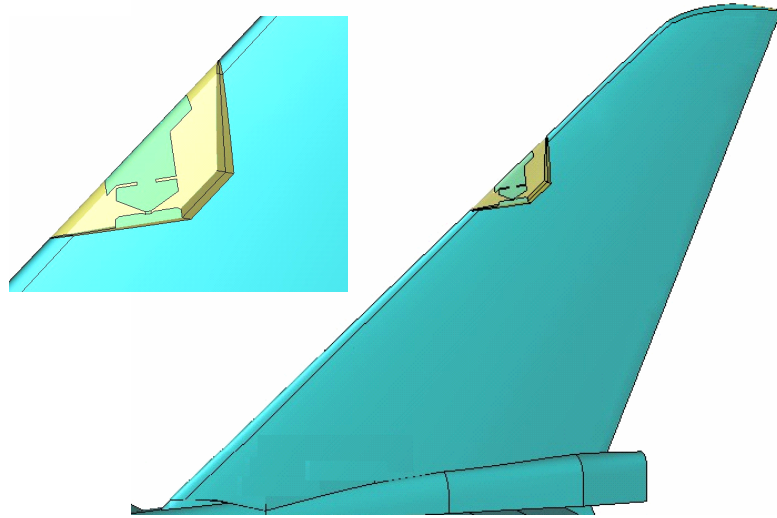


FIGURE 5.18: V/UHF antenna integration concept.

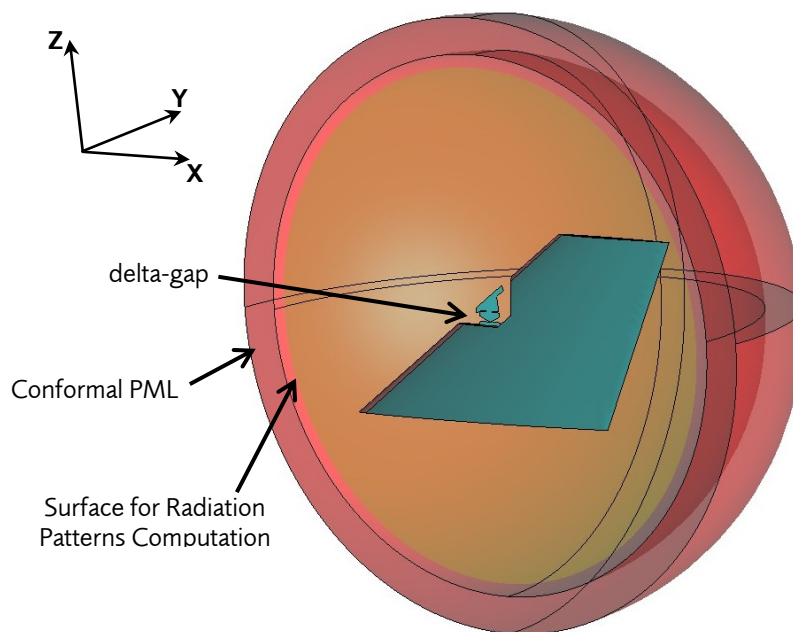


FIGURE 5.19: Installed V/UHF antenna simulation setup.

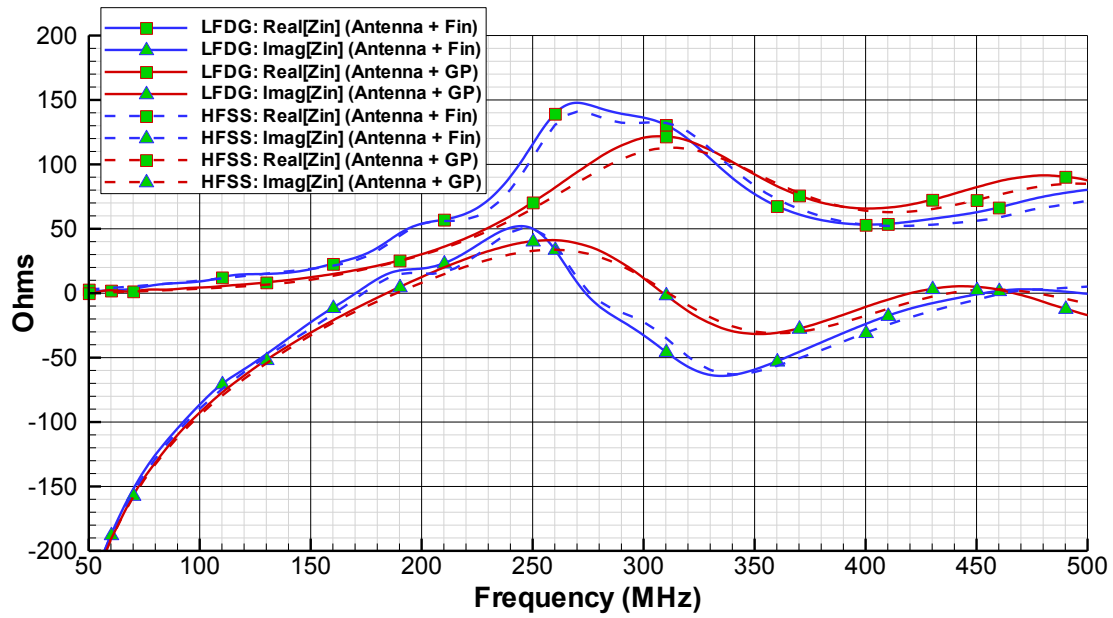


FIGURE 5.20: Input impedance with the V/UHF antenna installed on the leading edge of the fin. The results of the antenna installed on an infinite ground plane have been included. The same computations have been performed with HFSS commercial software.

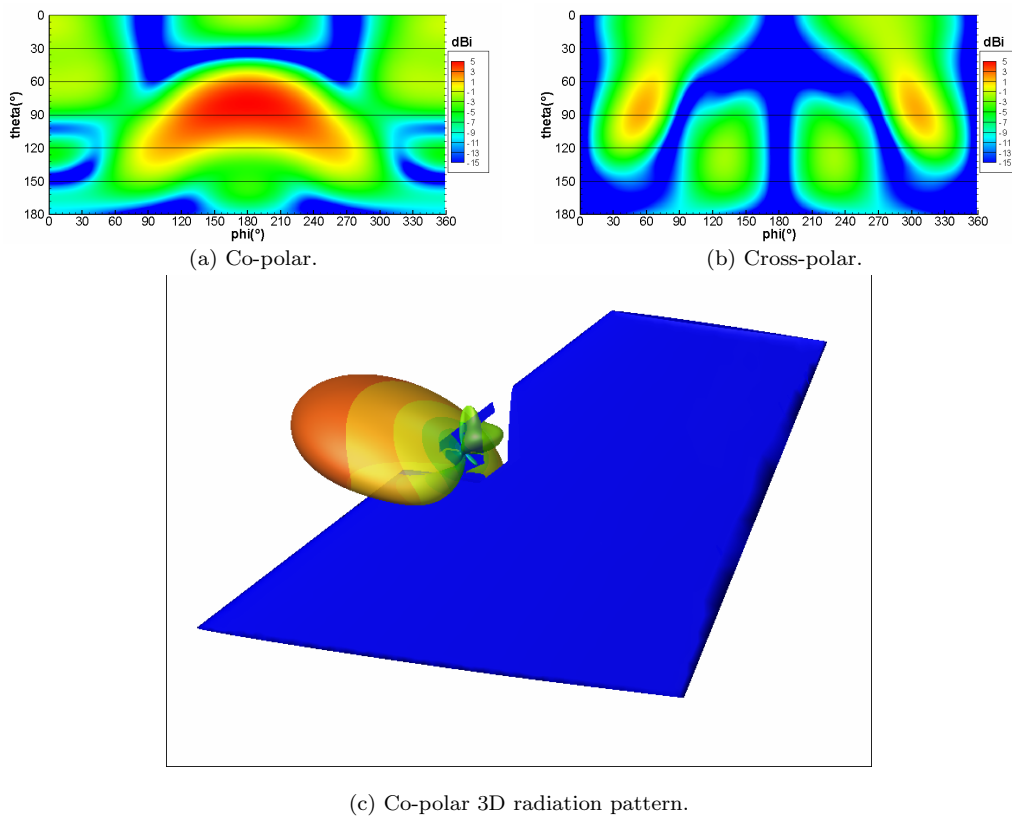


FIGURE 5.21: Radiation patterns for the V/UHF antenna installed in the leading edge of the fin at 132 MHz.

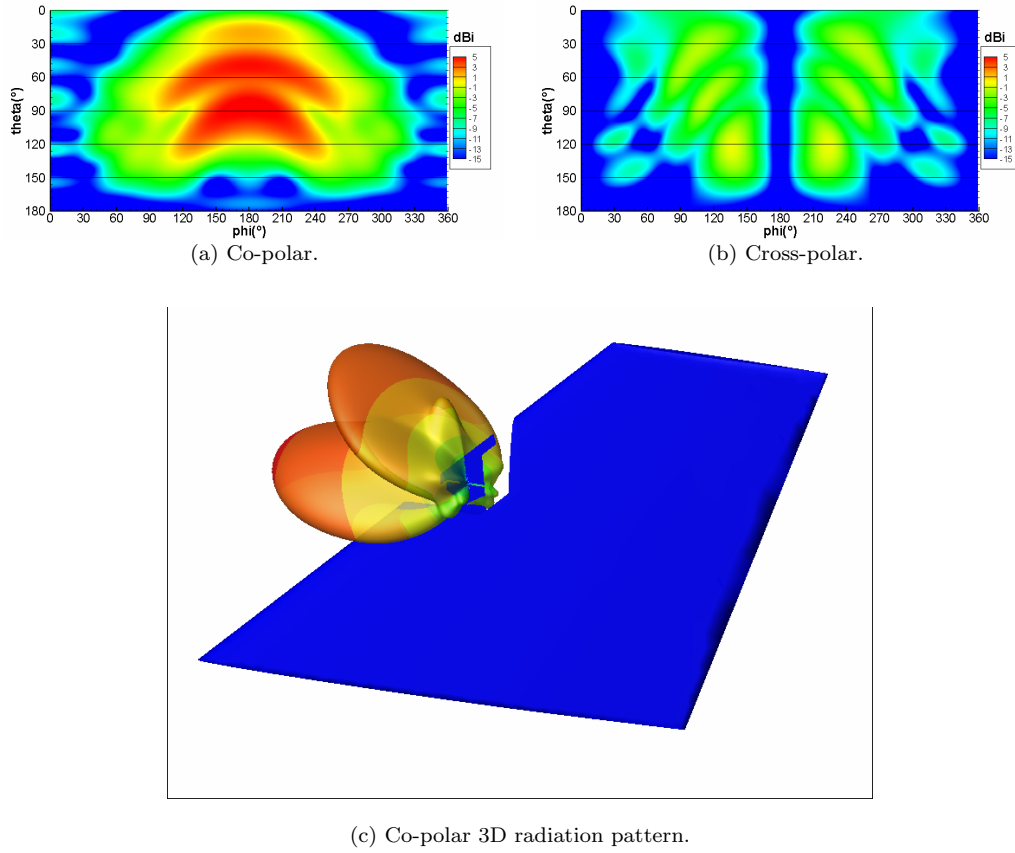


FIGURE 5.22: Radiation patterns for the V/UHF antenna installed in the leading edge of the fin at 312 MHz.

The geometrical definition of the PEC structure appears below,

Half ellipsoid: for $-0.416667 < t < 0.0$ and $-\pi < \psi < \pi$

$$\begin{cases} x = dt, \\ y = 0.193333 d \left(\sqrt{1 - \left(\frac{t}{0.416667} \right)^2} \right) \cos \psi, \\ z = 0.06444 d \left(\sqrt{1 - \left(\frac{t}{0.416667} \right)^2} \right) \sin \psi, \end{cases} \quad (5.4a)$$

Half elliptic ogive: for $-0.0 < t < 0.583333$ and $-\pi < \psi < \pi$

$$\begin{cases} x = dt, \\ y = 4.833450 d \left(\sqrt{1 - \left(\frac{t}{2.083350} \right)^2} - 0.96 \right) \cos \psi, \\ z = 1.611148 d \left(\sqrt{1 - \left(\frac{t}{2.083350} \right)^2} - 0.96 \right) \sin \psi, \end{cases} \quad (5.4b)$$

where $d = 2.5$ m, is the length of the structure.

Figure 5.23 shows the geometry under analysis. Apart from the PEC case, two different coated material cases have been studied, a perfect dielectric and a Radar Absorber

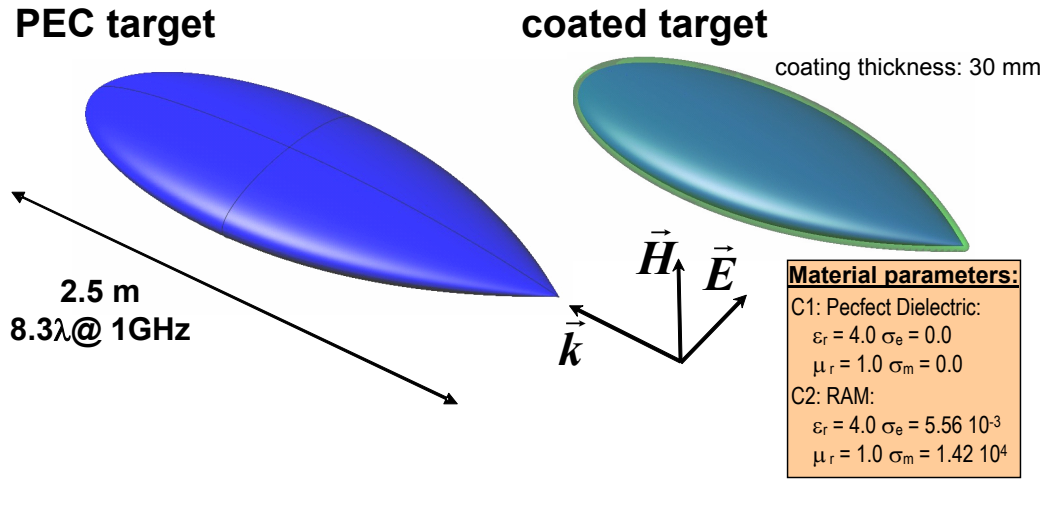


FIGURE 5.23: Geometry of the NASA almond.

Material (RAM). These cases were part of a JINA 2006 test case [167]. Note that these are complete double curvature geometries, where we can find, both smoothly and sharply curved zones, as well as a singular point, the ogive vertex. The right discretization of the curve surfaces (curvilinear 2nd-order tetrahedra), and also a care discretization of the fields close to the vertex (low value of h) are critical to achieve accurate results. Hence, small elements have been manually defined in the discretization of the vertex, as an *a priori* level of h -refinement.

We have required an accuracy for our simulations of 10^{-2} for the maximum frequency under analysis. Apart from the vertex, we have defined a maximum and optimal element size h during the mesh-generation process, corresponding to the value of $\frac{h}{\lambda}$ of $p = 3$ of Table 4.2, which is the optimal in terms of computational and required accuracy. Once we have generated the mesh, the order p in each element is chosen depending on the element size, assigning the minimum p that meets the required accuracy. For instance, in the simplest computed test (bistatic RCS at 1 GHz of the PEC case) the mesh was composed of 2018928 elements, of which 785678 were $p = 1$, 523786 $p = 2$, and 709464 $p = 3$.

Figure 5.24 gives some details of the simulation setup. First, a total-field region is defined in a way to minimize the size of the computational domain. Then, the scattered-field region is created. Finally, the conformal PML layer (see Section 3.4.1) is defined to close the computational domain. The surface, interface between total-field and scattered-field regions, is used to excite the problem in a weak way, through the flux terms, as Huygen sources. The same surface is used to compute the near-to-far-field transformation and calculate the RCS.

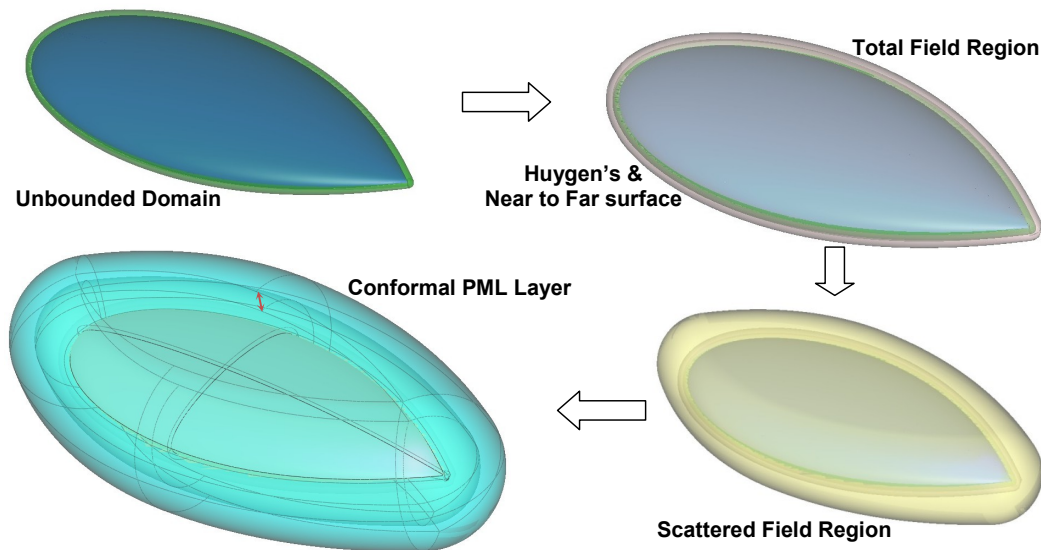


FIGURE 5.24: Simulation setup for the NASA Almond. Starting with the unbounded domain (upper left), a total-field region (with a conformal Huygen surface) is defined (upper right). This surface is used for the near-to-far field transformation operation. A scattered-field region is created (lower right) and, finally, the PML layer (lower left).

To reduce the computational cost, we have made use of the local time-stepping technique described in Section 3.5.2.3. We have classified the elements according to the Δt_{max} , and we have employed different time steps for each level. The structures are illuminated with a horizontal polarized plane wave, impinging on the almond at the vertex. The resulting copolar bistatic RCS at 1 GHz, computed with LFDG and compared the results with MoM, are shown in Figure 5.25 for the three cases analyzed. Excellent agreement is found in all cases. The monostatic RCS from 500 MHz to 2 GHz are shown in Figure 5.26. Excellent agreement is again found both for PEC and C2 (RAM material) cases. Minor differences are detected for the C1 (perfect dielectric) case. It is important to note that this is a challenging case for MoM, where the required number of iterations to solve iteratively the MoM linear system is quite high, and the number of unknowns cannot be too high in order to have a solution with affordable computational costs. The minor differences found so far are, in our opinion, due to the use of a coarse mesh in the MoM computations.

In Figure 5.25, we have also compared the PEC case with FDTD simulations, found with a 1.5 mm uniform mesh. Both for FDTD and LFDG, we use a padding of half a wavelength at 1 GHz between the almond and the PML region, and we simulate 50 nsec of the transient response. The FDTD problem employs 750 MCells and requires a CPU time of 24 hours in a 12 core Intel Xeon X5520 2.26Ghz architecture², while the

²The UGRFDTD MPI/OMP parallel code [117] benchmarking around 12 Mcells/core, has been employed.

LFDG code only requires 18 hours. Results for the bistatic RCS at 1 GHz confirm the superior accuracy of LFDG especially near the LO (monostatic) zone.

5.4 High Intensity Radiated Fields

The adverse effects caused by HIRF in any electronic device or in a very complex system, such as an aircraft, is a challenging topic from the standpoint of computational electromagnetics. The typical approach to tackle this electromagnetic compatibility problem is based mainly on testing. The development of efficient algorithms, able to deal with electrically large structures, and accurate methods, capable of estimating transfer functions between incident EM fields and internal fields, or induced currents in bundles, has recently been attracting a great deal of interest in the aerospace industry.

In this section the capability of the presented method to deal with very complex electromagnetic problems in an accurate way is proven. Firstly in a medium-size 3D object, where a wideband frequency response, considering a plane-wave illumination, is computed. Then, a electrically large problem is analyzed in order to assess the scalability of the method.

5.4.1 Medium size 3D Object

This validation geometry has been taken from a test-case proposed under the HIRF-SE project [116] for cross-validation with measurements of several numerical solvers. It consists on a $600 \times 500 \times 300$ mm brass box, with the front face open (see Figure 5.27), with a 30 mm wide flange around the edge. The box has two holes for N-type connectors on the top, labeled A and B in Figure 5.27(a). Between these holes and inside de box, a curved-wire is connected (see Figure 5.27(b)), made up of three semi-circles and two vertical straight sections. Its endings are soldered into the N-type bulkhead connectors A and B.

The box is illuminated perpendicularly to the open face using a linearly polarized plane wave, with electric vertical polarization, in the frequency band 1 to 6 GHz. The power received in the load of 50Ω at port A is taken for comparison (port B is grounded through a 50Ω load).

The results found with the LFDG algorithm are shown in Figure 5.28. They are compared to measurements, and FDTD simulations computed with the parallel UGRFDTD package [117]. Excellent agreement is found for LFDG and measurements, and minor deviations compared to FDTD. The main differences in the simulation of this test case

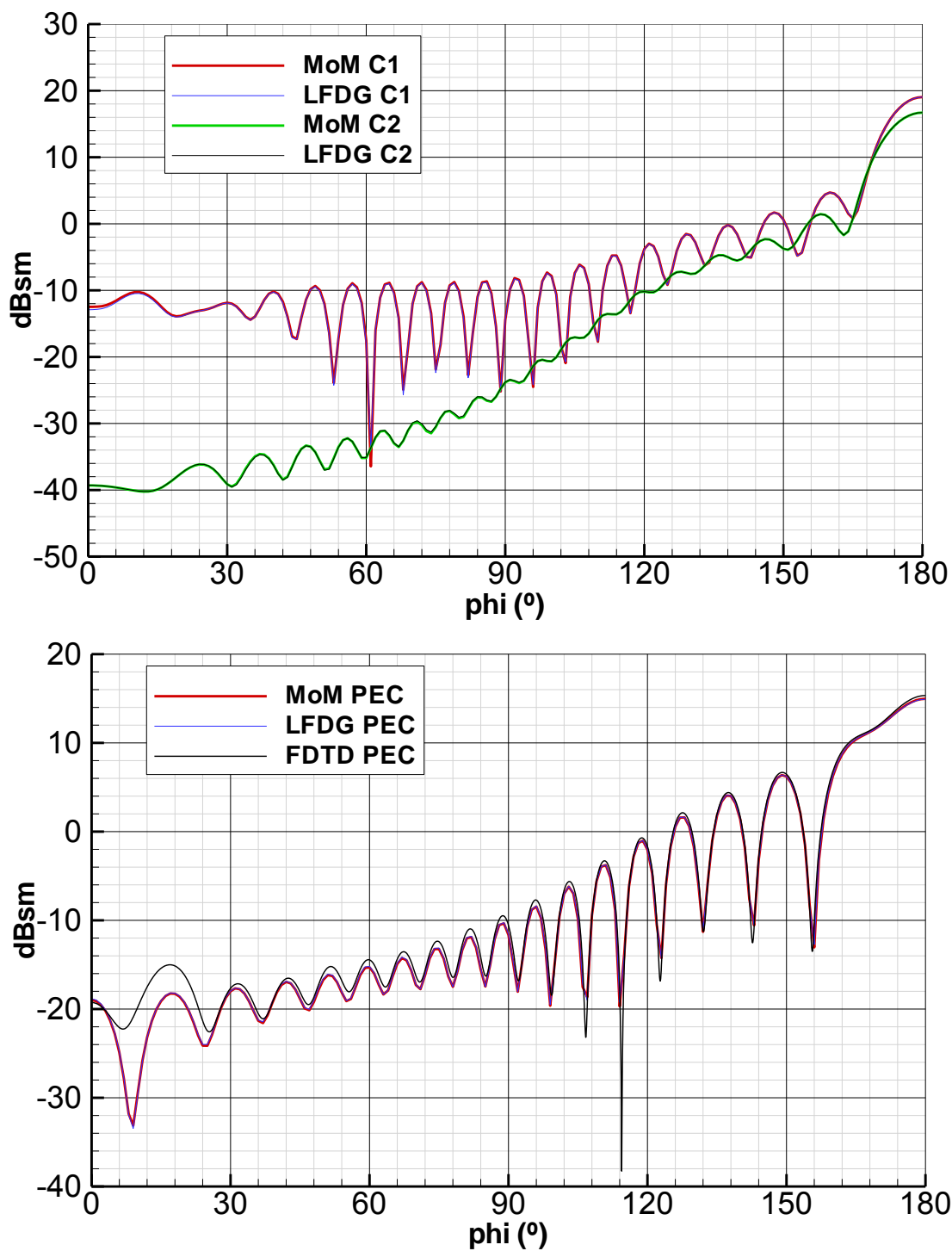


FIGURE 5.25: Bistatic radar cross sections of the NASA almond at 1 GHz. Comparison results between LFDG and MoM for the coated almond (upper), and LFDG, MoM and FDTD for the PEC case (lower).

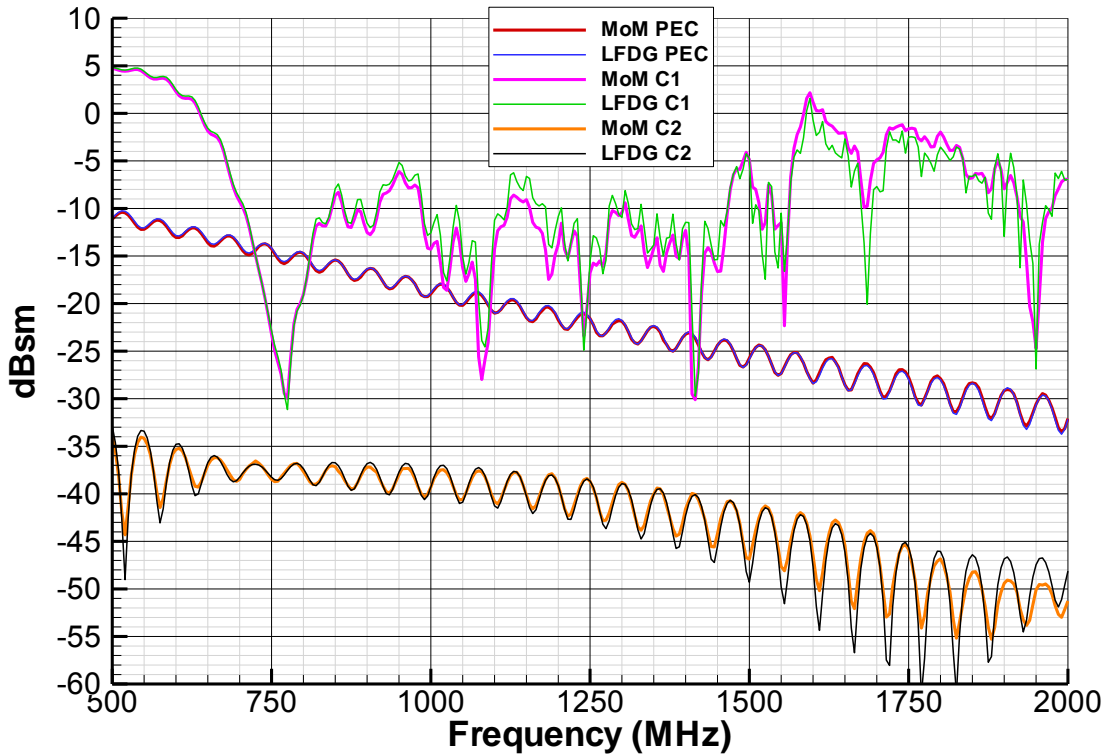


FIGURE 5.26: Monostatic radar cross sections of the NASA almond. Comparison results between LFDG and MoM.

with FDTD and LFDG methods is in the discretization of the curve cable, and in the modelization of the coaxial ports. In case of the FDTD, the staircasing approximation introduces errors in the geometrical discretization of the problem. For the LFDG, the use of second-order curvilinear tetrahedra minimizes this effect. Considering the coaxial ports, we have used a lumped 50Ω resistor to load the cable in the FDTD simulation. In the LFDG, we have meshed the coaxial port itself, truncating the port with a SM-ABC condition, where we have computed the received power. Fig. 5.29 illustrates this two aspect giving some visual details of the meshes.

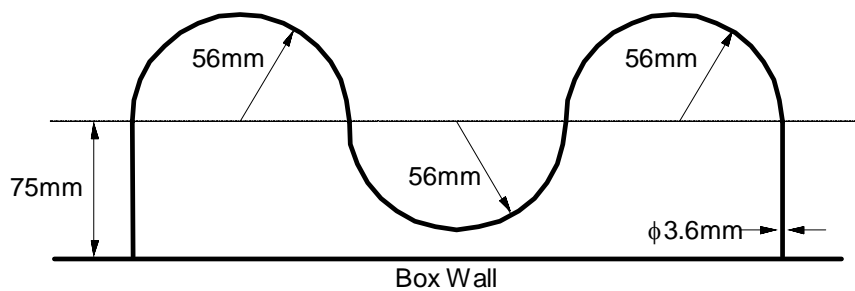
5.4.2 Aircraft Simulation Case

This problem consists of a 3D numerical test case based on a modified version of Evektor EV55 metallic aircraft (see Figure 5.30), also taken as a workbench for cross-validation of several simulators under the HIRF-SE project [116]³. The aircraft model consists on a PEC skin together with a generic part of the cabling. The electrical dimensions at 1 GHz are $(53.7 \times 47.4 \times 17.1)\lambda$. The PEC shell is considered with zero thickness, and the cable is modeled as a PEC cylinder of radius 3 cm. Some apertures exist in the

³The geometry files (both .igs and .gid format), disclosed by EVEKTOR, are publicly available upon request in the frame of the CEMEMC'13 HIRF-SE dissemination workshop (full info under www.cememc.org).



(a) Metallic box.



(b) Curved-wire geometry.

FIGURE 5.27: Setup of the medium size 3D object.

aircraft shell, cockpit, and fuselage windows, which permit the electromagnetic energy to couple into the airframe, where there are simplified models for some of the systems and cavities. The aircraft is illuminated with a plane wave coming at 45° below its nose, with the magnetic field in the horizontal plane (see Figure 5.30(a)).

Three different kind of probes have been chosen for comparison, for being representative of different coupling scenarios (see Figure 5.30(b)):

1. **O1.** The electric field at a surface test-point on top of the cockpit hidden from the illumination coming from underneath.
2. **O2.** The magnetic field in a point inside the airframe more weakly coupled to the illumination, and more susceptible to internal resonances.

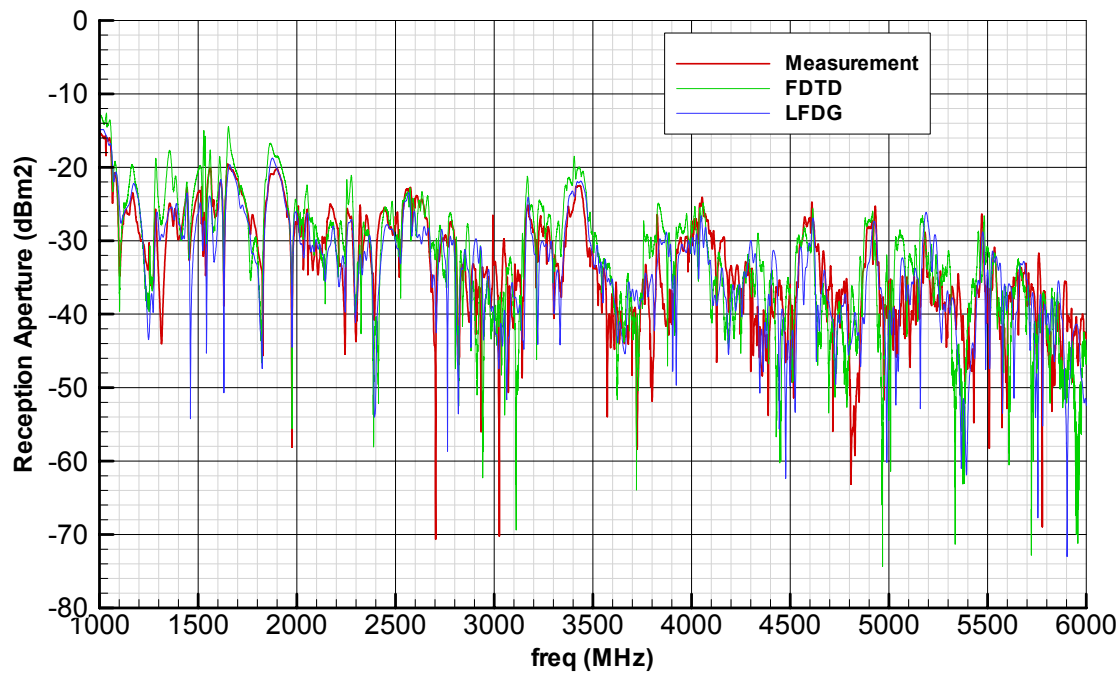
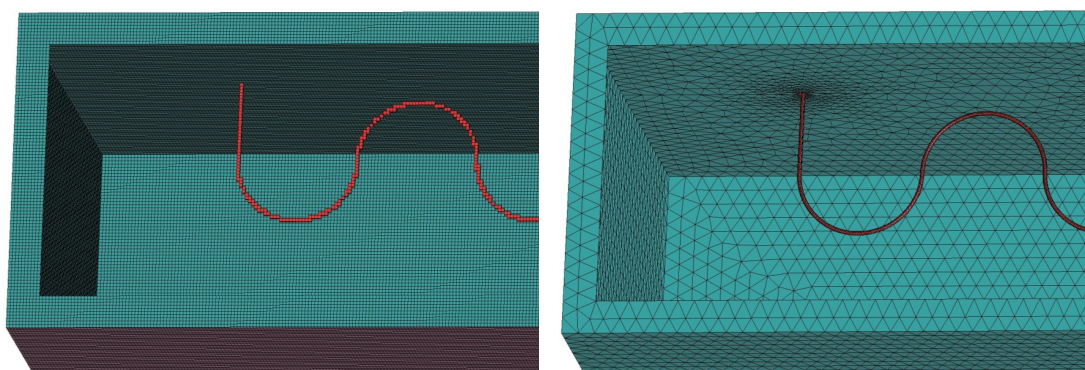


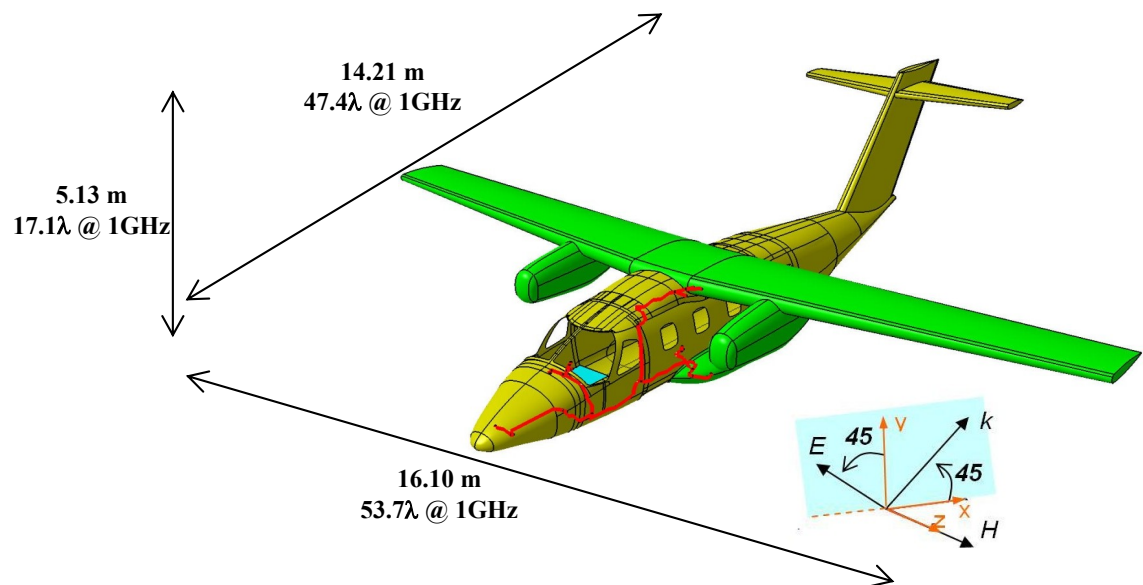
FIGURE 5.28: Reception aperture of the medium size 3D object, the reception aperture being the relation between the power received at port A, and the power density of the plane wave illuminating the box. Measurements are compared with results computed with LFDG and FDTD methods.



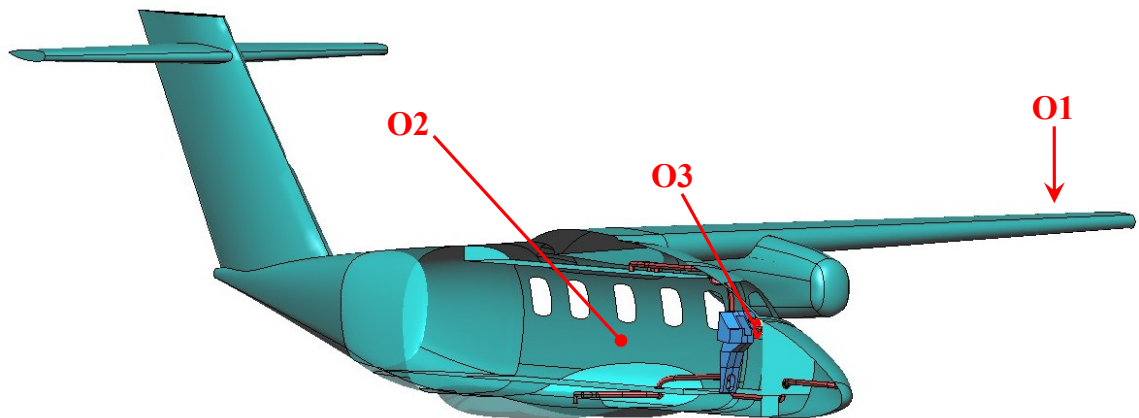
(a) Mesh used by FDTD method. The cable is loaded by a lumped 50Ω resistor.

(b) Mesh used by LFDG method. The coaxial ports have been meshed.

FIGURE 5.29: Screenshots of the meshes used for the computations. Only surface meshes have been plotted to visualize the differences of the geometrical discretization.



(a) External view and overall dimensions.



(b) Internal view and observation points.

FIGURE 5.30: External and internal geometry of the aircraft-simulation case. There is a cable modeled as a cylinder. There are some apertures in the aircraft shell, cockpit, and fuselage windows, and also different structures and cavities inside the airframe.

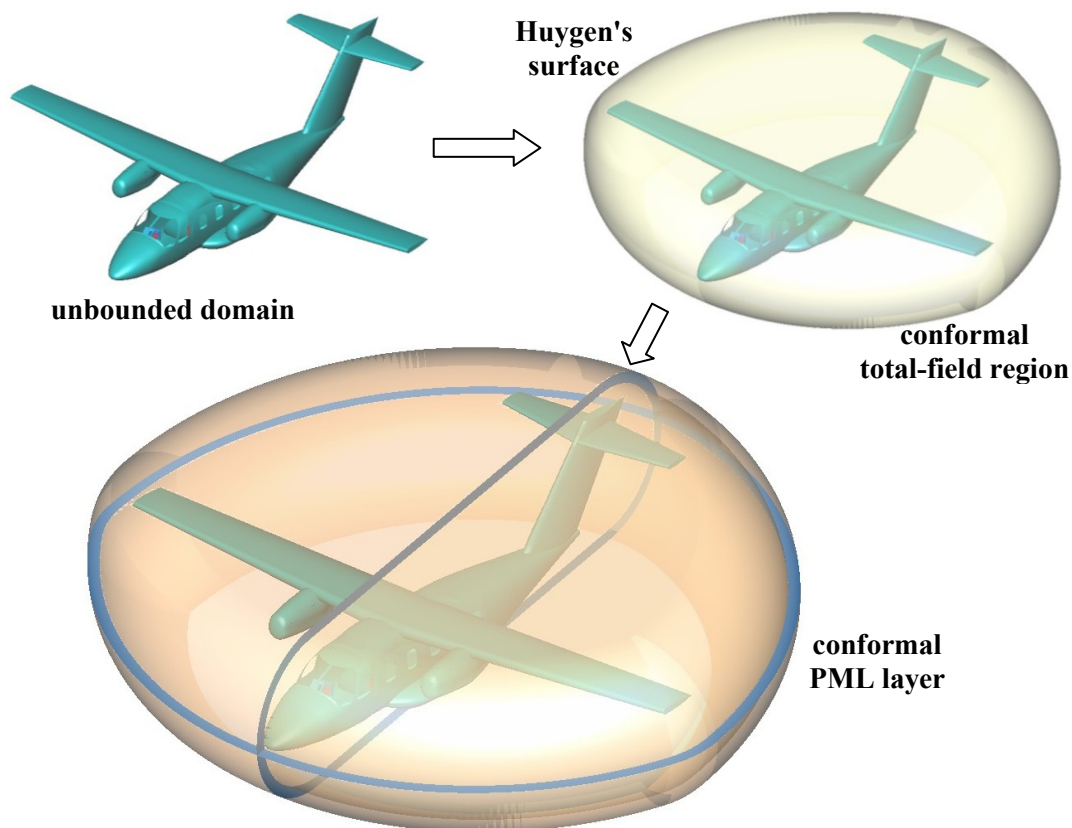


FIGURE 5.31: Simulation setup for the aircraft-simulation case. Starting with the unbounded domain (upper left), a total-field region (with a conformal Huygen surface) is defined (upper right). Then, from this surface, the conformal PML layer can be created (lower). It should be noted that the scattered-field region is collapsed to the conformal Huygen surface and is not needed, saving computational space.

3. O3. current at the termination of one of the grounded cables.

All these quantities have been found in time domain and computed in frequency domain as transfer functions (normalized to the incident field).

The simulation setup is shown in Figure 5.31. A total-field region is defined directly backed by the conformal PML interface. Thus, the scattered-field region is just the PML, with the subsequent computational saving. The surface at the total-field/PML interface layer is used to introduced the excitation as a Huygen source, through the flux terms, as described in Section 3.2.

The plane-wave source uses a Gaussian pulse time signal, with 14 dB bandwidth at 1 GHz. The problem has been simulated up to a physical time of 1.0 μsec . Some screenshots of the simulation appear in Figure 5.32 representing the total electrical field, and results are shown in Figure 5.33, in comparison with those found with FDTD (computed with UGRFDTD package [117]), reflecting very good agreement.

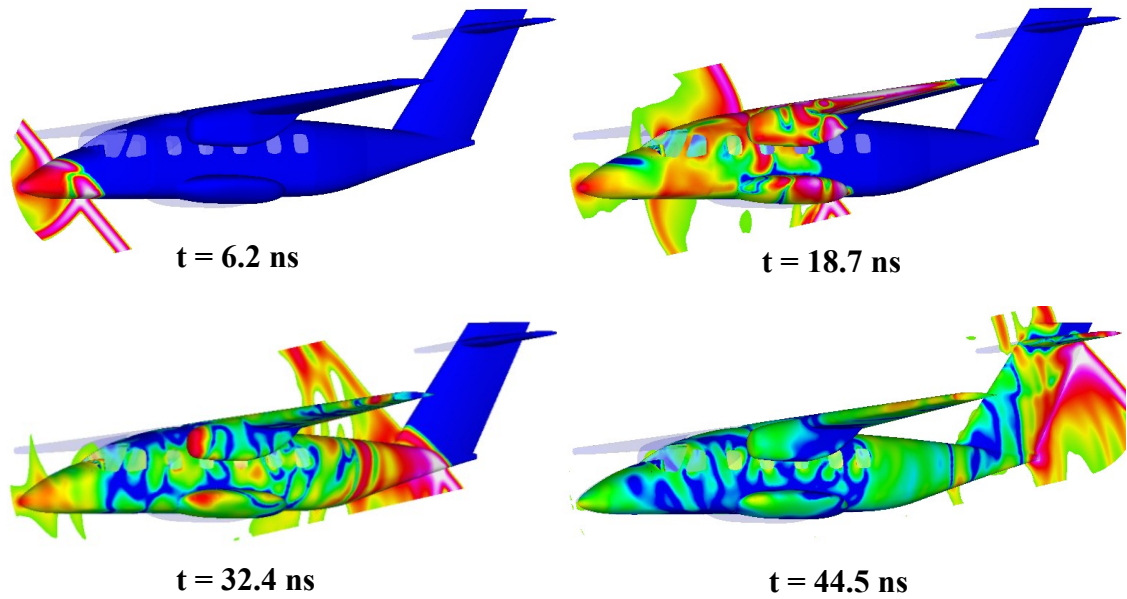


FIGURE 5.32: Screenshots of the aircraft-simulation case. Total electric field is represented on the aircraft structure and in a central plane.

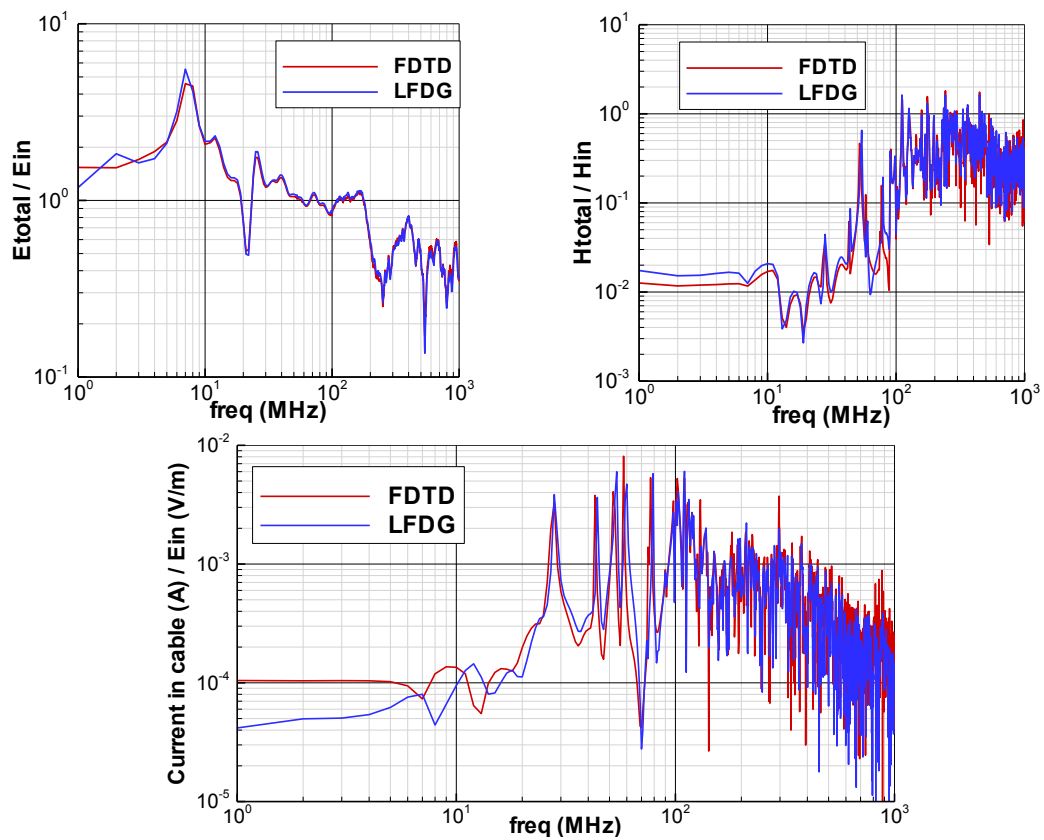


FIGURE 5.33: Computed transfer functions for the aircraft-simulation case. Comparison of results between LFDG and FDTD. Upper left: **O1**, upper right: **O2** and lower: **O3**

In case of the FDTD simulation, the cell size has been constant of 12 mm ($\frac{\lambda}{25}$ at 1 GHz). In both cases, the expected accuracy⁴ is about 10^{-2} per wavelength at 1 GHz. Details about the order of the basis functions used in this particular simulation appear in Table 5.7, and about the LTS, in Table 5.8. A comparison between LFDG and FDTD computational details is made in Table 5.9.

TABLE 5.7: Number of elements (M) for each set of basis functions for the aircraft simulation case. GxRy stand for x order for the gradient space, y order for the rotational space

	G1R1	G1R2	G2R2	G2R3	G3R3	Total
M	96572	6018789	2729857	59	0	8845279
M (%)	1.09	68.05	30.86	0.00	0.00	100.00
dof	3764112	300664960	204819600	6570	0	509255242
dof (%)	0.74	59.04	40.22	0.00	0.00	100.00

TABLE 5.8: Local time-stepping level distribution for the aircraft simulation case.

	L1	INTERFACE (L1/L2)	L2	INTERFACE (L1/L2)	L3
M	880	980	125602	217506	8500311
M (%)	0.01	0.01	1.42	2.46	96.10
Δt (ps)	1.59	4.77	4.77	14.32	14.32

TABLE 5.9: FDTD vs LFDG comparison

Method	$M(10^6)^1$	$\text{dof}(10^6)^2$	min. Δt	max. Δt	steps ³	memory	CPU ⁴	$M(10^6)/\text{sg}^5$
LFDG	8.845	509.3	1.59 ps	14.32 ps	69837	256.6 GB	114 h	52.2
FDTD	703.704	4394.8	18.00 ps	18.00 ps	55556	36.1 GB	14 h	638.4

¹ Number of elements (M) are 2^nd order tetrahedra for LFDG and Yee-cells for FDTD.

² Double precision (8 bytes per dof) for LFDG. Single precision (4 bytes per dof) for FDTD.

³ Number of steps for the max. Δt . The computed physical time has been 1.0 μs .

⁴ CPU time corresponds to 10 processors Intel Xeon X5680 6 cores, 3.33Ghz.

Hybrid Open MP/MPI implementations are used in both cases.

⁵ Updated mega-elements per second for the highest LTS level.

Different orders p have been used for each cell (Table 5.7) for LFDG.

For this case, the memory and CPU time is about one order of magnitude larger for LFDG than for FDTD. In case of FDTD, we use single precision variables since it is an advantage of this method, the use of double precision does not usually improve FDTD performance. However, double precision is recommended and used in case of LFDG, where we are using high-order functions, LTS and PML, double-precision variables are required to maintain accuracy and avoid instability due to rounding-off errors. Concerning computational cost, three remarks are due:

- The simplicity of the FDTD algorithm makes it easier for the compilers to obtain faster codes. Techniques such as vectorization and the better use of the cache

⁴Defining the accuracy as the L^2 -norm error per wavelength for a plane wave traveling in free space: $|e^{-jk_0\lambda} - e^{-j\tilde{k}_0\lambda}|$, λ being the wavelength, k_0 the analytical wavenumber, and \tilde{k}_0 the numerical one (see Sections 4.3 and 4.5.)

memory are key for speeding up FDTD algorithm. These techniques are not so effective for DGTD.

- Local time-stepping, the presence of PML and the use of different order p elements, make not only the workload prediction more difficult, but the workload balance as well to optimize the parallelization. In one complete time step of the highest LTS level, the workload is not constant across the mesh in the different steps of the LTS algorithm. In case of FDTD, the workload balance can be made in an almost perfect way.
- The mesh used in the FDTD computation is the simplest one, a uniform structured mesh. Thus, quite high discretization errors are expected because of the staircasing effect. Moreover, the FDTD mesh parses out what is irrelevant compared to cell size, which can be an advantage, if it is also electrically irrelevant, or not. In this case, for instance, a non-uniform mesh had been used, with a smaller cell (2.0 mm), the CPU time would have been very similar to that achieved with LFDG. In the case of LFDG, where curvilinear 2^{nd} -order tetrahedra have been used, the discretization error is very small. Furthermore, the finite-element mesh resolved every detail present in the geometrical model. This fact, concerning accuracy, it is clearly shown in the first case presented in the previous test-case, where we compare with measurements.

5.5 Anisotropic Materials

Finally, we validate the formulation developed in Section 3.3, where the flux terms and the semi-discrete scheme for the anisotropic material case where derived. For comparison, we have used two simple problems of scattering from a non-magnetic dielectric sphere ($\mu_r = 1$): the first one isotropic with $\varepsilon_r = 3.0$, and the second one anisotropic with

$$\bar{\varepsilon}_r^{XYZ} = \begin{pmatrix} 3.0 & 0.0 & 0.0 \\ 0.0 & 3.0 & 0.0 \\ 0.0 & 0.0 & 4.0 \end{pmatrix} \quad (5.5)$$

The sphere is illuminated with a x-polarized plane wave, and the bistatic RCS is computed at a frequency for which the sphere diameter is $D = 1.2\lambda$, with λ being the wavelength. For reference, results from [168], computed with a Finite Element-Boundary Integral-Multilevel Fast Multipole Algorithm, and also computed with Ansoft HFSS commercial software are used. Figure 5.34 shows a good agreement between results found by all methods. The maximum difference found in the anisotropic case compared to HFSS results has been of 0.35 dB.

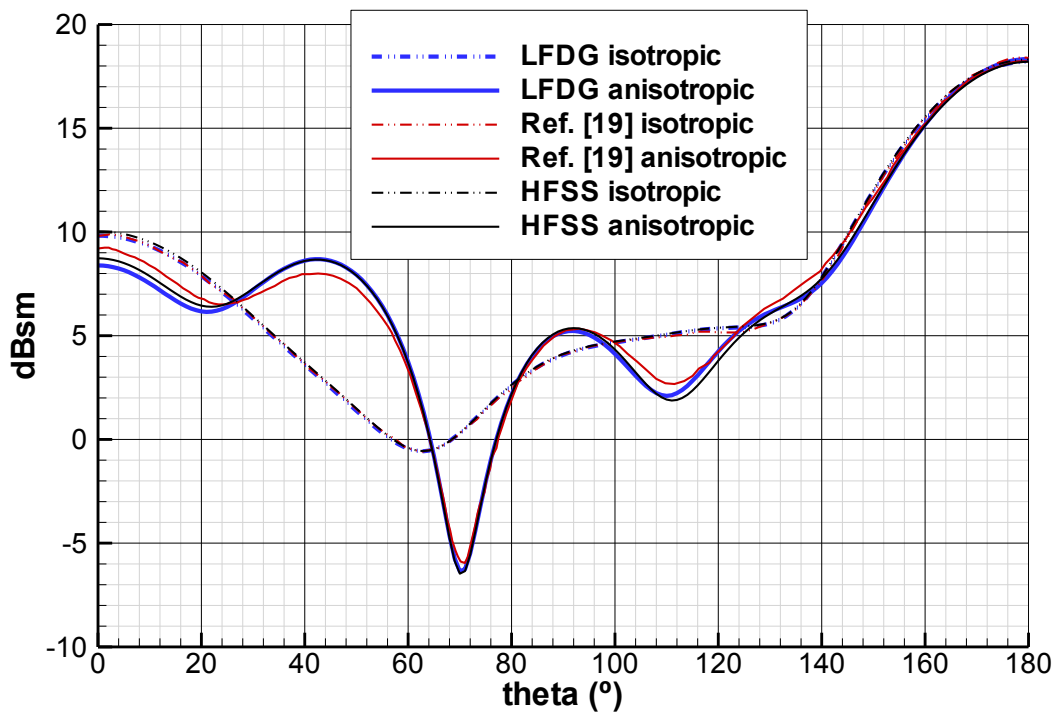


FIGURE 5.34: Bistatic RCS of an isotropic/anisotropic sphere ($D = 1.2\lambda$ and $\lambda = 1.0$ m). LFDG results are compared to those appearing in [168], and computed with Ansoft HFSS.

5.6 Summary

In this chapter, the LFDG algorithm was deeply validated with several EM problems. In all cases, measurements or direct comparison with results computed with other numerical methods were used. Concerning the computational cost, the required memory and CPU time were evaluated when solving complex and electrically large EM problems, showing the efficiency and competitiveness of the scheme.

Apart from the results shown in this chapter, SEMBA solver has been validated in the Workshop ISAE Radar Signatures 2012 [P19], being some of the contributions considered as reference results.

Chapter 6

Conclusion and Further Work

This dissertation has targeted two overall objectives: the first one, is to explore the applicability, numerical errors and fundamental limits of the DG spatial discretization to solve Maxwell equations in the time domain. The second one, is to implement, apply, and validate a LFDG-based computer code with realistic complex EM problems. This chapter first summarizes the main accomplishments and scientific contributions of this work, and then discusses on future topics of research to render this promising technique an all-purpose tool in electrical and electronic engineering.

6.1 Contributions

The main achievements of this work (most of them published or under submission in peer-reviewed journals [P14, P11, P10, P7, P6, P5]) can be summarized as follows:

1. **Formulation of the semi-discrete discontinuous Galerkin spatial discretization scheme.** The formulation has been developed in a general framework which unifies different flux-evaluation schemes successfully applied to this method. The formulation includes the treatment of the common boundary conditions, anisotropic materials, and absorbing boundary conditions, the so-called first-order Silver-Müller ABC, and the conformal uniaxial perfectly matched layer.
2. **Development of the leap-frog discontinuous Galerkin algorithm.** The well-known LF time-integration method has been applied to the DG semi-discrete scheme, to obtain the LFDG algorithm. In this context, a local time-stepping strategy has been successfully developed to overcome the critical limitation imposed by the stability condition of the LF explicit temporal discretization scheme.

3. **Analysis of the discontinuous Galerkin semi-discrete scheme, and the leap-frog discontinuous Galerkin algorithm.** The dispersion and dissipation of the numerical methods have been studied. The topic of the spurious modes has been reviewed. Additionally, the convergence rates of the dispersion and dissipation relationships, and the anisotropy of the errors of both schemes have been estimated and compared. In case of the LFDG algorithm, other topics have been studied, such as stability and computational cost. Thus, the limitations of the LFDG algorithm have been assessed, and an analysis of the computational cost vs. accuracy has been performed, and compared to the FDTD method.
4. **Parallel implementation of the leap-frog discontinuous Galerkin algorithm.** Taking advantage of the parallel nature of the LFDG, this algorithm has been implemented by using a hybrid OMP-MPI programming technique. This two-level parallelization fits well in modern computers (a number of medium/large shared-memory multi-element nodes, interconnected with Infiniband, Myrinet or Gigabit).
5. **Validation and application of the leap-frog discontinuous Galerkin algorithm.** The LFDG algorithm has been validated with microwave filters, antennas, and scattering problems, comparing the results with measurements and other numerical techniques. The method has been applied to real engineering problems, showing some important properties of the method, such as robustness, stability, versatility, efficiency, scalability and accuracy.

6.2 Further Work

Although many different computational electromagnetic methods have been thoroughly and widely developed to deal with most of the practical engineering problems, there are still gaps for which new techniques need to be explored. In this dissertation, a method that combines the advantages of finite-element methods, and explicit time-domain methods is implemented from scratch. To the discretion of the author, the following is a (non-exhaustive) list of the most immediate research topics in this area:

1. **Development of further capabilities.** LFDG technique has many similarities to FDTD. Hence, most of the capabilities fully assessed and validated in FDTD solvers can be adapted to LFDG. Some of them are dispersive and/or anisotropic thin-layer models, dispersive materials treatment, lumped circuit elements, thin wires, thin slots, etc..

2. Improvement of the temporal integration convergence rate of the LFDG.

Although the LFDG algorithm easily permits the selection of the order of the basis functions for the spatial discretization element-by-element, the main limitation of the method is the poor convergence rate of the temporal integration scheme. This fact imposes a limit in the use of p refinement techniques. The temporal integration algorithm should be improved to permit the selection, also element-by-element, of the convergence rate of the temporal discretization. Different alternatives to local time-stepping can be also explored to be closer to the optimum time step in each element.

3. Improvement of the versatility of the FEMTD methods.

Different alternatives could be developed to improve the versatility of FEMTD methods in real applications. Some of them are the following: (i) the use of hybrid meshes with different kinds of cells taking advantages of the different properties, for instance tetrahedra in complex regions, hexahedra in regions without details, and pyramids in the interface; (ii) the use of structured/unstructured meshes, saving memory in the structured zones sharing the local matrices; or (iii) the use of non-conforming locally refined grids, which can be very effective in the application of h-refinement, and simulation of problems with high contrast in the material properties.

4. Development of hp-adaptability techniques.

The electromagnetic problems addressed in this work show the importance of the use of hp-adaptability. The development of efficient hp-adaptability techniques in time-domain simulations will allow the application of the method in a more automatic and blind way. To this aim, a close integration of the mesher in the electromagnetic solver is a crucial point. The development of dynamic spatial hp-adaptability and arbitrary high-order in time, able to dynamically adapt the mesh and the time-integration method during the simulation, can save a large amount of CPU time in a complete simulation while maintaining the required accuracy.

5. Improvement of the applicability of the FEMTD methods.

One of the main difficulties expected for the applicability of FEMTD methods, compared to the FDTD, for the analysis of very complex systems (e.g. aircraft) is the generation of EM models and meshes. The starting point for these kinds of analysis is a complete digital mock-up, which contains every detail of the real structure (bolts, rivets, holes, etc.). The defeaturing of the digital mock-up to construct an EM model, containing all the EM information, and ready to be meshed, requires a huge amount of engineering work. This process has been developed for the FDTD method for years, and there are commercial tools to carry out this work, the result of which are finite-difference meshes of billions of cells. In the case of FEMTD,

this process is not mature, and must be developed further in order to offer to the industry tools to generate meshes of billions of cells in a reasonable amount of time in both the generation of the mesh itself and the development of complex EM models.

6. **Multi-physics simulation.** There is an increasing need of thermal-mechanical-EM coupled solvers able to deal with the full complexity of real problems (e.g. to predict the lightning effects in composite structures). DG methods based on unstructured tetrahedral meshes permit an easy multi-physics coupling with other numerical models that also use these kinds of meshes.

Appendix A

SEMBA: A parallel LFDG Computer Code for EM Analysis and Design

The leap-frog discontinuous Galerkin algorithm, including a LTS strategy, has been implemented from scratch in a Fortran 90 MPI parallel computer code called SEMBA (Simulador Electromagnético de Banda Ancha). Some implementation details and capabilities are described in this appendix.

A.1 Description of SEMBA

Some high-level details about the implementation are:

- It is programmed as a self-supporting Fortran 95 code. SEMBA does not make use of any external library, except MPI.
- It employs a hybrid OMP-MPI programming technique, which is well suited for the state-of-the-art computers composed by a number of medium/large shared-memory multi-element nodes, interconnected with Infiniband, Myrinet or Gigabit.
- It is a highly optimized code, both in algorithm and in computing resources (memory & CPU). Matrices which are independent of the element geometry are shared, while incomplete matrices are compressed.
- Most of the code uses double-precision variables. This makes it possible to keep the accuracy under control and avoids late-time instabilities.

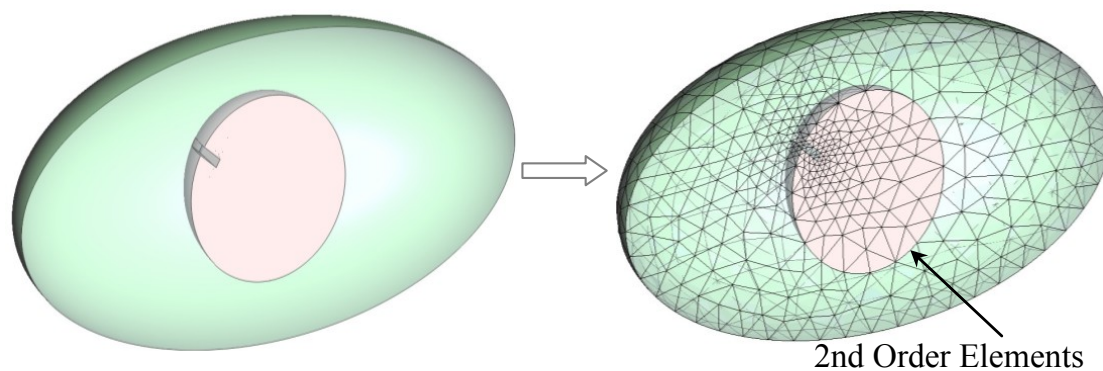


FIGURE A.1: Geometrical discretization.

A.2 Geometrical Discretization

The geometrical discretization is based on first- and second-order curvilinear tetrahedra. The use of curvilinear elements offers two main advantages. One is the accurate representation of curved boundaries and geometry, which introduces a dramatic improvement in the accuracy of the numerical approximation, in most real applications. The other advantage is the increment in the efficiency of the method, since curvilinear elements reduce the number of the elements in order to accurately discretize a geometry: the final mesh has bigger elements, allowing the use of larger time steps in the temporal integration.

Another important point is the capability of generating complex meshes with these kinds of elements. This requirement is fulfilled by most of the commercial CAD tools. In our case GiD [123] is employed for geometrical modeling, meshing and some visualization of the results.

A.3 Mesh Preprocessing

To increase the efficiency of the computations, and implement certain capabilities, before starting a numerical simulation SEMBA performs some preprocessing tasks. First of all, the mesh is distributed among the different parallel processes. Secondly, the order of the basis functions for each element is chosen, according to the required accuracy. Finally, the elements are organized into different sets, as required by the LTS algorithm.

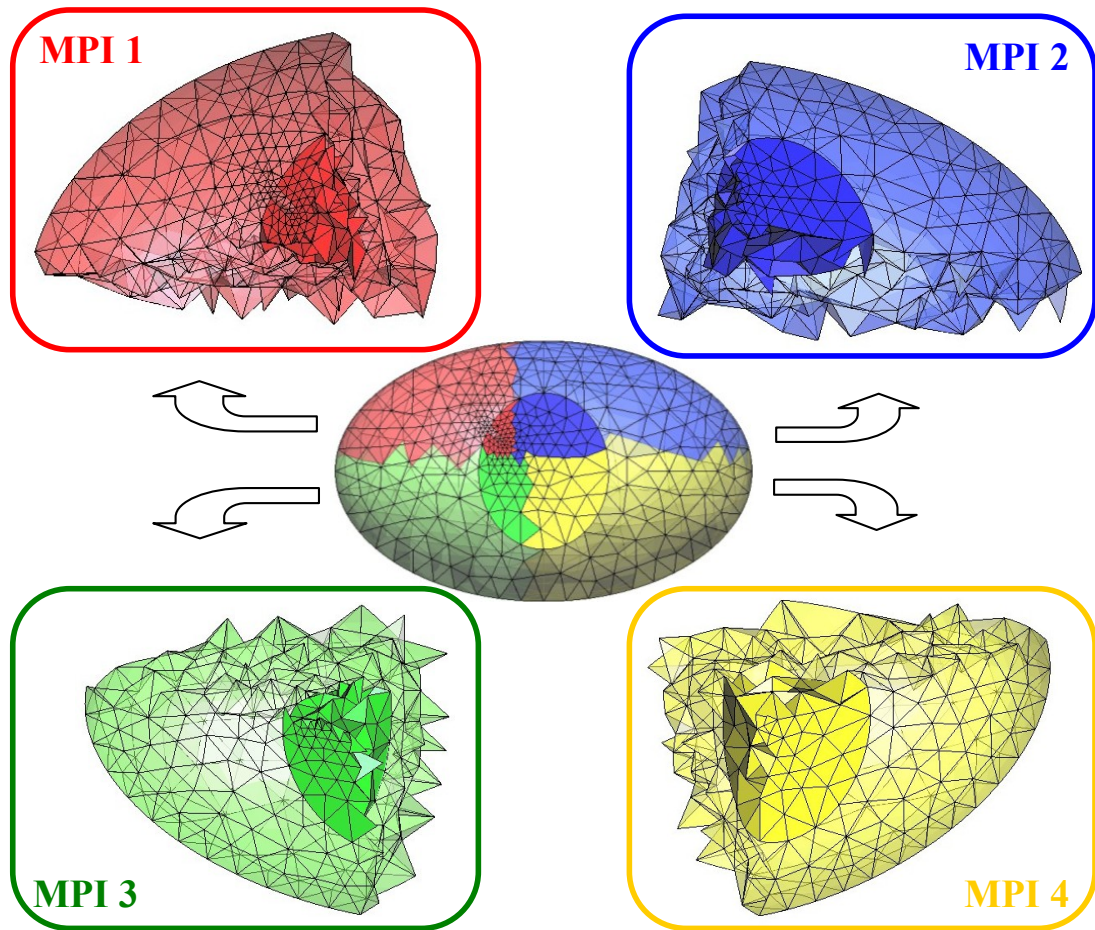


FIGURE A.2: Distribution of the mesh among the different MPI processes.

A.3.1 Mesh Distribution

One key advantage of discontinuous Galerkin methods is their simplicity for the parallelization in memory-distributed hardware architecture, making use of the Message-Passing Interface (MPI) standard. The mesh is distributed among the M processes available as depicted in Figure A.2. This is the first level of parallelization of the SEMBA solver. From the outset, in the reading of the mesh, the algorithm is fully parallelized among all MPI processes, achieving high scalability. The required geometrical information for each process is its own geometry, and the topological adjacent elements of the neighboring processes. This additional information will be used to compute the flux coming from these adjacent elements to its own computational domain. Some information will be necessary to be interchanged between neighboring processes in the numerical-simulation stage.

A.3.2 Selection of the Basis Function

An *a priori* hp-refinement heuristic strategy has been developed to choose the size of the mesh, and the order of the basis function in each tetrahedron. The objective is to ensure a given accuracy level, minimizing the computational cost. The required accuracy could differ across the computational domain, which is an input for SEMBA. The selection of the mesh size has to be made in the mesh-generation process, since there is an optimum element size that minimizes the computational cost for a required accuracy. The accuracy level, therefore, defines the optimum element size according to the results shown in Sections 4.3 and 4.5. In real meshes, the element sizes vary throughout the computational domain, and the accuracy is finally adjusted with the selection of the order p . The current implementation of SEMBA exploits the hp-refinement techniques by mixing different element sizes (h) and orders (p) following this *a priori* approach.

Therefore, once the mesh is generated, SEMBA selects element-by-element the order of the basis functions, depending on their size, and the required accuracy in the region where the element is located. The aim is to employ higher-order basis for larger tetrahedra, and lower orders for smaller ones. SEMBA combines gradient spaces of reduced order $p - 1$, with rotational spaces of complete order p [132]. The choices are based on the results found during this work, as those shown in Figure 4.20.

It bears noting that smaller elements need shorter time steps, but if lower orders are used in these elements, the stability condition is relaxed. In the same way, longer time steps can be used in bigger elements combined with higher orders. The combination and mixing different orders of the basis functions depending on element size, makes the time step among all the elements more homogeneous, reducing the number of levels required for the LTS algorithm.

This step is fully parallelized, carried out by each MPI process over its own geometry (an example is depicted in Figure A.3).

A.3.3 LTS Level Classification

The local time-stepping strategy described in Section 3.5.2.3 is implemented in SEMBA. The method requires a classification of all the elements according to their maximum time step (Δt_{max}^m) in several levels, L . The interfaces between levels are to be identified, since they need a special treatment in the numerical-simulation process. At each level l , a different time step is used in the simulation, $3^{(l-1)} \Delta t_1$, Δt_1 being the time step for the first level. This technique provides extraordinary savings in the CPU-time in real problems, where unstructured meshes contain very small and distorted elements. Figure

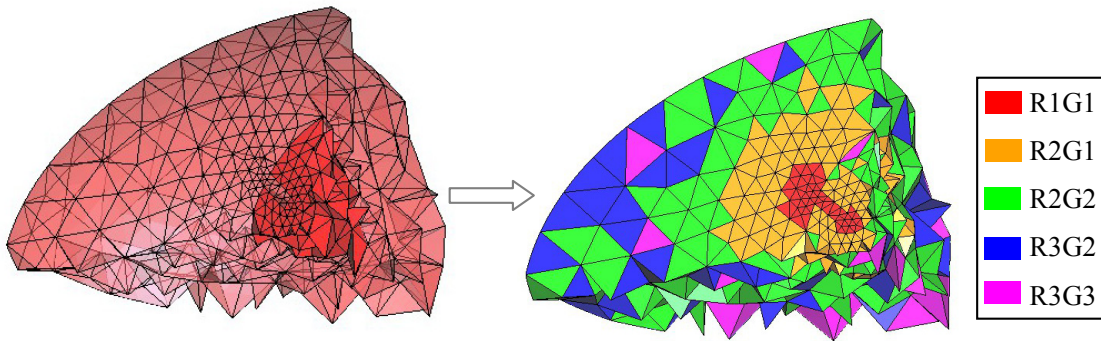


FIGURE A.3: Selection of the expansion function. RxGy stand for x order for the rotational space, y order for the gradient space.

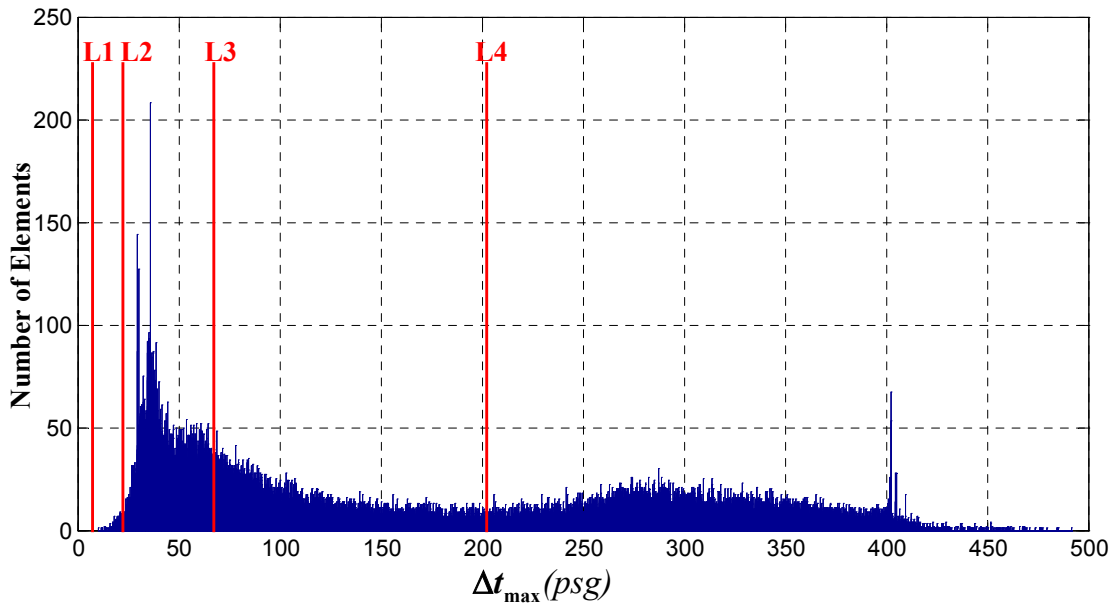


FIGURE A.4: Example of a distribution of Δt_{max}^m in a real problem (validation case described in Section 5.1.1). The choice of Δt_{min} and the time steps for the different levels ($L = 4$), have been included in the plot. The estimated average time step was 88.5 psg, compared to the minimum Δt_{max}^m (10.5 psg), a gain of about 8 is expected due to the application of LTS.

A.4 shows the distribution of the maximum time step for all the elements in a real problem. The right choice of Δt_1 is not the minimum Δt_{max}^m ; this value is actually tuned to provide the maximum average time step.

Finally, it should be pointed out that the proposed LTS strategy requires linear interpolation to find the updated samples in the interfaces between LTS levels. This operation is not exactly an average approximation, and second-order accuracy is slightly lost in these zones. This fact has a local effect in the stability of the scheme. The solution to

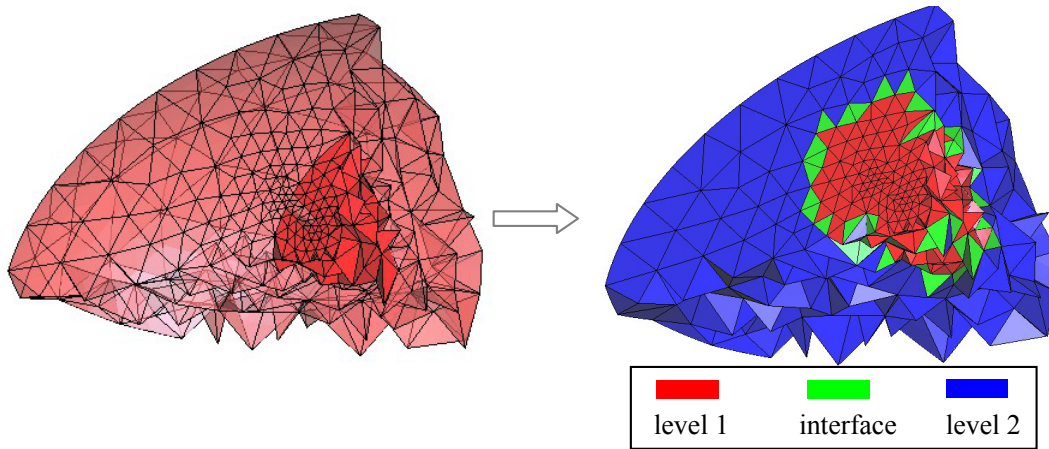


FIGURE A.5: Example of a LTS level classification with $L = 2$.

this problem is to penalize the stability condition only for the elements in the interfaces of the LTS levels by a factor (typically 0.8, [64, 95]). This introduces some complexity in the right selection of the Δt_1 , which is the parameter that fixes the interfaces.

Although some information related to the levels assigned to adjacent elements needs to be shared between MPI processes, this step can be carried out in parallel, each MPI process with its own geometry. An example with $L = 2$ is shown in Figure A.5.

A.4 Capabilities

A.4.1 Materials and Boundary Conditions

Concerning the material-modeling capabilities of electromagnetic problems, SEMBA includes the following possibilities:

- Isotropic dielectric and magnetic materials, with relative electric permittivity (ϵ_r) and magnetic permeability (μ_r) properties.
- Isotropic lossy electric and magnetic materials, with electric conductivity (σ_e) and magnetic conductivity (σ_m) properties.
- Anisotropic materials described by tensors: $\bar{\bar{\epsilon}}_r$, $\bar{\bar{\mu}}_r$, $\bar{\bar{\sigma}}_e$ and $\bar{\bar{\sigma}}_m$.
- Perfect electric conductor and perfect magnetic conductor boundary conditions. These conditions can be used to model geometry, infinite ground planes or symmetric planes.

- Periodic boundary condition. In this case two boundary parallel surfaces are virtually connected in a way that the flux coming out from one is introduced into the other, and *vice versa*. This condition is used to model infinite replicas of a geometry.
- Conformal uniaxial perfect match layer. The conformity of the PML geometry is defined making use of canonical geometries: planes, spheres, cylinders, and toroids.
- First-order impedance boundary condition. This boundary condition can effectively truncate TEM ports as coaxial, avoiding the use of PML. It can also be used to truncate the space, resulting the so-called first-order Silver-Müller absorbing boundary condition.

The treatment of the boundary conditions and material properties are included in the element matrices stored in the memory. Following this approach, time-marching is a very simple algorithm based only on vector-matrix products element-by-element.

A.4.2 Electromagnetic Sources

SEMBA makes use of the flux terms to excite the structures under analysis, following the Huygens principle. The sources are surface-current distributions which weakly inject the incident fields. This approach can be seen as the traditional incident-wave source condition or total-field/scattered-field technique.

Let us consider that, inside a Total-Field Zone (TFZ), a known wave is propagating, while outside of it (Scattered-Field Zone (SFZ)) the field is null. If \mathbf{E}^{inc} , \mathbf{H}^{inc} denote the wave fields at each point of the TFZ/SFZ interface (see Figure A.6), the flux across the face of an element m in the TFZ (with this face lying on the TFZ/SFZ interface) needs to take into account the equivalent surface currents

$$\begin{aligned}\mathbf{M}_s &= \hat{\mathbf{n}}^m \times \mathbf{E}^{inc} \\ \mathbf{J}_s &= -\hat{\mathbf{n}}^m \times \mathbf{H}^{inc}\end{aligned}$$

and if m is in the scattered field zone

$$\begin{aligned}\mathbf{M}_s &= -\hat{\mathbf{n}}^m \times \mathbf{E}^{inc} \\ \mathbf{J}_s &= \hat{\mathbf{n}}^m \times \mathbf{H}^{inc}\end{aligned}$$

This technique can be applied to incorporate any incident field. The different sources implemented in SEMBA are listed below:

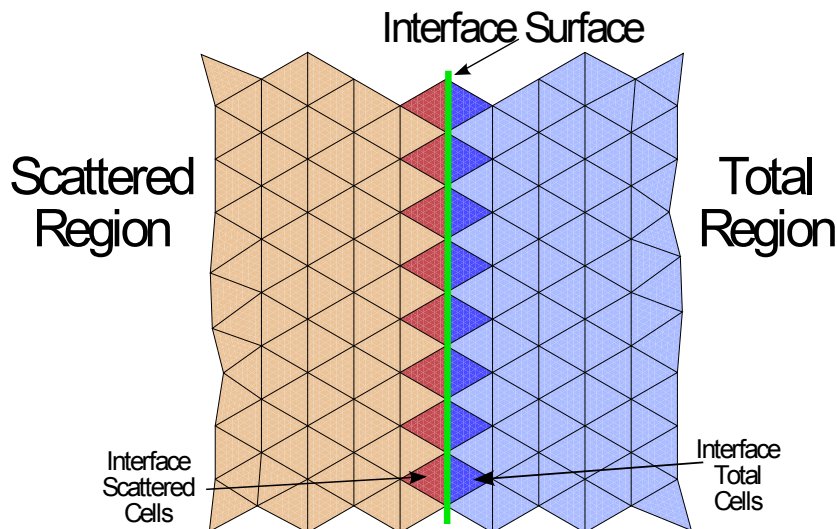


FIGURE A.6: Total field/scattered field decomposition. 2D representation.

- Plane-wave illumination.
- Coaxial port.
- TE₁₀ rectangular waveguide port.
- TE₁₁ circular waveguide port.
- Delta-gap port.

A.4.3 General Time-Marching Algorithm

The time-marching algorithm is based on the LTS LF scheme described in Section 3.5.2.3. The different steps are summarized below for $L = 2$, completed with the required MPI communications. The algorithm can be easily generalized to any problem with L levels.

- *Step 1.1. MPI communication of the electric dof: level 1.*
- *Step 1.2. Update magnetic dof: level 1, interface and level 2.*
- *Step 2.1. MPI communication of the magnetic dof: level 1, interface and level 2.*
- *Step 2.2. Update electric dof: level 1 and interface.*
- *Step 3.1. MPI communication of the electric dof: level 1 and interface.*
- *Step 3.2. Update magnetic dof: level 1.*
- *Step 4.1. MPI communication of the magnetic dof: level 1.*

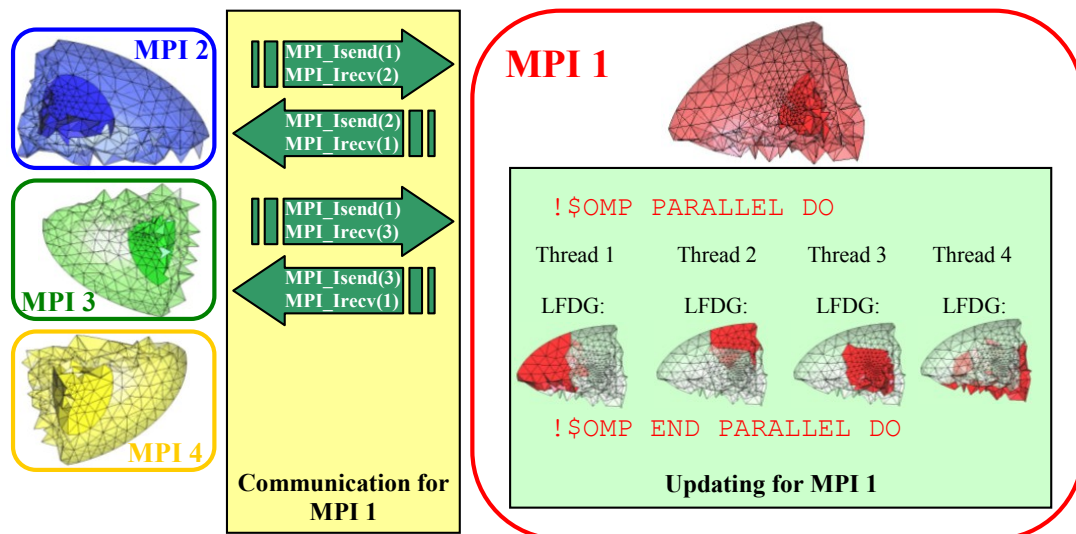


FIGURE A.7: MPI communication and updating schemes. The communication for the MPI 1 process takes place between the MPI 2 and MPI 3 processes. MPI 1 and MPI 4 are not in contact, so that no communication is required between them. Within the MPI processes, each thread updates the electromagnetic dof of a group of elements, making use of the LFDG algorithm.

- *Step 4.2. Update electric dof: level 1, interface and level 2.*
- *Step 5.1. MPI communication of the electric dof: level 1, interface and level 2.*
- *Step 5.2. Update magnetic dof: level 1 and interface.*
- *Step 6.1. MPI communication of the magnetic dof: level 1 and interface.*
- *Step 6.2. Update electric dof: level 1.*

Prior to each step of the LTS algorithm, a MPI communication of the fields (magnetic in case of electric-field updating, and *vice versa*), between adjacent MPI processes needs to be performed. The amount of data to be exchanged differs for each LTS step (sometimes no data), depending on the required samples, since not all elements are updated at each LTS step. Each updating step is computed in parallel by N multiple threads by making use of OMP directives (shared-memory multiprocessing), so that each thread takes care of updating a group of element. This is the core of the two-level parallelization of SEMBA (hybrid MPI/OMP) depicted in Figure A.7.

A.5 Postprocessing

SEMBA can provide the following postprocessing observables:

- Near-to-far field transformation for radiation patterns and RCS computations.
- S-parameter computations in ports (coaxial, TE₁₀ rectangular waveguide, TE₁₁ circular waveguide, and delta-gap).
- Impedance computations in ports.
- Current and voltage computations.
- Time/frequency domain field probes.
- Surface-density fields (time animations).

It is important to note that most of the postprocessing work is performed during the simulation stage. The main advantages of doing so in this way are: (i) to avoid saving a large amount of information in the hard disk and (ii) to preserve the parallelization of the algorithm, since none of the MPI processes knows the whole geometry of the problem. The postprocessing itself is also parallelized.

A.6 Performance

This section offers an overview of the performance of SEMBA and the difficulties of the proposed scheme from this standpoint.

The scalability of the implementation is tested here both for the MPI, and for the OMP parallelization levels, in two problems, one being a simple PEC sphere (of about 0.8 Mcells) and the other being the NASA Almond (with 3 Mcells) described in Section 5.3. In Figure A.8 the scalability with MPI and OMP is shown.

The test of OMP shows good scalability up to 6 threads, which are the cores per CPU, but poor scalability with 12 threads. This is the typical performance of the OMP parallelization technique. When the number of threads increases, the scalability is lost due to the cost of the management (creation and synchronization) of the threads. The scalability of the NASA Almond case is slightly higher because there are more cells to divide among the threads, and the weight of the management cost is slightly reduced in the overall computational cost.

For the MPI case, there is good scalability for the sphere in all cases, since it is very easy to distribute among all the processes due to the symmetry of the problem. In the case of the NASA Almond (for instance with 8 MPI processes), a symmetric distribution cannot be done, and there is no perfect scalability. There are crucial intrinsic features in the proposed method that make the distribution of the mesh a difficult task. On the

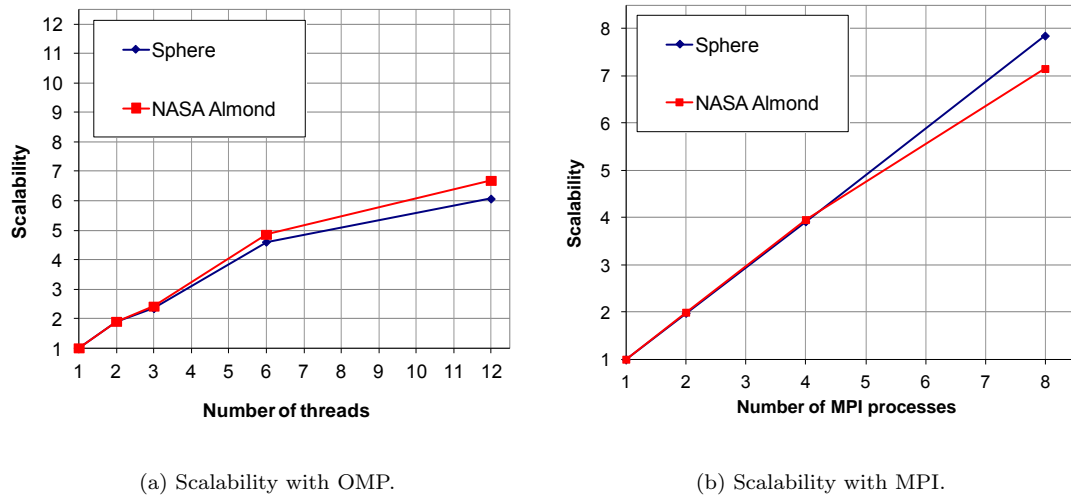


FIGURE A.8: SEMBA scalability. For the OMP case, two MPI processes have been executed with different threads, and for the MPI case, six OMP threads were used by each MPI process. The architecture of the computer was four nodes of two Intel Xeon X5680 6 cores (3.33Ghz) per node.

one hand, the cost per element is not constant (it depends on the order of the basis functions and whether it is PML or not), and, on the other hand, the LTS algorithm causes the workload to vary along the computation domain.

In terms of memory requirements, SEMBA shares some matrices among all the elements in a simulation, and others need to be kept in memory. Specifically, SEMBA needs to store at each tetrahedron (either in free-space or in a homogeneous material): the dof, one full local matrix, and two compressed matrices¹. In case of a PML element, it needs to store: the dof, four full local matrices, and one compressed matrix. The number of double-precision real numbers per simulation can be estimated as follows,

$$N_{real} = \sum_{m=1}^{M_{HOMO}} \left[2Q_m + Q_m^2 + 2\frac{Q_m^2}{3} \right] + \sum_{m=1}^{M_{PML}} \left[4Q_m + 4Q_m^2 + \frac{Q_m^2}{3} \right] \quad (\text{A.3})$$

with M_{HOMO} and M_{PML} being the number of elements in homogenous and PML domains, respectively, and Q_m the number of basis functions in the m element, which depends on the order p . Some additional memory is required in the interfaces of the LTS levels, but Equation (A.3) is a good estimation of the required memory. It is important to note that the main memory cost is in storing the local matrices. The alternative is the use of structured meshes in zones where there are no geometrical details, making it possible to share all the local matrices, and saving a large percentage of the memory.

¹Flux matrices can be compressed since are based on surface integrals, and some basis functions are zero in some faces of the tetrahedron (see Section 3.1.1).

Appendix B

Resumen de la Memoria

En esta Tesis se aborda el desarrollo de técnicas numéricas eficientes en el análisis de problemas realistas de propagación, radiación, dispersión y acoplamiento electromagnético. Para este objetivo, se investiga la utilización de elementos discontinuos de Galerkin (DG) y su aplicación a la resolución de las ecuaciones de Maxwell en el dominio del tiempo. Las principales aportaciones están basadas en la combinación del esquema de integración temporal del salto de la rana (LF) (junto con un algoritmo de avance local en tiempo (LTS)), con el método de discretización espacial DG. Nos referiremos al algoritmo propuesto como método discontinuo de Galerkin y salto de la rana (LFDG).

Se ha desarrollado la formulación espacial DG en su forma semi-discreta. La formulación se plantea de una forma general, unificando diferentes esquemas de evaluación de flujos, que han sido aplicados con éxito a este método. Se ha desarrollado un amplio rango de funcionalidades en el contexto de métodos DG, como las condiciones típicas de contorno (conductor eléctrico/magnético perfecto, condición de contorno de Silver-Müller de primer orden, interfaces entre materiales con propiedades eléctricas y/o magnéticas diferentes), modelización de materiales anisótropos, fuentes electromagnéticas (ondas planas, puertos coaxiales o en guía de onda, etc.), y condiciones de frontera conformes y uniaxiales perfectamente adaptadas. El esquema de integración LF se ha aplicado a la formulación DG semi-discreta, obteniendo el algoritmo LFDG. Además se propone un esquema de LTS explícito en combinación con el algoritmo LFDG.

Se han analizado el esquema semi-discreto DG y el algoritmo LFDG, y se han explorado los límites, en cuanto a precisión y coste computacional, del método LFDG. En primer lugar se revisa el problema de los modos espurios en el contexto de DG, y se estudian los espectros numéricos de ambos esquemas. Después, las relaciones numéricas de dispersión y disipación, y la convergencia y anisotropía de los errores de ambos métodos se comparan y analizan. Finalmente, se ha llevado a cabo un análisis en cuanto a coste

computacional frente a precisión del método LFDG, incluyendo una comparación con el método de diferencias finitas en el dominio del tiempo.

El algoritmo LFDG se ha implementado de forma paralela y escalable utilizando una técnica de programación híbrida OMP-MPI, en la que se explota la naturaleza paralela del algoritmo propuesto. Se demuestran las capacidades del método para calcular problemas eléctricamente grandes, manteniendo la precisión controlada, y considerando pequeños detalles geométricos gracias a la utilización del algoritmo de LTS. El método LFDG se ha aplicado a diferentes tipos de problemas electromagnéticos, comparando los resultados con medidas o con otros resultados obtenidos con diferentes métodos de cálculo. Finalmente, el algoritmo se ha validado y se han mostrado las propiedades más atractivas del método, que aún las ventajas de los métodos en el dominio del tiempo y de aquellos basados en elementos finitos.

B.1 Contribuciones Científicas y Futuras Líneas de Trabajo

Los objetivos principales que han guiado el desarrollo de esta Tesis han sido dos. El primero ha sido explorar las posibilidades que ofrece la discretización espacial basada en elementos discontinuos de Galerkin en la resolución de las ecuaciones de Maxwell en el dominio del tiempo. El segundo ha sido proponer, implementar y aplicar una de las alternativas de esta metodología denominada LFDG. A continuación se destacan las contribuciones científicas logradas a lo largo de este trabajo que sirve de resumen de los resultados obtenidos. Después aparece una lista de las futuras líneas de trabajo en esta área.

B.1.1 Contribuciones Científicas

Podemos resumir abreviadamente los logros conseguidos en este trabajo de investigación llevado en los siguientes puntos:

1. **Formulación del esquema espacial semi-discreto basado en elementos discontinuos de Galerkin.** La formulación se ha desarrollado de una forma general, unificando diferentes esquemas en la evaluación del flujo, que han sido aplicados con éxito a este método. La formulación incluye el tratamiento de las condiciones de contorno más comunes, materiales anisótropos y condiciones de contorno absorbentes, en particular las denominadas de Silver-Müller de primer

orden, además de las condiciones de frontera conformes y uniaxiales perfectamente adaptadas.

2. **Desarrollo del algoritmo LFDG.** El método de integración temporal conocido como salto de la rana se ha aplicado al esquema semi-discreto DG, obteniendo el algoritmo final LFDG. En este contexto, se ha desarrollado con éxito una estrategia de avance local en tiempo (LTS) que resuelve la limitación impuesta por la condición de estabilidad, crítica en los esquemas de discretización temporal explícitos.
3. **Análisis del esquema semi-discreto DG y del algoritmo LFDG.** La dispersión y la disipación de los métodos numéricos han sido estudiadas. El tema de los modos espurios ha sido revisado en detalle. Además, se han estimado los órdenes de convergencia de las relaciones de dispersión y disipación y estudiado la anisotropía de ambos errores. En el caso del algoritmo LFDG, se han estudiado otros temas como estabilidad y coste computacional. Se han explorado y evaluado los límites del algoritmo LFDG. Se ha llevado a cabo un análisis final estimando el coste computacional frente a precisión, comparando los resultados con el método de las diferencias finitas en el dominio del tiempo (FDTD).
4. **Implementación paralela.** Aprovechando la naturaleza paralela del algoritmo LFDG, su implementación se ha llevado a cabo haciendo uso de una técnica de programación híbrida OMP-MPI. Estos dos niveles de paralelización son habituales en los modernos ordenadores (número medio/alto de nodos, cada uno de ellos multi-CPU con memoria compartida, conectados con Infiniband, Myrinet o Gigabit).
5. **Validación y aplicación del algoritmo.** El algoritmo LFDG ha sido validado con filtros en microondas, antenas y problemas de dispersión electromagnética. Los resultados se han comparado con medidas u otras técnicas numéricas. El método ha sido aplicado a problemas reales de ingeniería, mostrando importantes propiedades: robustez, estabilidad, versatilidad, eficiencia, escalabilidad y precisión.

B.1.2 Futuras Líneas de Trabajo

Aunque muchos y muy diferentes métodos de cálculo electromagnético se han desarrollado en profundidad para estudiar la mayor parte de los problemas prácticos que nos encontramos en ingeniería, todavía existen vacíos para los que se hace imprescindible explorar nuevas técnicas. En esta Tesis, se ha desarrollado e implementado desde cero

un método que combina las ventajas de los métodos basados en elementos finitos para la integración espacial, y uno explícito para la temporal. En opinión del autor, algunas líneas de investigación para ampliar las capacidades del método son:

1. **Desarrollo e implementación de capacidades adicionales.** La técnica LFDG tiene muchas similitudes con FDTD. Por tanto, la mayor parte de las capacidades extensamente evaluadas y validadas en el método FDTD pueden ser adaptadas a LFDG. Entre ellos: modelos de capa delgada dispersivos y/o anisótropos, tratamiento de materiales dispersivos, elementos circuitales discretos, modelos de hilo delgado, ranuras delgadas, etc..
2. **Mejora de la convergencia de la integración temporal.** Aunque el algoritmo LFDG permite fácilmente la elección en cada uno de los elementos del orden de las funciones base de la discretización espacial de los campos electromagnéticos, la principal limitación del método es el bajo orden de convergencia del esquema de integración temporal. Ello impone un límite en el uso de técnicas de refinamiento p . El algoritmo de integración temporal debería mejorarse para permitir la selección, elemento a elemento, como en el caso espacial, del orden de convergencia de la discretización temporal. Además, diferentes alternativas de LTS pueden ser exploradas para aproximarse a la utilización del salto temporal óptimo en cada elemento.
3. **Mejora de la versatilidad en el uso de métodos de elementos finitos en el dominio del tiempo (FEMTD), en general.** Diferentes alternativas podrían ser desarrolladas para mejorar la versatilidad de los métodos FEMTD en simulaciones reales. Algunas son las siguientes: (i) utilización de mallas híbridas que contengan diferentes tipos de celdas, aprovechando las diferentes propiedades de cada una de ellas, por ejemplo tetraedros en regiones complejas, hexaedros en regiones sin detalles, y pirámides en las interfaces; (ii) utilización de mallas estructuradas/no estructuradas, para reducir el uso de memoria en zonas estructuradas donde las matrices locales pueden compartirse; o (iii) el uso de elementos no conformes que permitan refinar localmente la malla, muy efectivo en la aplicación de técnicas de refinamiento h , y en la simulación de problemas con un alto contraste en las propiedades de los materiales.
4. **Desarrollo de técnicas de adaptatividad tipo hp .** Los problemas electromagnéticos tratados en este trabajo demuestran la importancia de la utilización de adaptabilidad tipo hp . El desarrollo de técnicas de adaptación eficientes tipo hp en simulaciones en el dominio del tiempo permitirá la aplicación del método de una forma más automática y ciega. Para ello, un punto crucial es una estrecha integración del mallador en el simulador electromagnético. El desarrollo de

técnicas dinámicas de adaptatividad hp espaciales y de orden arbitrario en tiempo, capaces de adaptar dinámicamente la malla y el método de integración durante la simulación, pueden reducir notablemente los tiempos de cálculo de una simulación completa asegurando la precisión requerida.

5. **Mejora de la aplicabilidad de métodos FEMTD.** Una de las principales dificultades de aplicabilidad de métodos FEMTD, comparados con FDTD, para el análisis de sistemas complejos (como un avión) es la generación de los modelos electromagnéticos y las mallas. El punto de partida para este tipo de análisis es una maqueta digital completa con todos los detalles de la estructura real (tornillos, remaches, agujeros, etc.). La simplificación de la maqueta electrónica para construir un modelo que contenga toda la información electromagnética, listo para ser mallado, requiere una gran cantidad de trabajo de ingeniería. Este proceso se optimizó para el método FDTD durante años, y hay disponibles herramientas comerciales que facilitan la tarea. El resultado de este proceso son mallas de diferencias finitas con miles de millones de celdas. En el caso de métodos FEMTD este proceso no está maduro y debe desarrollarse para que la industria disponga de herramientas capaces de generar mallas de miles de millones de celdas en un tiempo razonable desde ambos puntos de vista, generación de la malla y desarrollo de un modelo electromagnético complejo.
6. **Simulación multi-física.** Existe una necesidad creciente de simulaciones acopladas térmicas-mecánicas-electromagnéticas capaces de manejar la complejidad de problemas reales (por ejemplo en la predicción de efectos de impacto de un rayo en estructuras de materiales compuestos). El uso de mallas no estructuradas basadas en tetraedros simplifica el acoplamiento multi-físico de diferentes modelos numéricos, que también utilizan este tipo de mallas.

Bibliography

- [1] K. S. Yee, “Numerical solution of initial boundary value problems involving Maxwell’s equations in isotropic media,” *IEEE Transactions on Antennas and Propagation*, vol. Ap14, no. 3, pp. 302–307, 1966.
- [2] P. B. Johns and R. L. Beurle, “Numerical solutions of 2-dimensional scattering problems using a transmission-line matrix,” *IEE Proceedings*, vol. 118, no. 9, pp. 1203–1208, 1971.
- [3] T. Weiland, “A discretization method for the solution of Maxwell’s equations for six-component fields,” *Archiv fuer Elektronik und Uebertragungstechnik*, vol. 31, no. 3, pp. 116–120, March 1977.
- [4] K. K. Mei, “Unimoment method of solving antenna and scattering problems,” *IEEE Transactions on Antennas and Propagation*, vol. 22, no. 6, pp. 760–766, November 1974.
- [5] Z. J. Cendes, D. N. Shenton, and H. Shahnasser, “Magnetic field computation using Delaunay triangulation and complementary finite element methods,” *IEEE Transactions on Magnetics*, vol. 19, no. 6, pp. 2551–2554, November 1983.
- [6] T. Orikasa, S. Washisu, T. Honma, and I. Fukai, “Finite element method for unbounded field problems and application to two-dimensional taper,” *International Journal for Numerical Methods in Engineering*, vol. 19, no. 2, pp. 157–168, February 1983.
- [7] S. Salon, “The hybrid finite element-boundary element method in electromagnetics,” *IEEE Transactions on Magnetics*, vol. 21, no. 5, pp. 1829–1834, September 1985.
- [8] A. Bossavit and J. C. Verite, “A mixed FEM-BIEM method to solve 3-D eddy current problems,” *IEEE Transactions on Magnetics*, vol. 18, no. 2, pp. 431–435, March 1982.

- [9] D. N. Shenton and Z. J. Cendes, "Three-dimensional finite element mesh generation using Delaunay tessellation," *IEEE Transactions on Magnetics*, vol. 21, no. 6, pp. 2535–2538, November 1985.
- [10] M. L. Barton and Z. J. Cendes, "New vector finite elements for three-dimensional magnetic field computation," *Journal of Applied Physics*, vol. 61, no. 6, pp. 3919–3921, April 1987.
- [11] J. F. Lee, R. Lee, and A. Cangellaris, "Time-domain finite-element methods," *IEEE Transactions on Antennas and Propagation*, vol. 45, no. 3, pp. 430–442, March 1997.
- [12] D. R. Lynch and K. D. Paulsen, "Time-domain integration of the Maxwell equations on finite elements," *IEEE Transactions on Antennas and Propagation*, vol. 38, no. 12, pp. 1933–1942, December 1991.
- [13] G. Mur, "The finite-element modeling of three-dimensional time-domain electromagnetic fields in strongly inhomogeneous media," *IEEE Transactions on Magnetics*, vol. 28, no. 2, pp. 1130–1133, March 1992.
- [14] J. F. Lee and Z. Sacks, "Whitney elements time domain (WETD) methods," *IEEE Transactions on Magnetics*, vol. 31, no. 3, pp. 1325–1329, May 1995.
- [15] J. F. Lee, "WETD-A finite element time-domain approach for solving Maxwell's equations," *IEEE Microwave and Guided Wave Letters*, vol. 4, no. 1, pp. 11–13, January 1994.
- [16] S. D. Gedney and U. Navsariwala, "An unconditionally stable finite-element time-domain solution of the vector wave equation," *IEEE Microwave Guided Wave Letters*, vol. 5, no. 10, pp. 332–334, October 1995.
- [17] J. M. Jin, M. Zunoubi, K. C. Donepudi, and W. C. Chew, "Frequency-domain and time-domain finite-element solution of Maxwell's equations using spectral Lanczos decomposition method," *Computation Methods in Applied Mechanics and Engineering*, vol. 169, no. 3–4, pp. 279–296, February 1999.
- [18] W. P. Carpes Jr, L. Pichon, and A. Razek, "A 3D finite element method for the modeling of bounded and unbounded electromagnetic problems in the time domain," *International Journal of Numerical Modelling: Electronic Networks, Devices and Fields*, vol. 13, no. 6, pp. 527–540, 2000.
- [19] D. Jiao and J. M. Jin, "A general approach for the stability analysis of the time-domain finite-element method for electromagnetic simulations," *IEEE Transactions on Antennas and Propagation*, vol. 50, no. 11, pp. 1624–1632, November 2002.

- [20] ———, “Three-dimensional orthogonal vector basis functions for time-domain finite element solution of vector wave equations,” *IEEE Transactions on Antennas and Propagation*, vol. 51, no. 1, pp. 59–65, January 2003.
- [21] Z. Lou and J. M. Jin, “Modeling and simulation of broad-band antennas using the time-domain finite element method,” *IEEE Transactions on Antennas and Propagation*, vol. 53, no. 12, pp. 4099–4110, December 2005.
- [22] R. Wang, H. Wu, A. C. Cangellaris, and J. M. Jin, “Incorporation of a feed network into the time-domain finite-element modeling of antenna arrays,” *IEEE Transactions on Antennas and Propagation*, vol. 56, no. 8, pp. 2599–2612, August 2008.
- [23] R. N. Rieben, G. H. Rodrigue, and D. A. White, “A high order mixed vector finite element method for solving the time dependent Maxwell equations on unstructured grids,” *Journal of Computational Physics*, vol. 204, pp. 490–519, 2005.
- [24] B. He and F. L. Teixeira, “Sparse and explicit FETD via approximate inverse Hodge (mass) matrix,” *IEEE Microwave and Wireless Components Letters*, vol. 16, no. 6, pp. 348–350, June 2006.
- [25] ———, “Differential forms, Galerkin duality, and sparse inverse approximations in finite element solutions of Maxwell equations,” *IEEE Transactions on Antennas and Propagation*, vol. 55, no. 5, pp. 1359–1368, May 2007.
- [26] B. Donderici and F. L. Teixeira, “Conformal perfectly matched layer for the mixed finite element time-domain method,” *IEEE Transactions on Antennas and Propagation*, vol. 45, no. 4, pp. 1017–1026, April 2008.
- [27] ———, “Mixed finite-element time-domain method for transient Maxwell equations in doubly dispersive media,” *IEEE Transaction on Microwave Theory and Techniques*, vol. 56, no. 1, pp. 113–120, January 2008.
- [28] R. S. Chen, L. Du, Z. Ye, and Y. Yang, “An efficient algorithm for implementing the Crank-Nicolson scheme in the mixed finite-element time-domain method,” *IEEE Transaction on Antennas and Propagation*, vol. 57, no. 10, pp. 3216–3222, October 2009.
- [29] S. G. Garcia, M. F. Pantoja, C. M. de Jong van Coevorden, A. R. Bretones, and R. G. Martin, “A new hybrid DGTD/FDTD method in 2-D,” *IEEE Microwave and Wireless Components Letters*, vol. 18, no. 12, pp. 764–766, December 08.
- [30] W. H. Reed and T. R. Hill, “Triangular mesh methods for the neutron transport equation,” *Los Alamos Scientific Laboratory*, vol. Technical report LA-UR-73-479, 1973.

-
- [31] P. Lesaint and P. A. Raviart, *On a finite element method for solving the neutron transport equation, in Mathematical Aspects of Finite Elements in Partial Differential Equations*. San Diego: Academic Press, 1974.
- [32] C. Johnson and J. Pitkäranta, “An analysis of the discontinuous Galerkin method for a scalar hyperbolic equation,” *Mathematics of Computation*, vol. 46, no. 173, pp. 1–26, January 1986.
- [33] G. R. Richter, “An optimal-order error estimate for the discontinuous Galerkin method,” *Mathematics of Computation*, vol. 50, no. 181, pp. 75–88, 1988.
- [34] T. Peterson, “A note on the convergence of the discontinuous Galerkin method for a scalar hyperbolic equation,” *SIAM Journal on Numerical Analysis*, vol. 28, no. 1, pp. 133–140, February 1991.
- [35] K. S. Bey and J. T. Oden, “hp-version discontinuous Galerkin methods for hyperbolic conservation laws,” *Computer methods in applied mechanics and engineering*, vol. 133, no. 3–4, pp. 259–286, 1996.
- [36] B. Cockburn and C. W. Shu, “TVB Runge-Kutta local projection discontinuous Galerkin finite element method for conservation laws II: General framework,” *Mathematics of Computation*, vol. 52, pp. 411–435, 1989.
- [37] B. Cockburn, S. Hou, and C. W. Shu, “TVB Runge-Kutta local projection discontinuous Galerkin finite element method for conservation laws III: One-dimensional systems,” *Journal of Computational Physics*, vol. 84, pp. 90–113, 1989.
- [38] B. Cockburn, S. Y. Lin, and C. W. Shu, “The Runge-Kutta local projection discontinuous Galerkin finite element method for conservation laws IV: The multidimensional case,” *Mathematics of Computation*, vol. 54, pp. 545–581, 1990.
- [39] B. Cockburn and C. W. Shu, “The Runge-Kutta local projection P1-discontinuous Galerkin finite element method for scalar conservation laws,” *Modélisation Mathématique et Analyse Numérique*, vol. 25, pp. 337–361, 1991.
- [40] —, “The Runge-Kutta discontinuous Galerkin method for conservation laws V: Multidimensional systems,” *Journal of Computational Physics*, vol. 141, pp. 199–224, 1998.
- [41] F. Bassi and S. Rebay, “A high-order accurate discontinuous finite element method for the numerical solution of the compressible Navier-Stokes equations,” *Journal of Computational Physics*, vol. 131, pp. 267–279, 1997.

- [42] B. Cockburn and C. W. Shu, “The local discontinuous Galerkin finite element method for convection-diffusion systems,” *SIAM Journal on Numerical Analysis*, vol. 35, pp. 2440–2463, 1998.
- [43] C. E. Baumann and J. T. Oden, “The local discontinuous Galerkin finite element method for convection-diffusion systems,” *Computer Methods in Applied Mechanics and Engineering*, vol. 175, no. 3–4, pp. 311–341, July 1999.
- [44] R. B. Lowrie, P. L. Roe, and B. V. Leer, “A space-time discontinuous Galerkin method for the time-accurate numerical solution of hyperbolic conservation laws,” *AIAA Computational Fluid Dynamics Conference, 12th, San Diego, CA; UNITED STATES*, pp. 135–150, June 1995.
- [45] R. B. Lowrie, “Compact higher-order numerical methods for hyperbolic conservation laws,” Ph.D. dissertation, The University of Michigan, 1996.
- [46] F. Q. Hu, M. Y. Hussaini, and J. L. Mantney, “Low dissipation and low dispersion Runge-Kutta schemes for computational acoustics,” *Journal of Computational Physics*, vol. 124, no. 1, pp. 177–191, March 1996.
- [47] F. Q. Hu, M. Y. Hussaini, and P. Rasetarinera, “An analysis of the discontinuous Galerkin method for wave propagation problems,” *Journal of Computational Physics*, vol. 151, no. 2, pp. 921–946, May 1999.
- [48] F. Q. Hu and H. L. Atkins, “Eigensolution analysis of the discontinuous Galerkin method with nonuniform grids,” *Journal of Computational Physics*, vol. 182, no. 2, pp. 516–545, November 2002.
- [49] D. A. Kopriva, S. L. Woodruff, L. Stephen, and M. Y. Hussaini, “Computation of electromagnetic scattering with a non-conforming discontinuous spectral element method,” *International journal for numerical methods in engineering*, vol. 53, no. 1, pp. 105–122, 2002.
- [50] I. Perugia and D. Schötzau, “The hp-local discontinuous Galerkin method for low-frequency time-harmonic Maxwell equations,” *Mathematics of Computation*, vol. 72, no. 243, pp. 1179–1214, July 2003.
- [51] P. Houston, I. Perugia, and D. Schötzau, “Mixed discontinuous Galerkin approximation of the Maxwell operator,” *SIAM journal on numerical analysis*, vol. 42, no. 1, pp. 434–459, July 2005.
- [52] B. Cockburn, F. Li, and C. W. Shu, “Locally divergence-free discontinuous Galerkin methods for the Maxwell equations,” *Journal of Computational Physics*, vol. 194, pp. 588–610, 2004.

- [53] J. S. Hesthaven and T. Warburton, “Nodal high-order methods on unstructured grids - i. time-domain solution of Maxwell’s equations,” *Journal of Computational Physics*, vol. 181, pp. 186–211, 2002.
- [54] —, “High-order nodal discontinuous Galerkin methods for the Maxwell eigenvalue problem,” *Philosophical Transactions: Mathematical, Physical and Engineering Sciences*, vol. 362, no. 1816, pp. 493–524, March 2004.
- [55] T. Warburton and M. Embree, “The role of the penalty in the local discontinuous Galerkin method for Maxwell’s eigenvalue problem,” *Computer methods in applied mechanics and engineering*, vol. 195, no. 25–28, pp. 3205–3223, July 2006.
- [56] M. Ainsworth, “Dispersive and dissipative behaviour of high order discontinuous Galerkin finite element methods,” *Journal of Computational Physics*, vol. 198, pp. 106–130, 2004.
- [57] M. Ainsworth, P. Monk, and W. Muniz, “Dispersive and dissipative properties of discontinuous Galerkin finite element methods for the second-order wave equation,” *Journal of Scientific Computing*, vol. 27, no. 1–3, pp. 3205–3223, June 2006.
- [58] M. J. Grote, A. Schneebeli, and D. Schötzau, “Interior penalty discontinuous Galerkin method for Maxwell’s equations: Energy norm error estimates,” *Journal of Computational and Applied Mathematics*, vol. 204, no. 2, pp. 375–386, July 2007.
- [59] M. H. Chen, B. Cockburn, and F. Reitich, “High-order RKDG methods for computational electromagnetics,” *Journal of Scientific Computing*, vol. 22–23, pp. 205–226, June 2005.
- [60] D. Sármany, M. A. Botchev, and J. J. W. van der Vegt, “Dispersion and dissipation error in high-order Runge-Kutta discontinuous Galerkin discretisations of the Maxwell equations,” *Scientific Computing*, vol. 33, no. 1, pp. 47–74, October 2007.
- [61] L. Fezoui, S. Lanteri, S. Lohrengel, and S. Piperno, “Convergence and stability of a discontinuous Galerkin time-domain method for the 3D heterogeneous Maxwell equations on unstructured meshes,” *ESAIM: Mathematical Modelling and Numerical Analysis*, vol. 39, no. 6, pp. 1149–1176, June 2005.
- [62] G. Cohen, X. Ferrieres, and S. Pernet, “A spatial high-order hexahedral discontinuous Galerkin method to solve Maxwell’s equations in time domain,” *Journal of Computational Physics*, vol. 217, pp. 340–363, 2006.

- [63] G. Cohen and M. Duruflé, “Non spurious spectral-like element methods for Maxwell’s equations,” *Journal of Computational Mathematics*, vol. 25, no. 3, pp. 282–304, 2007.
- [64] E. Montseny, S. Pernet, X. Ferrières, and G. Cohen, “Dissipative terms and local time-stepping improvements in a spatial high order discontinuous Galerkin scheme for the time-domain Maxwell’s equations,” *Journal of Computational Physics*, vol. 227, pp. 6795–6820, 2008.
- [65] N. Canouet, L. Fezoui, and S. Piperno, “Discontinuous Galerkin time-domain solution of Maxwell’s equations on locally-refined nonconforming cartesian grids,” *Compe-the International Journal for Computation and Mathematics in Electrical and Electronic Engineering*, vol. 24, pp. 1381–1401, 2005.
- [66] H. Fahs, L. Fezoui, S. Lanteri, and F. Rapetti, “Preliminary investigation of a non-conforming discontinuous Galerkin method for solving the time-domain Maxwell equations,” *IEEE Transactions on Magnetics*, vol. 44, no. 6, pp. 1254–1257, 2008.
- [67] H. Fahs, “Development of a hp-like discontinuous Galerkin time-domain method on non-conforming simplicial meshes for electromagnetic wave propagation,” *Int. J. Numer. Anal. Mod.*, vol. 6, no. 2, pp. 193–216, 2009.
- [68] H. Fahs and S. Lanteri, “A high-order non-conforming discontinuous Galerkin method for time-domain electromagnetics,” *Journal of Computational and Applied Mathematics*, vol. 234, pp. 1088–1096, 2010.
- [69] H. Fahs, “Discontinuous Galerkin method for time-domain electromagnetic on curvilinear domains,” *Applied Mathematical Sciences*, vol. 4, no. 19, pp. 943–958, 2010.
- [70] J. S. Hesthaven and T. Warburton, *Nodal Discontinuous Galerkin Methods. Algorithms, Analysis, and Applications*. Springer Science+Business Media, LLC, 233 Spring Street, New York, NY 10013, USA: Springer, 2008.
- [71] R. Diehl, K. Busch, and J. Niegemann, “Comparison of low-storage Runge-Kutta schemes for discontinuous Galerkin time-domain simulations of Maxwell’s equations,” *Journal of Computational and Theoretical Nanoscience*, vol. 7, pp. 1–9, 2010.
- [72] M. Dumbser, M. Käser, and E. F. Toro, “An arbitrary high order discontinuous Galerkin method for elastic waves on unstructured meshes V: Local time stepping and p-adaptivity,” *Geophysical Journal International*, vol. 171, no. 23, pp. 695–717, 2007.

- [73] A. Taube, M. Dumbser, C. D. Munz, and R. Schneider, “A high-order discontinuous Galerkin method with time-accurate local time stepping for the Maxwell equations,” *International Journal of Numerical Modelling: Electronic Networks, Devices and Fields*, vol. 22, pp. 77–103, 2009.
- [74] H. Fahs, “High-order leap-frog based discontinuous Galerkin method for the time-domain Maxwell equations on non-conforming simplicial meshes,” *Numerical Mathematics-Theory Methods and Applications*, vol. 2, no. 3, pp. 275–300, 2009.
- [75] A. Catella, V. Dolean, and S. Lanteri, “An unconditionally stable discontinuous Galerkin method for solving the 2-D time-domain Maxwell equations on unstructured triangular meshes,” *IEEE Transactions On Magnetics*, vol. 44, no. 6, pp. 1250–1253, June 2008.
- [76] V. Dolean, H. Fahs, L. Fezoui, and S. Lanteri, “Locally implicit discontinuous Galerkin method for time domain electromagnetics,” *Journal of Computational Physics*, vol. 229, pp. 512–526, 2010.
- [77] —, “Hybrid explicit-implicit time integration for grid-induced stiffness in a DGTD method for time domain electromagnetics,” in *Spectral and High Order Methods for Partial Differential Equations*, ser. Lecture Notes in Computational Science and Engineering, J. Hesthaven and E. Rønquist, Eds. Springer Berlin Heidelberg, 2011, vol. 76, pp. 163–170.
- [78] J. M. Sanz-Serna and M. P. Calvo, *Numerical Hamiltonian Problems*. London, U.K.: Chapman and Hall, 1994.
- [79] S. Piperno, “DGTD methods using modal basis functions and symplectic local time-stepping: Application to wave propagation problems,” *Journal of Computational Physics*, vol. 217, pp. 340–363, 2006.
- [80] —, “Symplectic local time-stepping in non-dissipative DGTD methods applied to wave propagation problems,” *ESAIM: Mathematical Modelling and Numerical Analysis*, vol. 40, no. 5, pp. 815–841, 2006.
- [81] J. E. Flaherty, R. M. Loy, M. S. Shephard, B. K. Szymanski, J. D. Teresco, and L. H. Ziantz, “Adaptive local refinement with octree load-balancing for the parallel solution of three-dimensional conservation laws,” *Journal of Parallel and Distributed Computing*, vol. 47, no. 2, pp. 139–152, 1997.
- [82] R. W. Davies, K. Morgan, and O. Hassan, “A high order hybrid finite element method applied to the solution of electromagnetic wave scattering problems in the time domain,” *Computational Mechanics*, vol. 44, no. 3, pp. 321–331, 2009.

- [83] F. Edelvik and G. Ledfelt, "A comparison of time-domain hybrid solvers for complex scattering problems," *International Journal of Numerical Modelling: Electronic Networks, Devices and Fields*, vol. 15, no. 5–6, pp. 475–487, September – December 2002.
- [84] V. Shankar, A. H. Mohammadian, and W. F. Hall, "A time-domain finite-volume treatment for the Maxwell equations," *Electromagnetics*, vol. 10, no. 1–2, pp. 127–145, 1990.
- [85] A. H. Mohammadian, V. Shankar, and W. F. Hall, "Computation of electromagnetic scattering and radiation using a time-domain finite-volume discretization procedure," *Computer Physics Communications*, vol. 68, pp. 175–196, 1991.
- [86] A. V. Kabakian, V. Shankar, and W. F. Hall, "Unstructured grid-based discontinuous Galerkin method for broadband electromagnetic simulations," *Journal of Scientific Computing*, vol. 20, no. 3, pp. 405–431, June 2004.
- [87] T. Xiao and Q. H. Liu, "Three-dimensional unstructured-grid discontinuous Galerkin method for Maxwell's equations with well-posed perfectly matched layer," *Microwave and Optical Technology Letters*, vol. 46, no. 5, pp. 459–463, September 2005.
- [88] S. D. Gedney and J. A. Roden, "The uniaxial perfectly matched layer (UPML) truncation of FDTD lattices for generalized media," *URSI Radio Science Meeting, Baltimore MD*, 1996.
- [89] F. L. Teixeira and W. C. Chew, "Analytical derivation of a conformal perfectly matched absorber for electromagnetic waves," *Microwave Optical Technology Letters*, vol. 17, no. 4, pp. 231–236, 1998.
- [90] —, "General closed-form PML constitutive tensors to match arbitrary bianisotropic and dispersive linear media," *IEEE Microwave and Guided Wave Letters*, vol. 8, no. 6, pp. 223–225, June 1998.
- [91] W. C. Chew and W. H. Weedon, "A 3d perfectly matched medium from modified Maxwell's equations with stretched coordinates," *Microwave Optical Tech. Letters*, vol. 7, no. 13, pp. 599–604, 1994.
- [92] K. Sankaran, C. Fumeaux, and R. Vahldieck, "Cell-centered finite-volume-based perfectly matched layer for time-domain Maxwell system," *IEEE Transaction on Microwave Theory and Techniques*, vol. 54, no. 3, pp. 629–651, March 2006.
- [93] —, "Uniaxial and radial anisotropy models for finite-volume Maxwellian absorber," *IEEE Transaction on Microwave Theory and Techniques*, vol. 54, no. 12, pp. 4297–4304, December 2006.

- [94] C. Fumeaux, K. Sankaran, and R. Vahldieck, "Spherical perfectly matched absorber for finite-volume 3-D domain truncation," *IEEE Transaction on Microwave Theory and Techniques*, vol. 55, no. 12, pp. 2773–2781, December 2007.
- [95] S. Dosopoulos and J. F. Lee, "Interior penalty discontinuous Galerkin finite element method for the time-dependent first order Maxwell's equations," *IEEE Transactions on Antennas and Propagation*, vol. 58, no. 12, pp. 192–197, December 2010.
- [96] T. Lu and P. Z. W. Cai, "Discontinuous Galerkin methods for dispersive and lossy Maxwell's equations and PML boundary conditions," *Journal of Computational Physics*, vol. 200, no. 2, pp. 549–580, November 2004.
- [97] J. Niegemann, M. König, K. Stannigel, and K. Busch, "Higher-order time-domain methods for the analysis of nano-phonic systems," *Photonics and Nanostructures – Fundamentals and Applications*, vol. 7, no. 1, pp. 2–11, February 2009.
- [98] S. D. Gedney, C. Luo, J. A. Roden, R. D. Crawford, B. Guernsey, J. A. Miller, T. Kramer, and E. W. Lucas, "The discontinuous Galerkin finite-element time-domain method solution of Maxwell's equation," *Journal in Applied Computational Electromagnetics Society*, vol. 24, no. 2, pp. 129–142, April 2009.
- [99] S. D. Gedney and B. Zhao, "An auxiliary differential equation formulation for the complex-frequency shifted PML," *IEEE Transactions on Antennas and Propagation*, vol. 58, no. 3, pp. 838–847, March 2010.
- [100] T. Lu and P. Z. W. Cai, "Discontinuous Galerkin time-domain method for GPR simulation in dispersive media," *IEEE Transactions on Geoscience and Remote Sensing*, vol. 43, no. 1, pp. 72–80, January 2005.
- [101] K. Stannigel, M. König, J. Niegemann, and K. Busch, "Discontinuous Galerkin time-domain computations of metallic nanostructures," *Optics Express*, vol. 17, no. 17, pp. 14 934–14 947, 2009.
- [102] M. König, K. Busch, and J. Niegemann, "The discontinuous Galerkin time-domain method for Maxwell's equations with anisotropic materials," *Photonics and Nanostructures*, vol. 8, no. 4, pp. 303–309, 2010.
- [103] L. Pebernet, X. Ferrieres, S. Pernet, B. L. Michielsen, F. Rogier, and P. Degond, "Discontinuous Galerkin method applied to electromagnetic compatibility problems: Introduction of thin wire and thin resistive material models," *IET Science, Measurement and Technology*, vol. 2, no. 6, pp. 395–401, 2008.

- [104] S. Chun and J. Hesthaven, “High-order accurate thin layer approximations for time-domain electromagnetics. Part I. General metal backed coatings,” *Journal of Computational and Applied Mathematics*, vol. 231, no. 2, pp. 598–611, September 2009.
- [105] S. Chun, H. Haddar, and J. S. Hesthaven, “High-order accurate thin layer approximations for time-domain electromagnetics, Part II: Transmission layers,” *Journal of Computational and Applied Mathematics*, vol. 234, no. 8, pp. 2587–2608, August 2010.
- [106] N. Gödel, T. Warburton, and M. Clemens, “Modeling effects of electromagnetic waves on thin wires with a high-order discontinuous Galerkin method,” in *Spectral and High Order Methods for Partial Differential Equations*, ser. Lecture Notes in Computational Science and Engineering, E. M. R. J.S. Hesthaven, Ed. Springer Berlin Heidelberg, 2011, vol. 76, pp. 209–218.
- [107] S. Dosopoulos and J. F. Lee, “Interconnect and lumped elements modeling in interior penalty discontinuous Galerkin time-domain methods,” *Journal of Computational Physics*, vol. 229, no. 22, pp. 8521–8536, 2010.
- [108] M. Bernacki, L. Fezoui, S. Lanteri, and S. Piperno, “Parallel discontinuous Galerkin unstructured mesh solvers for the calculation of three-dimensional wave propagation problems,” *Applied Mathematical Modelling*, vol. 30, no. 8, pp. 744–763, August 2006.
- [109] M. Bernacki, S. Lanteri, and S. Piperno, “Time-domain parallel simulation of heterogeneous wave propagation on unstructured grids using explicit, non-diffusive, discontinuous Galerkin methods,” *Journal of Computational Acoustics*, vol. 14, no. 1, pp. 57–81, 2006.
- [110] A. Klöckner, T. Warburton, J. Bridge, and J. S. Hesthaven, “Nodal discontinuous Galerkin methods on graphics processors,” *Journal of Computational Physics*, vol. 228, no. 21, pp. 7863–7882, November 2009.
- [111] X. Ji, T. Lu, W. Cai, and P. Zhang, “Discontinuous Galerkin time domain (DGTD) methods for the study of 2-D waveguide-coupled microring resonators,” *Journal of Lightwave Technology*, vol. 23, no. 11, pp. 3864–3874, November 2005.
- [112] C. Chauvière, J. S. Hesthaven, and L. Lurati, “High-order DGTD methods for dispersive Maxwell’s equations and modelling of silver nanowire coupling,” *SIAM Journal on Scientific Computing*, vol. 28, no. 2, pp. 751–775, 2006.

- [113] Y. Shi and C. H. Liang, "Simulations of the left-handed medium using discontinuous Galerkin method based on the hybrid domains," *Progress In Electromagnetics Research*, vol. 63, pp. 171–191, 2006.
- [114] X. Ji, W. Cai, and P. Zhang, "High-order DGTD methods for dispersive Maxwell's equations and modelling of silver nanowire coupling," *International Journal for Numerical Methods in Engineering*, vol. 69, no. 2, pp. 308–325, January 2007.
- [115] H. Songoro, M. Vogel, and Z. Cendes, "Keeping time with Maxwell's equations," *Journal of Computational and Applied Mathematics*, vol. 11, no. 2, pp. 42–49, April 2010.
- [116] H. S. Consortium. (2008) HIRF SE project. [Online]. Available: <http://www.hirf-se.eu>
- [117] S. G. Garcia, J. Alvarez, L. D. Angulo, and M. R. Cabello. (2011) UGRFDTD EM solver. [Online]. Available: <http://maxwell.ugr.es/ugrfdtd/>
- [118] G. R. Liu and S. S. Quek, *The Finite Element Method. A practical course*. Linacre House, Jordan Hill, Oxford OX2 8DP 200 Wheeler Road, Burlington MA 01803: Elsevier Science, 2003.
- [119] O. C. Zienkiewicz and R. L. Taylor, *The Finite Element Method*. London: McGraw-Hill, 1988.
- [120] J. E. Akin, *Finite Elements for Analysis and Design*. San Diego: CA: Academic Press, 1994.
- [121] P. P. Silvester and R. L. Ferrari, *Finite Elements for Electrical Engineers*. Cambridge: Cambridge University Press, 1990.
- [122] D. S. Burnett, *Finite Element Analysis*. Reading: MA: Addison-Wesley, 1987.
- [123] GiD, *The personal pre and post processor*. <http://www.gidhome.com>: International Center for Numerical Methods in Engineering (CIMNE), Barcelona, Spain., 2010.
- [124] J. Manges, Y. Xingchao, and Z. Cendes, "Spurious modes in finite-element methods," *IEEE Magazine of Antennas and Propagation*, vol. 37, no. 5, pp. 12–24, October 1995.
- [125] A. F. Peterson, *Computational Methods for Electromagnetics*. 445 Hoes Lane, P. O. Box 1331, Piscataway, NJ 08855-1331: IEEE Press, 1998.
- [126] A. Bossavit, "A rationale for 'edge-elements' in 3-D fields computations," *IEEE Transactions on Magnetics*, vol. 24, pp. 74–79, 1988.

- [127] K. D. Paulsen and D. R. Lynch, "Elimination of vector parasites in finite element Maxwell solutions," *IEEE Transactions Microwave Theory and Techniques*, vol. 39, pp. 395–404, 1991.
- [128] G. Mur, "The fallacy of edge elements," *IEEE Transactions on Magnetism*, vol. 34, pp. 3244–3247, 1998.
- [129] J. C. Nédélec, "Mixed finite elements in R^3 ," *Numerische Mathematik*, vol. 35, pp. 315–341, 1980.
- [130] —, "A new family of mixed finite elements in R^3 ," *Numerische Mathematik*, vol. 50, pp. 57–81, 1986.
- [131] J. L. Volakis, A. Chatterjee, and L. Kempel, *Finite element methods for electromagnetics: antennas, microwave circuits and scattering applications*. New York: IEEE Press, 1998.
- [132] J. P. Webb, "Edge elements and what they can do for you," *IEEE Transactions on Magnetism*, vol. 29, pp. 1460–1465, 1993.
- [133] F. Kikuchi, "Mixed and penalty formulations for finite element analysis of an eigenvalue problem in electromagnetism," *Computer Methods in Applied Mechanics and Engineering*, vol. 64, pp. 509–521, 1987.
- [134] R. Otin, "Regularized Maxwell equations and nodal finite elements for electromagnetic field computations," *Electromagnetics*, vol. 30, pp. 190–204, 2010.
- [135] R. Otin, L. E. Garcia-Castillo, I. Martinez-Fernandez, and D. Garcia-Donoro, "Computational performance of a weighted regularized maxwell equation finite element formulation," *Progress In Electromagnetics Research*, vol. 136, pp. 61–77, 2013.
- [136] S. D. Gedney, C. Luo, B. Guernsey, J. A. Roden, R. Crawford, and J. A. Miller, "The discontinuous Galerkin finite element time domain method (DGFETD): A high order, globally-explicit method for parallel computation," *2007 IEEE International Symposium on Electromagnetic Compatibility*, pp. 1–3, July 2007.
- [137] J. P. Webb and S. McFee, "The use of hierarchal triangles in finite-element analysis of microwave and optical devices," *IEEE Transactions on Magnetism*, vol. 27, no. 5, pp. 4040–4043, September 1991.
- [138] J. P. Webb, "Hierarchal vector basis functions of arbitrary order for triangular and tetrahedral finite elements," *IEEE Transactions on Antennas and Propagation*, vol. 47, no. 8, pp. 1244–1253, August 1999.

- [139] P. B. Monk, “A mixed method for approximating Maxwell’s equations,” *SIAM Journal on Numerical Analysis*, vol. 28, no. 6, pp. 1610–1634, December 1991.
- [140] J. L. Volakis, K. Sertel, and B. C. Usner, *Frequency Domain Hybrid Finite Element Methods for Electromagnetics*. Morgan & Claypool Publishers, 2006.
- [141] S. Wang, R. Lee, and F. L. Teixeira, “Anisotropic-medium PML for vector FETD with modified basis functions,” *IEEE Transactions on Antennas and Propagation*, vol. 54, no. 1, pp. 20–27, January 2006.
- [142] R. A. Chilton and R. Lee, “The discrete origin of FETD-Newmark latetime instability, and a correction scheme,” *Journal of Computational Physics*, vol. 224, no. 2, pp. 1293–1306, January 2007.
- [143] J. C. Nédélec, *Acoustic and Electromagnetic Equations*. Berlin, Heidelberg: Springer-Verlag, 2001.
- [144] K. Sankaran, “Accurate domain truncation techniques for time-domain conformal methods,” Ph.D. dissertation, ETH Zurich, Switzerland, 2007.
- [145] J. M. Jin and W. C. Chew, “Combining PML and ABC for finite element analysis of scattering problems,” *Microwave and Optical Technology Letters*, vol. 12, no. 4, pp. 192–197, July 1996.
- [146] Y. Xiao and Y. Lu, “Combining PML and ABC for scattering problem,” *IEEE Transactions on Magnetics*, vol. 37, no. 5, pp. 3510–3513, September 2001.
- [147] R. J. Leveque, *Finite-Volume Methods for Hyperbolic Problems*. Cambridge: Cambridge University Press, 2004.
- [148] B. Engquist and A. Majda, “Radiation boundary condition for the numerical simulation of waves,” *Mathematics of Computation*, vol. 31, pp. 629–651, 1977.
- [149] R. Higdon, “Absorbing boundary conditions for difference approximations to the multi-dimensional wave equation,” *Mathematics of Computation*, vol. 47, pp. 437–459, 1986.
- [150] ———, “Numerical absorbing boundary conditions for the wave equation,” *Mathematics of Computation*, vol. 47, pp. 65–90, 1987.
- [151] J. Blaschak and G. Kriegsmann, “A comparative study of absorbing boundary conditions,” *Journal Computational Physics*, vol. 77, pp. 109–139, 1988.
- [152] J. P. Bérenger, “A perfectly matched layer for the absorption of electromagnetic waves,” *Journal of Computational Physics*, vol. 114, no. 2, pp. 185–200, October 1994.

- [153] ———, “Numerical reflection from FDTD-PMLs: A comparison of the split PML with the unsplit and CFS PMLs,” *IEEE Transaction on Antennas and Propagation*, vol. 50, no. 3, pp. 258–265, March 2002.
- [154] K. P. Hwang and J. M. Jin, “Application of a hyperbolic grid generation technique to a conformal PML implementation,” *IEEE Microwave Guided Wave Letters*, vol. 9, no. 4, pp. 137–139, April 1999.
- [155] J. H. Williamson, “Low-storage Runge-Kutta schemes,” *Journal Computational Physics*, vol. 35, no. 1, pp. 48–56, March 1980.
- [156] M. H. Carpenter and C. A. Kennedy, “Fourth-order 2n-storage Runge-Kutta schemes,” *NASA-TM-109112*, pp. 1–24, 1994.
- [157] A. Taflove, *Computational Electrodynamics: The Finite-Difference Time-Domain Method*. Boston: Artech House, 1995.
- [158] A. J. Jerri, “The Shannon sampling theorem-Its various extensions and applications: A tutorial review,” *Proceedings of the IEEE*, vol. 65, no. 11, pp. 1565–1596, nov. 1977.
- [159] J. L. Mead and R. A. Renauty, “Optimal Runge-Kutta methods for first order pseudospectral operators,” *Journal of Computational Physics*, vol. 152, pp. 404–419, 1999.
- [160] J. R. Montejo-Garai and J. Zapata, “Full-wave design and realization of multi-coupled dual-mode circular waveguide filters,” *IEEE Transaction on Microwave Theory and Techniques*, vol. 43, no. 6, pp. 1290–1297, June 1995.
- [161] F. Alessandri, M. Chiodetti, A. Giugliarelli, D. Maiarelli, G. Martirano, D. Schmitt, L. Vanni, and F. Vitulli, “The electric-field integral-equation method for the analysis and design of a class of rectangular cavity filters loaded by dielectric and metallic cylindrical pucks,” *IEEE Transaction on Microwave Theory and Techniques*, vol. 52, no. 8, pp. 1790–1797, August 2004.
- [162] C. E. Brench and O. M. Ramahi, “Source selection criteria for FDTD models,” *1998 IEEE International Symposium on Electromagnetic Compatibility*, vol. 1, no. 1, pp. 491–494, 1998.
- [163] T. W. Hertel and G. S. Smith, “On the convergence of common FDTD feed models for antennas,” *IEEE Transactions on Antennas and Propagation*, vol. 51, no. 8, pp. 1771–1779, August 2003.

-
- [164] A. C. Woo, H. T. G. Wang, M. J. Schuh, and M. L. Sanders, "Benchmark radar targets for the validation of computational electromagnetic programs," *IEEE Antennas and Propagation Magazine*, vol. 35, no. 1, pp. 84–89, February 1993.
- [165] M. Taskinen and P. Yla-Oijala, "Current and charge integral equation formulation," *IEEE Transactions on Antennas and Propagation*, vol. 54, no. 1, pp. 58–67, January 2006.
- [166] M. Taskinen and P. S. Vanska, "Current and charge integral equation formulations and Picard's extended Maxwell system," *IEEE Transactions on Antennas and Propagation*, vol. 55, no. 12, pp. 3495–3503, December 2007.
- [167] *Workshop EM JINA, Nice, France*, November 2006.
- [168] X. Q. Sheng and Z. Peng, "Analysis of scattering by large objects with off-diagonally anisotropic material using finite element-boundary integral-multilevel fast multipole algorithm," *IET Microwaves, Antennas and Propagation*, vol. 4, no. 4, pp. 492–500, April 2010.

List of Publications

Journals Papers

- P1** J. Alvarez, J. M. Alonso-Rodriguez, H. Carbajosa-Cobaleda, M. R. Cabello, R. Gomez-Martin, and S. G. Garcia, "The NASA Almond: a benchmark for DGTD, MoM and FDTD methods," *IEEE Microwave and Wireless Components Letters*, vol. (submitted), no. –, pp. –, Month 2014.
- P2** G. G. Gutierrez, J. Alvarez, E. Pascual-Gil, B. Mauro, R. Guidi, V. Martorelli, and S. G. Garcia, "HIRF virtual testing on C-295 aircraft validated with FSV method," *IEEE Transaction on Electromagnetic Compatibility*, vol. (submitted), no. –, pp. –, Month 2014.
- P3** L. D. Angulo, J. Alvarez, F. Teixeira, A. R. Bretones, and S. G. Garcia, "Causal-Path Local Time-Stepping in the Discontinuous Galerkin Method for Maxwell's equations," *Journal of Computational Physics*, vol. (submitted), no. –, pp. –, 2014.
- P4** I. D. Flintoft, J. F. Dawson, S. G. Garcia, and J. Alvarez, "Digital filter implementation of an anisotropic surface impedance boundary condition in FDTD," *IEEE Transaction on Electromagnetic Compatibility*, vol. (submitted), no. –, pp. –, Month 2013.
- P5** J. Alvarez, L. D. Angulo, A. R. Bretones, and S. G. Garcia, "An analysis of the Leap-Frog Discontinuous Galerkin method for Maxwell equations," *IEEE Transactions on Antennas and Propagation*, vol. (submitted), no. –, pp. –, Month 2014.
- P6** J. Alvarez, L. D. Angulo, A. R. Bretones, C. M. Jong, and S. G. Garcia, "An efficient DGTD method including local time-stepping: application to antenna modeling," *IEEE Transactions on Antennas and Propagation*, vol. (submitted), no. –, pp. –, Month 2013.

- P7** J. Alvarez, L. D. Angulo, A. R. Bretones, and S. G. Garcia, "A leap-frog discontinuous Galerkin time-domain method for HIRF assessment," *IEEE Transaction on Electromagnetic Compatibility*, vol. (accepted), no. –, pp. –, Month 2013.
- P8** R. Jauregui, J. Alvarez, F. Silva, and S. G. Garcia, "Mesh generation in FDTD: guidelines and applications," *International Journal on Communications Antenna and Propagation*, vol. 2, no. 6, pp. 392–399, December 2012.
- P9** H. Lin, M. F. Pantoja, L. D. Angulo, J. Alvarez, R. G. Martina, and S. G. Garcia, "FDTD modeling of graphene devices using complex conjugate dispersion material model," *IEEE Microwave and Wireless Components Letters*, vol. 22, no. 12, pp. 612–614, December 2012.
- P10** J. Alvarez, L. D. Angulo, A. R. Bretones, C. de Jong, and S. G. Garcia, "3D discontinuous Galerkin time domain method for anisotropic materials," *IEEE Antennas and Wireless Propagation Letters*, vol. 11, pp. 1182–1185, 2012.
- P11** J. Alvarez, L. D. Angulo, A. R. Bretones, and S. G. Garcia, "A spurious-free discontinuous Galerkin time domain for the accurate modeling of microwave filters," *IEEE Transactions on Microwave Theory and Techniques*, vol. 60, no. 8, pp. 2359–2369, August 2012.
- P12** G. G. Gutierrez, S. F. Romero, J. Alvarez, S. G. Garcia, and E. P. Gil, "On the use of FDTD for HIRF validation and certification," *Progress In Electromagnetics Research Letters*, vol. 32, pp. 145–156, 2012.
- P13** L. D. Angulo, J. Alvarez, S. G. Garcia, and A. R. Bretones "Discontinuous Galerkin time-domain method for GPR simulation of conducting objects," *Near Surface Geophysics*, vol. 9, no. 3, pp. 257–263, June 2011.
- P14** J. Alvarez, L. D. Angulo, M. A. Fernandez Pantoja, A. R. Bretones, and S. G. Garcia, "Source and boundary implementation in vector and scalar DGTD," *IEEE Transactions on Antennas and Propagation*, vol. 58, no. 6, pp. 1997–2003, June 2010.
- P15** S. G. Garcia, F. Costen, M. Fernandez Pantoja, L. D. Angulo, and J. Alvarez, "Efficient excitation of waveguides in Crank-Nicolson FDTD," *Progress In Electromagnetics Research Letters*, vol. 17, pp. 39–46, 2010.
- P16** J. Alvarez, I. Gomez-Revuelto, J. M. Alonso, L. E. Garcia-Castillo, and M. Salazar-Palma, "Fully coupled multi-hybrid FEM-MoM-PO method for scattering and radiation problems," *Electromagnetics*, vol. 30, no. 1 & 2, pp. 3–22, January 2010.

Conference Proceedings

- P17** J. Alvarez, L. D. Angulo, A. R. Bretones, and S. G. García, "A comparison of the FDTD and LFDG methods for the estimation of HIRF transfer functions", *CEMEMC'13 Proceedings*, Granada, Spain, March 19-21, 2013.
- P18** G. Gutiérrez, E. Pascual, J. Alvarez, S. Fernández-Romero, and S. G. García, "LLSC Test for Shielded Harness using FDTD", *CEMEMC'13 Proceedings*, Granada, Spain, March 19-21, 2013.
- P19** J. Alvarez and S. G. Garcia, "Test case 2. EBG material. Test case 3a. Meta-Surface crossRoll. Test case 3b. Passive reflectarray antenna. Test case 7. Planar triplate stripline filter," *Proc. Workshop EM ISAE Radar Signatures 2012*, Toulouse, France, November 2012.
- P20** J. Alvarez, "Advances in time domain computational electromagnetics," *1th EM'tics Workshop*, Manching, Germany, October 2012.
- P21** J. Alvarez, L. Angulo, M. Bandinelli, H. D. Brüns, M. Francavilla, S. Garcia, R. Guidi, G. G. Gutierrez, C. Jones, M. Kunze, J. P. Martinaud, I. Munteanu, M. Panitz, J. P. Parmantier, P. Pirinoli, Z. Řezníček, G. Salin, A. Schröder, P. Tobola, and F. Vipiana, "HIRF interaction with metallic aircrafts. A comparison between TD and FD methods," *Proc. EMC Europe 2012*, Rome, Italy, September 2012.
- P22** G. G. Gutierrez, S. F. Romero, J. Alvarez, S. G. Garcia, and E. Pascual-Gil, "Strategies for HIRF simulations using FDTD," *Proc. EMC Europe 2012*, Rome, Italy, September 2012.
- P23** J. Alvarez, L. Angulo, M. Bandinelli, H. D. Brüns, M. Francavilla, S. Garcia, R. Guidi, G. G. Gutierrez, C. Jones, M. Kunze, J. P. Martinaud, I. Munteanu, M. Panitz, J. P. Parmantier, P. Pirinoli, Z. Řezníček, G. Salin, A. Schröder, P. Tobola, and F. Vipiana, "EV55: A numerical workbench to test TD/FD codes in HIRF EMC assessment," *Proc. EUROEM European Electromagnetic 2012*, Toulouse, France, July 2012.
- P24** J. Alvarez, G. G. Gutierrez, L. D. Angulo, H. Lin, A. R. Bretones, and S. G. Garcia, "Novel time domain FE/FD solvers for EMC assessment," *8th Iberian Meeting on Computational Electromagnetics*, Sesimbra, Portugal, November 2011.
- P25** J. Alvarez, E. Pascual-Gil, and S. G. Garcia, "From current methods to finite elements for EMC in aerospace," *New and future trends in simulation, NAFEMS Seminar*, Madrid, Spain, October 2011.

- P26** J. Alvarez, S. G. Garcia, L. D. Angulo, and A. R. Bretones, "Computational electromagnetic tools for EMC in aerospace," *PIERS Proceedings*, pp. 1840–1844, Marrakesh, Morocco, March 2011.
- P27** L. D. Angulo, J. Alvarez, A. R. Bretones, and S. G. Garcia, "Time domain tools in EMC assesment in aeronautics," *Proc. EMC Europe 2010*, Wroclaw, Poland, September 2010.
- P28** J. Alvarez, L. D. Angulo, S. G. Garcia, M. A. Fernandez-Pantoja, and A. R. Bretones, "A comparison between centered/upwind nodal/vector basis formulations of DGTD," *Proc. 2010 IEEE AP-S/URSI-USNC International Symposium*, Toronto, Canada, July 2010.
- P29** L. D. Angulo, J. Alvarez, S. G. Garcia, M. A. Fernandez-Pantoja, and A. R. Bretones, "CDGTD: A new reduced-error method combining FETD and DGTD," *Proc. of 2010 IEEE AP-S/URSI-USNC International Symposium*, Toronto, Canada, July 2010.
- P30** J. M. Alonso-Rodriguez, E. Pascual-Gil, and J. Alvarez, "Test case 1. PLACYL. Test case 2. Dilectric cube. Test case 3. Cylinder with cavity. Test case 4. Multilayer conesphere," *Proc. Workshop EM ISAE Radar Signatures 2008*, Toulouse, France, November 2008.
- P31** J. Alvarez, I. Gomez-Revuelto, J. M. Alonso-Rodriguez, L. E. Garcia-Castillo, and M. Salazar-Palma, "Método multi-híbrido FEM-MoM-PO para el análisis de problemas de dispersión y radiación," *XXIII Simposium Nacional de la URSI*, Madrid, Spain, September 2008.
- P32** J. Alvarez, I. Gomez-Revuelto, L. E. Garcia-Castillo, and M. Salazar-Palma, "Fully coupled multi-hybrid FEM-MoM-PO method for the analysis of 3D scattering and radiation problems," *9th International Workshop on Finite Elements for Microwave Engineering*, Bonn, Germany, May 2008.

Curriculum Vitae

Personal Information

Name: Jesus Alvarez
Nationality: Spanish
Date of birth: October 21, 1978
E-mail: jesus@ieee.org

Education

2008 – 2013: University of Granada, Spain.
Ph.D. in Physics & Space Science.
Specialization in Applied Physics.
Dissertation: "A Discontinuous Galerkin Finite Element Method for the Time-Domain Solution of Maxwell Equations"
Advisor: Dr. Salvador Gonzalez Garcia

2006 – 2008: University Carlos III of Madrid, Spain.
M.Sc. Multimedia & Communications.
Specialization in Signal Processing.
Special award of Master Multimedia & Communications.
Dissertation: "Fully Coupled Multi-Hybrid FEM-MoM-PO Method for the Analysis of 3D Scattering and Radiation Problems"
Advisor: Dr. Luis Emilio Garcia-Castillo

1996 – 2001: University of Cantabria, Spain.
M.Sc. Telecommunications Engineering.
Specialization in Radiocommunications.
Dissertation: "Design, Mounting and Characterization of the First 17 GHz Transmitter Prototype of WIND-FLEX System"
Advisor: Dr. Amparo Herrera Guardado

Professional Experience

- 2006 – current: Sr. EMC/Antenna Engineer – Cassidian, EADS-CASA, Spain.
Aviation & Aerospace
 Involved in the development of state-of-the-art computational electromagnetic (EM) simulation tools (HIRF SE (www.hirf-se.eu), UGRFDTD (www.ugrfdtd.es), HPTESP-MAT, SEMBA).
 Responsible for the definition, development and integration (technical manager) of new technologies and R&T projects in the EMC department.
 Specialist in EM modelization and simulation: antennas (design and integration on platforms), RF devices, HIRF, RCS, lightning, and EMC.
 Responsible for antenna integration (performance, coupling and installation) in military aircrafts; Eurofighter 2000 and UAVs (ATLANTE, Talarion).
 Responsible for controlling and assessing electromagnetic environmental effects (E3) on aerospace systems during design, production, and integration in the aforementioned programs.
 Chairman of Computational EM for EMC workshop (www.cememc.org).
- 2008 – current: Researcher – University of Granada, Spain.
Scientific Research
 Doctor of Philosophy Ph.D. at Electromagnetism Group, University of Granada.
 Current research interests include time and frequency domain computational electromagnetics methods: Discontinuous Galerkin Time Domain (DGTD) Method, Finite-Difference Time-Domain (FDTD), Method of Moments (MoM), fast algorithms for integral equations, and High Performance Computing (HPC, MPI, OMP). Application of numerical methods to aeronautical problems: EMC, HIRF, lightning strike, antennas, NEMP and RCS.
- 2009 – current: Part-time Lecturer Master Degree in Aircraft Systems Integration. University Carlos III of Madrid, Spain.
Higher Education
 A program oriented to develop competencies and skills for employees working for airframe manufacturers, (Airbus Military, Cassidian and Eurocopter). Responsible for 'Antenna Integration' subject, showing the engineering process for the integration of the complete set of antennas on a complex platform (airframe, ground station, etc.).
- 2007 – 2009: Part-Time Lecturer – University Carlos III of Madrid, Spain.
Higher Education
 Teaching engineering subjects ("Communications Electronics" and "Systems and Circuits") to under-graduate students (Telecommunication Engineering).
- 2002 – 2006: Electrical Engineer – RYMSA, Spain.
Defense & Electronics
 Company specialized in design/manufacturing of antennas and electronic systems. Definition and development of new products. Involved in the designing, prototyping, and certification/qualification phases.
 Responsible for the electrical design, test campaigns (electrical, mechanical, environmental, and EMC) and industrialization of prototypes.
 Planning and management of equipment manufacturing and system integration.
 Technical support to the commercial department.
 Main projects: SAAR 2000. Surveillance Radar Pedestal System; Satellite Base Stations boarded on High-Speed Trains; LPI. Radar Array Antenna System boarded on Military Ships; Land Radar Antenna. Antenna System for Coast Vigilance.
- 2002 – 2002: Communications Engineer Internship – X64, Matosinhos, Portugal.
Communications & Electronics
 Company specialized in design/manufacturing of wireless terminals.
 Analysis and definition of the integration of Bluetooth and IEEE 802.11 protocols in X64 wireless terminals.